ISBN 978-82-326-3176-6 (printed ver.)
ISBN 978-82-326-3177-3 (electronic ver.)
ISSN 1503-8181

Doctoral thesis

Vincent Canaguier

Doctoral theses at NTNU, 2018:193

NTNU
Norwegian University of Science and Technology
Thesis for the Degree of
Philosophiae Doctor
Faculty of Natural Sciences
Department of Materials Science and
Engineering

NTNU
Norwegian University of
Science and Technology

NTNU

Doctoral theses at NTNU, 2018:193

Vincent Canaguier

Synthesis and Reduction-Carburization of (Fe,Mg)(Cr,Al)$_2$O$_4$ Composite Spinel Solid Solution With CH$_4$

NTNU
Norwegian University of
Science and Technology

Vincent Canaguier

Synthesis and Reduction-Carburization of $(Fe,Mg)(Cr,Al)_2O_4$ Composite Spinel Solid Solution With CH_4

Thesis for the Degree of Philosophiae Doctor

Trondheim, June 2018

Norwegian University of Science and Technology
Faculty of Natural Sciences
Department of Materials Science and Engineering

NTNU
Norwegian University of
Science and Technology

NTNU
Norwegian University of Science and Technology

Thesis for the Degree of Philosophiae Doctor

Faculty of Natural Sciences
Department of Materials Science and Engineering

ISBN 978-82-326-3176-6 (printed ver.)
ISBN 978-82-326-3177-3 (electronic ver.)
ISSN 1503-8181

Doctoral theses at NTNU, 2018:193

Printed by NTNU Grafisk senter

Preface

This thesis is submitted to NTNU, the Norwegian University of Science and Technology, as partial fulfillment of the requirements for the degree of Philosophiae Doctor. The present work has been conducted at the Department of Material Science and Engineering at the Norwegian University of Science and Technology, Trondheim, Norway.

The funding was provided by the Research Council of Norway through the project "CORALSEA" (grant number 233825).

The author has conducted all the experimental and modeling work. The pelletizing was carried out by Edith Thomassen (past-SINTEF), the oxygen analyses were conducted by Anne Støre (SINTEF), and the microprobe analyses were conducted in collaboration with Morten Peder Raanes (NTNU).

Acknowledgements

First, I would like to acknowledge my supervisor Prof. Leiv Kolbeinsen (NTNU). I truly enjoyed these years of collaboration and learned so much from him, about metallurgy, Norway and more. He has always been available and helpful when I needed, and gave me the freedom to explore and venture the metallurgy field which I greatly value.

I would also like to thank my co-supervisor Dr. Eli Ringdalen (SINTEF) for her insights on the ferrochrome processes. I could always feel her passion for this field and I am glad we could work on this project together.

I am also grateful to Ingeborg-Helene Svenum (SINTEF), for her X-ray photoelectron spectroscopy analyses, as well as her valuable comments on the publications. I also want to thank the leader of my project, Halvor Dalaker (SINTEF), for the ideas and support.

For his accurate comments and our valuable discussion, I would like to acknowledge Prof. Tor Grande (NTNU).

Next, I would like to thank the whole SiManTi research group and its management, Profs. Merete Tangstad, Gabriella Tranell, Ragnhild Aune and Jafar Safarian. There might be three times more members in this group now that when I first joined, but each meeting still feels like a friendly gathering. Beyond the precious feedback, it was also a chance for socializing, networking and integration.

I am grateful to the technical staff of the Department of Material Science and Engineering at NTNU and of SINTEF Materials and Chemistry for the help and support. In particular, I would like to thank Dmitriy Slizovskiy, Jonas Einan Gjøvik, Ivar Andre Ødegård (NTNU) and Tine Eikevik (past-NTNU) for the technical support with the experimental work and Ingeborg Solheim as well as Bendik Sægrov-Sorte (SINTEF) for the help with the reduction-carburization set-up. Edith Thomassen (past-SINTEF) is also greatly acknowledged for the pelletizing. I am also grateful to Trygve Lindahl Schanche (NTNU) for the help with the sample preparation, and Yingda Yu and Morten Peder Raanes (NTNU) for the help with SEM and EPMA respectively. I would also like to acknowledge Anne Støre (SINTEF) for the oxygen analyses. Of course, the support from the administrative staff was also essential and I would like to thank Jostein Mårdalen, Elin Kaasen, Vidar Broholm and Hilde Nordø.

I could not thank enough my friends who helped me going through the long winter nights: David, Dehlia, Espen, Raghed (thanks for the rereading!) and Rune. They are my family here in Norway.

Finally, I want to thank my parents, Joëlle and Jean, for their tremendous support throughout the years. I always appreciated our calls, the Comté cheese packages and the holidays at home. I want to also thank my sister, Margaux, who cannot wait to come to the defense. I really appreciated each of her visits and her encouragements.

Abstract

Chromium is an essential alloying element for the stainless steel industry. It is usually produced as ferrochrome from chromite ore through electricity intensive processes. Pre-reduction of the chromite ore, using solid carbon as reductant, can also be used to relieve the smelting operation. But hydrocarbon gases could potentially be used instead as the carbon source, allowing a reaction at lower temperature.

This study focuses on the effect of magnesium and aluminium impurities on the reduction-carburization of chromite by methane gas. Previous work shows that methane readily carburizes chrome oxides at low temperatures, but that natural chromite ores, rich in impurities, are more challenging. To better understand the effect of impurities, chromites with controlled amounts of magnesium and aluminium are synthesized and further reacted in by methane-containing gas mixture.

Four chromite solid solutions compositions were produced by the induction skull melting technique from pure oxides and metallic iron. Their composition as well as the naming used throughout the present work are given in **Table 1**:

Table 1: Synthetic chromite composition and naming

Targeted stoichiometry	Referred composition	Referred code letter
$FeCr_2O_4$	$FeCr_2O_4$	A
$(Fe_{0.75}, Mg_{0.25})Cr_2O_4$	$(Fe, Mg)Cr_2O_4$	B
$Fe(Cr_{0.75}, Al_{0.25})_2O_4$	$Fe(Cr, Al)_2O_4$	C
$(Fe_{0.75}, Mg_{0.25})(Cr_{0.75}, Al_{0.25})_2O_4$	$(Fe, Mg)(Cr, Al)_2O_4$	D

After pelletization and hardening in argon gas, the material was reduced and caburized in a vertical alumina tube furnace. The gas analysis was used to follow the reduction reaction's progress. For each material, the temperature and duration were the main parameters used.

The four materials used behaved in a very different ways. Pure iron chromite was readily reduced-carburized, forming porous carbides as a product. Magnesium additions mostly stabilized the spinel solid solution, making the reaction more challenging. Aluminium additions, with or without the presence of magnesium, led to similar rates but extensive carbon deposition accompanied the reduction-carburization process. Kinetic modeling of the reaction revealed the importance of the diffusion control at 950 °C for these materials. The reaction of samples containing both magnesium and aluminium was significantly faster than when magnesium is the sole impurity.

Overall, the reduction-carburization of chromite by methane gas is promising, as high extents of reduction could be achieved at much lower temperatures than today's carbothermic pre-reduction processes.

Contents

List of Figures

List of Tables

List of Symbols

Chemical formulas

Al_2O_3	corundum
Ar	argon
CaO	calcium oxide
CH_4	methane
C_3H_8	propane
CO	carbon monoxide
CO_2	carbon dioxide
Cr_2O_3	chromium sesquioxide
Cr_3C_2	chromium carbide
Fe_2O_3	hematite
Fe_3O_4	magnetite
$FeAl_2O_4$	hercynite
$FeCr_2O_4$	iron chromite
H_2	dihydrogen
H_2S	dihydrogen sulfide
M^{2+}	divalent metallic cation
M^{3+}	trivalent metallic cation
M_iC_j	carbide with i metal atoms and j carbon atoms
M_iO_j	oxide with i metal atoms and j oxygen atoms
MgO	magnesium oxide
$MgAl_2O_4$	spinel
$MgCr_2O_4$	magnesiochromite
$MgFe_2O_4$	magnesioferrite
MnO	manganese oxide
SiO_2	silicon dioxide
TiO_2	titanium dioxide

Symbols

a_i	activity of solute i
a, b, c, d	stoichiometric coefficients
(ad)	adsorbed
d	for Bragg's law, lattice spacing
f^O	fraction of oxygen available
(g)	gas
g	as subscript, grain
$g_{F_i}(\alpha)$	chemical reaction conversion equation, $i = g$ or p
gr	as subscript, graphite
h_D	mass transfer coefficient
id	as superscript, ideal
k	reaction rate constant
k_0	frequency factor
m_i, m_f	initial and final mass
n	for Bragg's law, order
n, n_S	exponent for the JMAK and E-JMAK equations
n_i	amount of moles of i entering the furnace
$\overline{n}_i$	amount of moles of i leaving the furnace
nc	as superscript, non-configurational
p	as subscript, pellet
$p_{F_i}(\alpha)$	diffusion conversion equation, $i = g$ or p
r	as subscript, reaction
(s)	solid
t	time
t^*	dimensionless time
t_0	time delay
tot	as subscript, total
w_i, w_f	initial and final oxygen mass fraction
x_i	molar fraction of i entering the furnace
$\overline{x}_i$	molar fraction of i leaving the furnace
xs	as subscript, excess

A_g, A_p	external surface area of a grain or pellet
C_i	molar concentration of i
D	diffusivity of metal cations
D_e	effective diffusivity in the pellet
D_g	effective diffusivity of the product layer of a grain
E_a	activation energy
EoR	extent of reduction
F_g, F_p	shape factor of a grain or pellet
K_{eq}, K_E	equilibrium constant
P_i	partial pressure of i
N_{Sh^*}	modified Sherwood number
$\{\mathrm{N}_i\}$	fraction of i in tetrahedral sites of a (X,Y) spinel
$[\mathrm{N}_i]$	fraction of i in octahedral sites of a (X,Y) spinel
R	gas constant
R_g, R_p	radius of a grain or pellet
T	temperature
V	interface velocity
V_g, V_p	volume of a grain or pellet
X	ionic fraction of Mg^{2+} in the tetrahedral interstices of the spinel
Y	ionic fraction of Al^{3+} in the octahedral interstices of the spinel
Z	ionic fraction of Al^{3+} in the $(Cr, Al)_2O_3$ solid solution

α	fractional conversion
ΔG	change in Gibbs free energy
ΔH	enthalpy change
ϵ	porosity of the pellet plus volume occupied by inert solids
η_i	impingement parameter
θ	incident angle
λ	wavelength of the incident wave
Ω_{i-j}	binary parameter for $i - j$
ρ_s	molar concentration of solid reactant
$\hat{\sigma}^2$	generalized gas-solid reaction modulus
$\hat{\sigma}_g^2$	shrinking core reaction modulus for the grain

Abbreviations

AC	alternating current
ANSTO	Australian Nuclear Science and Technology Organisation
AR	Austin-Rickett
CCIF	cold crucible induction furnace
CDR	chrome direct reduction
CMI	Consolidated Metallurgical Industries
DC	direct current
EDS	energy-dispersive X-ray spectroscope
EPMA	electro probe microanalyzer
E-JMAK	extended Johnson-Mehl-Avrami-Kolmogorov
HCFeCr	high carbon ferrochrome
ISMT	induction skull melting technique
JMAK	Johnson-Mehl-Avrami-Kolmogorov
NTNU	Norwegian University of Science and Technology
SDK	Showa Denko
SEM	scanning electron microscope
SRC	solid state reduction process for chromium ore

Chapter 1

Introduction

1.1 Chromite and chromite ore

Chromite, also referred to as iron chromite $FeCr_2O_4$, is an iron chromium oxide composed of iron (II) oxide and chromium (III) oxide. But chromite also refers to a solid solution mineral whose end-members are iron chromite ($FeCr_2O_4$), hercynite ($FeAl_2O_4$), picrochromite or magnesiochromite ($MgCr_2O_4$), *spinel* ($MgAl_2O_4$), magnetite (Fe_3O_4) and magnesioferrite ($MgFe_2O_4$). Some other metals can be found in minor quantities hence $(Fe, Mg)(Cr, Al, Fe)_2O_4$ is often used to refer to mineral chromite [1]. In natural chromites, even after separation from the gangue minerals, other oxides such as SiO_2, CaO, MnO or TiO_2 can be found in limited amounts for example as inclusions [2]. Chrome ores, which contain chromite minerals, have different deposit types. These are by essence linked to the composition and quality of the ore and therefore to its end use. Chromite ore can be found in *stratiform*, *podiform*, beach sands and *laterite* deposits. A usual classification combining composition, type of deposit and main use is given in **Table 1.1**.

Table 1.1: Classification of chrome ore by composition, ore type and deposit [1]

Class of ore	Composition (wt%)	Type of deposit	Main use
High-Cr or Metallurgical grade	Cr_2O_3 46-55% Cr/Fe>2:1	Podiform and Stratiform	Metallurgical
High-Fe or Chemical grade	Cr_2O_3 42-46% Cr/Fe<2:1	Stratiform	Metallurgical and Chemical
High-Al or Refractory grade	Cr_2O_3 33-38% Al_2O_3 22-34%	Podiform	Refractory

1.2 The ferrochromium production routes

Chromium is used mainly in the form of ferrochromium as an additive to produce stainless steel. As an alloying element in steel, chromium has no substitute for its role and despite important world resources, chromite ores are of a strategic importance due to their geographical distribution [3]. Low and medium carbon ferrochrome are produced using high carbon ferrochromium as a raw material or by metallothermic chromite reduction reactions. Only the production of high carbon ferrochrome will be detailed hereafter because of its carbothermic nature and its importance.

1.2.1 Furnace technologies

In the present section, AC and DC arc furnaces are presented. AC arc furnaces represent the majority of the technologies in use [4].

Submerged arc AC furnaces

Submerged arc AC furnaces can be of open, semi-open or closed designs. In submerged arc AC furnaces for HCFeCr production three Søderberg electrodes are submerged into the charge. Heat is released by resistance heating, enabling high enough temperature for carbothermic reduction. A schematic of a submerged arc AC furnace is given in **Figure 1.1**.

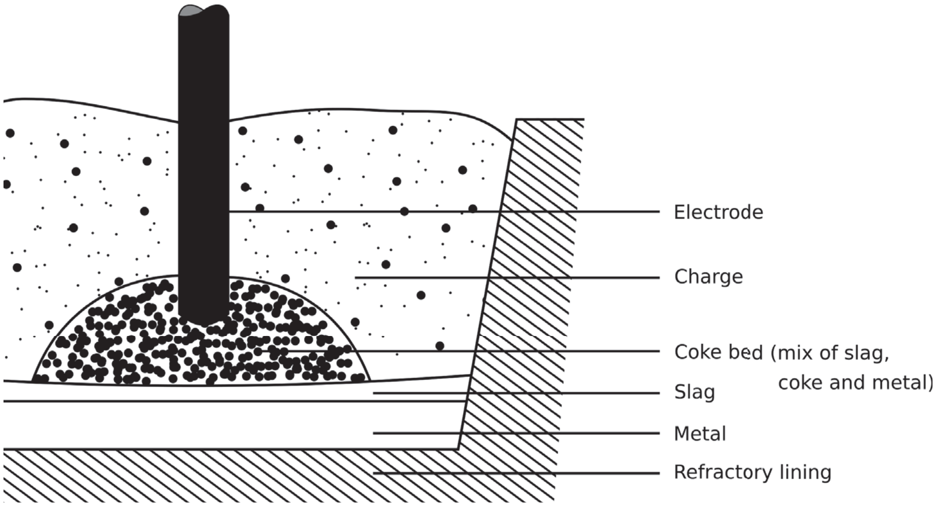

Figure 1.1: Schematic view of a submerged arc AC furnace

Open and semi-open submerged arc AC furnaces have no, or an open roof, which allow air to enter in the furnace. These furnaces are characterized by higher specific energy consumption, lower metallurgical efficiencies and are overall of a lower capacity than other technologies [4]. The capture of airborne emission is possible, but not always done. However, because of their design, open submerged arc furnaces are easier to operate. The raw materials requirements are lower, in particular concerning the fines content [4]. Closed submerged arc furnaces, as indicated by their name, have a closed roof. The larger size of these furnaces puts constrains on the raw materials, especially the sizing, as gaseous flow through the charge must be ensured. Because the electric energy used in arc furnaces is substantial, closed submerged arc AC furnaces preceded by a pre-heating or a pre-reduction unit have been developed. A pre-heating unit can advantageously use exhaust gases from the furnace, or a cheaper energy source. A pre-reduction unit can help to replace electrical energy by another form of energy, such as chemical, to reduce the electrical consumption during smelting. Multiple technologies have been established, although not all of them are in use, and are presented afterwards.

Open arc DC Furnace

Even though developed earlier than AC furnaces, open arc DC furnaces appeared in the smelting industry relatively recently. A schematic of a DC furnace is given in **Figure 1.2**. Because AC and DC furnaces' design are fundamentally different, the operating conditions are not alike. Overall, open arc DC furnaces offer better metallurgical efficiencies while working with lower constrains on the raw material sizing and quality [4]. These furnaces also impose a lower disturbance on the electrical grid [5]. However, open arc DC furnaces remain difficult to operate and have higher electrical energy consumption due to radiating heat losses [6].

1.2.2 Pre-heating technologies

In addition to the "natural" pre-heating due to ascending gases through the charge in submerged arc furnaces, an addition pre-heating stage can be installed upstream. A known example of pre-heating within the HCFeCr industry is found in the Outotec ferrochrome process [4; 7]. This process comprises a pre-heating shaft kiln above the furnace, where ascending gases are used. Thus, descending furnace charge are heated before entering the furnace. According to Slatter, pre-heating could be even more beneficial when using an open arc DC furnace smelting unit with gains in the order of 1 MWh/t alloy and an increase by 30% of the furnace output [6]. The DC technology uses

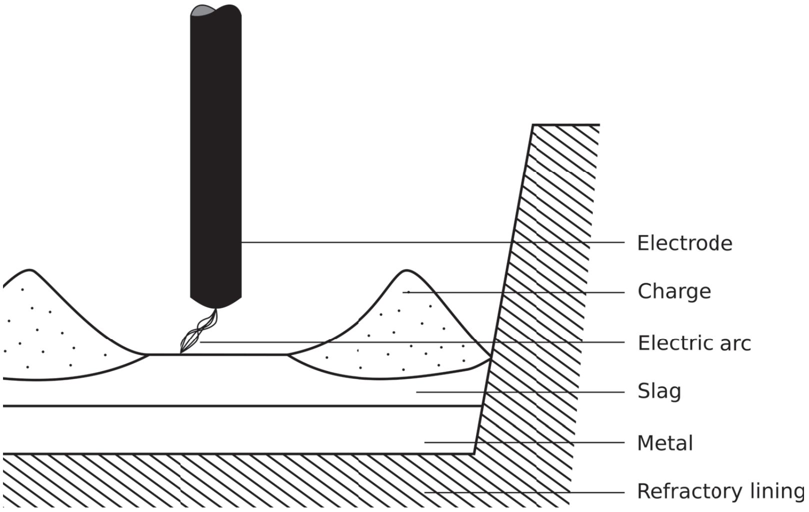

Figure 1.2: Schematic view of an open arc DC furnace

fines as a raw material, which makes conceivable the use of a fluidized bed reactor upstream. To the knowledge of the author, even though such equipment was ready for commercialization, is has not yet been installed on open arc DC furnaces [6].

1.2.3 Pre-reduction technologies

As mentioned earlier, pre-reduction units can be used to reduce the electrical energy consumption for the chromite smelting process. While several technologies have been established, only some are in use. Most of these technologies employ solid carbon as a reductant, but one must distinguish the uncommon process established by Kawasaki Steel Corporation [8], which did not lead to any industrial use.

Solid carbon-based technologies

All the pre-reduction processes that have been developed and used commercially can be seen as descendants of the SRC Process established in the seventies. This process, also called SDK/CMI process after its developer and user Showa Denko (SDK) and second user Consolidated Metallurgical Industries (CMI), used a rotary kiln where pellets of chromite mixed with coke are reacted at 1400 °C. The metallization degree obtained by this process was found to reach around 60% for Cr and Fe [6]. For Cr metallization specifically, the SDK plant reached values of 70%, while CMI plants only reached 50% [4]. Continuing with a rotary kiln based pre-reduction unit, the CDR process developed in the mid-eighties by Krupp, later with Middelburg Steel and Alloys (MS&A) and Samancor aimed at using non-agglomerated fines and low cost coal. The fines agglomerated while reacting at temperatures as high as 1500 °C and the metallization degree reached 80% to 90% [6; 7]. The latest and most energy effective rotary kiln process is Xtrata's (now Glencore) Premus process. This process developed from 1998 and in use from 2006 involves chromite fines pelletization with anthracite and binder, and later pre-reduction at temperatures up to 1300 °C [9]. The philosophy of this technology was the optimization of the energy use and not the metallization degree, which makes it the most energy efficient technology for ferrochromium production [9]. The last technology to mention for pre-reducing chromite ores with solid carbon is a rotary hearth furnace developed by INMETCO [10]. In this process, pellets are reacted with coal at temperatures reaching 1450 °C and metallization degrees up to 80%. However, the pellet would re-oxidize with this technology, which did not go past the pilot scale [6].

Hydrocarbon-based technologies

In the eighties, Kawasaki attempted to use methane (CH_4) and propane (C_3H_8) as reductants for pre-reduction in a fluidized bed reactor. The underlying idea is to take advantage of the low reaction temperature of chromite reduction-carburization with CH_4 to allow a fluidized bed technology [6]. Fines were successfully reacted at 1100°C in a bench scale reactor, reaching metallization degrees up to 71% for Fe and 40% for Cr [6], the best scenario involving C_3H_8 and pulverized coke additions [8]. As noted by Slatter, the reaction mechanism remains obscure at this stage and needs further investigation, and to the knowledge of this author, Kawasaki did not persist in elaborating a methane based pre-reduction technology [6].

1.2.4 Summary and process routes

Although each plant has its own features, the processes can be organized in four main routes [4]: open/semi-open submerged arc AC furnace (conventional route), DC arc furnace, closed submerged arc AC furnace and closed submerged arc AC furnace with pre-reduction unit. These routes and the most known processes associated are summed-up in **Figure 1.3**. The pilot technologies mentioned earlier as potential alternatives are distinguished by the use of a dashed line.

The overall evolution of the ferrochrome submerged arc furnaces-based processes, from the conventional route to the recent Premus process, indicate that improvements were achieved through a segmentation of the smelting activity in different work units. Pre-heating and pre-reduction steps were both key in reducing the electrical energy

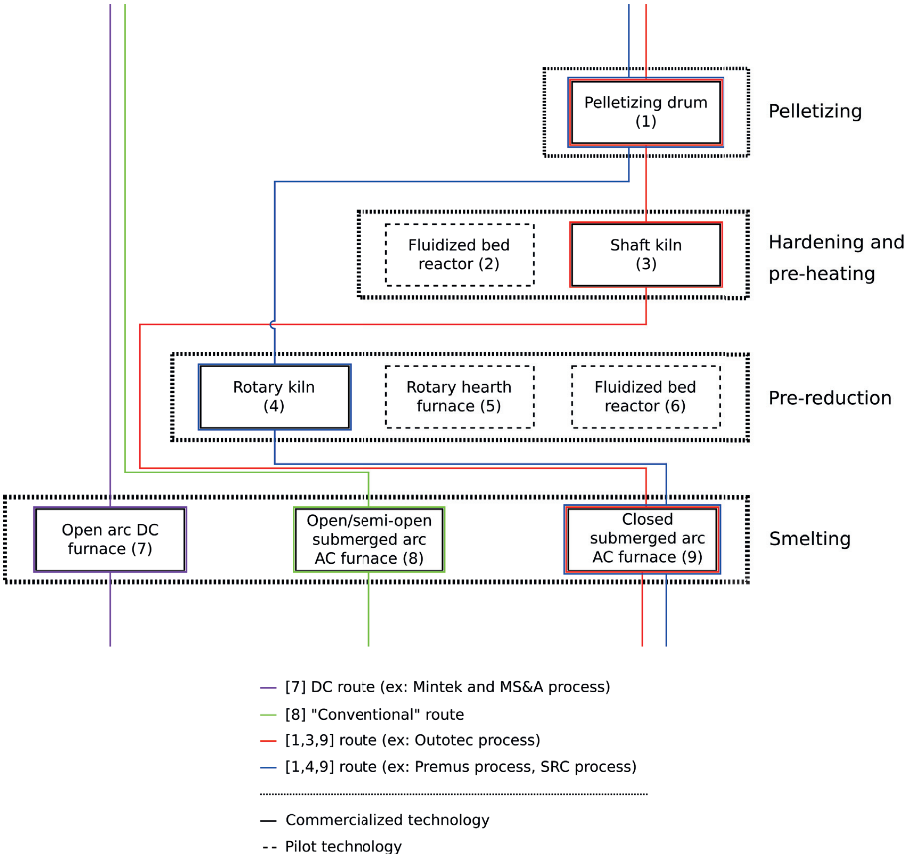

Figure 1.3: The principal features of the four main production routes for ferrochrome

use and to increase the smelting furnace outputs. This trend of "division of the smelting function" should persist according to Nelson, ultimately facilitating the increase in furnace size [11].

1.3 Scope of the thesis

There has been a lot of work to develop the chromite ore pre-reduction by solid carbon in rotary kilns, with a fair success. In comparison, the use of hydrocarbon gases has not been extensively considered. However, the important use of electricity with smelting technologies presented earlier and the steep price increase for electricity in South Africa, which tripled between 2008 and 2015 [12], is a certain driving force for the development of alternative technologies. Such technologies could possibly use the chemical energy available in methane. Although positive results were obtained by Kawasaki Steel Corporation [8] no commercial technology has been developed. Slatter avowedly noted that the reaction mechanisms were not fully understood [6].

The present work aims at studying the reduction-carburization reactions between synthetic chromite and methane containing gas mixtures between 950 and 1050 °C. With synthetic ores, a higher control on the composition and purity is made possible. The composition of the synthetic chromite is varied to investigate the influence of Mg and Al impurities on the reactions. The synthetic chromites are produced by the induction skull melting technique in which the amount of each impurity was controlled. For each chromite composition, the reduction-carburization mechanism is investigated by isothermal experiments. Many experimental parameters could be varied to better suit each material. However, in this work, the parameters were kept the same with the different material in order to have comparable results.

Kinetic modeling of the experiments is performed to evidence trends and differences between the solid solution's compositions. Ultimately, the intent of this study is to acquire a better understanding of the reactions between chromite and methane for pre-reduction purposes.

Chapter 2 provides the theoretical knowledge applicable to this work. Insights on the oxide and carbide phases are provided. A literature review of the relevant previous studies of chromium oxide and chromite interactions with methane is also given. Finally, theoretical elements relative to the kinetic modeling of the reaction are provided.

Chapter 3 describes the set-up used for the synthesis and the gas-solid reduction-carburization experiments. The procedure and experimental parameters are also detailed. Then, the analysis techniques employed are briefly introduced.

Chapter 4 reports the experimental results. This includes the results from the synthesis work and the product characterization as well as the reduction-carburization results. The series of experiment on each of the four chromite composition produced is reported in a distinct section. The last section aims at comparing the aforementioned series.

Chapter 5 presents the modeling work done on the kinetics of the reduction. The various parameters are discussed in the light of the experimental results, and a modeling is proposed. The modeling is mainly used as a tool to further discuss the consequences of Mg and Al impurities on the reaction mechanism.

Chapter 6 discusses the previous results and modeling sections. The findings are confronted with the theory and related studies. The effect of each impurity on the mechanism is explained on the basis of the findings.

Chapter 7 summarizes the study and highlights the main findings of the work.

Chapter 8 suggests directions which could be followed in the future to investigate the use of methane for pre-reduction of chromite.

The terms written in italics upon their first appearance in the text are further defined in the glossary available at the end of the thesis.

Chapter 2

Theory

This chapter provides the theoretical background for the present work. The oxide system is first considered in **Section 2.1** followed by the carbide system in **Section 2.2**. Previous studies on chromium oxide, synthetic and natural chromites are detailed in **Section 2.3**. The theoretical elements relevant to study the kinetics of the reaction are next given in **Section 2.4**. Finally, the structure changes and their consequences are presented in **Section 2.5**.

2.1 The oxide system

Although a variety of oxides can be found in natural chromite [2], the bulk is mainly composed of the chromite spinel solid solution. The aim of the following section is to provide knowledge on the spinel oxides, in terms of structure, composition and thermodynamic properties.

2.1.1 The spinel group

The spinel group has been thoroughly explained by Deer *et al.* [13]. The structure consists of a cubic close packing of oxygen atoms whose interstices are partly filled by metallic cations. Two types of interstices can be found in the cubic close packing of oxygen atoms: tetrahedral interstices and octahedral interstices which lies between four and six atoms of oxygen respectively. A representation of tetrahedral and octahedral interstices is given in **Figure 2.1**. For a cell containing 32 oxygen atoms, there is a total of 64 tetrahedral interstices and 32 octahedral interstices. Only 8 tetrahedral and 16 octahedral interstices are occupied by cations. In spinels termed as “normal”, 8 divalent cations are occupying tetrahedral sites and 16 trivalent cations are occupying octahedral sites. In “inverse” spinels, the 8 divalent cations are occupying octahedral sites while the 16 trivalent cations are equally split between tetrahedral and octahedral sites. The distribution of the cations in normal and inverse spinel can be found in **Table 2.1**.

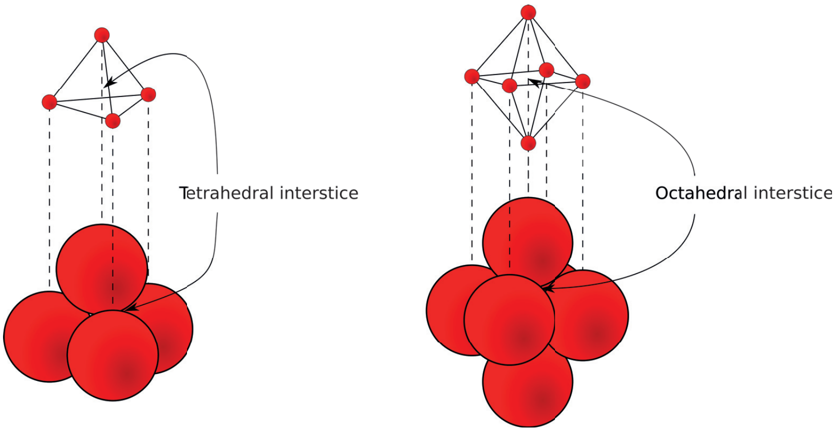

Figure 2.1: Position of tetrahedral and octahedral interstices in a cubic close packing of oxygen

Table 2.1: Distribution of cations in interstitial sites for normal and inverse spinels

Spinel type		Tetrahedral site	Octahedral site
Normal	Divalent cations	8/64	0/32
	Trivalent cations	0/64	16/32
Inverse	Divalent cations	0/64	8/2
	Trivalent cations	8/64	8/32

2.1.2 The natural chromites

The subspace of the spinel group corresponding to natural chromites can be written $(\mathrm{Fe}, \mathrm{Mg})[\mathrm{Cr}, \mathrm{Al}, \mathrm{Fe}]_2\mathrm{O}_4$ where the parentheses and brackets refer to the atoms in the tetrahedral and octahedral interstices respectively. It is delimited by four normal spinel end-members: chromite ($\mathrm{FeCr_2O_4}$), hercynite ($\mathrm{FeAl_2O_4}$), magnesiochromite ($\mathrm{MgCr_2O_4}$) and spinel ($\mathrm{MgAl_2O_4}$). Two inverse spinel end-members also limit the solid solution: magnetite ($\mathrm{Fe_3O_4}$) and magnesioferrite ($\mathrm{MgFe_2O_4}$). To account for the occurrence of each species, Stevens referred to natural chromite as $(\mathrm{Mg}, \mathrm{Fe})\mathrm{O} \cdot (\mathrm{Cr}, \mathrm{Al}, \mathrm{Fe})_2\mathrm{O}_3$ [14]. The natural chromite subspace is represented in **Figure 2.2** by a red outline and "x" is a variable between 1 and 1.5 [15].

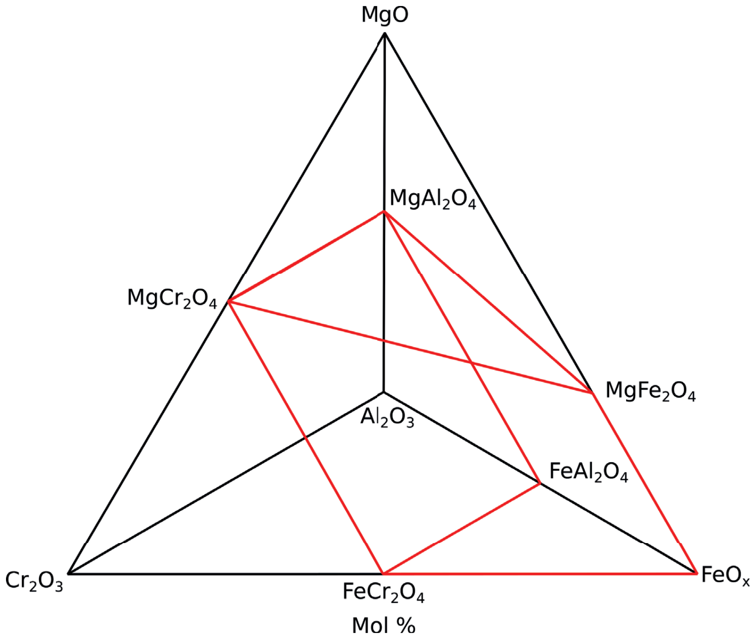

Figure 2.2: The natural chromite subspace [15]

The MO/M_2O_3 ratio between divalent and trivalent metal oxides in the spinel was studied by Stevens on American chromites. While most of the samples analyzed were in agreement with a ratio of 1, some samples exhibited large deviations which were attributed to an oxidation of divalent iron and further *exsolution* from the spinel [14]. Exsolution, resulting from exposure to an oxidative environment, was observed in a greater detail in natural ores [16], and experimentally at low temperature [17]. However, Muan noted that the natural chromite solid solutions do tolerate large variations in their MO/M_2O_3 ratios. These observations were made in the MgO-Fe_2O_3-Al_2O_3 domain at 1250 °C in air [15].

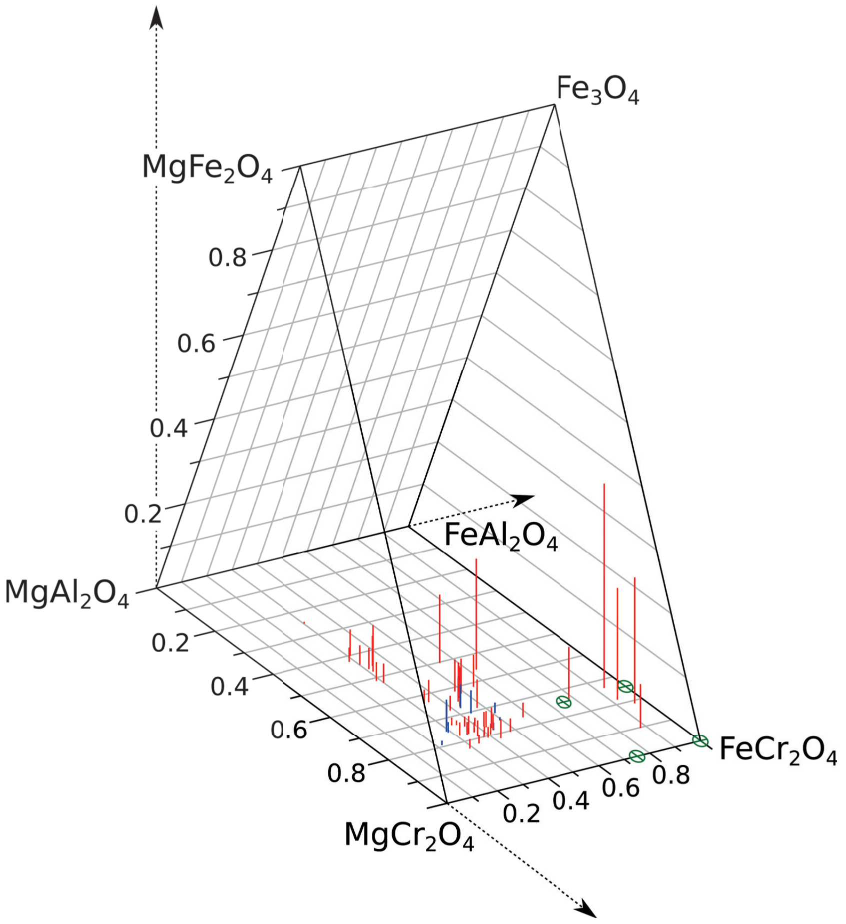

Figure 2.3: American chromites (red) and Indian chromites (blue) composition on the $(\mathrm{Fe, Mg})(\mathrm{Cr, Al, Fe})_2\mathrm{O}_4$ composition prism [14; 15]. The top of each line indicates the composition in the 3D figure. The synthesized samples produced in the current work are indicated by a circled green cross

The natural chromites can exhibit a broad range of compositions, which varies with the deposit and within the deposit. To illustrate these composition variations, American and Indian chromites were plotted on a composition prism in **Figure 2.3**. In this figure, the base of each composition line gives information on the Mg^{2+}/Fe^{2+} ratio as well as the Al^{3+}/Cr^{3+} ratio. The top of the line locates the composition in the prism. A majority of the natural chromite compositions reported in the figure exhibit a low amount of Fe^{3+} cations.

2.1.3 Thermodynamic considerations in the spinel system

The normal spinel end-members are $FeCr_2O_4$, $MgCr_2O_4$, $FeAl_2O_4$ and $MgAl_2O_4$. All these spinel compounds melt congruently as reported in **Table 2.2**. The melting points reported are obtained from the *Slag Atlas* (1995) [18] and the original work when applicable.

Table 2.2: Phase stability of the FeO-MgO-Cr_2O_3-Al_2O_3 spinel solution end-members

Compound	Melting point	Melting type	Reference
$FeCr_2O_4$	2100 °C	Congruent	[18]
$MgCr_2O_4$	2400 °C	Congruent	[18; 19]
$FeAl_2O_4$	1780 °C	Congruent	[20]
$MgAl_2O_4$	2135 °C	Congruent	[21; 22]

The iron-containing binary systems exhibited a very contrasting behavior in air. Muan and Somiya studied the phase relations in the $Cr_2O_3-FeO_x$ in air and evidenced that Cr_2O_3 had a stabilizing effect on the hematite structure [23]. Their results, shown in **Figure 2.4**, are projected on the $Fe_2O_3-Cr_2O_3$ axis.

Muan and Gee studied the phase relations in the $Al_2O_3-FeO_x$ system in air and 1 atm oxygen [24]. The phase relations for this system in air are represented in a pseudo-binary diagram in **Figure 2.5**. It was specifically noted that below 1380 °C the only stable phase consists of sesquioxides, namely hematite, corundum, or the $(Fe, Cr)_2O_3$ solid solution. At high temperature, ferric oxide dissociated to ferrous oxide and oxygen gas. This means that the control on the oxygen partial pressure is key to the stability of spinel compounds containing iron. During the hardening of the material, chromite will oxidize to a sesquioxide solid solution when exposed to air.

To estimate the melting temperature of the solid solution, the liquidus temperature was calculated discretely for various compositions of the solid solution, i.e. for multiple values of X and Y for the $(Fe_{1-X}, Mg_X)(Cr_{1-Y}, Al_Y)_2O_4$ formula. The data presented in **Figure 2.6**, calculated using the FactSage software, shows that an increased content

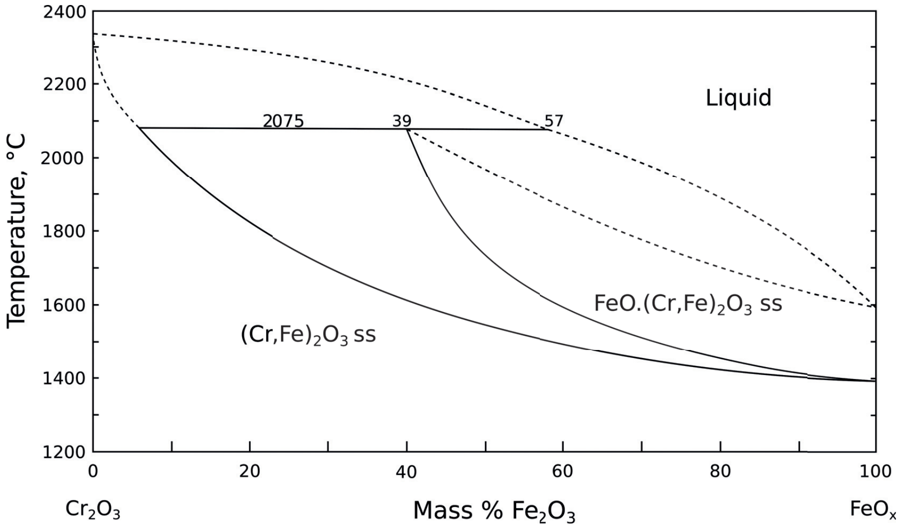

Figure 2.4: The $Cr_2O_3 - FeO_x$ binary system in air at 1 atm [18]

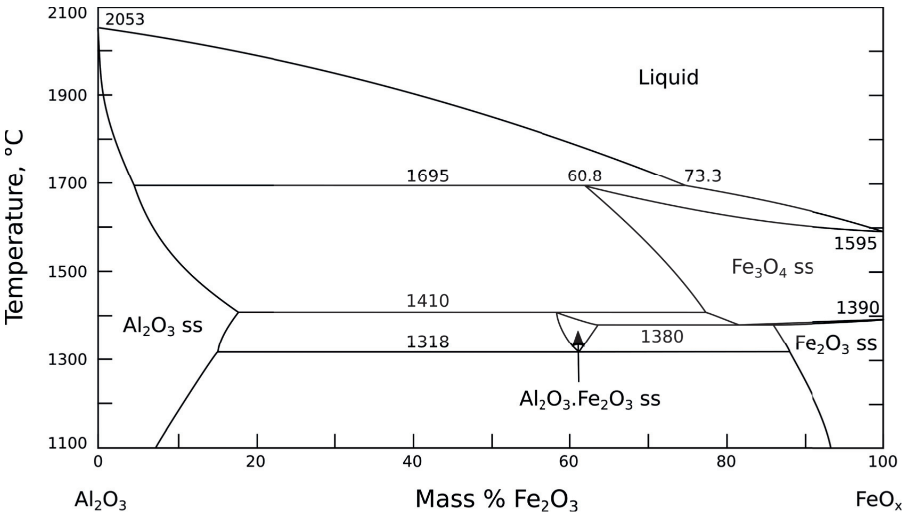

Figure 2.5: The $Al_2O_3 - FeO_x$ binary system in air at 1 atm [18]

of magnesium (increase of X) increases the liquidus temperature while an increased aluminium content (increase of Y) decreases the liquidus temperature.

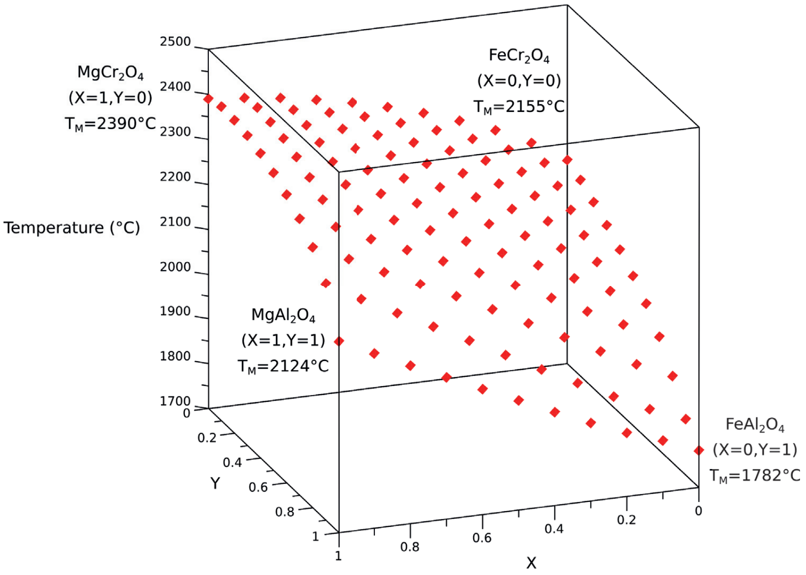

Figure 2.6: Discrete simulation of the liquidus surface of the $(Fe, Mg)(Cr, Al)_2O_4$ spinel solid solution

These data can be used to evaluate the adjustments needed in terms of power input during synthesis, if using a molten route.

2.1.4 Thermodynamic modeling of the $(Fe_{1-X}, Mg_X)(Cr_{1-Y}, Al_Y)_2O_4$ solid solution

Jacob and Behera developed a modified regular solution model to calculate the activity of the end-member constituents in the $(Fe, Mg)(Cr, Al)_2O_4$ reciprocal spinel solid solution [25]. From the start, they excluded the presence of trivalent iron cations to simplify the system on the basis on their easy reduction to divalent cations. The model is based on the distribution of cations in the tetrahedral and octahedral sites according to temperature, site preference energies and Jahn-Teller distortions [26; 27]. The cation distribution is used to compute the activities in the ideal spinel solid solution. Finally, non-ideal behavior is modeled by a regular solution based on binaries of the end members ($FeAl_2O_4$-$MgAl_2O_4$, $FeCr_2O_4$-$MgCr_2O_4$, $MgCr_2O_4$-$MgAl_2O_4$, $FeCr_2O_4$-$FeAl_2O_4$). In **Figure 2.7**, the flowchart used for the calculations is provided. The significance of the calculated quantities is explained is the next section.

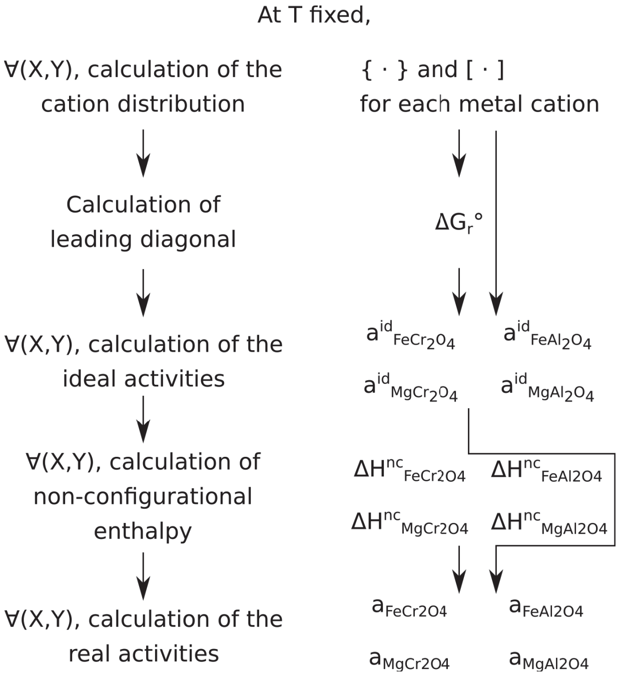

Figure 2.7: Flowchart of the thermodynamic modeling

The model was further used to consider an equilibrium between a $(\mathrm{Al}_Z,\mathrm{Cr}_{1-Z})_2\mathrm{O}_3$ phase and a $(\mathrm{Fe}_{1-X},\mathrm{Mg}_X)(\mathrm{Cr}_{1-Y},\mathrm{Al}_Y)_2\mathrm{O}_4$ spinel. The formulation of the model, as given by Jacob and Behera, is provided next.

Distribution of the cations

The first step consists in determining the distribution of divalent and trivalent cations in tetrahedral and octahedral interstices. The shift of a cation from one site to another corresponds to the intracrystalline ion exchange and is a measure at a given temperature of the disposition of the solid solution to form an inverse spinel from a normal one. In practice, upon heating, the following reactions are taken into account:

$$\{\mathrm{Fe}^{2+}\} + [\mathrm{Cr}^{3+}] \rightarrow \{\mathrm{Cr}^{3+}\} + [\mathrm{Fe}^{2+}] \tag{2.1}$$

$$\{\mathrm{Mg}^{2+}\} + [\mathrm{Cr}^{3+}] \rightarrow \{\mathrm{Cr}^{3+}\} + [\mathrm{Mg}^{2+}] \tag{2.2}$$

$$\{\mathrm{Fe}^{2+}\} + [\mathrm{Al}^{3+}] \rightarrow \{\mathrm{Al}^{3+}\} + [\mathrm{Fe}^{2+}] \tag{2.3}$$

$$\{Mg^{2+}\} + [Al^{3+}] \rightarrow \{Al^{3+}\} + [Mg^{2+}] \qquad (2.4)$$

where $\{\cdot\}$ indicates tetrahedral sites and $[\cdot]$ octahedral ones. To determine the ion distribution, the ion exchange reactions are taken at equilibrium under the constrain of mass balance equations. One should note that when Fe and Cr cations are involved, an additional entropy term is added to take into account distortions of the spinel structure. The mixing of the various cations is assumed to be ideal in both tetrahedral and octahedral sites resulting in the mole fraction to be calculated directly.

Calculation of the ideal activities

The spinel solid solution of interest $(Fe_{1-X}, Mg_X)(Cr_{1-Y}, Al_Y)_2O_4$ is a ternary reciprocal system, and two coordinates must be used to accurately describe its thermodynamic properties. Although each point in **Figure 2.8** can be obtained by a mixture of only three of the end-members, the four pure spinels indicated at the corners must be considered.

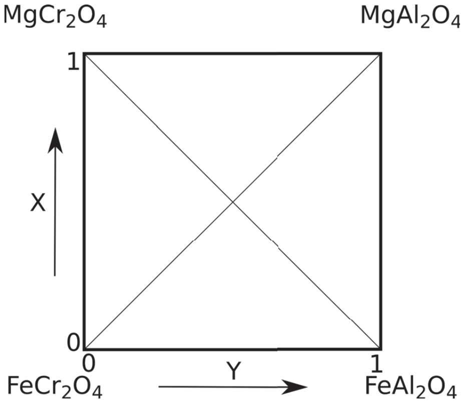

Figure 2.8: Ternary reciprocal system for the $(Fe, Mg)(Cr, Al)_2O_4$ spinel solid solution

In such systems it is of interest to determine the “leading diagonal” by calculating ΔG_r°, the Gibbs free energy of the reciprocal reaction provided in **Equation 2.5**. This result is based on the work on salts (in german) from Flood and coworkers, as reported by Rosenqvist [28]. In this equation, the spinels are taken at their standard state, that is in a pure form and without intracrystalline ion exchanges.

$$FeAl_2O_4 + MgCr_2O_4 = FeCr_2O_4 + MgAl_2O_4 \qquad (2.5)$$

Still assuming ideal mixing in the two cation sublattices, the activities of each end-member in the solid solution can be calculated as follows, taking $FeCr_2O_4$ as example:

$$a^{\mathrm{id}}_{\mathrm{FeCr_2O_4}} = \frac{\left\{\mathrm{N_{Fe^{2+}}}\right\}\left[\mathrm{N_{Cr^{3+}}}\right]^2}{\left\{\mathrm{N^0_{Fe^{2+}}}\right\}\left[\mathrm{N^0_{Cr^{3+}}}\right]^2}\exp\left(\frac{-XY\Delta G^\circ_{\mathrm{r}}}{RT}\right) \tag{2.6}$$

where “id” indicates that the activities are calculated for an ideal mixing in the cation sublattices.

Calculation of the real activities

If the cations are interacting with each others in the sublattices, deviations are likely to be observed. In the present case, these interactions are taken into account by a non-configurational enthalpy term ΔH^{nc} defined from the binary interactions and written as follows:

$$\begin{aligned}\Delta H^{\mathrm{nc}} &= X(1-X)(1-Y)\Omega^{nc}_{\mathrm{FeCr_2O_4-MgCr_2O_4}}\\ &+ X(1-X)Y\Omega^{nc}_{\mathrm{FeAl_2O_4-MgAl_2O_4}}\\ &+ X(1-Y)(1-X)\Omega^{nc}_{\mathrm{FeCr_2O_4-FeAl_2O_4}}\\ &+ Y(1-Y)X\Omega^{nc}_{\mathrm{MgCr_2O_4-MgAl_2O_4}}\end{aligned} \tag{2.7}$$

The partial non-configurational enthalpies for each end-members are then calculated from the plane tangent to the non-configurational enthalpy surface. Finally, the activity of an end-member is calculated from the ideal activity obtained earlier, and the non-configurational partial enthalpy as follows:

$$\mathrm{RTln}\left(a_{\mathrm{FeCr_2O_4}}\right) = \mathrm{RTln}\left(a^{\mathrm{id}}_{\mathrm{FeCr_2O_4}}\right) + \Delta H^{\mathrm{nc}}_{\mathrm{FeCr_2O_4}} \tag{2.8}$$

The procedure used by Jacob and Behera was replicated to obtain values in the same system, but at three other temperatures, based on their studies [25; 26]. In **Table A.1** to **A.3** in **Appendix A**, the calculated activities of $FeCr_2O_4$, $MgCr_2O_4$, $FeAl_2O_4$ and $MgAl_2O_4$ are provided for 1223, 1273 and 1323 K respectively. The calculated activities for $FeCr_2O_4$ at 1273 K are also shown in **Figure 2.9** where large deviations from ideality are observed.

Note that to obtain the activity of an end-member for a given solid solution composition, one has to calculate the cations distribution according to **Equation 2.1** to **2.4** and the mass balance and calculate each of the four ideal activities as in **Equation 2.6** for each (X,Y) couple. Finally, the real activities are calculated for each (X,Y) couple us-

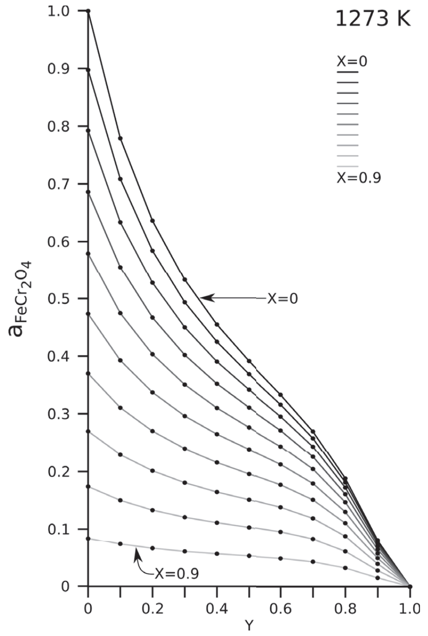

Figure 2.9: Activity of $FeCr_2O_4$ in the $(Fe_{1-X}, Mg_X)(Cr_{1-Y}, Al_Y)_2O_4$ spinel solid solution at 1273 K

ing **Equation 2.7** and, for $FeCr_2O_4$, **Equation 2.9**. This procedure must be replicated for each temperature considered.

Equilibrium with a $(Al_Z, Cr_{1-Z})_2O_3$ phase

Once the activities in the spinel have been determined, an equilibrium between the spinel and a corundum phase $(Al_Z, Cr_{1-Z})_2O_3$ can be considered. The equilibrium ratio of the activities of Cr_2O_3 and Al_2O_3 can be obtained from the reactions in **Equation 2.9** and **2.10**. The corundum composition is later deduced from the activities using the relationships available in the literature [29].

$$Cr_2O_3 + MgAl_2O_4 \rightarrow Al_2O_3 + MgCr_2O_4 \tag{2.9}$$

$$Cr_2O_3 + FeAl_2O_4 \rightarrow Al_2O_3 + FeCr_2O_4 \tag{2.10}$$

Again, this procedure from Jacob and Behera was replicated using the activities determined earlier. The equilibrium composition of the corundum phase was then calculated at 1223, 1273 and 1323 K as shown in **Table A.4** in **Appendix A**

2.2 The carbide system

Downstream from the reduction-carburization of the chromite oxides, the Fe-Cr-C system should be considered. This system was extensively studied in the past taking into consideration the M_3C, M_7C_3, $M_{23}C_6$ and Cr_3C_2 carbides, where M is Cr and Fe. The solubility of iron in Cr_3C_2 was reported to be low in many works, and is often considered zero [30].

Several models were developed to calculate the Fe-Cr-C ternary phase diagram. **Figure 2.10** presents one of the latest iterations calculated at 1273 K by Khvan and coworkers [31].

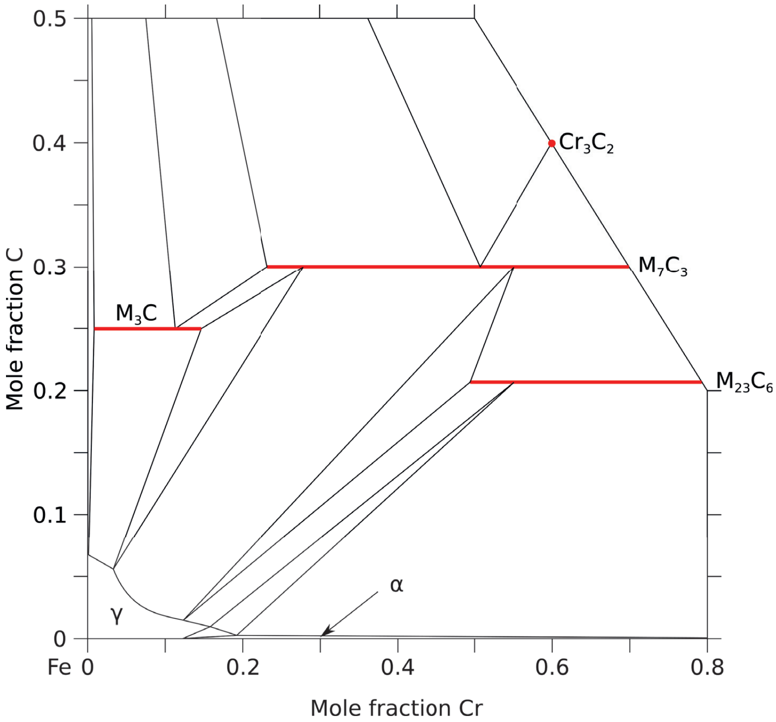

Figure 2.10: Fe-Cr-C ternary phase diagram at 1273 K, redrawn from Khvan *et al.* [31]

On this diagram, the M_3C, M_7C_3, $M_{23}C_6$ solid solution are represented by thick red lines, while the Cr_3C_2 compound is represented by a red dot. Since the raw data was not available, the Fe:Cr ratios in the M_7C_3 phase in equilibrium with graphite at 1273 K were estimated using **Figure 2.10**. There were found to range from 0.4 to 2.0.

2.3 Reduction-carburization of chrome containing oxides by CH_4

The use of natural chromite for the ferrochrome industry involves both chromium and iron oxides reduction-carburization. Of these two, chromium oxide is the most challenging to reduce. The viewpoint adopted in this section is that the study of the gaseous reduction-carburization of Cr_2O_3 by CH_4 gas offers a first step towards the gaseous reduction of natural chromite. Firstly, in **Section 2.3.1**, the studies about Cr_2O_3 reduction-carburization by CH_4 offer an assessment of the possibilities offered by hydrocarbon gases. Two reaction mechanisms are proposed to explain the reactions involving CH_4. Secondly, the studies on synthetic and natural chromite, detailed in **Section 2.3.2**, provide a deeper understanding of the singularities involved by the spinel composition. Thirdly, **Section 2.3.3** gives a brief overview of the role of sulfur observed in corrosion studies, and how sulfur could play a role when working with gaseous reduction-carburization of iron containing oxides.

2.3.1 Cr_2O_3 reduction-carburization by CH_4

Chromium carbide (Cr_3C_2) is ensued from the carburization of Cr_2O_3 by CH_4 gas [32; 33; 34; 35; 36]. This reaction is thermodynamically favorable as well as promising, as it is observed to occur at lower temperature than the reduction by the carbothermic reaction in an inert atmosphere[32; 34]. However, two opposing theories attempted to explain the reaction mechanism. The first theory, from Read and coworkers considered methane as a carbon carrier, and carbon and hydrogen as reductants. The second treated methane more as a reductant. The deposited carbon is still the reductant in effect, but its activity is taken from the activity of carbon in the metastable gas phase. A summary of the studies presented in this section is provided in **Table 2.3** on page 25.

CH_4 as a carbon carrier

In the seventies, a Canadian team explored the reduction of chromium oxide with CH_4 [32]. Their raw materials, consisted of a mixture of chromium sesquioxide (Cr_2O_3) and carbon in various ratios or of chromium sesquioxide solely. The experiments with Cr_2O_3 only were conducted under CH_4-H_2 gas flows while the carbon containing material was exposed to pure hydrogen gas. The reduction carburization started at temperatures lower than 800 °C in both experiments and the CO evolution was considered similar. To the authors, it appeared that methane did not take part in the reaction directly. This conclusion was based on the impossibility to show that the reaction speed depended on the partial pressure of methane in their experiments. Furthermore, they provided their understanding on what the reaction mechanism is as written in **Equations 2.11** to **2.14** [32]. This reaction mechanism considers that methane gas acts as a carbon carrier only, cracking and delivering carbon and hydrogen at the reaction zone according to **Equation 2.11**. Hydrogen gas further reacts with chromium oxide to form chromium metal following **Equation 2.12** and carbon reacts with the metallic chromium through a solid-solid reaction according to **Equation 2.13**. The total reaction is given in **Equation 2.15**.

$$13\,CH_4\,(g) = 13\,C\,(s) + 26\,H_2\,(g) \tag{2.11}$$

$$3\,Cr_2O_3\,(s) + 9\,H_2\,(g) = 6\,Cr\,(s) + 9\,H_2O\,(g) \tag{2.12}$$

$$6\,Cr\,(s) + 4\,C\,(s) = 2\,Cr_3C_2\,(s) \tag{2.13}$$

$$9\,H_2O\,(g) + 9\,C\,(s) = 9\,H_2\,(g) + 9\,CO\,(g) \tag{2.14}$$

$$3\,Cr_2O_3\,(s) + 13\,CH_4\,(g) = 2\,Cr_3C_2\,(s) + 9\,CO\,(g) + 26\,H_2\,(g) \tag{2.15}$$

After carburization, carbides such as such as Cr_3C_2, Cr_7C_3, $Cr_{23}C_6$, chromium metal and carbon were expected but only carbon and Cr_3C_2 were observed.

CH_4 as a "pseudo-reactant"

In 2004, Anacleto and Ostrovski objected to Read and coworkers on their description of the reduction-carburization reaction mechanism [34]. On multiple aspects, the results and deductions of this Australian team opposed the carbothermic view proposed earlier. Their non-isothermal experiments, aiming at imitating the work of Read *et al.*, gave notably different results. It was shown that the reduction by a methane containing gas mixture is faster than a reaction with solid carbon in H_2, Ar or vacuum. The role of methane was also reconsidered as the CH_4 partial pressure appeared to influence the reaction rate during isothermal experiments. Finally, carbon monoxide had a strong retarding effect on the reduction-carburization.

Among other results in the same study, it was found that the carburization of Cr_2O_3 leads to the production of chromium carbide Cr_3C_2. No other species were evidenced, whether it is carbides, such as Cr_7C_3 or $Cr_{23}C_6$, or reduced material, such as CrO or Cr.

The Australian team also proposed a description of the reduction-carburization of chromium sesquioxide by methane that is thermodynamically equivalent to a reduction by methane. The suggested reaction path proceeds through cracking of methane on the oxide surface, providing adsorbed carbon in an active form. **Equation 2.16** describes the reaction of chromium sesquioxide with methane [34]. This reaction is analogous to the reaction given in **Equation 2.18**, where the adsorbed carbon stemming from the methane cracking (**Equation 2.17**) has an activity different to the one of carbon in graphite.

$$\mathrm{Cr_2O_3\,(s)} + \frac{13}{3}\mathrm{CH_4\,(g)} = \frac{2}{3}\mathrm{Cr_3C_2\,(s)} + 3\,\mathrm{CO\,(g)} + \frac{26}{3}\mathrm{H_2\,(g)} \tag{2.16}$$

$$\mathrm{CH_4\,(g)} = \mathrm{C_{ad}} + 2\mathrm{H_2\,(g)} \tag{2.17}$$

$$\mathrm{Cr_2O_3\,(s)} + \frac{13}{3}\mathrm{C_{ad}} = \frac{2}{3}\mathrm{Cr_3C_2\,(s)} + 3\,\mathrm{CO\,(g)} \tag{2.18}$$

Regarding the cracking of methane, Grabke studied the reaction in the case of carburization of iron with carbon activities below unity [37]. He proposed the mechanism shown in **Equation 2.19** to **2.24**, with the rate determining step being the decomposition of CH_3(ad) to CH_2(ad) and H(ad). Later, the activity of carbon in methane-hydrogen gas mixtures, with values above unity, was calculated from the partials pressures of methane and hydrogen according to **Equation 2.25** [38]. In this equation, K_{eq} corresponds to the equilibrium constant of the reaction in **Equation 2.26** with C_{gr} being carbon as graphite [34; 38]. The carbon activity is therefore essentially a function of the metastable gas composition and of the temperature.

$$\mathrm{CH_4\,(g)} = \mathrm{CH_4\,(ad)} \tag{2.19}$$

$$\mathrm{CH_4\,(ad)} = \mathrm{CH_3\,(ad)} + \mathrm{H\,(ad)} \tag{2.20}$$

$$\mathrm{CH_3\,(ad)} = \mathrm{CH_2\,(ad)} + \mathrm{H\,(ad)} \tag{2.21}$$

$$\mathrm{CH_2\,(ad)} = \mathrm{CH\,(ad)} + \mathrm{H\,(ad)} \tag{2.22}$$

$$\mathrm{CH\,(ad)} = \mathrm{C\,(ad)} + \mathrm{H\,(ad)} \tag{2.23}$$

$$\mathrm{C\,(ad)} = \mathrm{C(dissolved)} \tag{2.24}$$

$$a_C = K_{eq} \cdot \left(\frac{P_{CH_4}}{{P_{H_2}}^2} \right) \tag{2.25}$$

$$CH_4(g) = C_{gr} + 2H_2(g) \tag{2.26}$$

The high activity of adsorbed carbon, compared the activity of carbon as graphite, has been named as a key factor to explain the thermodynamic feasibility as well as the high rate of Cr_2O_3 reduction using methane by Anacleto and Ostrovski. The calculation of the carbon activity in CH_4-H_2 gas mixtures in their work was the same as the one previously derived in corrosion science and given in **Equation 2.25**. From these relations, Anacleto and Ostrovski expressed the activity of adsorbed carbon as given in **Equation 2.27**, where the subscript "gr" indicates that the gas ratios are taken at equilibrium with graphite.

$$a_C = \left(\frac{P_{CH_4}}{{P_{H_2}}^2} \right) \Big/ \left(\frac{P_{CH_4}}{{P_{H_2}}^2} \right)_{gr} \tag{2.27}$$

Furthermore, the authors viewed the reduction-carburization reaction as a carbon sink. Reversely, carbon deposition as graphite would acts as a stopper. According to Anacleto and Ostrovski, the fast reduction reaction of chromium sesquioxide by active carbon is what prevents the formation of a graphite build-up on the surface. This competition between carbon "utilization" and graphite build-up is therefore central in the reduction-carburization by methane. Other oxide materials may behave in a different manner. This question has also been raised by studies in the corrosion field, and will be further discussed in **Section 2.3.3**, especially concerning the effect of sulfur adsorption.

Other studies on Cr_2O_3 reduction-carburization by CH_4

Other studies focused on the reaction temperature, the structure or the phases observed. The reduction-carburization of Cr_2O_3 was discussed in many articles, with a general consensus on the reaction product (Cr_3C_2), its porous nature and the low reaction temperature [33; 35; 36]. Xing and coworkers discussed the pore formation during the reaction [39]. Their results showed that the porous structure observed in Cr_3C_2 is mainly due to the 55% volume reduction during the reaction from Cr_2O_3 to Cr_3C_2. The pore size was found closely related to the reaction temperature. Other studies also evidenced new phases. Metastable Cr_3C_{2-x} carbide formed when reacting nanosized particles of chromium oxide in a CH_4-H_2 atmosphere [40]. In this study, nanosized Cr_2O_3 was fully converted to Cr_3C_{2-x} at only 800 °C. The Cr_7C_3 carbide was also evidenced as an intermediary phase [41].

Table 2.3: Summary of the Cr_2O_3 reduction-carburization studies using methane gas

Ref.	Year	Solid reactants	Gas composition	Maximum temperature [°C]	Products	Notable findings
[32]	1974	Cr_2O_3	14% CH_4 - 86%H_2	1200	Cr_3C_2+C	CH_4 cracked, C and H_2 are the reductants.
		Cr_2O_3+C	100%H_2	1200	Cr_3C_2	
[33]	1993	Cr_2O_3	5%CH_4 - 95%Ar	1000	Cr_3C_2	The Cr_3C_2 exhibits significant porosity, a 20-40 nm carbon film on Cr_3C_2.
[34]	2004	Cr_2O_3	CH_4 up to 30% (in 50%H_2 20%Ar)	1200	Cr_3C_2	The reduction by CH_4 is not carbothermic, a_C is a measure of the gas reducing power.
[36]	2006	Cr_2O_3	CH_4 up to 70%	975	Cr_3C_2	The reaction with CH_4 started at 870 °C.
[41]	2009	Cr_2O_3	2%CH_4 - 98%H_2	1050	Cr_7C_3, Cr_3C_2	Cr_7C_3 is an intermediary product
[35]	2010	Cr_2O_3	CH_4 up to 50%	1100	Cr_3C_2	The reaction with CH_4 started at 850 °C.
[40]	2010	Cr_2O_3 (nanosized)	10%CH_4 - 90%H_2	850	Cr_3C_{2-x}, Cr_3C_2	At 800 °C, a metastable state was observed
[39]	2011	Cr_2O_3	2%CH_4 - 98%H_2	1300	Cr_3C_2	The pore size can be controlled

2.3.2 Chromite and synthetic chromite reduction-carburization by CH_4

The use of hydrocarbon gases for the reduction-carburization of chromite ores has received limited attention and the reaction mechanism remains relatively poorly understood. Nevertheless some notable works on natural and/or synthetic chromite reduction should be mentioned.

Use of CH_4 for the beneficiation of chromite ores

The exposition of chromite to methane has been investigated early by Boericke in 1946 [42]. Reduction-carburization of American chromite by methane was evaluated even though the chemical reactions at stake were not investigated as such. The aim pursued by the Bureau of Mines was to develop a beneficiation process using methane, that would carburize preferentially FeO in $FeO \cdot Cr_2O_3$ to Fe_3C. Some of the Cr_2O_3 was also carburized and was considered as a loss in this study. A temperature increase from 1000 °C to 1050 °C was found to increase the carburization of the chromium present in chromite ore. Such an increase was also observed concerning the iron part of the ore, but in a lower extent. Concerning the methane-hydrogen gas mixture, a low methane content (12.5% - 33.3%) was beneficial for the carburization. At high methane content, 50% and 100%, soot deposits were observed out of the furnace. Some of the efficient trials were carried out at 1050 °C and 20% CH_4 and showed a carbon utilization close to 100%.

Reaction mechanism for the reduction of chromite

Synthetic and natural chromite reduction-carburization were studied by Qayyum *et al.* [43], with a similar experimental approach as Read *et al.* [32]. The description of the carburization reaction is though somewhat more detailed. One must note here that the gas-solid experiments with methane are "simulated" by forming methane in the reaction medium. No methane is introduced as such, but is instead formed by hydrogenation of carbon. This keeps the activity of the gas phase ≤1, favoring carburization processes over solid carbon deposition. If the conditions for methane cracking were not reached, the reduction carburization mechanism was thought to follow **Equation 2.28** above 800 °C [43].

$$3\,FeO \cdot Cr_2O_3\,(s) + 17\,CH_4\,(g) = 2\,Cr_3C_2\,(s) + Fe_3C\,(s) + 34\,H_2\,(g) + 12\,CO\,(g) \qquad (2.28)$$

Above 1000 °C, solid-solid reactions were also expected to take place according to **Equation 2.29**.

$$3\,FeO\cdot Cr_2O_3\,(s) + 17\,C\,(s) = 2\,Cr_3C_2\,(s) + Fe_3C\,(s) + 12\,CO\,(g) \tag{2.29}$$

When the methane cracking conditions were fulfilled before 1000 °C, Qayyum and coworkers considered that solid carbon and hydrogen gas from methane cracking reacted with chromite following the reactions given in **Equation 2.30** to **Equation 2.34** [43].

$$17\,CH_4\,(g) = 17\,C\,(s) + 34\,H_2\,(g) \tag{2.30}$$

$$3\,FeO\cdot Cr_2O_3\,(s) + 12\,H_2\,(g) = 6\,Cr\,(s) + 3\,Fe\,(s) + 12\,H_2O\,(g) \tag{2.31}$$

$$6\,Cr\,(s) + 6\,C\,(s) = 2\,Cr_3C_2\,(s) \tag{2.32}$$

$$3\,Fe\,(s) + C\,(s) = Fe_3C\,(s) \tag{2.33}$$

$$3\,FeO\cdot Cr_2O_3\,(s) + 17\,CH_4\,(g) = 2\,Cr_3C_2\,(s) + Fe_3C\,(s) + 34\,H_2\,(g) + 12\,CO\,(g) \tag{2.34}$$

Regardless of the mechanism, this study was promising concerning the carburization of synthetic and natural chromite by methane as fairly high reduction degrees were reached, even when reducing natural chromites. Concerning the synthetic chromites, only $(Fe_{0.5}, Mg_{0.5})(Cr_{0.75}, Al_{0.25})_2O_4$ showed strong limitations during carburization [43]. Later, Anacleto and Ostrovski disagreed with this reaction mechanism in their article [34]. The authors judged the reaction mechanism given by Qayyum *et al.* unrealistic when it comes to the cementation of iron from iron metal and graphite. They pointed out that researches on cementite stability in CH_4-H_2-Ar gas mixtures with $a_C>1$ showed in particular that an increase in temperature above 750 °C made cementite more unstable [44].

Other studies on natural chromite

Fewer studies have been conducted and published on the reduction-carburization of chromite by methane. Kawazaki Steel Corporation developed a process involving pre-reduction of natural Philippine sandy chromite ores by hydrocarbon gases in the eighties. They were however not extensive on the description of the chemical process, although they indicated that methane was the reductant. Both methane and propane were investigated with additions of coke or CaO. The best carburization results were obtained at 1100 °C, using propane gas and coke additions [8]. To the knowledge of the author, this work did not lead to further development of the technology.

De Campos and Eric studied the chromite ore from the LG-6 layer of the Bushveld complex at temperatures up to 1300 °C [45]. They evidenced a shrinking core mechanism, along with a zoning phenomenon. To explain the reaction, de Campos and Eric considered a reduction by CO and H_2, rapidly regenerated by the cracking of CH_4.

Lastly, the carburization of Kemi chromite ore concentrate was studied by Leikola [46]. An extensive experimental work was done at various temperatures, reduction times and gas compositions. A shrinking core followed by a collapsing of the core was found to appropriately describe the phase change. This result is similar to the aforementioned study by de Campos and Eric. Energy-dispersive X-ray spectroscopy (EDS) showed that the reduction affects both the iron and the chromium, but iron is reduced faster. The deposited carbon content in the product was found to increase with time, but not necessarily with temperature. However, at higher temperatures, the carbon was suspected to deposit early in other parts of the furnace.

Table 2.4: Summary of the synthetic or natural chromite reduction-carburization studies using or simulating the use of methane gas

Ref.	Year	Solid reactants	Gas composition	Maximum temperature [°C]	Products	Notable findings
[42]	1946	Montana Chromite (Benbow and Davies)	CH_4 up to 100%	1100	Not detailed	Fast reduction of Fe fully after 60 min at 1000 °C.
[43]	1976	$FeCr_2O_4$+C	100% H_2	975	Cr_3C_2+Fe_3C	The reaction started at 800 °C.
		$Fe(Fe, Cr)_2O_4$+C	100% H_2	Not detailed	Cr_3C_2+Fe_3C	Reaction similar to that of $FeCr_2O_4$ rather than Fe_3O_4.
		$(Fe, Mg)Cr_2O_4$+C	100% H_2	Not detailed	Cr_3C_2+Fe_3C	Mg hindered the reaction rate.
		$Fe(Cr, Al)_2O_4$+C	100% H_2	Not detailed	Cr_3C_2+Fe_3C	Al hindered the reaction rate.
		$(Fe, Mg)(Cr, Al)_2O_4$+C	100% H_2	Not detailed	Cr_3C_2+Fe_3C	Mg and Al together slowed the reaction even more.
		Transvaal and Bird River Chromite	100% H_2	1000	Cr_3C_2+Fe_3C	The natural ores are essentially reduced fully after 60 min at 1000 °C.
[8]	1986	Philippine sandy Chromite	Not detailed, CH_4 and C_3H_8 are used.	1100	Not detailed	High reduction degree low temperatures, C_3H_8 with coke gave the best results.
[45]	2006	Bushveld Chromite	CH_4 up to 30% (in 70%H_2 or Ar)	1250	Fe-Cr Carbides/Alloys Mg-rich spinels	Shrinking core and zoning, CO and H_2 are the reductants.
[46]	2015	Kemi Chromite	CH_4 up to 30% (in 70%H_2)	1350	Fe-Cr Carbides/Alloys Mg-rich spinels	Shrinking core and collapsing of the core, Fe reduced faster than Cr

2.3.3 Related corrosion studies – a possible use of sulfur ?

The carburization by metastable methane relies, according to Anacleto and Ostrovski, on the reaction of the oxide with active carbon [34]. However, the high temperature conditions also enhances the deposition of low activity carbon which is an undesired phenomenon. Dalaker and Tetlie underlined that the degree of metastability of methane varies with the oxides it is exposed to, even without reduction of the oxide [47]. The knowledge of the metal dusting phenomenon detailed next gives an insight on how graphite forming could be an obstacle for the carburization. Limiting this graphite formation on iron might be the key for the parallel carburization of chromium and iron in chromite.

The effect of sulfur additions

The metal dusting of iron is a destructive corrosion process happening at $a_C>1$. This phenomenon is due to the formation of graphite from the C-saturated iron, causing a complete destruction of the material. The mechanism is as follow [48]:

(i) Carbon transfer from the C-rich gas in the iron matrix through the surface until saturation

(ii) Formation of cementite (Fe_3C)

(iii) Nucleation of graphite on the cementite surface, forcing the carbon activity to be $a_C=1$. With these conditions, cementite starts to decompose

(iv) Decomposition of cementite: $Fe_3C = 3Fe + C$
Iron agglomerates in particles

(v) Growth of carbon through a decomposition process on the metal particles

When the gas environment consisted of a CH_4-H_2 mixture, Grabke noted that the decomposition of methane was very low on pure iron. Grabke also found that when T>700 °C, the decomposition of cementite during the metal dusting process can lead to the formation of a dense iron layer that acts as a barrier. Carbon will have to diffuse through this layer to access the graphite, and this diffusion step becomes rate limiting. This can potentially slow down the metal dusting rate tremendously.

Metal dusting in CH_4-H_2-H_2S gas mixtures

Sulfur addition to the reacting gas can efficiently prevent the metal dusting. Sulfur is readily adsorbed on the iron surface and retards the carbon transfer by occupying the reaction sites. In spite of the sulfur adsorption, the carburization is not fully blocked. The reaction is rather slowed down, but carbon can still penetrate the sulfur layer thanks to its smaller radius [49]. According to Schneider and coworkers, the sulfur adsorbed on iron allows the growing of the Fe_3C phase according to steps (i) and (ii) presented above although the reaction rate is reduced [50]. But this sulfur layer also suppresses efficiently the graphite nucleation on the Fe_3C surface formed. This corresponds to a blockage of step (iii) presented earlier. Because no graphite is formed, the cementite is not placed in contact with graphite whose carbon activity is a_C=1. As a result, cementite is less likely to decompose. The sulfur phase and the absence of graphite layer also enable to formation of lower carbides, such as the so called Hägg particle Fe_5C_2 [50].

2.4 Kinetic modeling theories

The two studies investigating the reduction-carburization of chromite ore by methane gas reported a reaction occurring through a shrinking core mechanism at the grain scale [46; 45]. The oxide reactant, upon reaction, formed a product layer at the edge of the particle. This reacted layer grows with time as the oxide is carburized. To model such a system, the "extended grain model" could be of use and is presented in **Section 2.4.1**. In addition, many models have been developed to describe solid state reactions, based on various descriptions of the mechanisms involved [51]. Special attention is devoted to two nucleation and growth based equations in **Section 2.4.2** and **2.4.3**

2.4.1 Extended grain model

The grain model was established by Szekely and coworkers to account for the porous nature of a reacting solid, especially for pellets [52]. The model, in the context of interest, assumes the solid reactant to be a spherical pellet having a shape factor $F_p = 3$, made of particles of a shape to be determined and thus $F_g = 1, 2$ or 3. Mathematically, a value of $F_g = 3$ corresponds to spherical grains, $F_g = 2$ to long cylinders and $F_g = 1$ to infinite slabs. None of these cases are a perfect representation of reality and in practice, a value of $F_g = 2$ can represent a distribution of grains between sphere and slabs. This model takes into account the chemical reaction, as well as the diffusion within the pellet.

The extended grain model (EGM) presented below is an enriched version of the grain model in which the diffusion through the layer of product material formed around a grain of material is not disregarded. A general gas-solid reaction is as written in **Equation 2.35**:

$$aA(g) + bB(s) = cC(g) + dD(s) \tag{2.35}$$

Taking into account a first order chemical reaction, the diffusion in the pellet and in the product layer in the grain and the external mass transfer from the gas, the dimensionless time (t^*) as a function of the fractional conversion (α) can be written as follows:

$$t^* = \underbrace{g_{F_g}(\alpha)}_{\substack{\text{Chemical}\\ \text{reaction}}} + \underbrace{\hat{\sigma}_g^2 \cdot p_{F_g}(\alpha)}_{\substack{\text{Diffusion}\\ \text{in the grain}\\ \text{product layer}}} + \hat{\sigma}^2 \left(\underbrace{p_{F_p}(\alpha)}_{\substack{\text{Diffusion}\\ \text{in the}\\ \text{pellet}}} + \underbrace{\frac{2\alpha}{N_{Sh^*}}}_{\substack{\text{External}\\ \text{mass}\\ \text{transfer}}} \right) \tag{2.36}$$

In this equation and the following, the subscript p refers to the pellet and g refers to the grain. The relationship between the dimensionless time (t^*) and the time (t) is given in **Equation 2.37**:

$$t^* = \frac{bk}{\rho_s}\left(C_{As} - \frac{C_{Cs}}{K_E}\right)\left(\frac{A_g}{F_g \cdot V_g}\right)t \tag{2.37}$$

For particles of unchanging size, the chemical reaction part g_{F_g} can be expressed as a function of the geometry of the grains as:

$$g_{F_g}(\alpha) = 1 - (1-\alpha)^{\frac{1}{Fg}} \tag{2.38}$$

For pellets and grains, the diffusion conversion equation is written (for $i = p$ or g):

$$\begin{aligned} p_{F_i}(\alpha) &= \alpha^2 \quad \text{for } F_i = 1 \\ &= \alpha + (1-\alpha)\cdot ln(1-\alpha) \quad \text{for } F_i = 2 \\ &= 1 - 3(1-\alpha)^{\frac{2}{3}} + 2(1-\alpha) \quad \text{for } F_i = 3 \end{aligned} \tag{2.39}$$

The shrinking core reaction modulus for the grain ($\hat{\sigma}_g^2$) is defined by **Equation 2.40**:

$$\hat{\sigma}_g^2 = \frac{k}{2D_g}\frac{V_g}{A_g}\left(1 + \frac{1}{K_E}\right) \tag{2.40}$$

The generalized gas-solid reaction modulus ($\hat{\sigma}^2$) is defined by **Equation 2.41**:

$$\begin{aligned} \hat{\sigma}^2 &= \left(\frac{V_p}{A_p}\right)^2\left(\frac{(1-\epsilon)kF_p}{2D_e}\cdot\frac{A_g}{F_g V_g}\right)\left(1 + \frac{1}{K_E}\right) \\ &= R_p^2 \cdot \left(\frac{(1-\epsilon)k}{2D_e F_p}\cdot\frac{A_g}{F_g V_g}\right)\left(1 + \frac{1}{K_E}\right) \\ &= \left(\frac{R_p^2}{R_g}\right)\cdot\left(\frac{(1-\epsilon)k}{2D_e F_p}\right)\left(1 + \frac{1}{K_E}\right) \end{aligned} \tag{2.41}$$

Finally, the modified Sherwood number is defined in **Equation 2.42**:

$$\begin{aligned} N_{Sh^*} &= \frac{h_D}{D_e}\frac{F_p V_p}{A_p} \\ &= \frac{h_D}{D_e}\cdot R_p \end{aligned} \tag{2.42}$$

Because this model has a physical origin, it is possible to interpret the parameters and evidence which step of the process is rate limiting. In addition, variations of these parameters with the experimental conditions can evidence a change in the rate limiting step and possibly a change in the reaction mechanism.

2.4.2 Extended JMAK

The Johnson-Mehl-Avrami-Kolmogorov (JMAK) equation is specifically used in nucleation and growth kinetics with a wide range of applications. This equation relies on several restrictive assumptions on the system studied, such as random distribution of the product phases and isotropic growth [53]. Its general equation is given in **Equation 2.43**:

$$\alpha(t) = 1 - \exp\left[-(k(T)t)^n\right] \tag{2.43}$$

where α is the conversion, $k(T)$ the rate constant, and the exponent n a parameter of the equation. Later, an extended version was proposed including the impingement parameter η_i [53]. This equation was found to accurately fit to reactions where the JMAK equation could not be used. The extended JMAK (E-JMAK) equation is written:

$$\alpha(t) = 1 - \left[\frac{(k(T)t)^{n_S}}{\eta_i} + 1\right]^{-\eta_i} \tag{2.44}$$

α is the conversion, $k(T)$ the rate constant, n_S is a parameter similar to n, and η_i the impingement parameter.

2.4.3 Austin-Rickett equation

The Austin-Rickett (AR) equation can be seen as a special case of the extended JMAK equation presented above. It corresponds to the case where $\eta_i = 1$. This equation was found to give good fits for precipitation reactions [54]. The Austin-Rickett equation is written:

$$\alpha(t) = 1 - \left[(k(T)t)^n + 1\right]^{-1} \tag{2.45}$$

where α is the conversion, $k(T)$ the rate constant, and the exponent n a parameter of the equation.

2.4.4 Influence of temperature on the rate

To express the temperature dependence of a chemical reaction, the Arrhenius equation and the activation energy concept can be used. However, the use of the activation energy must be restricted to well defined chemical reaction steps.

The rate expressions for the chemical reaction in the extended grain model presented in **Section 2.4.1** can be given as [51]:

$$g(\alpha) = kt \tag{2.46}$$

where k is the rate constant and g the integral form of the rate equation and α the conversion. The temperature dependence of the rate constant expressed using the Arrhenius equation gives [28; 51]:

$$k = k_0 e^{\frac{-E_\mathrm{a}}{RT}} \tag{2.47}$$

where k_0 is the frequency factor, E_a the activation energy, T the temperature and R the gas constant.

At a given value of α, for example 40%, one can write:

$$g(\alpha = 40\%) = kt_{40\%} \tag{2.48}$$

Which gives:

$$\ln(g(\alpha = 40\%)) = \ln(k) + \ln(t_{40\%}) \tag{2.49}$$

$\ln(k)$ can therefore be expressed as in **Equation 2.50** and **Equation 2.51**:

$$\ln(k) = \ln(k_0) - \frac{E_\mathrm{a}}{R} \cdot \frac{1}{T} \tag{2.50}$$

$$\ln(k) = -\ln(t_{40\%}) + \ln(g(\alpha = 40\%)) \tag{2.51}$$

Thus:

$$-\ln(t_{40\%}) = -\frac{E_\mathrm{a}}{R} \cdot \frac{1}{T} + \ln(k_0) - \ln(g(\alpha = 40\%)) \tag{2.52}$$

The activation energy can therefore be determined from the slope of the plot of $-\ln(t)$ vs $\frac{1}{T}$ for given values of α.

2.5 Structural changes

The structural changes in gas-solid reduction reactions have been studied extensively by Hayes because of their critical importance in the rate of the reactions [55]. First, Hayes noted that different type of product growth were formed with the same chemical system. Considering the driving force for oxygen removal and the interface velocity for the reaction, he established a criteria for instability formation analogous to what is found in the solidification field. This criteria considers variations along the z-axis perpendicular to the gas-solid surface and is given in **Equation 2.53**:

$$\frac{\Delta G}{dz} < (C_{\text{interface}} - C_{\text{bulk}}) \cdot \frac{V}{D} \tag{2.53}$$

Where $\frac{\Delta G}{dz}$ is the gradient of driving force for the reaction, $(C_{\text{interface}} - C_{\text{bulk}})$ is the metal cation concentration difference, V is the interface velocity and D the diffusivity of metal cations. This equation indicates that instability is favored at low reaction driving force and low cation diffusivity. Although the derivation was done for reduction reactions only, it is of interest to bear in mind the thinking proposed by Hayes for reduction-carburization processes.

Chapter 3

Experimental Procedure

This chapter presents the methodology as well as the equipment used throughout the experimental work. The aim of the project is to study the interactions between methane gas and chromite spinels but in fact, this aim is twofold. The work was divided in two main activities: the synthesis of the said oxides in a pure form and secondly the reduction-carburization study using methane at elevated temperatures. A flow sheet which sums-up the stages of the experimental work is presented in **Figure 3.1**.

The cold crucible induction furnace (CCIF) and the vertical alumina tube furnace, presented in **Section 3.1**, were the two main equipment used in this work respectively to synthesize and reduce-carburize the samples. The experimental procedure, including the experimental parameters, from pure oxides raw materials to carburized pellets is presented in **Section 3.2**. At each step of this work, various analysis methods were employed to ensure the quality of intermediary products and to analyze the reacted phases as presented in **Section 3.3**.

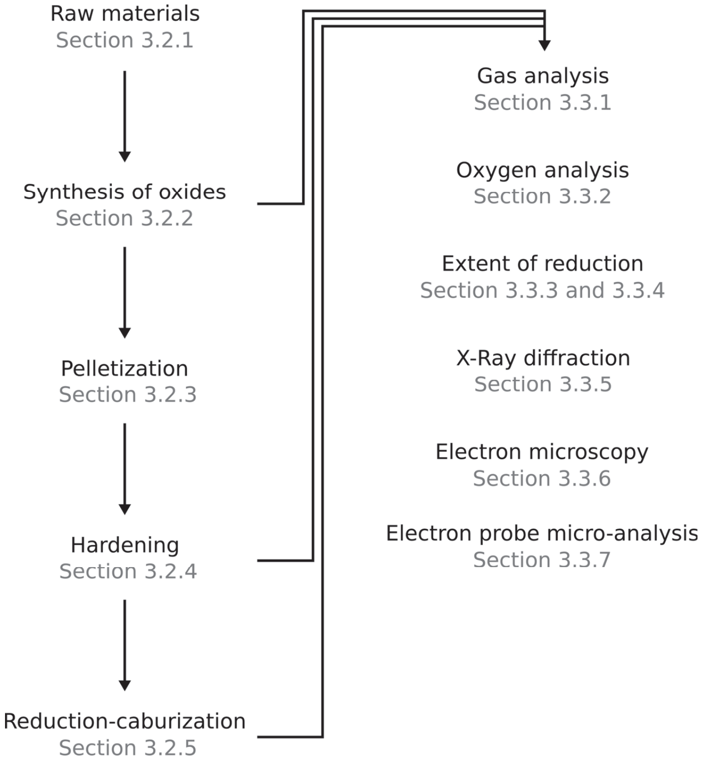

Figure 3.1: Flow sheet of the experimental work and the relevant section in the chapter

3.1 Apparatus

The two main furnaces employed are presented in detail in this section. The cold crucible induction furnace is presented first and is used to carry out the skull melting of oxides. The vertical tube furnace, employed for the reduction-carburization is presented next.

3.1.1 The cold crucible induction furnace

In this section, the equipment used for the synthesis of chromite samples is presented. The skull melting technology appeared to be a convenient route for the production of chromite samples: it involves a complete melting of the raw materials and subsequent fast freezing by simply stopping the heating and keeping the water cooling. The induction skull melting technique is explained in another publication [56]. This technology has developed mainly around the production of monoxides and is now used to produce high purity oxides, especially zirconium dioxide. A work on the synthesis of Fe_3O_4-Fe_2TiO_4 spinel solid solutions by controlling the oxygen fugacity through a CO/CO_2 gas atmosphere is worth mentioning [57]. Within the Norwegian University of Science and Technology, the skull melting technique was used to synthesize ilmenite with various impurities [58; 59; 60].

The equipment used is a cold crucible high frequency induction furnace shown in **Figure 3.2**. The induction heating is generated using an induction solenoid with eight wire wraps connected to a radio frequency power generator from Farfield Electronics PTY Ltd (750kHz, 75kVA). The container is a water-cooled cylindrical copper crucible supplied by ANSTO (Australian Nuclear Science and Technology Organisation). The copper crucible's wall and bottom are composed of sixteen "fingers" placed around the circular cylinder's axis and separated by an interstice aiming at limiting the induction in the crucible itself. These fingers feature inner channels which are water-cooled in operation. A boron nitride coating is applied on the crucible's inner surface to avoid the penetration of molten material in the intra fingers' gap and to avoid the sticking of the melt onto the crucible.

The schematic in **Figure 3.3** presents the components of the furnace set-up. The copper crucible (6) is connected to the cooling water circuit (8). The enclosure delimiting the furnace interior is ensured by a glass tube (3) while rubber gaskets (2)(7) make the contact between different components impervious to gases. The interior of the furnace can be evacuated and the atmosphere replaced by a chosen gas mixture supplied at a desired flow. The gases circulate from the hub located above the glass tube (1). A

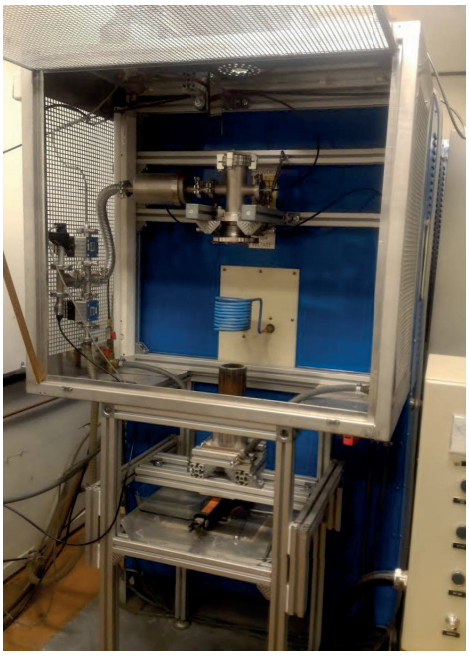

Figure 3.2: Picture of the cold crucible induction furnace

rotary pump is used for the evacuation, down to pressures below 10 hPa. Additional glass tubes (3) are used as protection against splashing of the melt. Mica sheets (4) are used as thermal insulators. The crucible is placed inside the induction coil (5).

A window is located above the setup and gives a direct view of the melt's surface. There, two different devices have been used, though not simultaneously. A first set-up configuration used a spectropyrometer of type FMP2 from FAR Associates to measure the temperature of the melt surface. The distance between the melt and the sensor is set to one meter even though the actual distance varies in operation due to a change of the melt surface position. This pyrometer can work at temperatures between 800-2500 °C. Large differences between the measured temperatures at molten state and the reported melting temperature in thermodynamics literature were observed. A possible explanation could be the covering of the window by dust carried by the exhaust gases. Because of these deviations, the use of the spectropyrometer has not been continued. The second equipment used was a Sony NEX-5N Camera, placed on a support to record videos of the melting and cooling during the synthesis. The camera focus was set manually on the raw materials' surface before the start of the induction heating. Light filters were added to decrease the light exposure of the camera, while the shuttering time was manually varied during the experiment to negate the variation of light emissions.

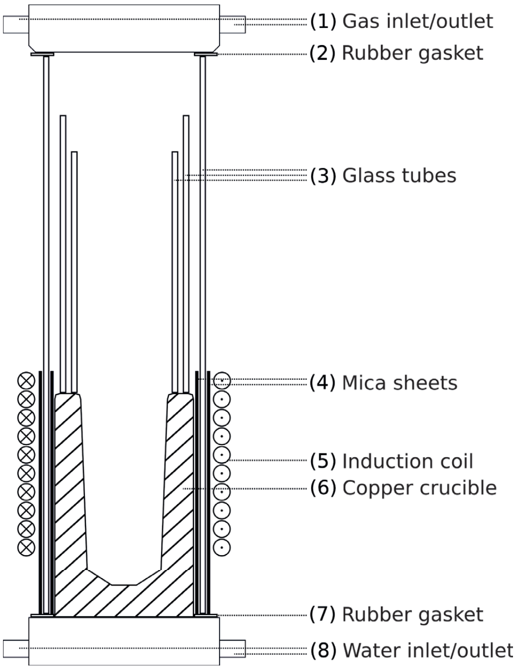

Figure 3.3: Schematics of the cold crucible induction furnace with a cut view

3.1.2 The vertical tube furnace

This section presents the setup for reduction-carburization experiments, illustrated in **Figure 3.4** and schematically represented in **Figure 3.5**.

The vertical tube furnace was supplied by Entech. It uses Kanthal molybdenum disilicide heating elements and a Eurotherm 2404 programmer.

The furnace interior shown on **Figure 3.5** is delimited by an Alsint® tube (4) held by a clamp resting on the furnace top. Alsint® sheath (1) and crucible are also used in the chamber. The crucible is designed with three elements: a tube carrying the process gases (8) is glued to a bottomless crucible (5) where a porous plug (7) supports the sample. The crucible, the thermocouple sheath and the main tube are all removable and reusable after pyrolysis to remove any deposited carbon. The top and bottom furnace lids hold the tube tightly in position as they are fastened to the casing (9). O-ring seals (3) placed on each lid holds tight the crucible while a similar construction holds the thermocouple sheath on the top lid. Therefore, the S-type thermocouple and its sheath can be inserted down to the reaction zone.

The input gas atmosphere is controlled using an Alicat MC-Series mass flow controller for each gas species. When leaving the furnace interior, gases are analyzed us-

Figure 3.4: Picture of the vertical tube furnace

ing an Advance Optima AO2020 continuous gas analyzer with the Uras26 and Caldos27 modules. Then, the process gas flows through a gas bubbler before exiting to the exhaust gas system. To verify that the exhaust gas did not contain any water, one experiment was carried out with an parallel device. When the process gas was introduced, the exhaust gas flow was deviated before the gas analyzer and directed to a chamber containing CaO as a drying agent. The mass change in the CaO during the reduction-carburization was used as an indicator of the presence or absence of H_2O in the exhaust gas.

A computer is used to control the heating of the furnace using the programmed heating procedure and feedback information from a B-type thermocouple placed in the furnace wall. The gas flow controllers are set manually. Temperature measurements from both the S and B type thermocouples are recorded by the software and can be compared to the command value. The values obtained from the gas analyzer are also registered simultaneously using the same interface.

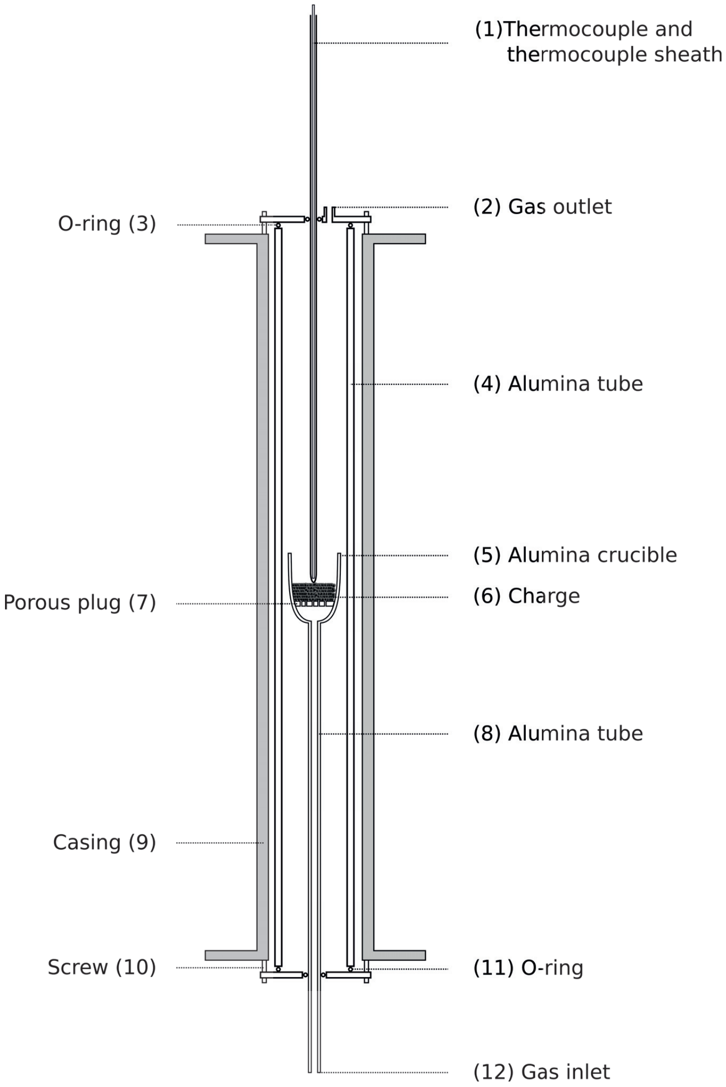

Figure 3.5: Schematics of the furnace setup

3.2 Procedure

A description of the experimental procedure is given in a sequential order in this section. Synthetic oxides from the $(\mathrm{Fe, Mg})(\mathrm{Cr, Al})_2\mathrm{O}_4$ spinel solid solution system were produced for further use in reduction-carburization experiments. Four compositions were produced:

- Pure iron chromite samples $\mathrm{FeCr_2O_4}$
- Magnesium enriched chromite $(\mathrm{Fe, Mg})\mathrm{Cr_2O_4}$
- Aluminium enriched chromite $\mathrm{Fe}(\mathrm{Cr, Al})_2\mathrm{O}_4$
- Magnesium and aluminium enriched chromite $(\mathrm{Fe, Mg})(\mathrm{Cr, Al})_2\mathrm{O}_4$

These samples were then hardened in argon and reduced-carburized with different temperatures and gas mixtures. The raw materials used are detailed in **Section 3.2.1** before a description of the synthesis work in **Section 3.2.2**. The pelletization, hardening and reduction-carburization experimental procedures are reported in **Section 3.2.3**, **3.2.4** and **3.2.5** respectively.

3.2.1 Raw materials

Metallic iron and various metal oxides supplied by Sigma-Aldrich were used as reagents for the synthesis. The metallic iron chips were of electrolytic quality (Fe, 99.98%). The metal oxides used were chromium (III) oxide powder ($\mathrm{Cr_2O_3}$, purity 98%), iron (III) oxide powder ($\mathrm{Fe_2O_3}$, size $\leq 5\ \mu\mathrm{m}$, purity $\geq 99\%$), aluminium (III) oxide powder ($\mathrm{Al_2O_3}$, size $\leq 10\ \mu\mathrm{m}$, purity $\geq 99.5\%$) and magnesium (II) oxide powder (MgO, assay 98-100.5% for dried substance).

3.2.2 Synthesis of oxides

The synthesis of the oxides was done in the cold crucible induction furnace presented in **Section 3.1.1** under argon atmosphere. Several experiments were necessary to develop and refine the synthesis route. The raw materials were introduced in the stoichiometric quantities following the reactions given in **Equation 3.1** to **3.4**. These compositions are referred to as presented in **Table 3.1**.

Table 3.1: Synthetic chromite composition and naming

Targeted stoichiometry	Referred composition	Referred code letter
$FeCr_2O_4$	$FeCr_2O_4$	A
$(Fe_{0.75}, Mg_{0.25})Cr_2O_4$	$(Fe, Mg)Cr_2O_4$	B
$Fe(Cr_{0.75}, Al_{0.25})_2O_4$	$Fe(Cr, Al)_2O_4$	C
$(Fe_{0.75}, Mg_{0.25})(Cr_{0.75}, Al_{0.25})_2O_4$	$(Fe, Mg)(Cr, Al)_2O_4$	D

Synthesis reaction for the solid solution A: $FeCr_2O_4$

$$\frac{1}{3}Fe + \frac{1}{3}Fe_2O_3 + Cr_2O_3 = FeCr_2O_4 \tag{3.1}$$

Synthesis reaction for the solid solution B: $(Fe, Mg)Cr_2O_4$

$$\frac{1}{4}Fe + \frac{1}{4}Fe_2O_3 + \frac{1}{4}MgO + Cr_2O_3 = (Fe_{0.75}, Mg_{0.25})Cr_2O_4 \tag{3.2}$$

Synthesis reaction for the solid solution C: $Fe(Cr, Al)_2O_4$

$$\frac{1}{3}Fe + \frac{1}{3}Fe_2O_3 + \frac{3}{4}Cr_2O_3 + \frac{1}{4}Al_2O_3 = Fe(Cr_{0.75}, Al_{0.25})_2O_4 \tag{3.3}$$

Synthesis reaction for the solid solution D: $(Fe, Mg)(Cr, Al)_2O_4$

$$\frac{1}{4}Fe + \frac{1}{4}Fe_2O_3 + \frac{1}{4}MgO + \frac{3}{4}Cr_2O_3 + \frac{1}{4}Al_2O_3 = (Fe_{0.75}, Mg_{0.25})(Cr_{0.75}, Al_{0.25})_2O_4 \tag{3.4}$$

The oxide powders were mixed and placed in the crucible before being packed. The metallic iron pieces were placed above the oxide mixture. Iron was often added in excess as it was found to improve the melting while having a minor consequence on the composition. After evacuation of the reaction chamber down to 10 hPa, the atmosphere was filled with argon and the gas outlet was opened to allow gases to leave the chamber. A flow of argon of 1.19 l/min was kept during the experiments. The power delivered in the crucible was set by controlling the electric current flowing in the induction coil. In **Table 3.2** to **3.5**, the composition of the charge, the power delivered by the induction and duration of the syntheses are provided for all the experiments. In these tables, Fe_{xs} indicate the quantity of iron that is in excess relative to the stoichiometry. As it is already accounted for under the “Fe” quantity, Fe_{xs} is not counted once more in the total mass. Thus, Total mass = mass of $Fe+Fe_2O_3+Cr_2O_3+Al_2O_3+MgO$. The products crystallized when cooled down by stopping the heating and keeping the cooling unchanged.

Table 3.2: Experimental parameters for the synthesis of $FeCr_2O_4$

Experiment	Fe [g]	Fe_{xs} [g]	Fe_2O_3 [g]	Cr_2O_3 [g]	Al_2O_3 [g]	MgO [g]	Total mass [g]	Duration [min]	Power [kW]
A-1	16.74	0.00	47.56	135.87	0.00	0.00	200.17	6’00	67.5 → 52.5
A-2	13.30	0.00	38.03	108.63	0.00	0.00	159.96	10’00	52.5
A-3	16.63	0.00	47.48	135.85	0.00	0.00	199.96	5’30	63.75
A-4	20.71	4.00	51.76	135.81	0.00	0.00	208.28	5’00	63.75
A-5	18.61	2.00	47.50	135.84	0.00	0.00	201.95	5’00	63.75
A-6	18.61	2.00	47.57	135.81	0.00	0.00	201.99	5’00	63.75
A-7	18.63	2.00	47.56	135.85	0.00	0.00	202.04	5’00	63.75

Table 3.3: Experimental parameters for the synthesis of $(Fe_{0.75}, Mg_{0.25})Cr_2O_4$

Experiment	Fe [g]	Fe_{xs} [g]	Fe_2O_3 [g]	Cr_2O_3 [g]	Al_2O_3 [g]	MgO [g]	Total mass [g]	Duration [min]	Power [kW]
B-1	12.92	0.00	36.96	140.72	0.00	9.34	199.94	10’00	63.75
B-2	20.28	7.30	36.99	140.8	0.00	9.50	207.57	10’00	67.5 → 52.5
B-3	14.90	2.00	36.96	140.72	0.00	9.30	201.88	5’00	63.75
B-4	14.95	2.00	36.97	140.69	0.00	9.35	201.96	3’00	63.75
B-5	14.91	2.00	36.99	140.71	0.00	9.36	201.97	3’00	63.75

Table 3.4: Experimental parameters for the synthesis of $Fe(Cr_{0.75}, Al_{0.25})_2O_4$

Experiment	Fe [g]	Fe_{xs} [g]	Fe_2O_3 [g]	Cr_2O_3 [g]	Al_2O_3 [g]	MgO [g]	Total mass [g]	Duration [min]	Power [kW]
C-1	17.65	0.00	50.38	107.97	24.12	0.00	200.12	10’00	63.75
C-2	19.65	2.00	50.36	107.89	24.09	0.00	201.99	5’00	63.75
C-3	19.62	2.00	50.36	107.85	24.13	0.00	201.96	5’00	63.75

Table 3.5: Experimental parameters for the synthesis of $(Fe_{0.75}, Mg_{0.25})(Cr_{0.75}, Al_{0.25})_2O_4$

Experiment	Fe [g]	Fe_{xs} [g]	Fe_2O_3 [g]	Cr_2O_3 [g]	Al_2O_3 [g]	MgO [g]	Total mass [g]	Duration [min]	Power [kW]
D-1	15.76	2.00	39.28	112.06	25.02	9.99	202.11	3’00	63.75 → 75
D-2	17.91	4.00	39.28	112.09	25.09	9.92	204.29	3’34	67.5
D-3	15.73	2.00	39.23	112.09	25.06	9.93	202.04	3’00	67.5
D-4	15.75	2.00	39.25	112.06	25.07	9.90	202.03	3’12	67.5

3.2.3 Pelletization

The synthesized materials were first crushed using a Vibratory Disc Mill RS 200 (930 rpm, 30 s). Hardened steel and tungsten carbide grinding tools were used to crush the synthetic chromite lumps. The pelletization was done by Edith Thomassen from SINTEF Materials and Chemistry using a pelletizing drum and without any binder. For each chromite composition, two successful synthesis batches were utilized: A-6 and A-7 for $FeCr_2O_4$, B-4 and B-5 for $(Fe,Mg)Cr_2O_4$, C-2 and C-3 for $Fe(Cr,Al)_2O_4$ and D-3 and D-4 for $(Fe,Mg)(Cr,Al)_2O_4$. The pellets were sized to a diameter between 1-1.6 mm. After being formed, the pellets were dried overnight at 105 °C. A picture of the pelletizing drum is shown in **Figure 3.6**.

Figure 3.6: Picture of the pelletizing drum

3.2.4 Hardening of pellets

The hardening was done in a Nabertherm N17 muffle furnace at 900 °C for 2 h. The green pellets were placed in Alsint boats positioned inside of a steel box in a flow of argon. This argon flow was maintained during the ramp-up, retention and cooling stages to avoid oxidation. Because of the use of argon and to avoid degradation by thermal shock, the samples were loaded before the ramp-up to the holding temperature. No weight change was observed during the hardening. X-ray diffraction analysis, performed to verify the absence of reaction during the hardening, was conclusive as only a spinel phase was detected.

3.2.5 Reduction-carburization

The equipment used for the reduction carburization experiments is an alumina tube furnace presented in **Section 3.1.2**. This equipment was used for isothermal and non-isothermal reduction-carburization reactions using Ar-CH_4-H_2 gas mixtures. During the non-isothermal experiment, the process gas was used during the ramping in temperature above 600 °C. For the isothermal ones, argon gas was used during the heating and replaced by the process gas after stabilization of the temperature around the set point. The experimental work was organized in series which are detailed below. In the tables below, one should note that T.A.10%CH_4 and AT2.104 is the same experiment under two different names.

The Test-series consisted of six experiments to assess the reduction-carburization procedure. The five first experiments were using $FeCr_2O_4$ as raw material, one was non-isothermal while the others were isothermal with various gas atmospheres. The duration of the experiments in this series was not chosen as a parameter. The sixth experiment was set-up to verify the absence of water in the gas leaving the furnace, using $(Fe, Mg)(Cr, Al)_2O_4$ as a material. The experimental parameters are provided in **Table 4.6**.

The A-series studied reduction-carburization of pure iron chromite spinel $FeCr_2O_4$. This material was regarded as a reference, by being free of impurities. The experimental parameters for the A-series are given in **Table 3.7**. As for the following series, the first experiment was carried out at 1000 °C and long duration. For the next experiments, the temperature was varied, and the reaction was interrupted after two durations: 30 min and 120 min.

Table 3.6: Experimental parameters for the Test-series

Experiment name	Sample composition	Sample mass [g]	Temperature targeted [°C]	Gas composition Ar% / CH_4% / H_2%
T.A.Non_Iso	$FeCr_2O_4$	5.00	600-1000	50 / 25 / 25
T.A.50%CH_4	$FeCr_2O_4$	5.00	1000	50 / 50 / 0
T.A.25%CH_4	$FeCr_2O_4$	5.00	1000	50 / 25 / 25
T.A.10%CH_4	$FeCr_2O_4$	5.00	1000	50 / 10 / 40
T.A.0%CH_4	$FeCr_2O_4$	5.00	1000	50 / 0 / 50
T.D.H_2O	$(Fe, Mg)(Cr, Al)_2O_4$	5.00	1050	50 / 10 / 40

Table 3.7: Experimental parameters for the A-series

Experiment name	Sample mass [g]	Temperature targeted [°C]	Gas composition Ar% / CH_4% / H_2%	Duration [min]
AT1.030	5.00	950	50 / 10 / 40	30
AT2.030	5.00	1000	50 / 10 / 40	30
AT3.030	5.00	1050	50 / 10 / 40	30
AT1.120	5.00	950	50 / 10 / 40	120
AT2.104	5.00	1000	50 / 10 / 40	104
AT3.120	5.00	1050	50 / 10 / 40	120

The B-series focused on studying the effect of magnesium additions in tetrahedral interstices of the chromite solid solution of formula $(Fe_{0.75}, Mg_{0.25})Cr_2O_4$. Only chromium and iron oxides were expected to be reduced, while magnesium was expected to have a stabilizing effect. The gas mixture used previously (50%Ar-10%CH_4-40%H_2) as well as isothermal conditions were kept for these experiments. The experimental parameters including targeted temperatures and durations are included in **Table 3.8**. An experiment was also carried out at 1020 °C to offer an additional curve for the kinetics modeling.

Table 3.8: Experimental parameters for the B-series

Experiment name	Sample mass [g]	Temperature targeted [°C]	Gas composition Ar% / CH_4% / H_2%	Duration [min]
BT1.030	5.00	950	50 / 10 / 40	30
BT2.030	5.00	1000	50 / 10 / 40	30
BT4.030	5.00	1050	50 / 10 / 40	30
BT1.120	5.00	950	50 / 10 / 40	120
BT2.206	5.00	1000	50 / 10 / 40	206
BT3.120	5.00	1020	50 / 10 / 40	120
BT4.120	5.00	1050	50 / 10 / 40	120

The C-series studied the Fe$(Cr_{0.75}, Al_{0.25})_2O_4$ solid solution resulting from the addition of aluminium to replace part of the chromium atoms in the octahedral interstices of the spinel. Similarly to the B-series containing magnesium, aluminium oxides were not expected to be reduced contrary to chromium and iron oxides. The gas mixture used for the A-series (50%Ar-10%CH_4-40%H_2) was kept for these experiments which were all run under isothermal conditions. Temperatures and durations were the only parameters varied for the C-series as shown in **Table 3.9**.

Table 3.9: Experimental parameters for the C-series

Experiment name	Sample mass [g]	Temperature targeted [°C]	Gas composition Ar% / CH_4% / H_2%	Duration [min]
CT1.030	5.00	950	50 / 10 / 40	30
CT2.030	5.00	1000	50 / 10 / 40	30
CT3.030	5.00	1050	50 / 10 / 40	30
CT1.120	5.00	950	50 / 10 / 40	120
CT2.182	5.00	1000	50 / 10 / 40	147-182*
CT3.120	5.00	1050	50 / 10 / 40	120

*The heating was interrupted after 147 min while the process gas was maintained for 182 min.

The D-series permitted the study of the impact of both aluminium and magnesium simultaneously in solid solution. The aluminium atoms are found in the octahedral sites, while the magnesium atoms fill tetrahedral site; the composition is thus written $(Fe_{0.75}, Mg_{0.25})(Cr_{0.75}, Al_{0.25})_2O_4$. Magnesium and aluminium oxides are not expected to be reduced under the conditions of the study. The experimental conditions for the D-series are provided in **Table 3.10**.

Table 3.10: Experimental parameters for the D-series

Experiment name	Sample mass [g]	Temperature targeted [°C]	Gas composition Ar% / CH_4% / H_2%	Duration [min]
DT1.030	5.00	950	50 / 10 / 40	30
DT2.030	5.00	1000	50 / 10 / 40	30
DT3.030	5.00	1050	50 / 10 / 40	30
DT1.120	5.00	950	50 / 10 / 40	120
DT2.141	5.00	1000	50 / 10 / 40	141
DT3.120	5.00	1050	50 / 10 / 40	120

3.3 Analysis

The equipment used for analysis as well as the necessary calculations are given in this section.

3.3.1 Gas analysis

The equipment used for the experiment can provide live measurement of CO, CO_2, CH_4 and H_2 concentration in the exhaust gas. The gas composition was obtained using an Advance Optima AO2020 continuous gas analyzer with the Uras26 and Caldos27 modules. The Uras26 module is an infrared analyzer and provides information on the CO, CO_2 and CH_4 content. This technology is based on the infrared radiation absorption by the gas mixture, and offers good selectivity for most gases, excluding O_2, N_2, H_2, Cl_2 and inert gases [61]. For the present use, the infrared analyzer should provide an acceptable quantification of the content of CO, CO_2 and CH_4 in the gas. The Caldos27 module provides information on the H_2 content based on the thermal conductivity of the exhaust gas mixture, as if H_2 was mixed with Ar. This method is however limited in the current context [61], as it lacks selectivity: the background gas, containing Ar, CO and CH_4 and possibly H_2O, is not constant.

The analysis set-up was tested against various known gas compositions. The results revealed that the H_2 content measurement was consistently underestimated, while CO and CH_4 measurements were more accurate.

Of the substances measured, only CO and CH_4 were used for the calculations. The H_2 detection was judged too unreliable for further use, and the CO_2 content was negligible.

3.3.2 Oxygen analysis

The oxygen content in the raw materials and in the product phases was analyzed using an ON836 Oxygen/Nitrogen Analyzer (later referred as O-LECO). The sample is first weighted before being placed in a graphite crucible, and then burned at high temperature forming CO and CO_2 gas. The emitted gases are supplied by a flow of inert gas, and analyzed by an infrared analyzer. With this method, the oxygen mass fractions were determined both in the “initial” hardened pellets (noted w_i^O) and in the “final” products after reduction-carburization (noted w_f^O).

3.3.3 Extent of reduction

The extent of reduction "EoR" at the end of the experiment was deduced from the oxygen analysis mentioned earlier and the mass of the sample before and after experiment. The weight loss in a sample could not be used alone as an accurate way to evaluate the quantity of oxygen removed as carbon is added to the sample due to methane cracking or carburization of the sample. The reduction was assumed to only happen for chromium and iron oxides present in the solid solution, a 100% reduction meaning that all chromium and iron are present as metal or carbides, while aluminium and magnesium are present in their initial oxidation state. The extent of reduction, when calculated from the oxygen analysis, was obtained as follows:

$$\mathrm{EoR(in\ \%)} = 100 \cdot \frac{m_{\mathrm{O\ removed}}}{m_{\mathrm{O\ available}}} \tag{3.5}$$

where the numerator corresponds to the mass of oxygen removed from the sample calculated as shown in **Equation 3.6** using the initial and final sample masses (m_i and m_f) and the oxygen mass fraction before and after the experiment (w_i^O and w_f^O). The denominator corresponds to the mass of oxygen bound with iron and chromium that is to be extracted, and can be obtained using **Equation 3.7**.

$$m_{\mathrm{O\ removed}} = m_i \cdot w_i^O - m_f \cdot w_f^O \tag{3.6}$$

$$m_{\mathrm{O\ available}} = m_i \cdot w_i^O \cdot f^O(X,Y) \tag{3.7}$$

$$f^O : (X,Y) \to \frac{(1-X) + 3\cdot(1-Y)}{4}; X, Y \in [0,1] \tag{3.8}$$

The function f^O, defined in **3.8**, gives the fraction of oxygen available from the spinel for a raw material of composition $(\mathrm{Fe_{1-X}, Mg_X})(\mathrm{Cr_{1-Y}, Al_Y})_2\mathrm{O_4}$.

3.3.4 Extent of reduction as a function of time

Assuming that the oxygen removal occurs via the CO gas only and taking into consideration the variation of the exhaust gas flow, it is possible to give an estimation of the extent of reduction during the experiment as a function of time. First, the variations in the flow of the exhaust gas should be considered. This can be calculated assuming a steady state, and that the gas mixture follows the perfect gas law, *i.e.* that the volume occupied by the gas mixture is proportional to the amount of moles of gas.

The change in the flow of gas is due to the decomposition of methane, whether this leads to reduction-carburization or carbon deposition as shown in **Equation 3.9** to **3.11**. The CO and H_2 gases released by these reactions increase the flow of gas and decrease the concentration of the other gases. As mentioned earlier, only the CO and CH_4 measurements from the gas analyzer are judged reliable enough to be considered. It is then possible to calculate the flow out of the furnace, as explained below, and thus to calculate the CO and CH_4 flows out.

$$\mathrm{CH_4}(g) = \mathrm{CO}(g) + 2\mathrm{H_2}(g) \tag{3.9}$$

$$\mathrm{CH_4}(g) = \mathrm{C}_{\text{in carbide}} + 2\mathrm{H_2}(g) \tag{3.10}$$

$$\mathrm{CH_4}(g) = \mathrm{C}_{\text{graphite}} + 2\mathrm{H_2}(g) \tag{3.11}$$

For n_{tot} moles of incoming gas, and assuming that only CH_4, H_2 and Ar are present in the gas mixture, one can write **Equation 3.12** where n_{x} is the amount of moles of x entering the furnace.

$$n_{\text{tot}} = n_{\mathrm{CH_4}} + n_{\mathrm{H_2}} + n_{\mathrm{Ar}} \tag{3.12}$$

Accordingly, the total amount of gas leaving the furnace $\overline{n}_{\text{tot}}$ can be written as in **Equation 3.13** where the $\overline{n}_{\text{x}}$ are the amount of moles of x leaving the furnace.

$$\overline{n}_{\text{tot}} = \overline{n}_{\mathrm{CO}} + \overline{n}_{\mathrm{CH_4}} + \overline{n}_{\mathrm{H_2}} + \overline{n}_{\mathrm{Ar}} \tag{3.13}$$

In addition using **Equation 3.9** to **3.11**, one can write:

$$\begin{aligned} \Delta n_{\mathrm{H_2}} &= \overline{n}_{\mathrm{H_2}} - n_{\mathrm{H_2}} \\ &= 2 \cdot (n_{\mathrm{CH_4}} - \overline{n}_{\mathrm{CH_4}}) \end{aligned} \tag{3.14}$$

The amount of moles of CO and CH_4 leaving the furnace, $\overline{n}_{\mathrm{CO}}$ and $\overline{n}_{\mathrm{CH_4}}$ can be written in terms of their respective molar fraction ($\overline{x}_{\mathrm{CO}}$ and $\overline{x}_{\mathrm{CH_4}}$) known by the gas analysis, and the total amount of gas leaving the furnace:

$$\overline{n}_{\mathrm{CO}} = \overline{x}_{\mathrm{CO}} \cdot \overline{n}_{\text{tot}} \tag{3.15}$$

$$\overline{n}_{\mathrm{CH_4}} = \overline{x}_{\mathrm{CH_4}} \cdot \overline{n}_{\text{tot}} \tag{3.16}$$

Argon is unreacted throughout the process, thus :

$$\overline{n}_{\mathrm{Ar}} = n_{\mathrm{Ar}} \tag{3.17}$$

Using **Equation 3.12** to **3.17**, one can write:

$$\begin{aligned}\overline{n}_{\mathrm{tot}} &= \overline{n}_{\mathrm{CO}} + \overline{n}_{\mathrm{CH_4}} + \overline{n}_{\mathrm{H_2}} + \overline{n}_{\mathrm{Ar}} \\ &= \overline{n}_{\mathrm{CO}} + \overline{n}_{\mathrm{CH_4}} + n_{\mathrm{H_2}} + 2\cdot(n_{\mathrm{CH_4}} - \overline{n}_{\mathrm{CH_4}}) + n_{\mathrm{Ar}} \\ &= \overline{n}_{\mathrm{tot}}\cdot(\overline{x}_{\mathrm{CO}} - \overline{x}_{\mathrm{CH_4}}) + n_{\mathrm{H_2}} + 2\cdot n_{\mathrm{CH_4}} + n_{\mathrm{Ar}} \\ &= \overline{n}_{\mathrm{tot}}\cdot(\overline{x}_{\mathrm{CO}} - \overline{x}_{\mathrm{CH_4}}) + n_{\mathrm{tot}} + n_{\mathrm{CH_4}}\end{aligned} \tag{3.18}$$

Since $1 - \overline{x}_{\mathrm{CO}} + \overline{x}_{\mathrm{CH_4}} > 0$,

$$\overline{n}_{\mathrm{tot}} = \frac{n_{\mathrm{tot}} + n_{\mathrm{CH_4}}}{1 - \overline{x}_{\mathrm{CO}} + \overline{x}_{\mathrm{CH_4}}} \tag{3.19}$$

Using **Equation 3.15** and **3.19**, the amount of CO can be calculated. As a result the measurement of CO in the exhaust gas, expressed in molar fraction, can be converted to a flow curve expressed in mol/s showing the rate of oxygen removal. This can be further integrated to obtain the oxygen removed as a function of time. The integrated extent of reduction curves are considered reliable as a trend, but not in magnitude: large differences were observed between the quantities of oxygen removed calculated by the integrating the CO flow curve and by O-LECO analysis presented in **Section 3.3.2**. As a result the extent of reduction at the end of the experiments, obtained from oxygen analysis, was used to scale the extent of reduction curve. This technique is detailed for each series in the Results chapter.

3.3.5 X-ray diffraction

The X-ray diffraction analysis was carried out using a Bruker D8 DaVinci equipment. The X-ray diffraction technique relies on the detection of the constructive interferences formed by scattering on the crystal atoms [62]. A source of X-ray, such as a copper anode in the present case, generates electromagnetic waves. The incident electromagnetic beam, when reaching the crystal, is scattered by the atoms forming its structure. If the atoms are ordered in planes, constructive interferences can occur when the phase shift is congruent to zero modulo π, which is for an incident angle θ where Braggs law is fulfilled (**Equation 3.20**). In these circumstances, peaks of intensity are observed by the detector and form a characteristic pattern of the crystal structure.

$$\mathrm{n}\lambda = 2\mathrm{d}\sin(\theta) \tag{3.20}$$

A change in the crystal structure, such as the replacement of some atom by one of another element in a solid solution, can modify the spacing between crystallographic planes. This, in return, has an impact on the pattern observed by X-ray diffraction.

3.3.6 Electron microscopy

The samples were prepared for electron microscopy by embedding using epoxy resin. For the synthetic chromite, fractions of the produced lumps were used. For the hardened or reduced-carburized materials, a few dozen pellets were embedded. The samples were next polished using silicon carbide paper and diamond solutions down to 1 µm. The reduced-carburized pellets, some of which contained undoubtedly a high quantity of deposited carbon, were directly polished using diamond suspensions. This intended to avoid a too brutal scratching of this carbon, and an alteration of the samples. The pellet containing samples were also subjected to charging effect. This was answered using carbon evaporation on the specimen. The electron microscopy was performed using field emission scanning electron microscopes (FESEM Zeiss Supra or FESEM Zeiss Ultra). Both secondary electron and back scattered electron imaging were used to obtain the texture and the average atomic mass mapping respectively. These microscopes were both equipped with energy-dispersive spectroscopes (EDS) to determine the chemical composition at the points of interest.

3.3.7 Electron probe micro-analysis

An electron probe micro-analyzer (EPMA) JEOL JXA 8500 was used to generate elemental mapping of some selected samples. The sample preparation was identical to what was explained in **Section 3.3.6**. The EPMA provided high resolution mapping for Fe, Mg, Cr, Al, C and O to observe in detail the phase transformation in the material. The electron probe micro-analysis of the selected samples and areas was operated by Morten Peder Raanes from NTNU.

Chapter 4

Results

This chapter provides the results of the experimental work. The first part, in **Section 4.1**, focuses on the spinel pellets production from pure raw materials. The second part, given in **Section 4.2**, gives the results of the test experiments of the T-series where diverse parameters are varied. Next, from **Section 4.3** to **4.6**, the results of the reduction-carburization experiments are given for the four compositions of interest: $FeCr_2O_4$, $(Fe,Mg)Cr_2O_4$, $Fe(Cr,Al)_2O_4$ and $(Fe,Mg)(Cr,Al)_2O_4$. Finally, **Section 4.7** combines part of the previous results to compare the series.

4.1 Cold crucible work and pellet preparation

The results from the synthesis of oxides to the hardening of pellets are detailed in this section. The philosophy of the synthesis work was to find a satisfactory synthesis route by determining the power input, the duration, the raw material positioning and load. Experiments with the cold crucible induction furnace were by nature transient, difficult to predict and relatively unstable. A decrease in temperature could not necessarily be reverted, as the heat transfer is a function of the material state. However, the success of the synthesis was relatively easy to confirm by XRD.

Considerations on the mechanism observed and product phases obtained are reported in **Section 4.1.1**. The electron microscopy of the selected batches is presented next in **Section 4.1.2**. The XRD analyses of the selected batches before and after hardening are given in **Section 4.1.3** and finally the oxygen analysis of the hardened pellets is reported in **Section 4.1.4**.

4.1.1 Synthesis mechanism

After melting and cooling, the synthesis resulted in lumps of crystalline material as shown on the example in **Figure 4.1**, picture (a). Picture (b) in **Figure 4.1** shows an example of crust formed during an unsuccessful melting. This crust was held in position, sticking to the crucible's inner wall. Crystals in the chromite lump grew radially from the walls where the heat is extracted. An empty pocket was generally observed in the middle of the chromite lump, and an iron bead could be found close to the lump's bottom.

The mechanism observed is as follows:

1. Heating of the iron pieces by the induction
2. Heating of the surrounding oxides by the iron and subsequent melting
3. Meltdown of the charge into a liquid bath
    - If the iron is not spread enough on the surface, a crust might appear at this stage
4. Decrease of the level of the bath due to the melting of the charge underneath
5. Stop of the induction, solidification of the oxide

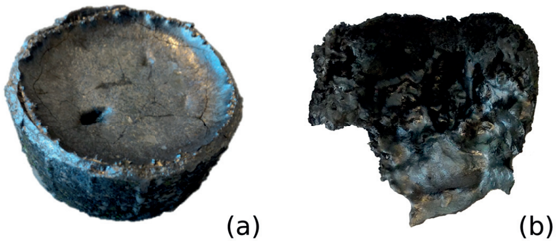

Figure 4.1: Picture of a synthetic chromite sample after synthesis: (a) chromite lump (b) unreacted crust

In the subsections below, the synthesis experiments are commented based on the product aspect and XRD analyses.

Solid solution A ($FeCr_2O_4$)

A-1 Fot this first test, the load was 200 g of a stoichiometric mixture of raw materials. the initial power input was set at 67.5 kW. It was later reduced during the reaction to counter the ongoing splashings. Going from 67.5 to 52.5 kW was detrimental to the synthesis: the liquid bath froze rapidly before all the material placed below could melt.

A-2 To avoid splashings, the power input was reduced and the material load limited to 160 g. The melting was incomplete with these parameters which were not kept further.

A-3 Synthesis A-3 was similar to A-1, but with a power input of 63.75 kW. The power input was balanced to ensure melting while preventing splashings. Some Cr_2O_3 was found left in the product.

A-4 For this batch, 4 g excess iron was added. The product material contained small amounts of metallic iron.

A-5 Using only 2 g of excess iron led to the best results and gave a solid solution of a satisfactory purity. A-6 and A-7, which used the same experimental parameters, led to similar good results.

Solid solution B ($(Fe, Mg)Cr_2O_4$)

B-1 The first $(Fe, Mg)Cr_2O_4$ synthesis trial was run with a stoichiometric mixture of raw materials, 200 g of charge and a power input of 63.75 kW. The melting was incomplete due to the sintering of a crust above the melt. This was interpreted as a lack of iron.

B-2 To ensure melting, a large amount of excess iron was used in this batch. As expected, this helped the melting, but also caused splashing. The power input was reduced from 63.75 to 52.5 kW during the synthesis. The product was found to contain a lot of iron.

B-3 Only 2 g of excess iron were used in this batch. The melting was satisfactory, so was the product material. These parameters were later kept for the B-4 and B-5 batches, giving similar results.

Solid solution C ($Fe(Cr, Al)_2O_4$)

C-1 The first $Fe(Cr, Al)_2O_4$ synthesis trial was run with a stoichiometric mixture of raw materials, 200 g of charge and a power input of 63.75 kW. Some crust formed on the top of the charge and led to failed product.

C-2 The second trial was done with 2 g of excess iron. The melting and products were found satisfactory. Another batch, C-3, was produced following the same the same recipe.

Solid solution D ($(\mathbf{Fe,Mg})(\mathbf{Cr,Al})_2\mathbf{O}_4$)

D-1 The first $(Fe, Mg)(Cr, Al)_2O_4$ synthesis trial was run with 2 g of iron in excess from the stoichiometric composition, 200 g of charge and a power input of 63.75 kW. The power was increased to 75 kW during the reaction as it seemed insufficient to melt the oxides. In spite of this increase, the melting was incomplete.

D-2 The power was increased to 67.5 kW at the start, and the excess iron to 4 g. The product was found satisfactory.

D-3 This experiment was carried out with a lower amount of excess iron, in an attempt to obtain a good melting with an oxide mixture closer to the stoichiometry. This trial was conclusive, and the parameters were kept for D-4.

In conclusion, the synthesis of spinel solid solution with the cold crucible induction furnace was successful. The general recipe involved 200 g of raw materials in stoichiometric amounts, with an addition of 2 g iron in excess. The power input to use was 63.75 kW for the A, B and C solid solutions and 67.5 kW for solid solution D.

4.1.2 Electron microscopy

The following micrographs and point analyses present the four synthetic material produced. The oxygen analysis obtained by EDS measurement is considered unreliable. All the samples did not exhibit an extensive porosity, although some large pores were visible with the naked eye. The following pictures show the main phase, but minor inclusions of iron were found in all the samples. The little amount of measurements and their proximity make them indicative rather than decisive.

A-6

An electron micrograph of the A material is presented in **Figure 4.2** together with the corresponding EDS measurements in **Table 4.1**.

The Fe:Cr ratios are ranging from 0.44 to 0.46, lower than the targeted 0.50 value.

Table 4.1: EDS point measurements for A-6

Point	Element [at%]			
	Fe	Cr	O	C
1	13.48	29.83	53.79	2.90
2	12.81	28.83	55.53	2.84
3	13.42	29.32	53.75	3.51
4	13.66	29.60	53.85	2.88
5	13.91	31.32	51.36	3.41

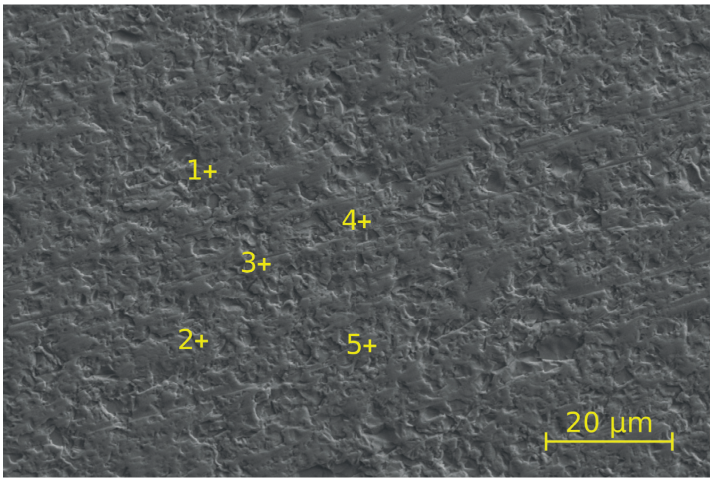

Figure 4.2: Secondary electron micrograph of A-6

B-4

An electron micrograph of the B material is presented in **Figure 4.3** together with the corresponding EDS measurements in **Table 4.2**.

Table 4.2: EDS point measurements for B-4

Point	Element [at%]				
	Fe	Mg	Cr	O	C
1	9.97	3.48	31.58	51.87	3.10
2	12.16	2.84	33.74	47.64	3.61
3	11.74	2.88	31.69	50.18	3.52
4	11.25	3.17	30.59	52.50	2.48
5	10.88	2.83	30.03	52.81	3.45

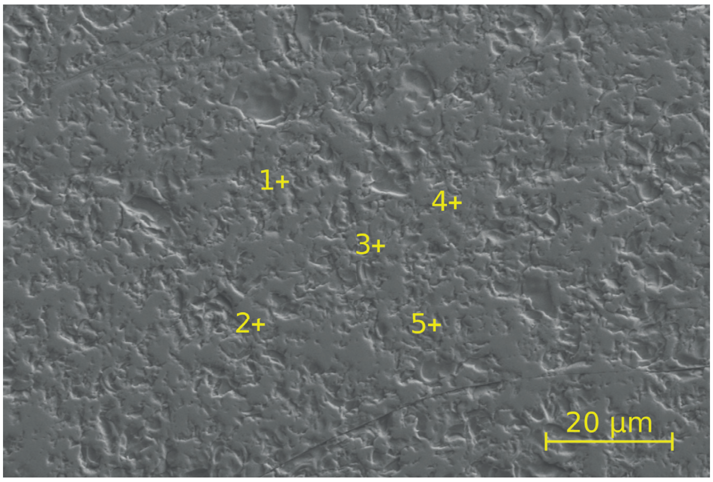

Figure 4.3: Secondary electron micrograph of B-4

The Mg:Fe ratios are ranging from 0.23 to 0.35, showing the variations of the Mg content around the 0.33 target value. The (Fe+Mg):Cr ratios are ranging from 0.42 to 0.47, below the 0.50 targeted value.

C-2

An electron micrograph of the C material is presented in **Figure 4.4** together with the corresponding EDS measurements in **Table 4.3**.

Table 4.3: EDS point measurements for C-2

Point	Element [at%]				
	Fe	Cr	Al	O	C
1	14.79	22.23	7.33	51.86	3.80
2	13.79	22.67	7.23	53.44	2.86
3	13.76	22.51	7.23	52.93	3.58
4	13.57	22.96	7.01	53.53	2.94
5	14.17	22.72	7.10	53.48	2.54

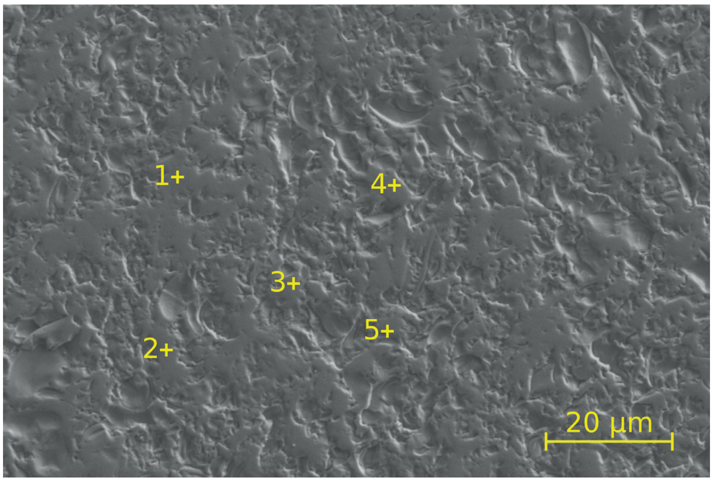

Figure 4.4: Secondary electron micrograph of C-2

The Al:Cr ratios are ranging from 0.31 to 0.33, close to the targeted 0.33 value. These variations are also limited compared to the other solid solutions. The Fe:(Cr+Al) ratios are ranging from 0.45 to 0.50, close to the 0.50 target. The analyses describe a material very close to the objective in terms of metal ratios.

D-3

An electron micrograph of the D material is presented in **Figure 4.5** together with the corresponding EDS measurements in **Table 4.4**.

Table 4.4: EDS point measurements for D-3

Point	Element [at%]					
	Fe	Mg	Cr	Al	O	C
1	11.82	2.32	21.68	7.63	53.19	3.36
2	11.04	2.33	21.51	7.80	54.06	3.26
3	11.50	2.37	21.70	7.60	53.73	3.10
4	12.15	2.21	21.81	7.93	52.37	3.53
5	10.69	2.53	21.27	7.87	54.27	3.37

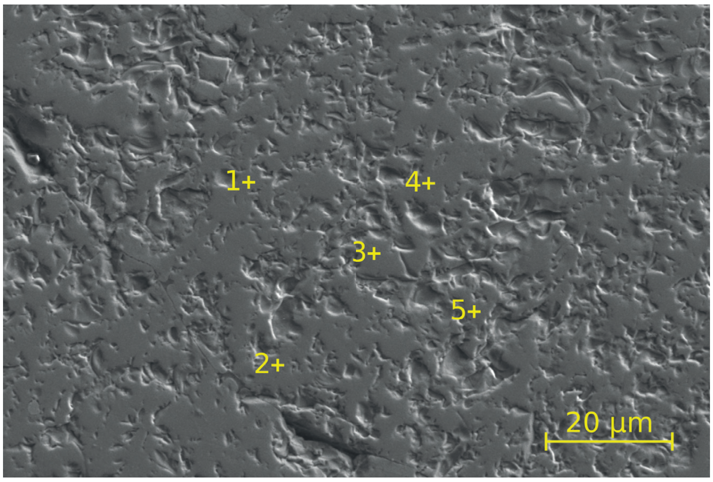

Figure 4.5: Secondary electron micrograph of D-3

The Mg:Fe ratios are ranging from 0.18 to 0.24, significantly lower than the expect 0.33 value. The Al:Cr ratios are ranging from 0.35 to 0.37, slightly higher than the targeted 0.33 value. Finally, the (Fe+Mg):(Cr+Al) ratios are ranging from 0.45 to 0.48, close to the 0.50 target. Overall, the EDS measurements indicate that the sample is lacking magnesium, and is rich in aluminium relative to the targeted solid solution.

4.1.3 X-ray diffraction

The analyses from XRD revealed the spinel nature of the product phase for all the compositions. Minor phases, such as iron of Cr_2O_3 were occasionally evidenced, but were neglected because of their very low peak intensity. The last two batches for each composition (A-6 and A-7, B-4 and B-5, C-2 and C-3, D-3 and D-4) were considered successful. After their mixing, pelletizing and hardening, no significant change could be evidenced in the XRD patterns.

4.1.4 Oxygen content

The oxygen weight content in the synthetic chromite solid solution, after hardening, was analyzed by O-LECO oxygen analyzer, and is reported in **Table 4.5**. The mass of oxygen measured is compared to theoretical amount in each solid solution given the compositions targeted by the synthesis.

Table 4.5: Oxygen weight content in the chromite solid solutions after synthesis and hardening compared to the theoretical oxygen content.

Experiment	Theoretical oxygen content [wt%]	Oxygen in the sample [wt%]
Solid solution A	28.6	28.2
Solid solution B	30.3	29.1
Solid solution C	29.6	28.3
Solid solution D	31.5	29.7

A limited gap is always observed between the two values, the measured oxygen content being inferior to the theoretical one.

4.2 T-series (Test experiments)

The T-series aggregates some preliminary experimental results together with more specific investigations of the reduction-carburization process. The first aim was to determine a temperature range and a gas mixture which would be relevant for the A, B, C and D-series. The experimental parameters of importance for each experiment are provided in **Table 4.6**.

Table 4.6: Main experimental parameters for the T-series of experiment

Experiment name	Material	Sample mass [g]	Temperature [°C]	Gas composition Ar% / CH_4% / H_2%
Test.A.Non_Iso	$FeCr_2O_4$	5.00	600-950	50 / 25 / 25
Test.A.50%CH_4	$FeCr_2O_4$	5.00	1000	50 / 50 / 0
Test.A.25%CH_4	$FeCr_2O_4$	5.00	1000	50 / 25 / 25
Test.A.10%CH_4	$FeCr_2O_4$	5.00	1000	50 / 10 / 40
Test.A.0%CH_4	$FeCr_2O_4$	5.00	1000	50 / 0 / 50
Test.D.H_2O	$(Fe, Mg)(Cr, Al)_2O_4$	5.00	1050	50 / 10 / 40

The experiment Test.A.Non_Iso evaluated the temperature range which would be relevant to investigate the reduction-carburization process. The four next experiments, Test.A.50%CH_4, Test.A.25%CH_4, Test.A.10%CH_4 and Test.A.0%CH_4 evaluated the impact of changes on the CH_4 partial pressure and assisted the selection of a convenient gas mixture to reduce and carburize synthetic spinel solid solutions. Finally, Test.D.H_2O was carried out to verify the absence of water in the exhaust gas during the reduction-carburization.

4.2.1 Non-isothermal experiment

On **Figure 4.6**, the CO volume fraction in the exhaust gas is plotted together with the crucible temperature. Only part of the experiment was carried out with a temperature ramp as the targeted temperature was 950 °C.

The reaction start was observed more than 20 min after the introduction of CH_4. Defining the start of the reaction when the CO content in the process gas is above 0.1 vol%, the reaction was found to start at 818.5 °C. If the CO content threshold is chosen at 0.01%, the temperature found was 758.8 °C. The ramping rate of 10 °C/min employed was too important to accurately determine the reaction start but still allows to estimate it.

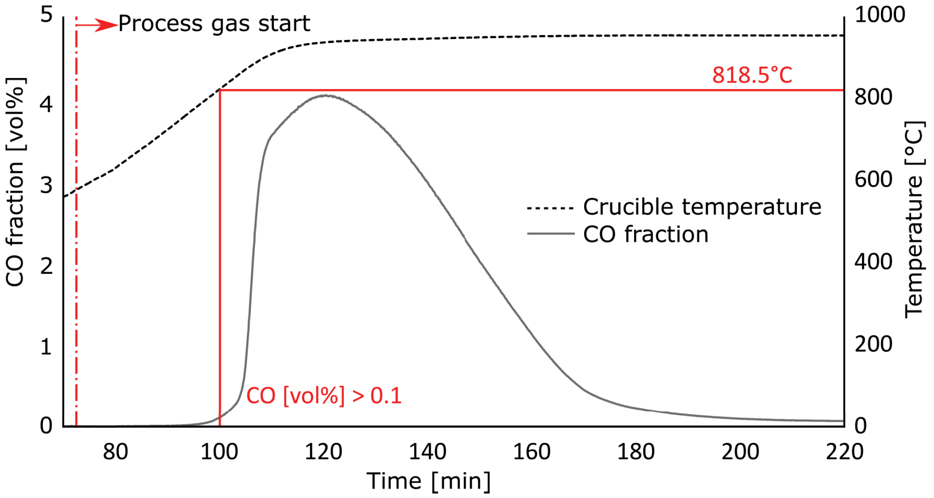

Figure 4.6: CO content in the exhaust gas and crucible temperature for Test.A.Non_Iso

4.2.2 Effect of the CH_4 content

Four gas mixtures were used to investigate the effect of the CH_4 content. In practice, both CH_4 and H_2 were varied while the argon volume fraction was kept at 50 vol% and the gas flow at 1 l/min. Recordings of the CO volume fraction in the exhaust gas are provided in **Figure 4.7**. According to these results, an increase in CH_4 content (accompanied by a decrease of the H_2 content) leads to an increase of the CO volume fraction in the exhaust gas and therefore an increase of the reaction rate. In addition, the shape of the CO curves possibly indicated a change in the mechanism with an increasing CH_4 content shifting from a fast reaction with a brutal drop in the rate to a slow but steady reaction. Only a negligible amount of CO was measured during the experiment carried out in an Ar-H_2 atmosphere, as expected from the absence of a carbon source.

Table 4.7: Oxygen weight content after reduction-carburization for the T-series for varying CH_4 content

Experiment	Sample mass [g]	Oxygen available [g]	Product mass [g]	Oxygen in the product [wt%]	Extent of reduction [%]
Test.A.50%CH_4	5.00	1.41	4.41	2.71	91.51
Test.A.25%CH_4	5.00	1.41	4.30	1.59	95.28
Test.A.10%CH_4	5.00	1.41	3.97	1.52	95.73
Test.A.0%CH_4	5.00	0.35	4.86	23.74	72.69

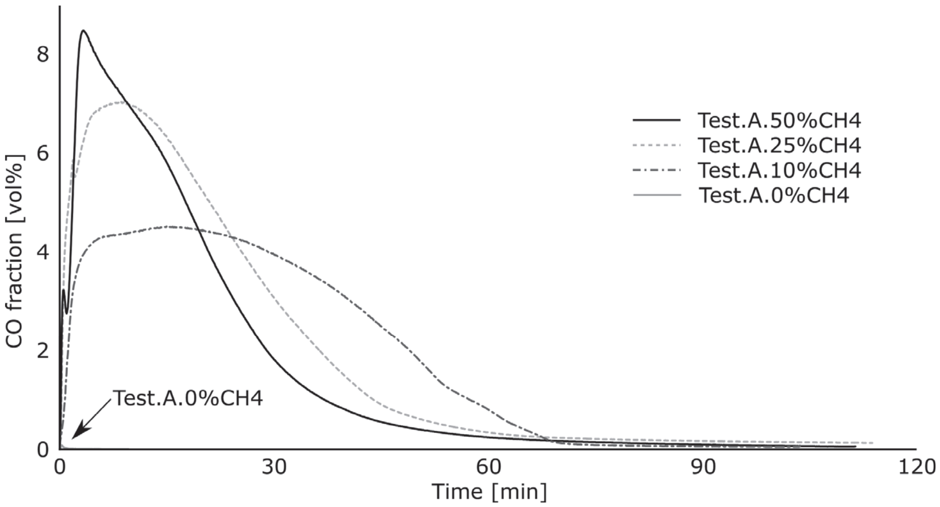

Figure 4.7: CO content in the exhaust gas for the T-series for varying CH_4 contents

The oxygen content in the reacted samples was analyzed using an O-LECO oxygen analyzer and the results reported in **Table 4.7**. The mass of oxygen available was calculated based on the stoichiometry used in the synthesis experiment and for a reduction of iron and chromium oxides. The extent of reduction was little influenced by the gas composition, and a decrease of the methane content resulted in a slight increase of the extent of reduction. For the Test.A.0%CH_4 experiment, only iron is expected to be reduced by hydrogen. The mass loss and oxygen analysis indicate that a significant share of the iron was reduced.

4.2.3 H_2O content in the exhaust gas

To answer the issue of the potential presence of water in the exhaust gas, an experiment was carried out on an $(Fe,Mg)(Cr,Al)_2O_4$ sample. The experiment Test.D.H_2O was done using a set-up presented in **Section 3.1.2**. Before the experiment, 4.02 g of calcined CaO were introduced and no mass change was observed after 60 min of contact with the exhaust gas. It is therefore concluded that the exhaust gas was free of water, and assumed that this result also applies to the other reduction-carburization experiments.

4.3 A-series ($FeCr_2O_4$)

The A-series aims at evaluating the reduction-carburization of pure $FeCr_2O_4$ by methane gas following two purposes. Firstly, it is to study a material containing no impurity elements, which can be used as a benchmark for the B, C and D-series. Secondly, the reduction-carburization of $FeCr_2O_4$ by CH_4 can be compared to that of Cr_2O_3 from the literature. All the experiments of this series have been carried out under a 1 l/min flow of 50%Ar-10%CH_4-40%H_2. The other experimental conditions of interest are reminded in **Table 4.8**.

Table 4.8: Main experimental parameters for the A-series of experiment

Experiment name	Temperature targeted [°C]	Duration [min]
AT1.030	950	30
AT2.030	1000	30
AT3.030	1050	30
AT1.120	950	120
AT2.104	1000	104
AT3.120	1050	120

XRD, SEM, EDS, EPMA and O-LECO were employed on the reacted samples. The live measurements and the post-reaction analysis were used to compute the extent of reduction curves.

4.3.1 Temperature measurements

For the A-series, the temperature ramp-up was carried out in argon atmosphere, avoiding any gas-solid reaction. The reaction temperature was set using a control of the wall temperature, significantly different from the crucible temperature. An offset of about 70 °C was generally observed between these two values. The process gas was introduced after stabilizing of the temperature. Deviations from the targeted temperatures were regularly observed due to the combined action of the heating and the chemical reactions. **Figure 4.8** shows an example of the temperature profiles observed, while **Table 4.9** reports the targeted, minimum, maximum and average temperatures observed during the reaction for each experiment.

Table 4.9: Targeted, minimum, average and maximum temperatures during the reduction-carburization of the A-series

Experiment	Temperature [°C]			
	Targeted	Min.	Avg.	Max.
AT1.030	950	949.3	950.8	952.9
AT2.030	1000	996.3	998.3	1005.8
AT3.030	1050	1043.1	1044.5	1049.1
AT1.120	950	952.3	961.3	968.0
AT2.104	1000	1004.1	1008.5	1014.7
AT3.120	1050	1053.3	1063.7	1068.9

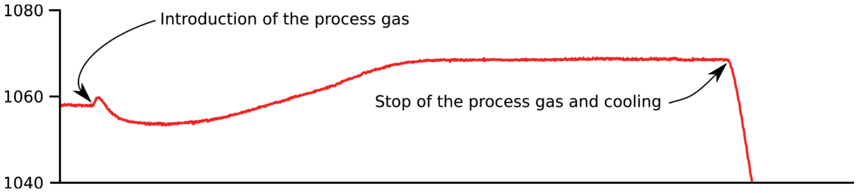

Figure 4.8: Typical crucible temperature profile during the reaction (here for AT3.120)

The temperature profiles for the A-series typically exhibited a decrease of the crucible temperature after introduction of the process gas, followed by a subsequent increase of the temperature over the initial value.

4.3.2 Exhaust gas measurements

When the Ar gas was replaced by the process gas, peaks of CH_4 were observed. The CH_4 content typically peaked at the start, followed by a fast decrease and a subsequent slow increase. **Table 4.10** reports the values of the CH_4 peaks, as well as the temperature at the peak. No clear link was evidenced between the peak height and the peak temperature.

Table 4.10: CH_4 peak and temperature at the process gas introduction for the A-series

Experiment	CH_4 peak [%]	Temperature at the peak [°C]
AT1.030	7.65	951.6
AT2.030	7.76	1005.8
AT3.030	4.47	1048.7
AT1.120	6.37	961.7
AT2.104	7.58	1006.8
AT3.120	4.06	1059.6

The CO curves for the A-series are provided in **Figure 4.9**. On this graph, the CO curves are only displayed for the period when the pellets are in contact with the process gas, and not with the pure Ar atmosphere.

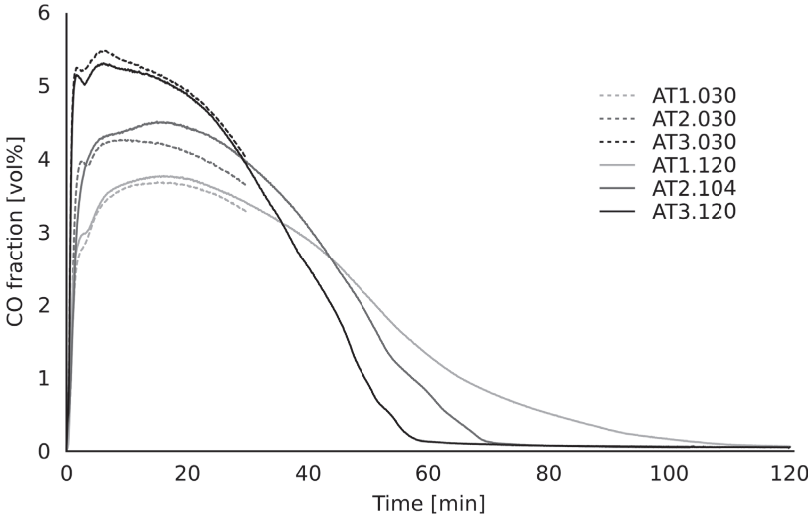

Figure 4.9: CO content in the exhaust gas for the A-series

The CO content varied moderately during the first stages of the experiment, indicating a rather constant reaction rate. In addition, there is a good fit between the CO content in the exhaust gas for experiments carried out at a similar temperatures. This shows the good precision of the CO measurement, and suggests that once integrated, it can likely be used as a comparative measurement for the oxygen removal during reduction. After the stopping of the process gas, some CO was still observed in the exhaust gas but not shown on the figure.

4.3.3 Sample mass

The sample mass was measured before and after each experiment. It reflects both the mass intake because of the cracking of methane and the carburization, as well as the mass loss from the reduction. The results are gathered in **Table 4.11**.

The sample mass loss is clearly linked to the temperature after 30 min reduction-carburization, going from -12% at 950 °C to -18.4% at 1050 °C. After extensive reduction-carburization, it appears that the duration had little effect on the mass change. The samples AT1.120, AT2.120 and AT3.120 show mass losses over -20%, the highest temperature still giving the highest mass loss. This is a first indication that the cracking was very limited for the A-series, but cracking cannot be excluded yet.

Table 4.11: Sample mass change for the A-series

Experiment	Final sample mass [g]	Mass change [%]
AT1.030	4.40	-12
AT2.030	4.28	-14.4
AT3.030	4.08	-18.4
AT1.120	4.01	-19.8
AT2.104	3.97	-20.6
AT3.120	3.93	-21.4

4.3.4 Oxygen content

The oxygen content of the product was first determined analyzing the samples after reaction using the O-LECO. In parallel, the CO content in the gas was integrated over the course of the reaction. The two set of data are finally combined to calculate "reconciled" values.

From the O-LECO analyzer

The oxygen weight content was measured by an O-LECO oxygen analyzer, and is reported in **Table 4.12**. The mass of oxygen was compared to the measurements of unreacted pellets mentioned in **Section 4.1.4**. The mass of oxygen available was calculated based on the stoichiometry used in the synthesis experiment and for a reduction of iron and chromium oxides. The extent of reduction was obtained using the final mass, the oxygen content in the product samples and the oxygen available in the sample.

Table 4.12: Oxygen weight content after reduction-carburization for the A-series

Experiment	Sample mass [g]	Oxygen available [g]	Product mass [g]	Oxygen in the product [wt%]	Extent of reduction [%]
AT1.030	5.00	1.41	4.40	15.90	50.42
AT2.030	5.00	1.41	4.28	14.10	57.16
AT3.030	5.00	1.41	4.08	8.70	74.80
AT1.120	5.00	1.41	4.01	1.94	94.49
AT2.104	5.00	1.41	3.97	1.52	95.73
AT3.120	5.00	1.41	3.93	0.76	97.87

The calculated extent of reduction shows that the oxygen was readily removed during the reaction. After 30 min, more than 50% of the oxygen was taken out of the samples at all the temperatures considered. The sample reacted at 1050 °C was reduced significantly faster than the 950 and 1000 °C samples. When the samples were kept for longer durations, most of the oxygen was removed from the $FeCr_2O_4$ samples. Long reaction times damped out the benefit of higher temperatures.

From the CO curves

In addition to the measurement from the final product, one can integrate the CO measured in the process gas to find the amount of oxygen removed. The CO considered here was taken not only from the "active" part of the experiment when the process gas was on, but also from the CO expelled after stopping of the process gas. Moreover, the flow change due to reduction-carburization and cracking reactions was taken into consideration using the formula given in **Section 3.3.4**.

Table 4.13: Oxygen content from integration of the CO curve after reduction-carburization for the A-series

Experiment	Sample mass [g]	Oxygen available [g]	Oxygen removed [g]	Extent of reduction [%]
AT1.030	5.00	1.41	0.83	58.65
AT2.030	5.00	1.41	0.99	70.21
AT3.030	5.00	1.41	1.26	89.01
AT1.120	5.00	1.41	1.57	111.35
AT2.104	5.00	1.41	1.60	113.48
AT3.120	5.00	1.41	1.62	115.04

The results are presented in **Table 4.13**. A similar trend is observed between the results from both methods, but the integrated CO values exceed the amount of oxygen contained in the material, questioning the accuracy of the CO measurement.

Reconciling O-LECO and integrated CO

For the A-series, the O-LECO and integrated CO contents gave the same trends. The integrated CO content, however, gave notably too high values as explained earlier. It is believed however that the integrated CO content is more precise while the O-LECO analysis is more accurate. In order to reconcile both measurements, one measurement from the O-LECO analyzer was used as a reference and all the integrated CO values were scaled according to it. The experiment used as a reference was chosen to give the least difference between the rescaled integrated CO contents and O-LECO measurements, calculated by the sum of the differences squared. For the A-series, the best reference was found to be AT2.104. The extents of reduction calculated from this method are given in **Table 4.14**

Table 4.14: Extent of reduction calculated from integrated CO and O-LECO for the A-series

Experiment	Extent of reduction [%] with O-LECO	Extent of reduction [%] with CO content	Extent of reduction [%] calculated
AT1.030	50.42	58.65	49.48
AT2.030	57.16	70.21	59.23
AT3.030	74.80	89.01	75.09
AT1.120	94.49	111.35	93.94
AT2.104	95.73	113.48	95.73
AT3.120	97.87	115.04	97.05

For the A-series, the values obtained by the reconciliation method are close to those from O-LECO analysis. Therefore, the data led to the same conclusions those from the previous analysis.

4.3.5 X-ray diffraction

In addition to the parent $FeCr_2O_4$ spinel, two phases are identified by XRD: Cr_7C_3 and Cr_2O_3. The absence of a Fe-containing product phase will be discussed later on, using other analyses. **Figure 4.10** presents the XRD patterns for the A-series. The temperature notably influenced the reaction speed as indicated by the relative heights of the $FeCr_2O_4$ and Cr_7C_3 peaks in AT1.030, AT2.030 and AT3.030. The Cr_2O_3 phase was present in many samples but always as a minor compound. After prolonged reduction-carburization, as in samples AT1.120, AT2.104 and AT3.120, the $FeCr_2O_4$ phase disappeared and no spinel was remaining. Minor quantities of Cr_2O_3 were observed in AT1.120 but the material is nearly fully carburized to a M_7C_3 phase. Metal Fe or a Fe-Cr alloy phase could, to some extent, be hidden by the carbide peaks and its absence is not fully disproved by the XRD patterns.

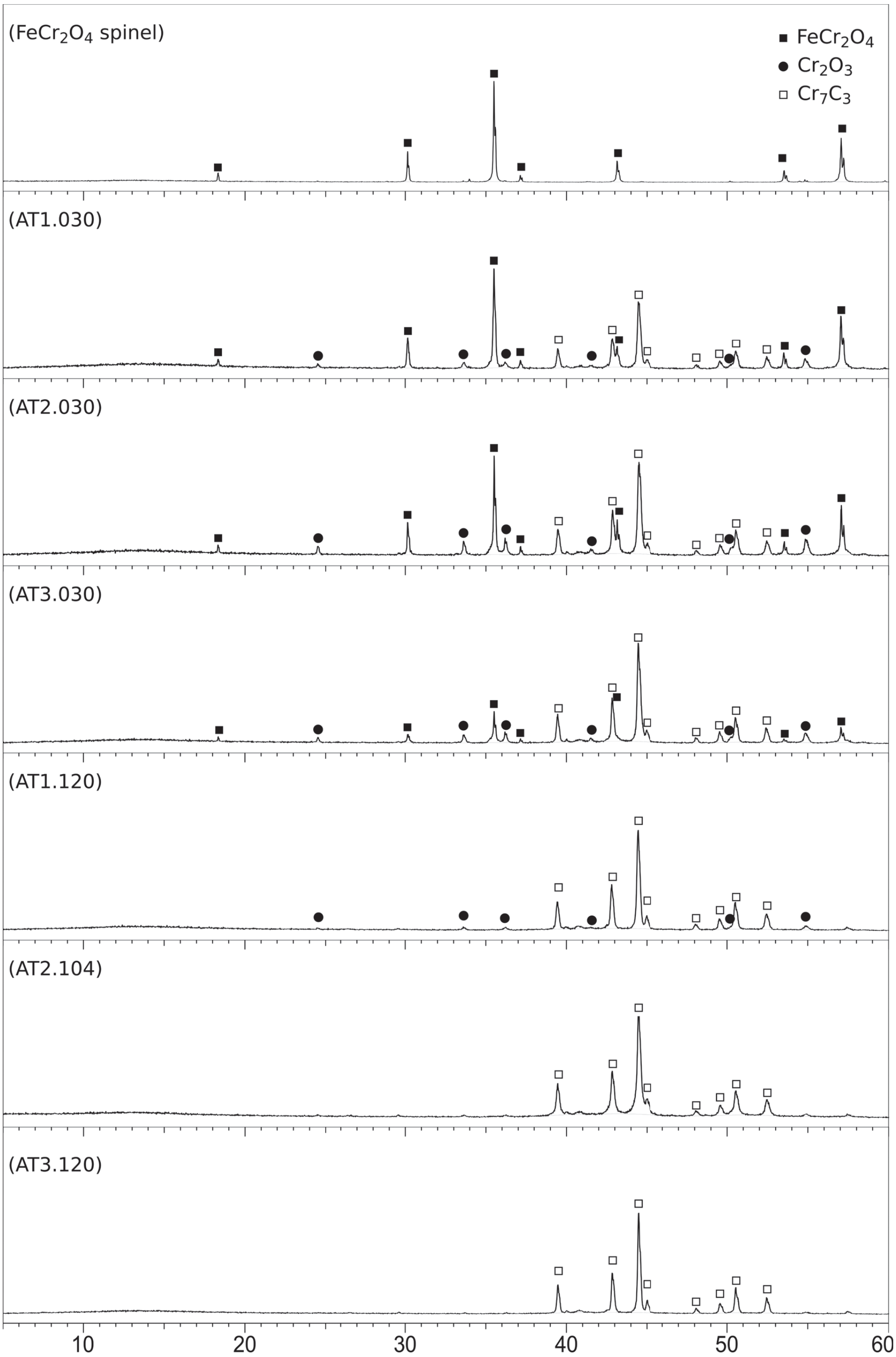

Figure 4.10: XRD patterns for the A-series

4.3.6 Extent of reduction curves

Figure 4.11 provides the extent of reduction curves as a function of time for the A-series. These curves were obtained by integration CO flow out of the furnace, based on the CO content curves given in **Figure 4.9** and the volume change obtained by the formula given in **Section 3.3.4**. The curves are next rescaled based on the calculated extent of reduction at the end of the experiment given in **Section 4.3.4**.

On **Figure 4.11**, there is a close fit between the experiments carried out at similar temperatures. The extent of reduction, calculated in **Section 4.3.4** led to extent of reduction curves showing trends similar to those of the CO curves. In particular, the difference between AT2.030 and AT2.104, already observed in terms of CO, is still found in the extent of reduction curves.

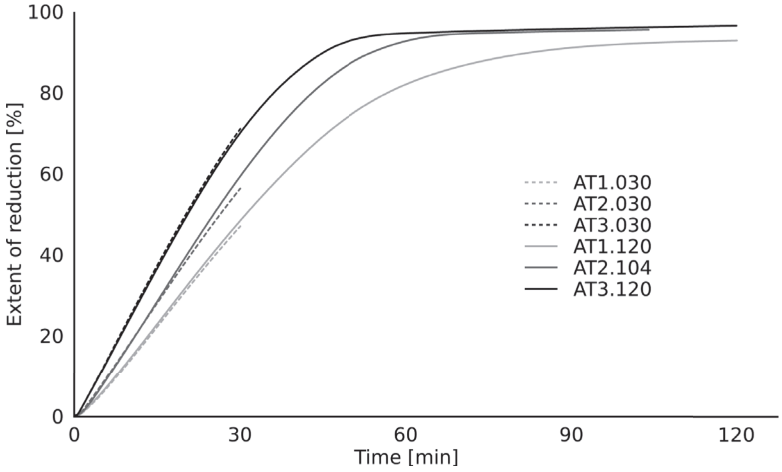

Figure 4.11: Extent of reduction curves for the A-series

These time-dependent curves also show a quite constant reduction rate at the beginning of the reaction. This reaction rate is influenced by the temperature, as shown by the dissimilar slopes between AT1, AT2 and AT3. For the long experiments, the curves approach the extent of reduction calculated in **Section 4.3.4**. For AT2 and AT3, the final extent of reduction was reached in a short time but the reaction needed a substantially longer time at 950 °C for AT1.120. The temperature had a limited effect of the extent of reduction.

4.3.7 Electron microscopy

The product pellets stemming from each experiment were analyzed by SEM, together with EDS point measurements. The carbon content obtained by EDS is indicative but hardly measurable. Its detection is also disturbed by the use of a carbon coating. The oxygen analysis is slightly off and only given as a qualitative result. For some selected samples, micrographs by EPMA were also recorded. In the section below, the significant findings are reported sample by sample.

AT1.030

The electron micrographs presented in **Figure 4.12** show three different pellets from experiment AT1.030, the corresponding EDS point analyses are given in **Table 4.15**.

Table 4.15: EDS point measurements for AT1.030

Point	Element [at%]			
	Fe	Cr	O	C
1	23.56	36.76	16.00	23.68
2	16.35	28.10	47.68	7.87
3	17.18	27.17	48.38	7.26
4	12.89	24.11	48.49	14.51
5	35.10	14.88	11.72	38.3
6	15.60	29.96	48.26	6.18
7	14.71	30.40	48.56	6.33
8	15.93	29.69	48.00	6.38
9	15.42	29.44	48.41	6.74
10	23.72	34.97	7.01	34.3
11	20.58	32.99	6.08	40.35
12	15.70	29.55	48.03	6.72
13	24.38	41.69	···	33.93
14	25.73	42.22	5.30	26.75
15	···	39.92	52.73	7.36
16	22.02	38.34	5.15	34.49
17	25.72	45.04	···	29.24
18	21.97	40.59	···	37.44
19	22.09	42.61	5.06	30.24

The first picture displays uniform and dense grains of material, comparable to the micrograph of the hardened pellets. On the edge of some grains, smaller particles are observable. The EDS analyses for points 1 and 5 indicate the presence of phase richer in carbon, but slightly depleted of oxygen when compared to the analyses for point 2, 3 and 4. These two phases can be interpreted as a carbide and an oxide respectively. The presence of oxygen in the reduced phases can be explained by the limited resolution of the equipment, and the presence of oxide in the surroundings.

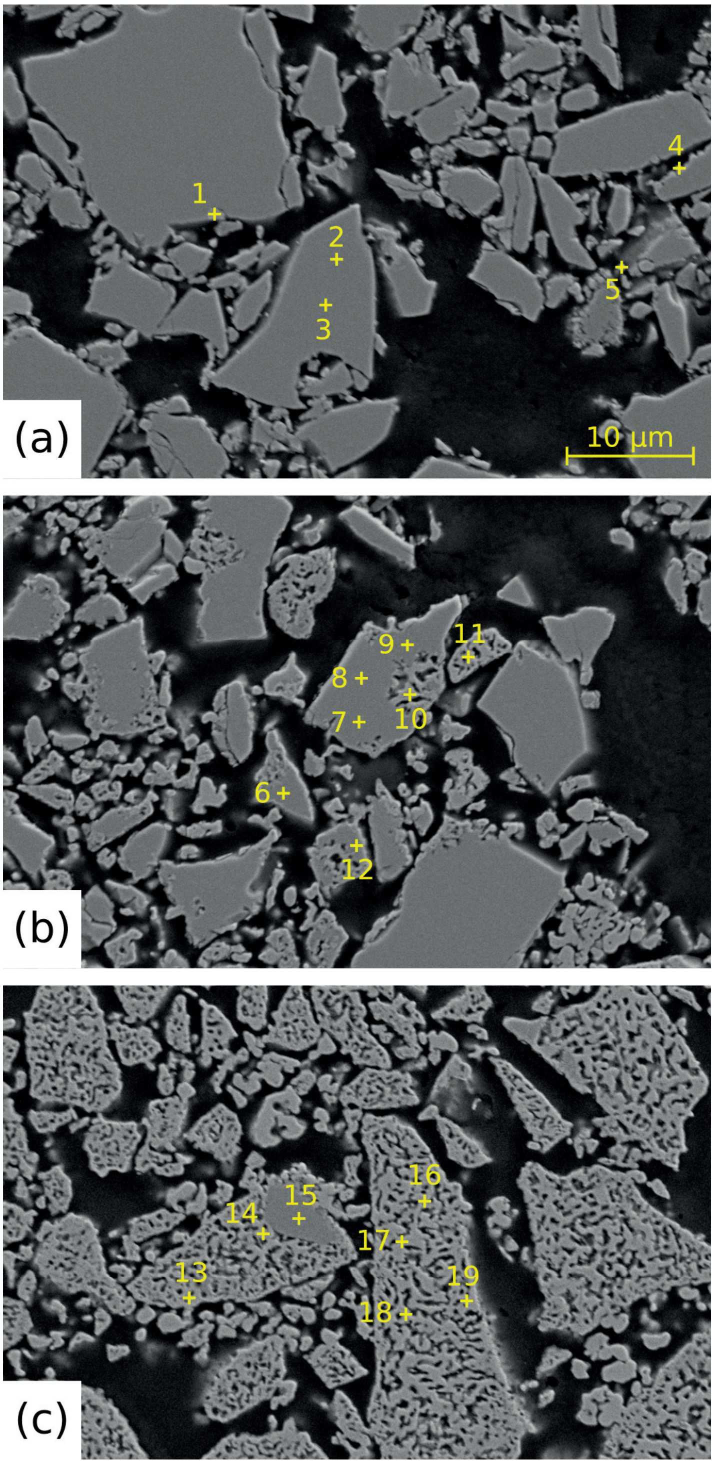

Figure 4.12: Secondary electron micrographs from the AT1.030 experiment on three different pellets

The second picture shows similar grains with a new phase. While the dense material is an iron-chromium oxide, significant amount of the reduced phase appear in specific spots of the grains.

The third picture presents grain almost fully reduced-carburized. The product phase is porous, but the shape of the initial grains was conserved. The oxygen has almost disappeared of the sample, but an unreduced chromium oxide remains in one location.

Given the XRD analyses presented in **Section 4.3.5**, the iron-chromite oxide phase can be identified as $FeCr_2O_4$ which is subsequently converted to a mixture of M_7C_3 and Cr_2O_3 during the reduction-carburization. At the end, only an M_7C_3 phase remains.

AT2.030

An electron micrograph showing a partly reacted grain from experiment AT2.030 is shown in **Figure 4.13**. This picture reveals a new morphology for the reacted phase, but the previous morphologies evidenced with AT1.030 were also found. A shrinking core is observable at the grain scale: the edge is porous, while the center is dense and unreacted. The point analyses, provided in **Table 4.16**, confirm that the edge is reduced, though not fully, while the center is an oxide. It is reasonable to assume that the phases at the edge and center consist of a mixture of M_7C_3 and Cr_2O_3, and the center of $FeCr_2O_4$. At the outermost, the content of iron is relatively high compared to the rest of the measurements and could indicate that iron was reduced first and concentrated towards the grain's surface. This shrinking core morphology is only observed on large grains, and is possibly only relevant for these.

Table 4.16: EDS point measurements for AT2.030

Point	Element [at%]			
	Fe	Cr	O	C
1	33.84	17.55	10.69	37.92
2	12.18	31.52	24.55	31.75
3	9.15	32.06	24.36	34.44
4	12.74	26.10	41.93	19.23
5	12.67	25.91	41.89	19.53
6	12.76	25.99	41.83	19.43

Figure 4.14 shows elemental mappings using the EPMA. These mappings confirm the previous EDS measurements: the edge of the grains is depleted of oxygen, but the center remained unreduced. Carbon and oxygen contents are contrary: the oxide phases contain only small amounts of carbon probably due to the carbon coating while the edges, depleted of oxygen, are richer in carbon. Iron and chromium are spread in

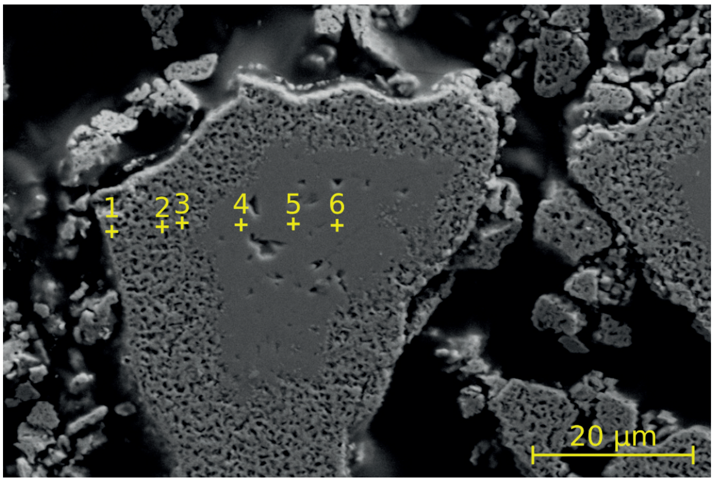

Figure 4.13: Secondary electron micrograph of AT2.030

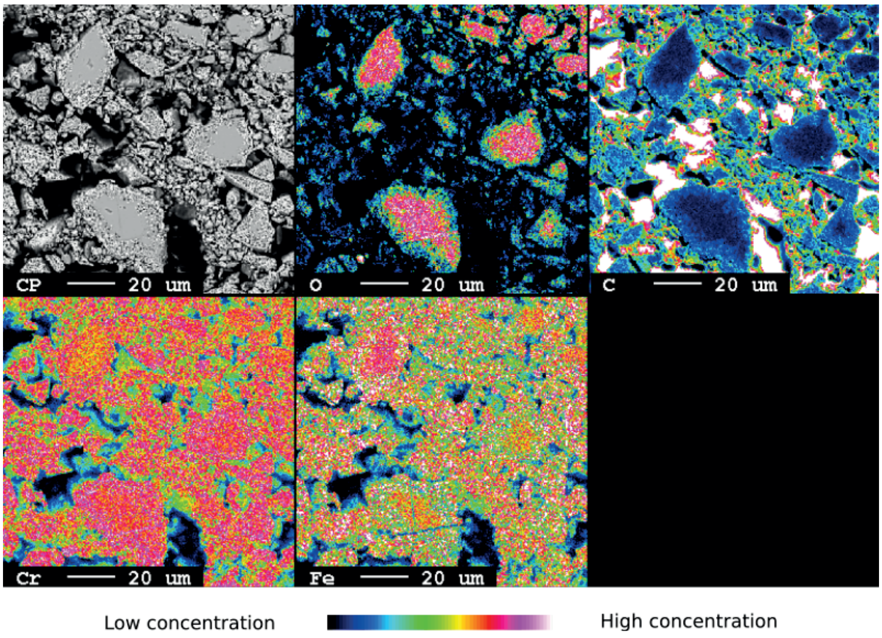

Figure 4.14: Elemental mapping of AT2.030

the grains and found both in the edge and in the center. However, due to the inconsistent amount of oxygen and carbon in the sample, it is not clear whether or not the Fe:Cr ratio changes from the grain's edge to the grain's interior.

AT3.030

The electron micrographs for this sample evidenced similar features as those mentioned above, namely the presence of fully reacted and unreacted grains and pellets in the same batch.

However, this sample provided additional information on the reaction interface at the scale of the pellet. **Figure 4.15** and **4.16** show mappings of a partly reacted pellet at high and low magnification respectively.

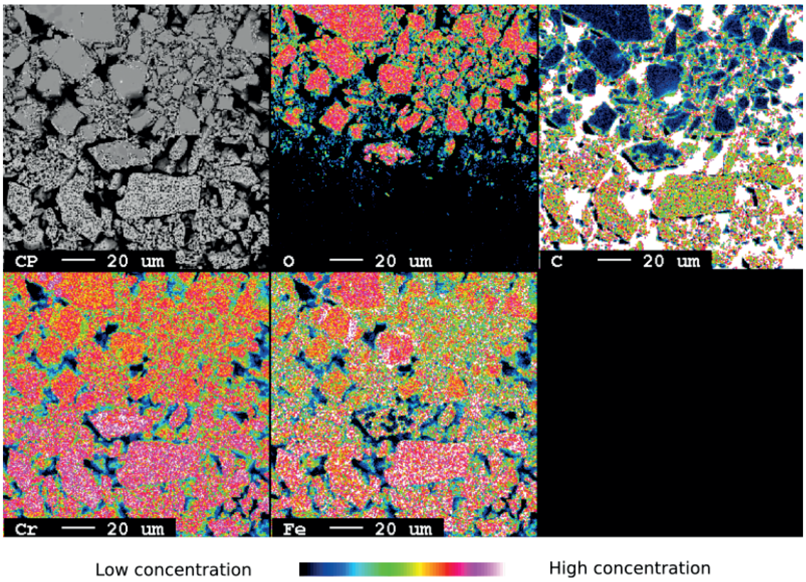

Figure 4.15: Elemental mapping of AT3.030 at the reaction front

On the first set of pictures, a reaction interface is clearly delineated by the removal of the oxygen. Proofs of a shrinking core at the grain scale as observed in AT2.030 is hardly evidenced on this mapping. On the second mapping, the reaction interface is again easily noticed by the absence of oxygen and the change in carbon content.

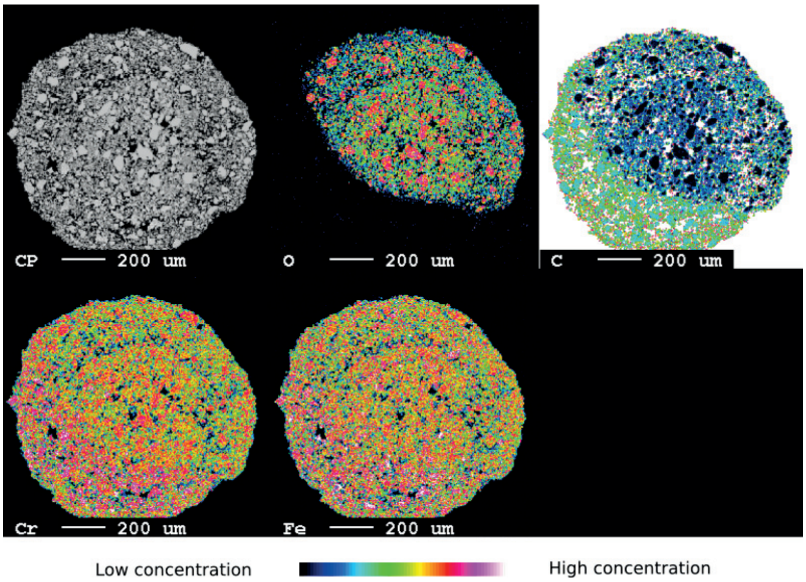

Figure 4.16: Elemental mapping of AT3.030 for a pellet

The reaction did not proceed following a shrinking core mechanism at the pellet scale: the oxygen removal progressed from the lower left corner, likely where the process gas hit the sample.

AT1.120

Intricate pore channels are observed on the electron micrographs of the reacted pellets from AT1.120. On **Figure 4.17**, the reduced-carburized material forms convoluted networks separated by thin empty spaces. The EDS measurements, provided in **Table 4.17** indicate that the material is essentially carburized, but still containing small amounts of oxygen.

Table 4.17: EDS point measurements for AT1.120

Point	Element [at%]			
	Fe	Cr	O	C
1	16.25	37.47	···	46.29
2	16.40	33.82	9.06	40.71
3	53.56	5.01	···	41.43
4	52.54	7.82	···	39.63
5	12.55	33.75	17.49	36.21
6	15.07	37.96	···	46.98

Points 3 and 4 possibly indicate the presence of a Fe-Cr alloy. This is suggested by the dense aspect of this phase, characteristic of metallic phases, and the high Fe:Cr ratios in the EDS analyses of point 3 and 4. Although not evidenced by XRD, such a phase is not inconceivable.

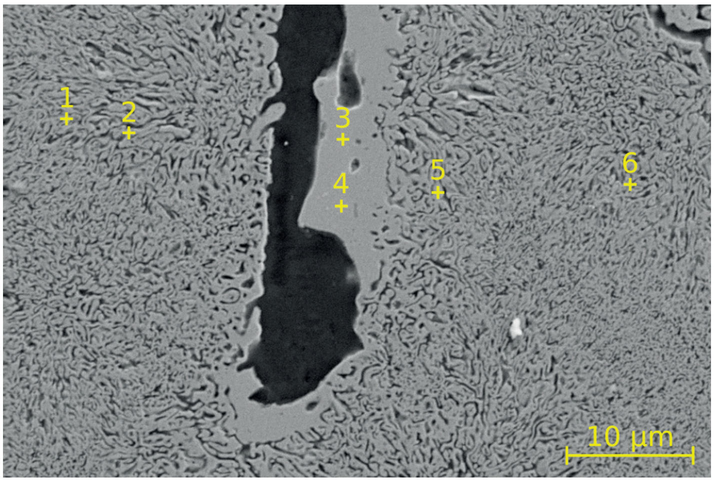

Figure 4.17: Secondary electron micrograph from the AT1.120 experiment

AT3.120

The sample from experiment AT3.120 have been subjected to the strongest reducing conditions in the series. The measurements given in **Table 4.18**, corresponding to the points in **Figure 4.18**, confirm that the reduction was nearly complete.

Table 4.18: EDS point measurements for AT3.120

Point	Element [at%]			
	Fe	Cr	O	C
1	25.96	44.77	···	29.27
2	25.70	44.38	···	29.92
3	26.28	45.51	···	28.21
4	24.76	42.01	···	33.23
5	19.55	34.73	···	45.72
6	26.62	44.06	···	29.32
7	17.93	29.25	···	52.82
8	32.04	37.89	···	30.06
9	30.33	39.87	···	29.80
10	29.60	38.94	···	31.47
11	21.13	26.57	4.89	47.41
12	27.13	36.32	4.69	31.86
13	26.56	37.07	6.90	29.43

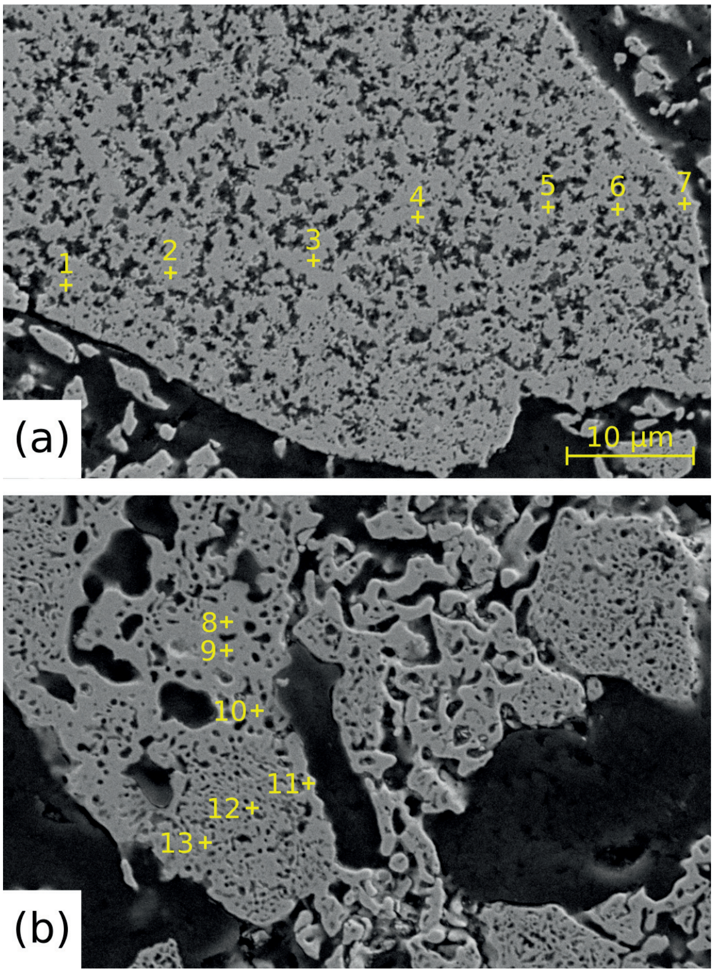

Figure 4.18: Secondary electron micrographs from the AT3.120 experiment of two different pellets

The Fe:Cr ratios in these measurements are varying significantly, but no link with the position of the measurement was evidenced. The grain from the second pellet from experiment AT3.120 exhibits a higher iron content, which might be linked to a higher iron content in the parent spinel. The morphologies observed in the two pictures of **Figure 4.18** are strikingly different. In the first pellet, the carbide/pore interface is rough and seem to branch from the pore channels. The carbide phase formed large and dense fields on most of the grain. In the second picture the carbide/pore interface is smoother but the carbide fields also formed dense fields.

4.3.8 Summary of the A-series

At the temperatures of the study, $FeCr_2O_4$ was readily reduced-carburized by a 50%Ar-10%CH_4-40%H_2 gas mixture to $(Cr, Fe)_7C_3$. The increase of temperature enhanced the reaction rate, but the extent of reduction was little affected after 120 min. Full carburization of $FeCr_2O_4$ is within reach.

During the reaction the iron oxides were reduced faster. Therefore, a composition gradient was observed in the product carbide together with unreduced Cr_2O_3 after 30 min of reaction. The initial shape of the grains seemed well kept, but the product phase was extensively porous. The pores' aspect varied from grain to grain.

The micrographs showed that the reaction proceeded in a shrinking core manner at the grain scale. The micrographs of a whole pellet evidenced a sharp reaction interface, its position indicating that the reaction proceeded from one side of the pellet rather than from all directions.

4.4 B-series ($(Fe, Mg)Cr_2O_4$)

The B-series focused on studying the effect of Mg-addition on the reaction mechanism of chromite reduction-carburization. The gas mixture employed consisted of 1 l/min of 50%Ar-10%CH_4-40%H_2. The main parameters for the experiments carried out on $(Fe, Mg)Cr_2O_4$ are provided in **Table 4.19**.

Table 4.19: Main experimental parameters for the B-series of experiment

Experiment name	Temperature targeted [°C]	Duration [min]
BT1.030	950	30
BT2.030	1000	30
BT4.030	1050	30
BT1.120	950	120
BT2.206	1000	206
BT3.120	1020	120
BT4.120	1050	120

These parameters were kept alike those from the A, C and D-series. However another experiment at 1020 °C was added to offer additional data for the modeling. The results from the characterization by weight measurement, XRD, SEM, EDS, EPMA and O-LECO are given next. Finally, a calculated extent of reduction curve is given for each experiment, based on both the live measurements and the analysis of the products.

4.4.1 Temperature measurements

The temperature ramp-up was done in argon atmosphere. The process gas replaced argon after stabilizing of the crucible temperature. Again, deviations were observed between the targeted temperature and the measured ones, because of the furnace heating and the chemical reactions. The deviations induced by the chemical reactions were negative, as expected from endothermic reactions, and similar to those in the A-series. These were however moderate in comparison. Characteristic temperature values during the reduction-carburization are reported in **Table 4.9**. In some occurrences, the targeted temperature was changed during operation to avoid too large deviations from the target. This was the case in experiment BT2.030 and BT2.206 but this practice was abandoned afterwards to avoid further complication of the gas curves.

Table 4.20: Targeted, minimum, average and maximum temperatures during the reduction-carburization of the B-series

Experiment	Temperature [°C]			
	Targeted	Min.	Avg.	Max.
BT1.030	950	948.7	954.7	956.6
BT2.030	1000	995.9	1001.4	1005.7
BT4.030	1050	1045.3	1048.7	1052.4
BT1.120	950	960.1	965.8	967.4
BT2.206	1000	998.6	1003.5	1009.9
BT3.120	1020	1016.4	1028.8	1033.2
BT4.120	1050	1043.8	1056.6	1061.3

4.4.2 Exhaust gas measurements

For the B-series, two gas peaks were observed at the early stages of the reaction. Firstly, a CH_4 peak appeared in a similar way to what was found in the A-series, indicating a delay before methane enters in reaction. The CH_4 content in the exhaust gas decreased after its peak value, and next increased back up to a value equal to its volume fraction in the input gas. Secondly, a CO peak appeared indicating the beginning of the reduction. This peak rapidly decreased in an exponential decay fashion, down to a non-zero value. An example of the CH_4 and CO peaks is given in **Figure 4.19** and **4.20** for experiments BT2.030 and BT2.206 respectively.

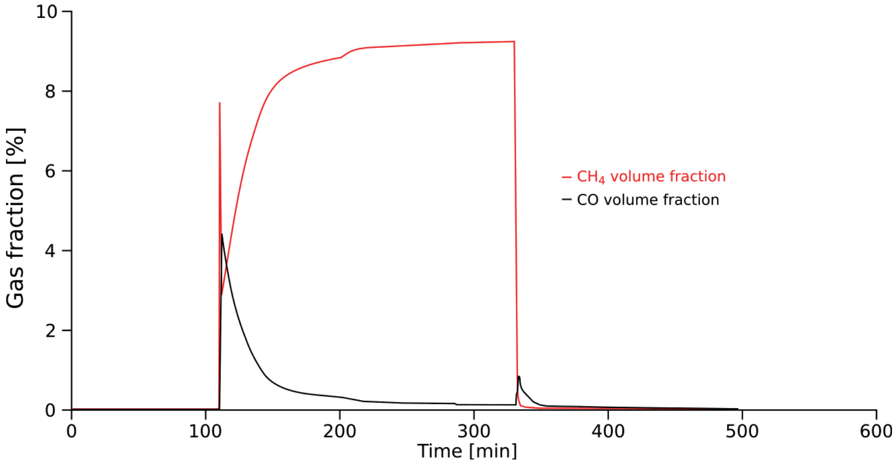

Figure 4.19: CH_4 and CO content in the exhaust gas for experiment BT2.030

On **Figure 4.20**, a bump is observed after 200 min on both curves due to a brutal change in temperature. The gas peaks previously mentioned are reported in **Table 4.21**, together with the temperature at the introduction of the process gas. On the left, the values are shown ordered by experiment name, while the data is ordered by the starting temperature on the right side. Because the temperature variation between the two peaks was limited, only one temperature was considered. The CO peak height seemed to be favored at high temperatures, while the CH_4 peak is instead favored at low temperatures, indicating both a faster methane use and faster reduction with higher temperatures.

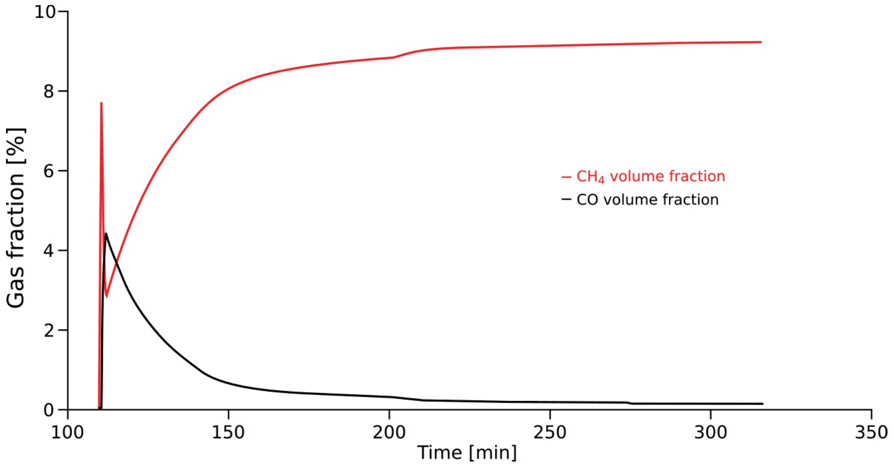

Figure 4.20: CH_4 and CO content in the exhaust gas for experiment BT2.206

Table 4.21: CH_4 and CO peak and temperature at the process gas introduction for the B-series

Experiment	Temp. at start [°C]	CH_4 [%]	CO [%]	Experiment	Temp. at start [°C]	CH_4 [%]	CO [%]
BT1.030	948.7	8.464	3.279	BT1.030	948.7	8.464	3.279
BT2.030	999.1	8.001	4.389	BT1.120	961.1	7.925	3.398
BT4.030	1049.9	6.027	5.445	BT2.030	999.1	8.001	4.389
BT1.120	961.1	7.925	3.398	BT2.206	1003.3	7.769	4.511
BT2.206	1003.3	7.769	4.511	BT3.120	1022.8	6.154	5.262
BT3.120	1022.8	6.154	5.262	BT4.030	1049.9	6.027	5.445
BT4.120	1050.7	5.644	5.487	BT4.120	1050.7	5.644	5.487

Towards the end of the experiment, another CO peak was occasionally observed. This CO peak was found only during the long experiments, the short ones exhibiting a slow decrease of the CO content instead as shown in **Figure 4.19** and **4.20**. The CH_4 content at the end of the long experiments, essentially when the reduction is finished, can also provide information on the methane cracking. The related measurements are given in **Table 4.22**. The high CH_4 volume fraction indicates a limited amount of cracking after reduction-carburization of the material, even at fairly high temperatures. This inclination of CH_4 to remain stable was decreased with increasing temperatures, but the CH_4 content remained notably higher than its equilibrium value.

Table 4.22: CH_4 content and temperature at the gas replacement for the long experiments of the B-series

Experiment	Temp. at stop [°C]	CH_4 [%]
BT1.120	966.6	9.328
BT2.206	1001.7	9.279
BT3.120	1032.4	8.821
BT4.120	1060.0	8.436

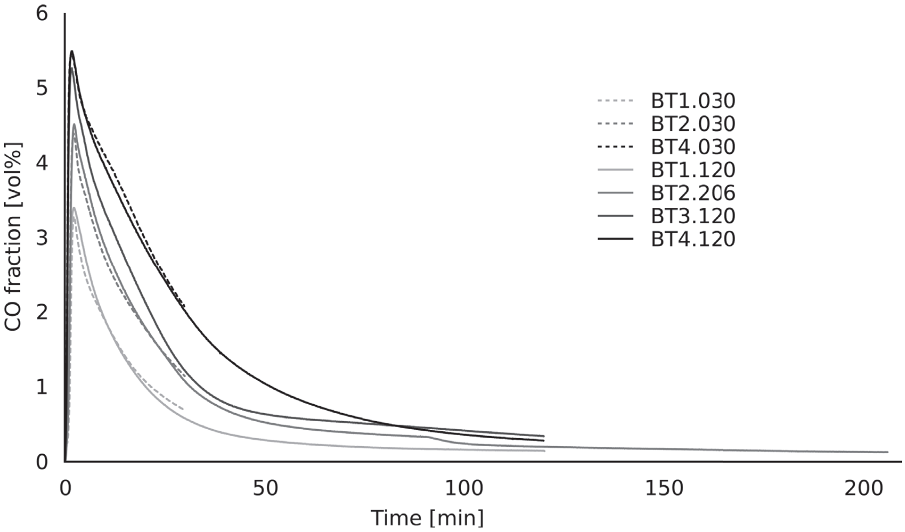

Figure 4.21: CO content in the exhaust gas for the B-series

The CO curves for the B-series are provided in **Figure 4.21**. These curves were cut at the end of the exposure to the process gas, neglecting the CO peaks after re-introduction of the argon atmosphere. Like for the A-series, a good fit was observed between the CO content curves for the experiments carried out at the same temperature.

4.4.3 Sample mass

Table 4.23 shows the sample mass change during the experiments of the B-series. Again, the mass change is a coupled expression of the reduction, the carburization and the carbon deposition phenomena.

Table 4.23: Sample mass change for the B-series

Experiment	Final sample mass [g]	Mass change [%]
BT1.030	4.77	-4.6
BT2.030	4.60	-8.0
BT4.030	4.35	-13.0
BT1.120	4.82	-3.6
BT2.206	4.72	-5.6
BT3.120	4.59	-8.2
BT4.120	4.43	-11.4

The initial sample mass was 5.00 g for each experiment. An increase of temperature visibly increased the mass loss for a set duration, going from -4.6% to -13% for 30 min experiments and from -3.6% to -11.4% for 120 min experiments. This could indicate a higher extent of reduction since the loss of mass can only be explained by the removal of oxygen from the oxide. However, an increase of the reaction time led to a decrease of the mass loss. This is easily explained by the cracking of methane, and deposition of graphite. Overall, the data here is incomplete to provide a good understanding of the reaction, since it is not possible to distinguish the individual impact of the reduction, carburization and cracking reactions.

4.4.4 Oxygen content

The oxygen content of the product was first determined analyzing the samples after reaction using the O-LECO. In parallel, the CO content in the gas was integrated over the course of the reaction. The two set of data are finally combined to calculate “reconciled” values.

From the O-LECO analyzer

Table 4.24 provides the oxygen weight content from the O-LECO analyzer. The measured content is compared to the amount available in the synthetic oxide. For the B-series, the oxygen atoms bound to iron and chromium are considered “removable”, while those bound to magnesium are not. The extent of reduction was obtained from the final mass, the oxygen content measured, and the oxygen available.

Table 4.24: Oxygen weight content after reduction-carburization for the B-series

Experiment	Sample mass [g]	Oxygen available [g]	Product mass [g]	Oxygen in the product [wt%]	Extent of reduction [%]
BT1.030	5.00	1.33	4.77	24.1	20.04
BT2.030	5.00	1.33	4.60	21.5	32.13
BT4.030	5.00	1.33	4.35	16.3	53.22
BT1.120	5.00	1.33	4.82	21.3	29.27
BT2.206	5.00	1.33	4.72	14.1	56.45
BT3.120	5.00	1.33	4.59	12.8	62.46
BT4.120	5.00	1.33	4.43	7.2	82.61

The calculated extent of reduction revealed the significant influence of temperature. The amount of oxygen withdrawn was more than doubled between samples BT1.030 and BT4.030 by increasing the temperature by 100 °C. Contrary to the A-series, the reduction degree after 120 min was also heavily influenced by the temperature. It appeared that 950 °C was a too low temperature to reduce extensively the $(\mathrm{Fe,Mg})\mathrm{Cr_2O_4}$ spinel solid solution as an extent of reduction of only 29.21% was reached. The gradual increase of temperature led to higher extents of reduction up to 82.61% at 1050 °C.

From the CO curves

The extent of reduction was also calculated by integration of the CO curve and taking into consideration the change of flow using **Section 3.3.4**. Again, the CO measured after stopping of the process gas was taken into account. The results are provided in **Table 4.25**.

Table 4.25: Oxygen content from integration of the CO curve after reduction-carburization for the B-series

Experiment	Sample mass [g]	Oxygen available [g]	Oxygen removed [g]	Extent of reduction [%]
BT1.030	5.00	1.33	0.34	30.12
BT2.030	5.00	1.33	0.52	49.69
BT4.030	5.00	1.33	0.82	69.28
BT1.120	5.00	1.33	0.50	37.65
BT2.206	5.00	1.33	0.91	76.05
BT3.120	5.00	1.33	1.01	79.07
BT4.120	5.00	1.33	1.28	97.14

While these results show trends similar to those presented in **Table 4.24**, the extent of reduction was generally found higher than the O-LECO measurement reaching up to 97.14%.

Reconciling O-LECO and integrated CO

By scaling the calculated extent of reduction using a reference measurement from the O-LECO analyzer, new values were obtained. The procedure used was the same as what was done for the A-series. For the B-series, the experiment BT3.120 was used as the reference for the scaling. The calculation results are presented in **Table 4.26**.

Table 4.26: Extent of reduction calculated from integrated CO and O-LECO for the B-series

Experiment	Extent of reduction [%] with LECO	Extent of reduction [%] with CO content	Extent of reduction [%] calculated
BT1.030	20.04	30.12	23.79
BT2.030	32.13	49.69	36.88
BT4.030	53.22	69.28	54.73
BT1.120	29.27	37.65	29.74
BT2.206	56.45	76.05	60.08
BT3.120	62.46	79.07	62.46
BT4.120	82.61	97.14	76.74

Once rescaled, the extent of reduction obtained from the integrated CO content was found close to the measured value from O-LECO.

4.4.5 X-ray diffraction

Figure 4.22 shows the XRD patterns of the B-series. Peaks matching $(Fe,Mg)Cr_2O_4$ were evidenced in all samples. These peaks correspond to a solid solution of $FeCr_2O_4$-$MgCr_2O_4$ but no accurate information is obtainable on the Fe:Mg ratio at this stage. The reduction-carburization reactions are observed thanks to the rise of the Cr_7C_3 peaks together with the drop of the $(Fe,Mg)Cr_2O_4$ peaks. For experiments BT1.030, BT2.030 and BT4.030 corresponding to 30 min reduction-carburization at 950, 1000 and 1050 °C respectively, the increase of temperature clearly improved the formation of the carbide phase. This was also observed for the long experiments BT1.120, BT2.206, BT3.120 and BT4.120. For the first two, a Cr_2O_3 phase also appears, but this phase was not present at higher temperatures. Peaks matching graphitic carbon were also evidenced for the long experiments at the highest temperatures.

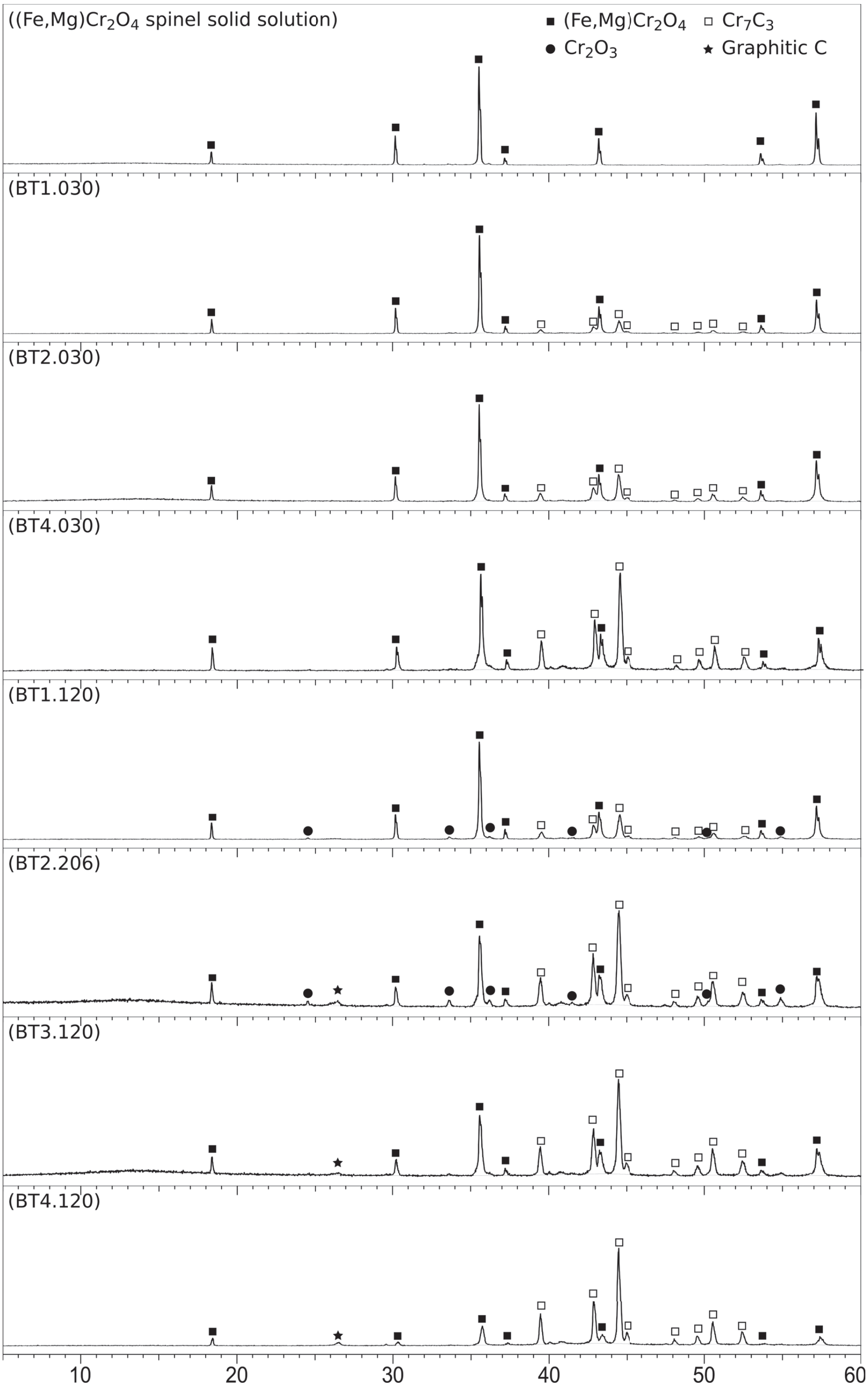

Figure 4.22: XRD patterns for the B-series

These patterns indicated that the temperature range used are at a turning point. After 30 min of reaction, there were significant differences in the carbide formation from 950 to 1050 °C. The drawback of the use of high temperatures was the growth of graphitic carbon, although it was only evidenced for the long experiments.

4.4.6 Extent of reduction curves

Figure 4.23 provides the extent of reduction curves as a function of time for the B-series. These curves were obtained by integration of the CO flow out of the furnace, based on the CO content curves given in **Figure 4.21** and the volume change obtained by the formula given in **Section 3.3.4**. The curves are next rescaled based on the calculated extent of reduction at the end of the experiment given in **Section 4.4.4**.

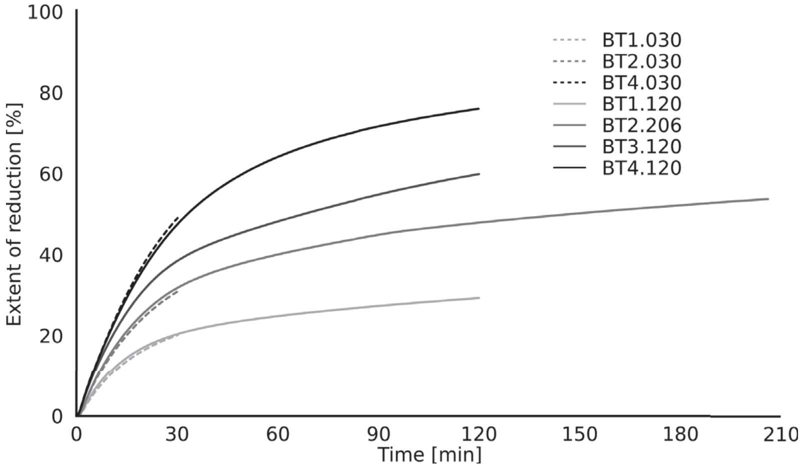

Figure 4.23: Extent of reduction curves for the B-series

The curves corresponding to experiments carried out at similar temperatures were found close to each other, validating the method for the calculation of the extent of reduction. In addition, all the curves exhibited a similar shape, although temperature had a critical impact on the extent of reduction.

An increase of the temperature from 950 to 1050 °C had a dramatic effect on the kinetics. There is a clear increase in the reaction speed at each increase. For the reaction duration considered, this resulted in different extent of reduction at the end of the experiment, the kinetics of reaction being relatively low. It is however unclear if the extent of reduction observed are only influenced by the kinetics or also by thermodynamic limitations. The curve for experiment BT2.206 shows that the reaction continues further at a decreasing but non negligible rate.

4.4.7 Electron microscopy

Most of the samples from the B-series were analyzed by SEM, together with EDS. The carbon content, altered by the carbon coating, is only indicative. The oxygen analysis is also a qualitative result. Micrographs using EPMA were recorded for samples BT2.030, BT4.030 and BT4.120.

BT1.030

Figure 4.27 shows a secondary electron micrograph of a few grains in a pellet from the BT1.030 experiment.

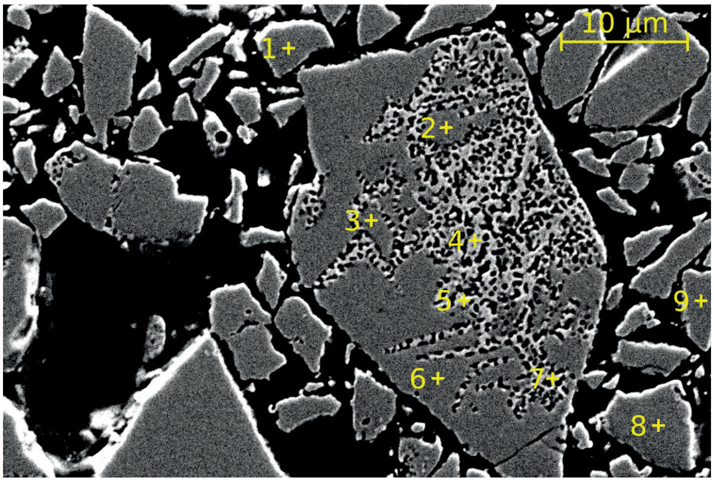

Figure 4.24: Secondary electron micrographs from the BT1.030 experiment

Table 4.27: EDS point measurements for BT1.030

Point	Element [at%]				
	Fe	Mg	Cr	O	C
1	13.54	3.11	26.48	44.85	12.01
2	12.13	3.10	27.78	46.22	10.77
3	14.35	3.34	28.05	41.64	12.63
4	15.54	···	44.63	6.37	33.46
5	12.82	···	38.01	9.84	39.33
6	12.51	3.12	26.45	43.87	14.06
7	14.61	···	39.26	10.28	35.85
8	12.80	2.66	26.91	44.82	12.80
9	12.73	2.99	27.14	45.55	11.59

The product phase formed extensively and deep in one of the grains, leaving the surrounding others unreacted. In terms of morphology of the product phase, the BT1.030 sample contrasted with the A-series. The carbide formed following particular directions, possibly advantageous crystallographic planes. The EDS measurement given in **Table 4.27** evidenced two phases: the dark gray fields match an oxide containing Fe, Mg and Cr while the light gray phases match a carbide containing Cr and Fe. Given the results from XRD and the previous findings, these phases are interpreted as $(\mathrm{Fe,Mg})\mathrm{Cr_2O_4}$ and $(\mathrm{Cr,Fe})_7\mathrm{C}_3$ respectively. The analyses of the carbide phase revealed oxygen leftovers, which might come from an underlying oxide layer. Throughout the oxide and carbide phases, little variations are observed in the metal ratios.

BT2.030

Figure 4.25 shows two secondary electron micrographs from the BT2.030 experiment. The point analyses given in **Table 4.28** indicate that the carbide analyzed mostly containing chromium. These carbide phases formed following noticeable morphologies: planar along points 1 and 2, wedged as at points 5 and 10, or following cracks or grain boundaries at point 17. These morphologies could indicate that the carbide phase nucleated on the grain surface, and grew in favorable directions. The analyses of the surrounding oxide could not evidence any enrichment in magnesium around the product phases despite the absence of magnesium in the carbidic phase.

Table 4.28: EDS point measurements for BT2.030

Point	Element [at%]				
	Fe	Mg	Cr	O	C
1	4.89	0.07	45.15	6.40	43.48
2	7.66	0.06	47.27	9.92	35.10
3	9.53	3.12	24.92	43.11	19.32
4	9.81	2.96	24.75	43.34	19.15
5	1.97	0.38	42.76	5.07	49.83
6	9.91	2.92	24.68	43.11	19.38
7	9.94	2.98	24.97	43.15	18.96
8	10.02	3.01	25.21	42.30	19.47
9	10.21	2.92	24.81	42.81	19.25
10	1.89	0.16	42.85	4.230	50.87
11	9.61	2.80	23.14	42.21	22.24
12	10.11	2.86	25.03	42.92	19.09
13	10.68	2.48	24.77	43.19	18.89
14	9.99	2.99	24.83	42.97	19.21
15	10.31	2.87	24.75	42.87	19.0 2
16	10.19	2.57	24.89	42.58	19.76
17	2.18	0.18	43.73	7.49	46.43
18	6.62	1.40	29.28	43.66	19.05
19	10.78	2.24	24.82	42.77	19.39
20	10.86	2.27	24.74	42.67	19.45

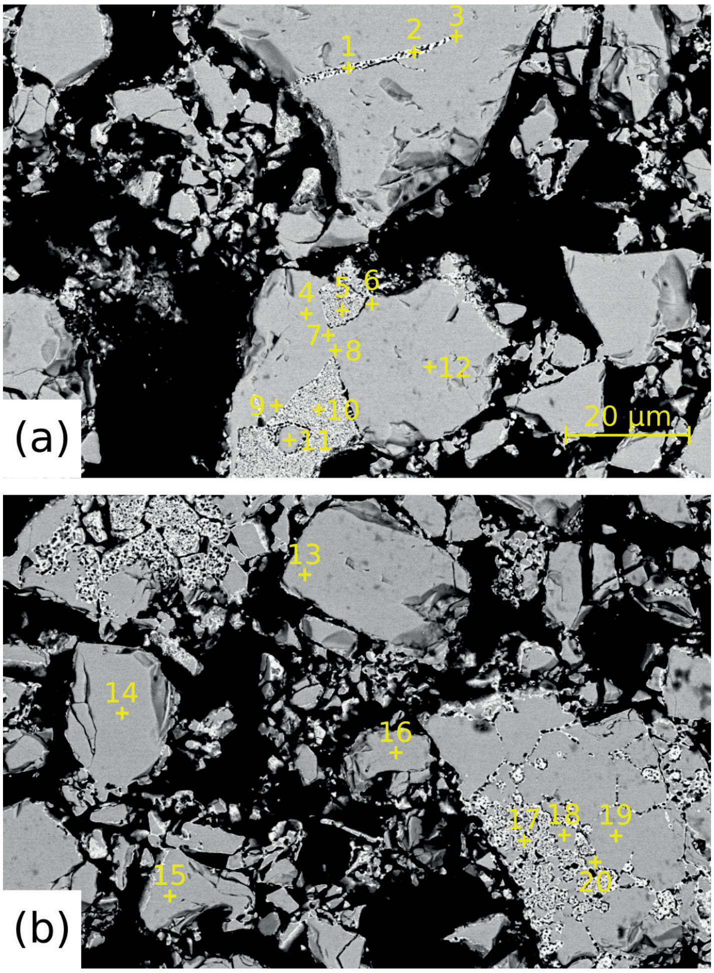

Figure 4.25: Secondary electron micrographs from the BT2.030 experiment of two different pellets

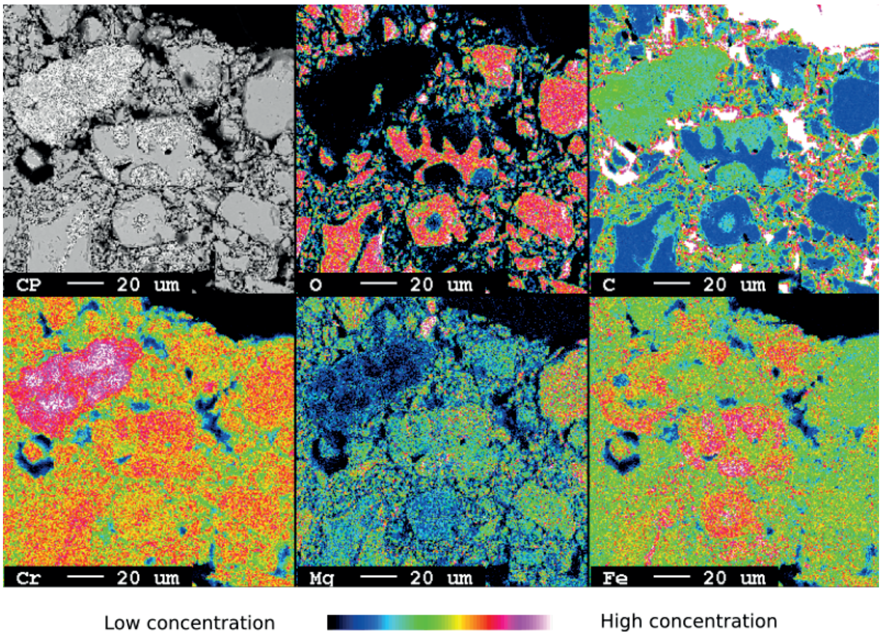

Figure 4.26: Elemental mapping of BT2.030

The EPMA mapping shown in **Figure 4.26**, to some extent, supports the nucleation and growth mechanism. The carbide phases on the center of the picture also suggest a growth phenomenon around a nucleation point. The carbide phase, in this case, is containing both iron and chromium.

BT4.030

Figure 4.27 and **4.28** present EPMA mappings of two grains from the BT4.030 experiment. On **Figure 4.27**, planar grown carbides were found. This morphology is similar to what was found in sample BT2.030, shown in **Figure 4.25**. The elemental mapping indicates that the Fe:Cr ratios in the carbide is lower than in the parent spinel. In addition to this planar carbides, carbide fields exhibiting a higher iron content were also evidenced. The grain shown on **Figure 4.28** presents a more advanced stage of reaction. Only the core of the grain, stripped by carbide planes, consist of oxide material. Artifacts of previously formed planar carbides, similar to those in **Figure 4.27** are also found. These are recognizable by their lower Fe:Cr ratio and low magnesium content. The second carbide phase, assumed to have formed afterwards, still contains magnesium, potentially trapped in a carbide matrix. The iron mapping, in the bottom right picture, indicates that the iron accumulated mainly on the edge of the grain.

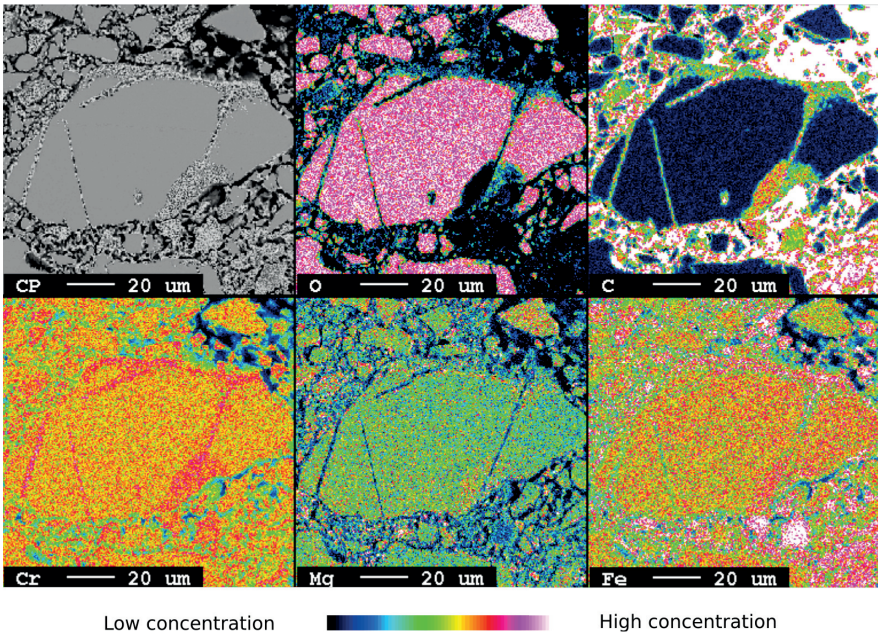

Figure 4.27: Elemental mapping of BT4.030

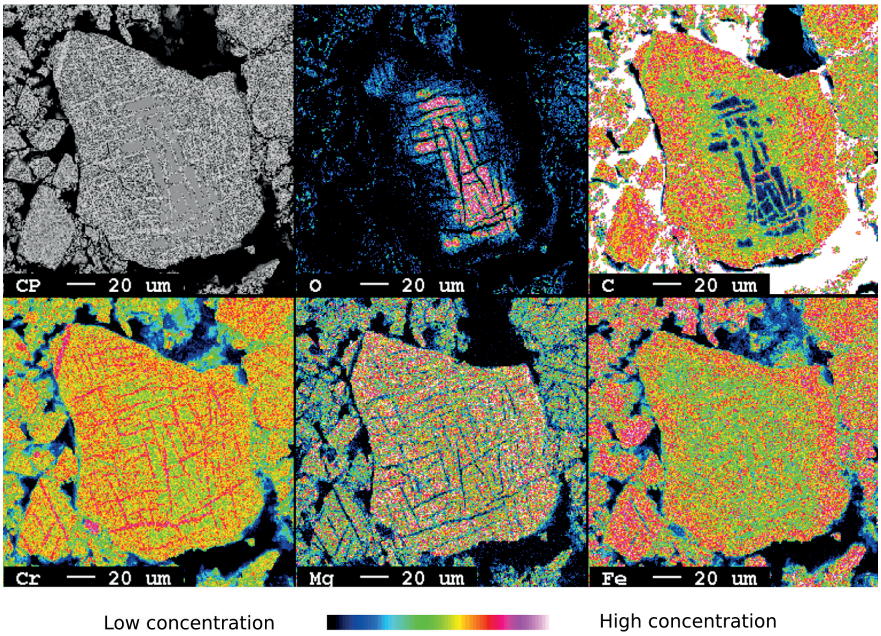

Figure 4.28: Elemental mapping of BT4.030

BT1.120

Figure 4.29 shows a secondary electron micrograph of a reacted pellet from the BT1.120 experiment, while the associated EDS analysis is given in **Table 4.29**.

Table 4.29: EDS point measurements for BT1.120

Point	Element [at%]				
	Fe	Mg	Cr	O	C
1	22.46	···	31.34	3.93	42.27
2	9.57	2.99	29.90	46.34	11.20
3	11.19	2.87	28.69	46.84	10.41
4	11.76	2.86	28.48	46.72	10.18
5	22.53	···	38.51	···	38.95

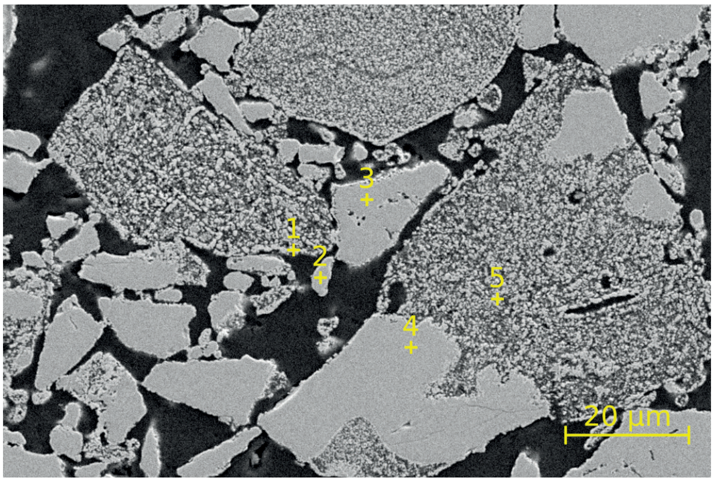

Figure 4.29: Secondary electron micrographs from the BT1.120 experiment

The point analysis in the reacted fields only evidenced an iron chromium carbide. No magnesium oxide was found. In addition, the analysis of point 4 showed that the spinel field was not enriched in magnesium. This result is similar to what was found in sample BT2.030, despite a larger fraction of the grain being reacted.

BT4.120

With increasing temperatures, as in sample BT4.120, the carbide phase formed in a less localized fashion. In **Figure 4.30**, a partially reacted sample is presented.

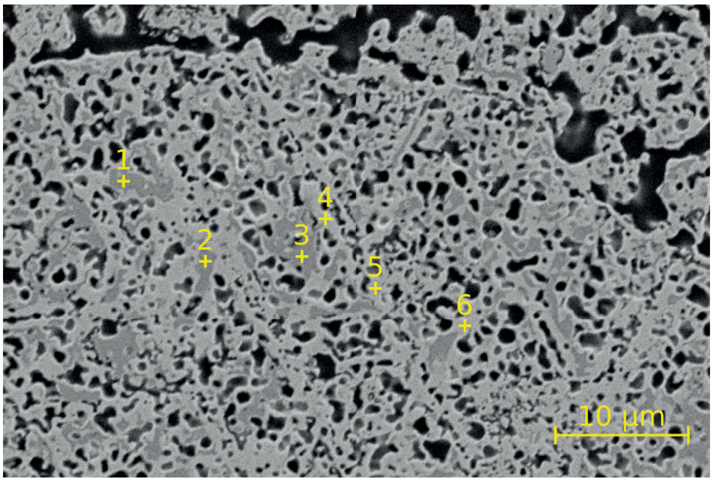

Figure 4.30: Secondary electron micrographs from the BT4.120 experiment

A dense pore network has formed in the material together with a carbide phase. The carbide, appearing in light gray on the picture is chiefly located around the pores. Another phase, in dark gray, is situated away from the pores.

Table 4.30: EDS point measurements for BT4.120

Point	Element [at%]				
	Fe	Mg	Cr	O	C
1	3.63	8.28	29.51	45.79	12.79
2	2.51	9.58	29.79	45.82	12.30
3	2.68	9.02	30.20	45.95	12.15
4	22.60	···	43.09	···	34.31
5	20.91	···	47.02	···	32.06
6	20.40	···	43.82	···	35.78

The EDS analyses provided in **Table 4.30** indicate that this material is an oxide phase, rich in magnesium. The composition seemed to indicate that the Mg atoms diffused from the reaction interface towards the spinel, balanced by the outward diffusion of Fe. The Mg:Fe ratios in the oxide phase were locally found higher than 3, while the theoretical Mg:Fe ratio in the synthetic $(Fe, Mg)Cr_2O_4$ is only $\frac{1}{3}$.

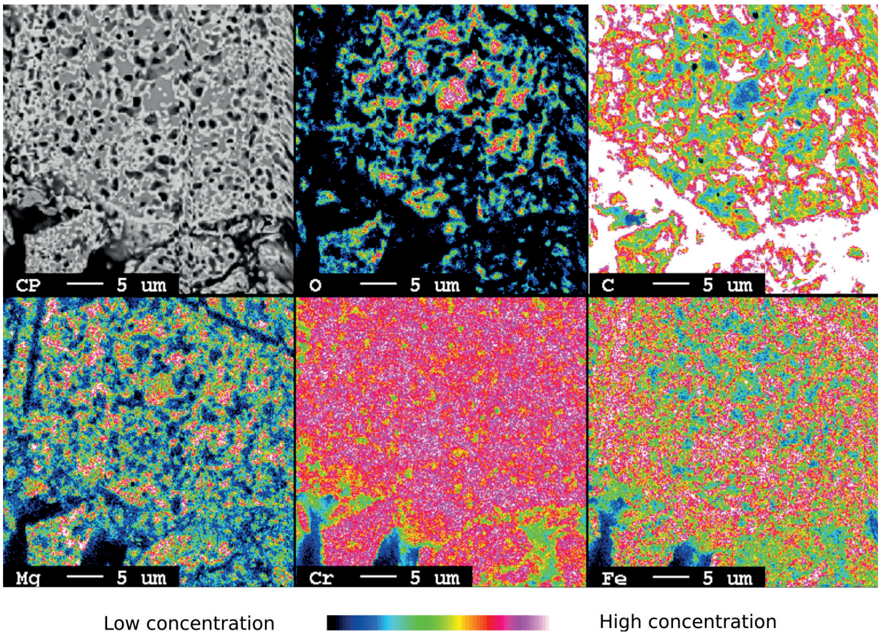

Figure 4.31: Elemental mapping of BT4.120

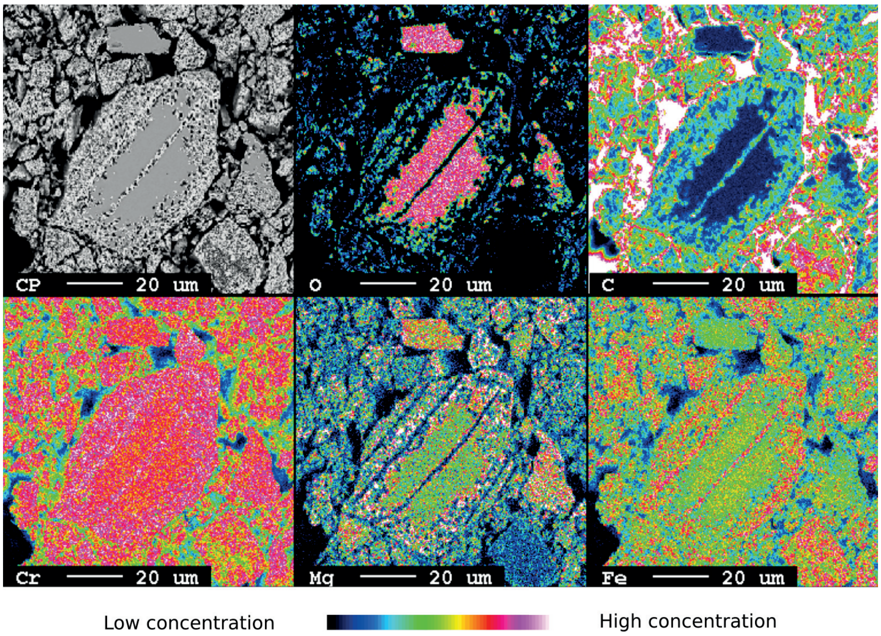

Figure 4.32: Elemental mapping of BT4.120

The EPMA mapping in **Figure 4.31** also corroborates this reading: iron is mostly found out of the oxide phase, contrary to magnesium. Chromium is present in both phases, confirming the EDS measurements. The second EPMA mapping given in **Figure 4.32** offers information on the mechanism. Planar carbides, such as those evidenced in BT2.030, formed through the whole length of the grain. The elemental mapping indicates however a high content of iron, contrary to the carbides poor in iron evidenced in BT2.030. From the edges of the grain, another carbide phase formed. Another morphology was observed here as the reaction seemed to follow a shrinking core: the edges were reacted in a uniform manner while the center remained as an oxide phase.

4.4.8 Summary of the B-series

At the temperatures of the study, $(Fe,Mg)Cr_2O_4$ was reduced-carburized by a 50%Ar-10%CH_4-40%H_2 gas mixture to $(Cr,Fe)_7C_3$ and $(Mg,Fe)Cr_2O_4$. The reduction was never total, and the product phase consisted of $(Cr,Fe)_7C_3$ encapsulating small Mg-rich spinels fields. Cr_2O_3 was also observed by XRD analysis. The reaction was accompanied by a limited graphitic carbon deposition at high temperatures.

The increase of temperature enhanced the reaction rate dramatically, and influenced the extent of reduction severely after 120 min. Full carburization of $(Fe,Mg)Cr_2O_4$ seemed within reach only at high temperatures, possibly higher than those considered in the present work (>1050 °C), and long durations. During this reaction, the iron oxides are reduced slightly faster, accumulating iron towards the edge of the reacted grains and causing variations in the Fe:Cr ratios observed in the carbide phase.

The initial shape of the grains seemed well kept, but various growth morphologies were observed for the carbide phase such as planar, wedged or intergrain structures. Because of the morphologies observed, a nucleation and growth model could be considered. However, some grains' structure also suggested that the shrinking core model could be relevant. The micrographs also showed that the reacted material was porous. Finally, the Mg-rich spinel leftovers, spread throughout the original grain, seemed to concentrate away from the pores.

4.5 C-series ($Fe(Cr, Al)_2O_4$)

The C-series focused on the effects of the replacement of Cr atoms by Al in the spinel solid solution. The process gas composition remained unchanged, being 1 l/min of 50%Ar-10%CH_4-40%H_2. During experiment CT2.182, the power was stopped while the gas mixture was kept by inadvertence. This state was maintained for an additional 35 min after the cooling debuted. In view of the results presented thereafter, it is believed that these additional 35 min of exposure to the process gas had little effect on the reduction. However, it may have a substantial impact on the carbon deposition. The main parameters of the experiments are given in **Table 4.31**.

Table 4.31: Main experimental parameters for the C-series of experiment

Experiment name	Temperature targeted [°C]	Duration [min]
CT1.030	950	30
CT2.030	1000	30
CT3.030	1050	30
CT1.120	950	120
CT2.182	1000	147-182[1]
CT3.120	1050	120

The characterization of the products was ensured by weight measurement, XRD, SEM, EDS, EPMA and O-LECO. The live measurements and the post-reaction analysis were used to compute the extent of reduction curves.

4.5.1 Temperature measurements

The rise of temperature was done under argon gas. Similarly to what was done for the A, B and D-series, the process gas was introduced after stabilizing of the crucible temperature at the desired value. The deviations measured between the targeted and the crucible temperatures are reported in **Table 4.32**.

---

[1] The heating was interrupted after 147 min while the process gas was maintained for 182 min.

Table 4.32: Targeted, minimum, average and maximum temperatures during the reduction-carburization of the C-series

Experiment	Temperature [°C]			
	Targeted	Min.	Avg.	Max.
CT1.030	950	953.7	956.1	958.4
CT2.030	1000	1002.2	1005.6	1008.6
CT3.030	1050	1041.5	1043.8	1046.6
CT1.120	950	946.4	952.4	953.3
CT2.182	1000	993.2	996.9	998.0
CT3.120	1050	1045.7	1051.9	1055.2

For the experiment CT2.182, these values are only reported for the period before the cooling. Overall, the deviations are fairly limited in all the samples considered.

4.5.2 Exhaust gas measurements

The exhaust gas measurements from the C-series exhibited trends similar to those of the B-series during the first seconds of reaction. Both CH_4 and CO peaks are observed and reported in **Table 4.33**. The table on the left is arranged by experiment name, while the one on the right is arranged by temperature. Although a temperature increase seemed to generally result in an increase of the CO peak and a decrease of the CH_4 peak, no clear correspondence was found.

Table 4.33: CH_4 and CO peak and temperature at the process gas introduction for the C-series

Experiment	Temp. at start [°C]	CH_4 [%]	CO [%]
CT1.030	957.3	6.679	4.633
CT2.030	1004.3	4.797	5.890
CT3.030	1046.6	4.575	6.574
CT1.120	946.4	6.836	4.263
CT2.182	993.2	4.198	6.016
CT3.120	1050.7	3.942	5.865

Experiment	Temp. at start [°C]	CH_4 [%]	CO [%]
CT1.120	946.4	6.836	4.263
CT1.030	957.3	6.679	4.633
CT2.182	993.2	4.198	6.016
CT2.030	1004.3	4.797	5.890
CT3.030	1046.6	4.575	6.574
CT3.120	1050.7	3.942	5.865

After a peak and a subsequent drop, the CH_4 content increased again. A striking difference with the A and B-series is the slow increase of the CH_4 content, despite the drop of the CO content. This may indicate that a substantial share of the CH_4 cracked and deposited carbon without accomplishing any reduction. **Figure 4.33** shows an example of a the measured CH_4 content during experiment CT2.182, contrasting with **Figure 4.19** on page 87 from the B-series. In **Table 4.34**, the CH_4 content in the exhaust gas at the end the experiment is reported for the longest experiments of the C-series. For those, the reduction-carburization is close to complete as indicated by the low CO content and shown on **Figure 4.33**. For the CT2.182 experiment, the reported value is taken at 147 min before the cooling. The measured CH_4 at the end is significantly lower than the measured values reported for the B-series: an extensive cracking and carbon deposition is therefore expected.

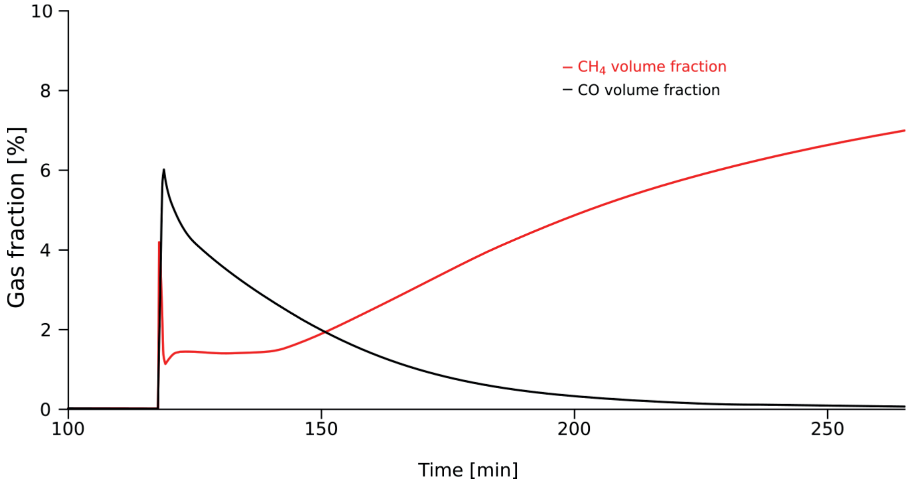

Figure 4.33: CH_4 and CO content in the exhaust gas for experiment CT2.182

Table 4.34: CH_4 content and temperature at the gas replacement for the long experiments of the C-series

Experiment	Temp. at stop [°C]	CH_4 [%]
CT1.120	951.9	7.228
CT2.182	997.8	6.995
CT3.120	1054.8	6.805

The CO curves for the C-series are given in **Figure 4.34**. As for the previous series, the curves were cut at the end of the exposure to the process gas, but the CO peaks after re-introduction of the argon atmosphere were taken into consideration in further calculations. A fairly good fit was observed between the experiments done at a similar temperature and little difference was found between the CO curves for the experiments at 1000 and 1050 °C, suggesting a similar reaction speed.

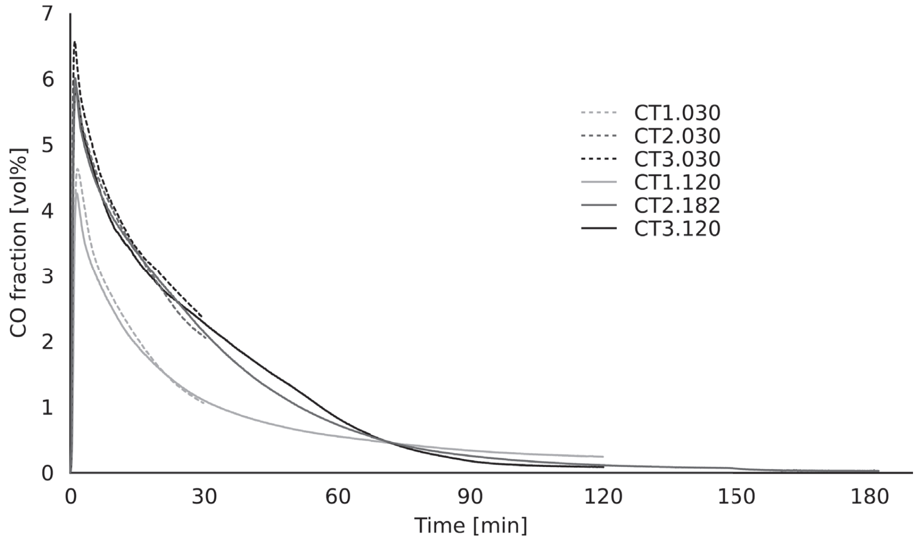

Figure 4.34: CO content in the exhaust gas for the C-series

4.5.3 Sample mass

The sample mass changes for the C-series are reported in **Table 4.35**. For $Fe(Cr,Al)_2O_4$, the mass change is heavily influenced by the carbon deposition, as some samples gained mass during the experiment. The sample CT2.030 showed a higher mass loss than the sample CT3.030, but the present analyses cannot distinguish between a higher extent of reduction and a lower carbon deposition. The reduction-carburization of the samples CT1.120, CT2.182 and CT3.120 was visibly accompanied by substantial carbon deposition. The samples mass increased by up to 42.4% for CT2.182. The higher mass gained observed in CT2.182 compared to CT3.120 can be explained by the longer duration of the experiment.

Table 4.35: Sample mass change for the C-series

Experiment	Final sample mass [g]	Mass change [%]
CT1.030	4.84	-3.2
CT2.030	4.63	-7.4
CT3.030	4.87	-2.6
CT1.120	5.92	+18.4
CT2.182	7.12	+42.4
CT3.120	6.24	+24.8

4.5.4 Oxygen content

The oxygen content of the product was first determined analyzing the samples after reaction using the O-LECO. In parallel, the CO content in the gas was integrated over the course of the reaction. The two set of data are finally combined to calculate “reconciled” values.

From the O-LECO analyzer

Table 4.36 reports the oxygen content in the product sample for the C-series. The oxygen weight content is provided together with the theoretical amount of available oxygen assuming a reduction of iron and chromium oxides. The extent of reduction was obtained from the final mass, the oxygen content measured, and the oxygen available.

Table 4.36: Oxygen weight content after reduction-carburization for the C-series

Experiment	Sample mass [g]	Oxygen available [g]	Product mass [g]	Oxygen in the product [wt%]	Extent of reduction [%]
CT1.030	5.00	1.18	4.85	19.4	43.59
CT2.030	5.00	1.18	4.63	13.6	69.86
CT3.030	5.00	1.18	4.87	14.3	64.17
CT1.120	5.00	1.18	5.92	13.9	53.55
CT2.182	5.00	1.18	7.12	5.18	91.90
CT3.120	5.00	1.18	6.24	6.30	89.83

First, it appears from **Table 4.36** that 950 °C was a too low temperature to achieve a high extent of reduction. At this temperature, it was only marginally improved from 43.59% to 53.55% by increasing the reaction duration by 300%. The large weight difference between these two samples shows that the CH_4 from the process gas was mostly decomposed to carbon and dihydrogen.

The “CT2” samples, reacted at temperatures around 1000 °C, led to the best extents of reduction. This statement must be nuanced by the longer duration of CT2.182, but holds for CT2.030 according to this analysis method. The extent of reduction for the long duration experiments did not vary significantly between CT2.182 and CT3.120, but both were significantly higher than their 30 min equivalent.

From the CO curves

The results obtained by integration of the CO curves contrasted with those from O-LECO concerning experiments CT2.030 and CT3.030. For these short experiments, the two methods gave opposite trends. In addition, a subsequent increase of the extent of reaction was observed for the CT1.120 sample compared to CT1.030.

Table 4.37: Oxygen content from integration of the CO curve after reduction-carburization for the C-series

Experiment	Sample mass [g]	Oxygen available [g]	Oxygen removed [g]	Extent of reduction [%]
CT1.030	5.00	1.18	0.51	49.30
CT2.030	5.00	1.18	0.84	77.51
CT3.030	5.00	1.18	0.89	79.02
CT1.120	5.00	1.18	0.82	67.95
CT2.182	5.00	1.18	1.31	109.89
CT3.120	5.00	1.18	1.30	109.24

However, similarly to the A-series, these values are likely not to be accurate as noted by the extent of reduction higher than 100% for CT2.182 and CT3.120.

Reconciling O-LECO and integrated CO

Reconciling the two series of results here implied to choose one description of the results over the other. In addition to the arguments used for the previous series, the X-ray diffraction patterns presented in the following section seemed to lie more on the side of the description given by the integrated CO content. This is especially valid concerning the extent of reduction of the CT1.120 sample.

Table 4.38: Extent of reduction calculated from integrated CO and O-LECO for the C-series

Experiment	Extent of reduction [%] with LECO	Extent of reduction [%] with CO content	Extent of reduction [%] calculated
CT1.030	43.59	49.30	41.23
CT2.030	69.86	77.51	64.82
CT3.030	64.17	79.02	66.08
CT1.120	53.55	67.95	56.82
CT2.182	91.90	109.89	91.90
CT3.120	89.83	109.24	91.35

The new calculated extent of reduction was obtained using the experiment CT2.182 as a reference and are provided in **Table 4.38**. Significant differences are observed between the various methods.

4.5.5 X-ray diffraction

Figure 4.35 shows the X-ray diffraction patterns recorded from the C-series. The pattern for the initial $Fe(Cr, Al)_2O_4$ solid solution used is also provided.

After reduction-carburization, the peaks corresponding to the spinel solid solution are still observed in various samples. However, these peaks are broadened, most likely indicating an alteration of the spinel. Again, the peaks corresponding to Cr_7C_3 evidenced in all the reacted samples are interpreted as a $(Cr, Fe)_7C_3$ carbide. A notable difference with the previous series is the presence of a graphite peak at all experiment conditions, indicating once more an important carbon deposition phenomenon in the C-series. Apart from the least and most reduced samples according to oxygen analysis, all samples also appeared to contain a $(Cr, Al)_2O_3$ phase. Finally, one can note that various minor peaks could not be matched in these XRD patterns.

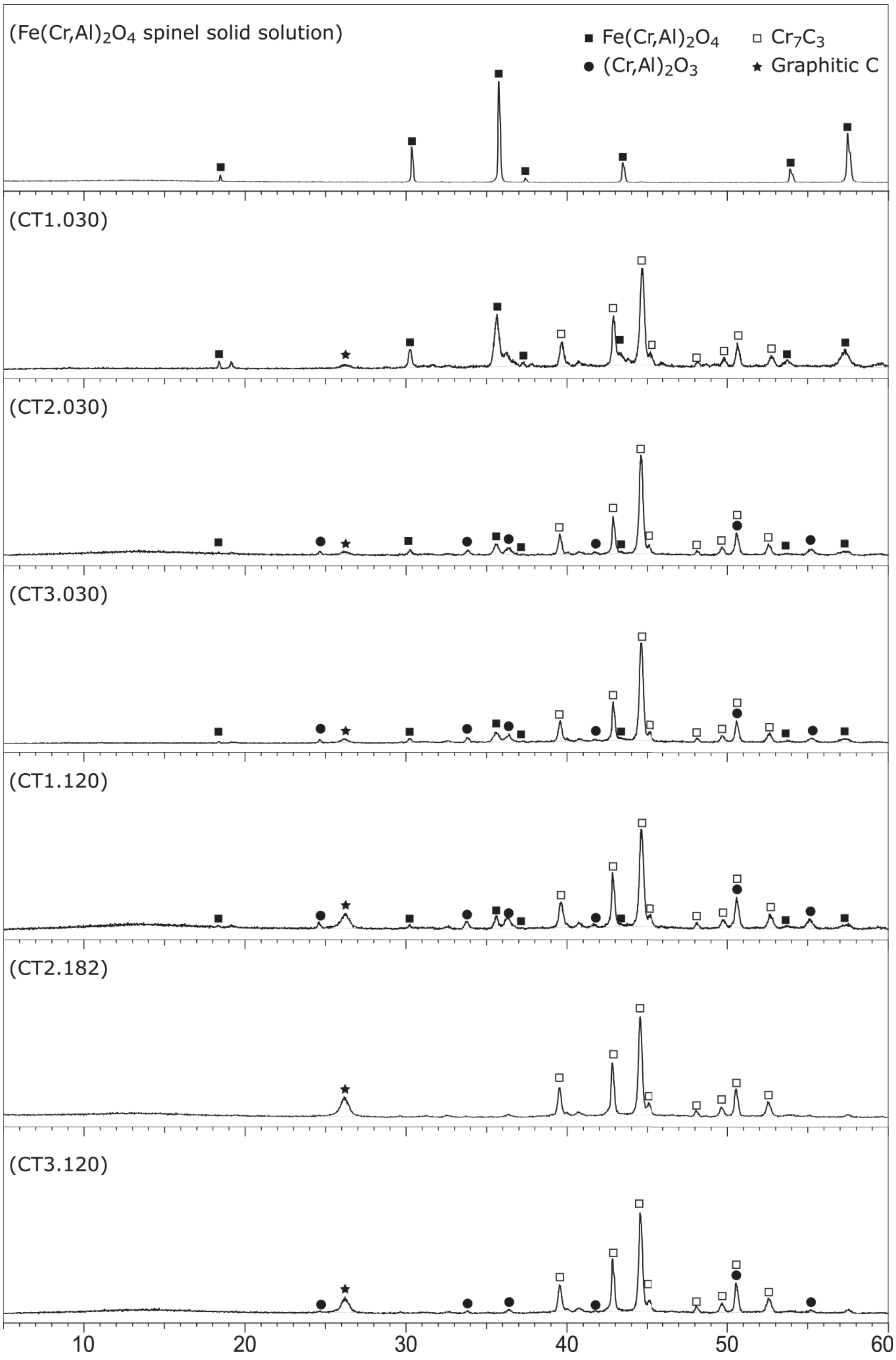

Figure 4.35: XRD patterns for the C-series

4.5.6 Extent of reduction curves

Figure 4.36 provides the extent of reduction curves as a function of time for the C-series. These curves were obtained by integration CO flow out of the furnace, based on the CO content curves given in **Figure 4.34** and the volume change obtained by the formula given in **Section 3.3.4**. The curves are next rescaled based on the calculated extent of reduction at the end of the experiment given in **Section 4.5.4**.

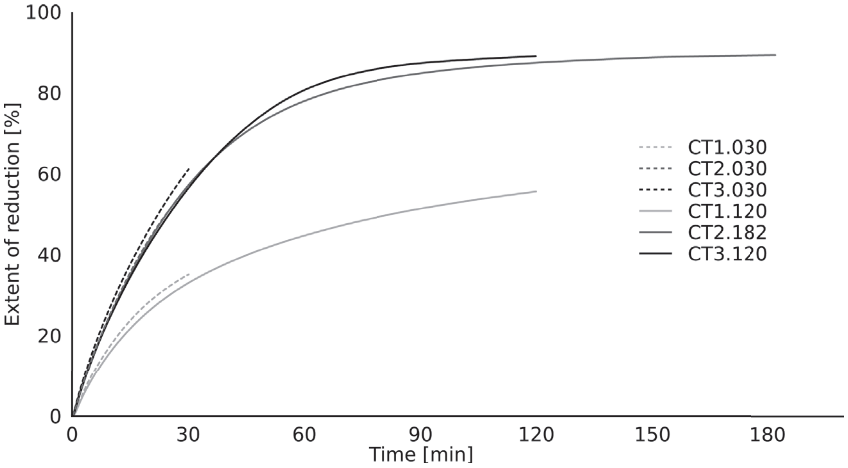

Figure 4.36: Extent of reduction curves for the C-series

The good fit between the extent of reduction curves for experiments carried out at similar temperature again validate the method. The curve representing CT2.030, hardly distinguishable on **Figure 4.36**, overlaps the one for CT2.182.

For the C-series, the temperature increase from 950 to 1000 °C had a clear positive impact on the reaction rate and extent. There was however no significant difference between the samples reacted at 1000 and 1050 °C. For CT2.182 and CT3.120, the extent of reduction curves reach a plateau, while the shape of the curve for CT1.120 could indicate that the reduction-carburization is unfinished and could continue.

4.5.7 Electron microscopy

The samples for the C-series were analyzed using SEM, EDS and EPMA. The presence of extensive amounts of deposited carbon was detrimental to the microscopy study on the most reacted samples.

CT1.030

Figure 4.37 shows an electron micrograph of a sample reacted 30 min at 950 °C, while **Table 4.39** reports the corresponding EDS point analyses.

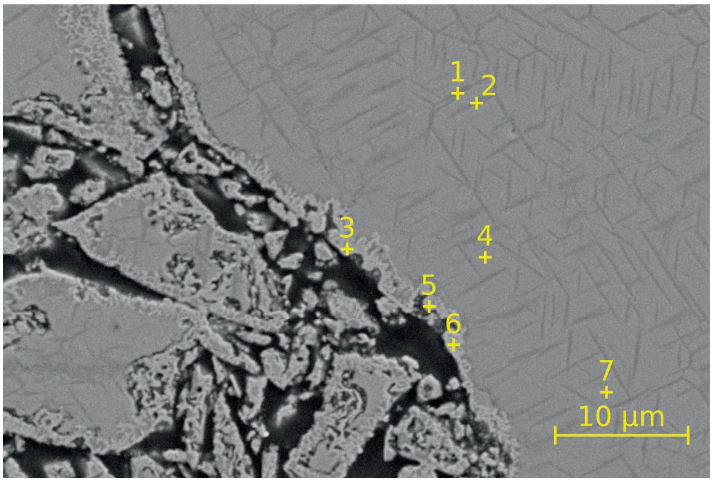

Figure 4.37: Secondary electron micrographs from the CT1.030 experiment

Table 4.39: EDS point measurements for CT1.030

Point	Element [at%]				
	Fe	Cr	Al	O	C
1	4.65	22.94	14.27	50.31	7.83
2	8.79	24.66	9.30	50.17	7.08
3	43.84	13.42	8.16	18.34	16.20
4	16.04	24.61	3.48	48.99	5.88
5	22.91	12.21	9.08	24.26	31.53
6	52.53	6.42	···	4.02	37.02
7	16.71	25.52	3.96	48.34	5.47

Two main field are distinguishable on this reacted grain. Firstly, two phases are present in the core of the grain. The EDS point analysis in 4 and 7, together with the previously mentioned XRD patterns, suggest that the main phase is a $Fe(Cr, Al)_2O_4$ spinel, while the darker lamellae found in 1 and 2 could consist of $(Cr, Al)_2O_3$. These lamellae are visible across the core and are positioned in an ordered fashion. The low aluminium content in the spinel, compared with the high content in the lamellae suggests a segregation mechanism possibly by exsolution.

Secondly, a light gray layer is found around the whole grain, often accompanied by pores. This layer is not uniform in width and its interface with the rest of the grain appear as a succession of high curvature tines or branches. Between those, a dark gray material is found. Because of the small size of both phases, precise EDS point analyses are challenging. Nevertheless, this layer is found to be rich in iron but also contains other elements, and in particular some oxygen. On the top left corner, a large field seem to consist of an intricate mixture of these two materials.

CT2.030

New structures were observed at 1000 °C. **Figure 4.38** shows a back-scattered electron micrograph of a sample reacted 30 min at 1000 °C. On the picture, various elements are distinguishable.

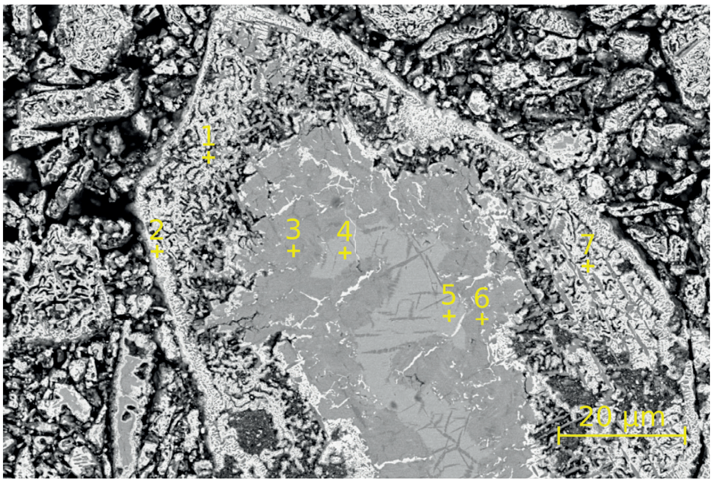

Figure 4.38: Back-scattered electron micrographs from the CT2.030 experiment

The reacted grain presented a distinct layer on its edge. This layer, present on point 2, together with the structure formed inwards at point 1, contained important amounts of carbon, and low amounts of oxygen. One could view this material as a mixture of $(Cr, Fe)_7C_3$ carbide and $(Cr, Al)_2O_3$ oxide. Zoning is observed in the core on **Figure 4.38**: two fields are found and identified as inner and outer fields. Points 3 and 6 revealed that the outer field was made of a Cr and Al containing oxide and freed of iron, possibly a $(Cr, Al)_2O_3$ phase. The inner field, analyzed at points 4 and 5 was impoverished in aluminium. The reading of the EDS analyses suggests that this phase is an Al depleted $Fe(Cr, Al)_2O_4$ spinel solid solution.

Table 4.40: EDS point measurements for CT2.030

Point	Element [at%]				
	Fe	Cr	Al	O	C
1	14.06	33.38	3.19	10.87	38.50
2	20.02	30.58	3.40	8.74	37.25
3	0.25	27.97	7.74	46.32	17.72
4	11.92	23.65	2.45	43.12	18.86
5	11.74	23.39	3.03	43.06	18.78
6	1.84	29.42	5.82	44.64	18.27
7	4.39	17.15	16.52	33.94	27.99

Additional features which were not analyzed are also found: a bright phase, possibly metallic was found in newly formed cracks. Also, lamellae similar to those of evidenced in sample CT1.030 were found in the inner core.

CT3.030

Figure 4.39 shows electron micrographs of two pellets representative of different levels of reduction. On the first picture, the reacted grain is alike what was found on CT2.030 where similar layering, zoning, exsolution and cracks were found. The EDS point analyses given in **Table 4.41** also corroborate the previous findings. In addition, the lamellae found in the inner field of the core and analyzed on point 1 could consist of a $(Cr, Al)_2O_3$ oxide. The bright phase seeping out in the cracks was also identified as a iron rich metallic phase, as evidenced on points 5 and 6.

On the second picture of **Figure 4.39**, large amounts of carbon were evidenced, making the analyses difficult. However, the results from points 9 and 10 seem to indicate the presence of a $(Cr, Fe)_7C_3$ carbide together with limited amounts of aluminium containing oxide.

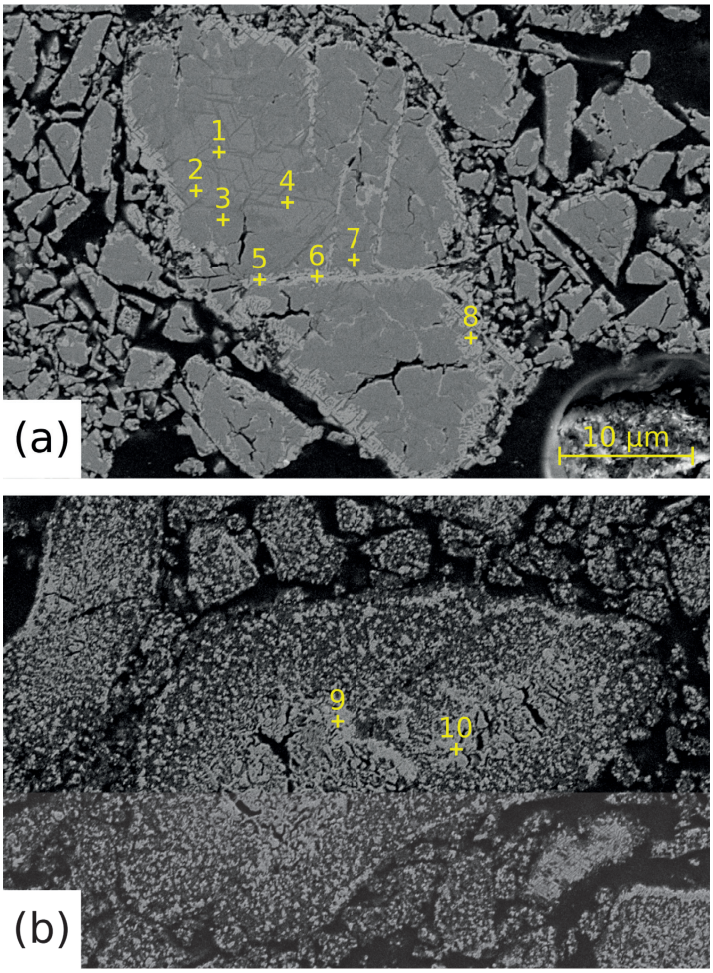

Figure 4.39: Secondary electron micrographs from the CT3.030 experiment on two pellets

Table 4.41: EDS point measurements for CT3.030

Point	Element [at%]				
	Fe	Cr	Al	O	C
1	4.46	22.95	13.57	49.68	9.33
2	14.09	28.02	2.22	48.20	7.48
3	···	36.58	4.50	51.96	6.97
4	13.91	28.27	2.27	49.00	6.55
5	78.03	3.94	1.09	···	16.94
6	77.91	3.73	···	···	18.36
7	···	34.88	5.51	52.86	6.74
8	68.78	7.21	3.09	5.42	15.50
9	21.88	41.59	3.10	7.85	25.59
10	22.41	44.42	···	6.84	26.33

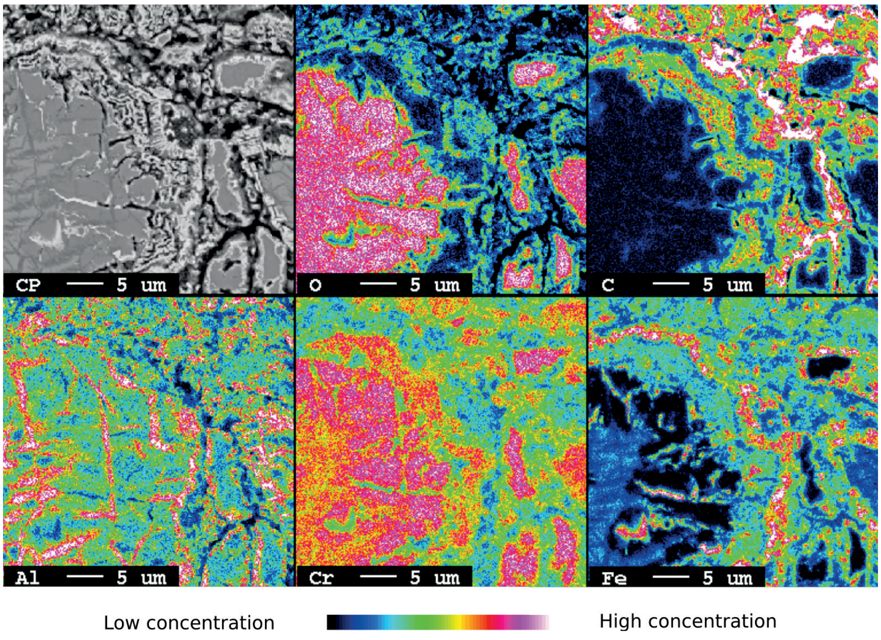

Figure 4.40: Elemental mapping of CT3.030

The EPMA mapping on **Figure 4.40** shows in detail the various phases involved. Overall, iron migrated to the edge forming a metallic layer in close contact with a aluminium containing oxide. Iron is also present together with chromium as a carbide when reaching deeper layers in the material. In the core, the oxide in the outer field is iron depleted, all the iron being drained out as a metallic phase. The inner field still contains iron. The aluminium distribution is also to notice: it was found chiefly in the lamellae, both in the inner and the outer fields of the core. While the lamellae are easily distinguished in the inner field, they are more challenging to observe in the outer field even with back-scattered micrographs. The aluminium, could also have segregated early during the grain's reduction and remained as lamellae throughout the reaction.

CT1.120

The sample subjected to a reduction-carburization at 950 °C for 120 min presented a very limited alteration. While the aspect is close to what was observed previously, a reacted layer on the edge and exsolution in the spinel, dark fields also appeared on the sample. These fields seem to belong to the original grain's form but seem to have been decomposed, turned into dust. The analyses of these fields, evaluated by EDS in the locations shown on **Figure 4.41**, are reported in **Table 4.42**. The high levels of carbon found could indicate that the deposition occurred in these areas. Among the trace elements found, aluminium was present to an abnormally high level. On point 4, aluminium was the most represented metal, while being the least represented in the parent spinel.

Table 4.42: EDS point measurements for CT1.120

Point	Element [at%]				
	Fe	Cr	Al	O	C
1	5.90	4.39	2.58	5.46	81.67
2	2.97	3.81	3.37	6.28	83.56
3	5.48	1.88	3.23	9.35	80.06
4	1.11	1.76	2.94	6.39	87.80

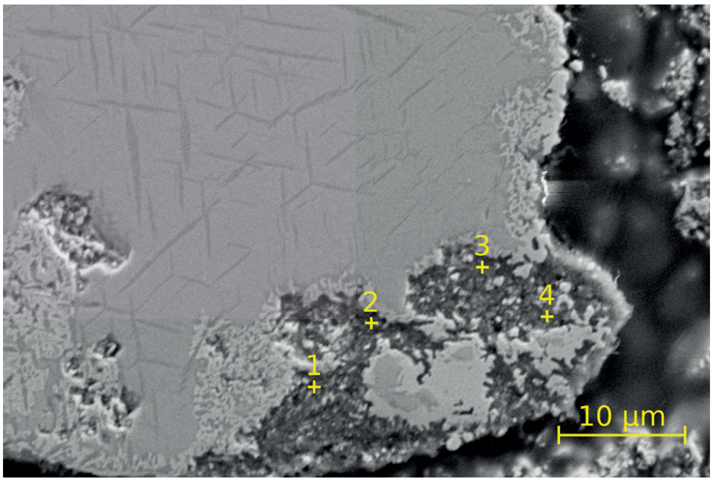

Figure 4.41: Secondary electron micrographs from the CT1.120 experiment

One could consider that Al_2O_3 is a cause in the extensive cracking of the C-series, as aluminium seem to be placed in the vicinity of carbon.

CT2.182

The sample from experiment CT2.182 exhibited the highest mass gain among all the samples, mass gain mostly explained by carbon deposition from cracking.

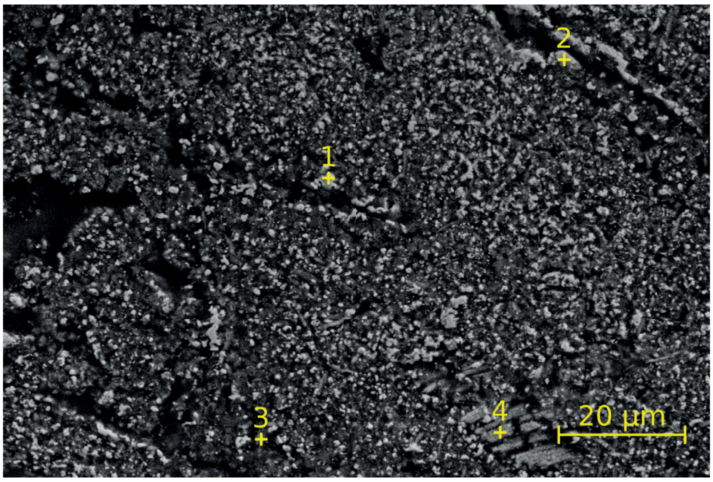

Figure 4.42: Secondary electron micrographs from the CT2.182 experiment

Table 4.43: EDS point measurements for CT2.182

Point	Element [at%]				
	Fe	Cr	Al	O	C
1	46.27	22.77	0.21	0.87	29.89
2	29.95	26.17	0.18	0.90	42.80
3	4.65	5.81	6.73	16.88	65.93
4	3.80	12.00	11.13	21.69	51.38

The picture in **Figure 4.42** shows a reacted grain after extensive reaction and carbon deposition, **Table 4.43** providing the EDS measurements' results. The bright phases, analyzed on points 1 and 2, consist of a $(\mathrm{Cr,Fe})_7\mathrm{C}_3$ carbide. Points 3 and 4, analyzing a darker gray phase, evidenced the simultaneous presence of a chromium aluminium oxide, together with large quantities of carbon. Similarly to what was found in sample CT1.120, carbon and aluminium seem to be present together.

CT3.120

The last sample of the C-series is shown in **Figure 4.43**. Two different regions are presented: the first picture shows the center of the pellet and the second shows a region closer to the edge. These pictures are intriguing because the center of the pellet looked further reacted than the edge.

Table 4.44: EDS point measurements for CT3.120

Point	Element [at%]				
	Fe	Cr	Al	O	C
1	31.25	33.37	···	3.24	32.15
2	···	33.75	5.31	52.62	8.32
3	···	34.22	4.62	50.94	10.21
4	···	1.88	4.15	7.00	86.97
5	···	32.89	6.07	52.77	8.28
6	···	1.98	3.21	5.45	89.36
7	17.10	39.15	4.02	11.06	28.67
8	1.60	4.41	3.22	7.27	83.50
9	13.73	29.53	2.36	8.87	45.50
10	18.61	40.82	1.04	···	39.53

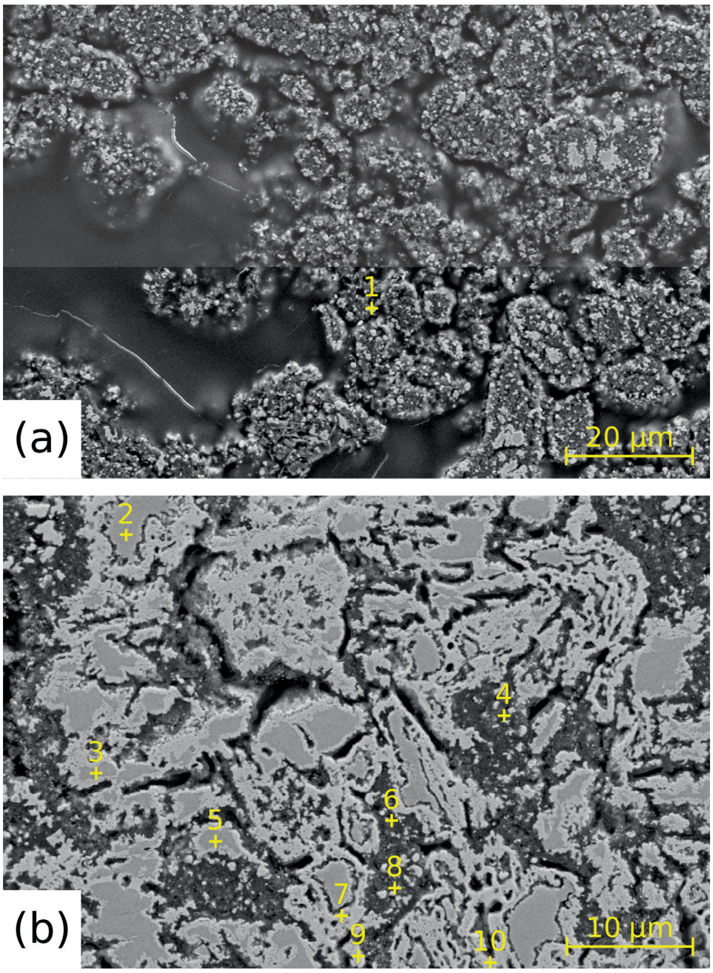

Figure 4.43: Secondary electron micrographs from the CT3.120 experiment on two locations of the same pellet: (a) In the center (b) towards the edge

According to the EDS point analysis given in **Table 4.44**, the light gray material is a $(Cr,Fe)_7C_3$ carbide. Variable Fe:Cr ratios were evidenced in these carbides, and some oxide was also present as shown by the analyses of points 6 and 7. A second phase, surrounded by the $(Cr,Fe)_7C_3$ material, was also found. This second phase can be interpreted as a $(Cr,Al)_2O_3$ oxide and is present in points 3 and 5. One can note that the Al:Cr ratio in this oxide was lower than in the parent spinel. The darker region is found again to contain a large amount of carbon, together with an aluminium rich oxide. There, the Al:Cr ratios were significantly higher than those of the parent spinel.

4.5.8 Summary of the C-series

At the temperatures of the study, $Fe(Cr,Al)_2O_4$ was reduced-carburized by a 50%Ar-10%CH_4-40%H_2 gas mixture to $(Cr,Fe)_7C_3$ and $(Cr,Al)_2O_3$. The reduction was close to complete after 120 min for temperatures above 1000 °C. The reaction was accompanied by an extensive cracking of CH_4 and carbon deposited heavily, increasing the pellets weight and size significantly.

The increase of temperature increased the reaction rate significantly, but only up to 1000 °C. Further temperature increase had little impact on both the kinetics and the extent of reduction. Full carburization of $Fe(Cr,Al)_2O_4$ seemed attainable with high temperatures and long durations.

The reaction seemed to follow a shrinking core mechanism at the grain scale. At first, an iron rich layer was formed towards the edge, accompanied by an exsolution phenomenon in the oxide phase. The exsolved lamellae were positioned in an organized fashion and consisted of an aluminium-chromium oxide, possibly $(Cr,Al)_2O_3$. Further reacted grains exhibited a zoning phenomenon and the oxide core was separated in two phases: the outer oxide was depleted of iron and formed $(Cr,Al)_2O_3$ while the inner core was depleted of aluminium and consisted of low-Al $Fe(Cr,Al)_2O_4$. Cracks tended to form in the oxide, in which metallic iron accumulated. At last, the most reduced grains also contained extensive amounts of carbon found in the vicinity of aluminium.

4.6 D-series ($(Fe, Mg)(Cr, Al)_2O_4$)

The D-series studied the synthetic material which is the closest to natural ores in terms of composition. This material, containing both magnesium and aluminium impurities provided a support to investigate their possible interactions and their combined effect on the reduction-carburization processes. The process gas was kept at a 1 l/min flow of 50%Ar-10%CH_4-40%H_2. Similar experimental conditions were kept for this series as presented in **Table 4.45**.

Table 4.45: Main experimental parameters for the D-series of experiment

Experiment name	Temperature targeted [°C]	Duration [min]
CT1.030	950	30
CT2.030	1000	30
CT3.030	1050	30
CT1.120	950	120
CT2.141	1000	141
CT3.120	1050	120

The products were characterized by weight measurement, XRD, SEM, EDS, EPMA and O-LECO. The live measurements and the post-reaction analysis were used to compute the extent of reduction curves.

4.6.1 Temperature measurements

Similarly to the A, B and C-series, the temperature increase was carried out in argon, prior to the introduction of the process gas. When argon was replaced, a brief temperature increase was followed by a temperature drop, and a subsequent increase. The characteristics values for the temperature measurements are reported in **Table 4.46**.

Table 4.46: Targeted, minimum, average and maximum temperatures during the reduction-carburization of the D-series

Experiment	Temperature [°C]			
	Targeted	Min.	Avg.	Max.
DT1.030	950	960	962.1	964.2
DT2.030	1000	995.7	998.6	1000.0
DT3.030	1050	1045.1	1046.6	1049.7
DT1.120	950	953.0	958.6	960.2
DT2.141	1000	995.2	1010.3	1003.3
DT3.120	1050	1046.2	1053.9	1058.1

Overall, the experiments of the D-series were characterized by minor changes in the measured temperature when compared to the experiments on other materials.

4.6.2 Exhaust gas measurements

The gas measurements in of the D-series are alike those of the C-series during the whole span of the experiment, giving recordings very close to those given in **Figure 4.33**. Both CO and CH_4 peaks were observed in the early stages, with values reported in **Table 4.47**. However, no clear correspondence was found between the temperature at the start and the initial gas peak heights.

Table 4.47: CH_4 and CO peak and temperature at the process gas introduction for the D-series

Experiment	Temp. at start [°C]	CH_4 [%]	CO [%]
DT1.030	952.2	7.241	3.540
DT2.030	995.7	7.946	4.317
DT3.030	1046.6	6.131	4.499
DT1.120	954.2	6.980	3.479
DT2.141	1005.5	8.375	3.998
DT3.120	1051.6	4.674	5.391

Experiment	Temp. at start [°C]	CH_4 [%]	CO [%]
DT1.030	952.2	7.241	3.540
DT1.120	954.2	6.980	3.479
DT2.030	995.7	7.946	4.317
DT2.141	1005.5	8.375	3.479
DT3.030	1046.6	6.131	4.499
DT3.120	1051.6	4.674	5.391

In a similar way to what was observed for the C-series, the CH_4 content was found to slowly increase after the initial peaks and drops. An extensive amount of carbon deposition is expected because of the low amount of CH_4 in the exhaust gas even after the decrease of the CO curve and thus the end of the reduction process. **Table 4.48** gives the CH_4 measurements and the temperature at the end of the long duration experiments. While only a small difference of CH_4 content is observed between DT1.120 and DT2.141, DT3.120 exhibits a significantly lower CH_4 volume fraction.

Table 4.48: CH_4 content and temperature at the gas replacement for the long experiments of the D-series

Experiment	Temp. at stop [°C]	CH_4 [%]
DT1.120	959.1	7.582
DT2.141	995.2	7.558
DT3.120	1057.2	6.703

The CO curves for the D-series are provided in **Figure 4.44**. The curves are similar to those of **Figure 4.34** for the C-series although the peaks are larger for the D-series.

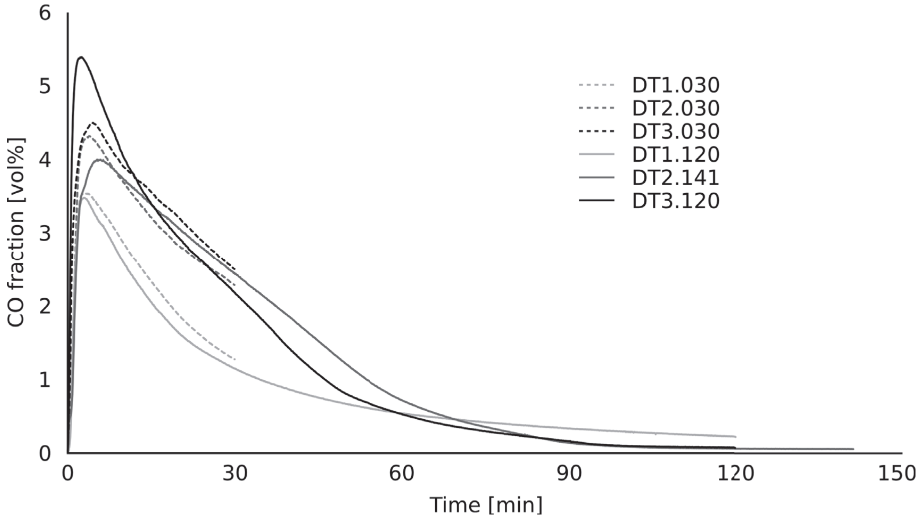

Figure 4.44: CO content in the exhaust gas for the D-series

The CO curves for the short and long experiments carried at 950 and 1000 °C fitted closely with each other, but fairly large deviations were observed between DT3.030 and DT3.120 both in terms of peak height and delay before its apparition.

4.6.3 Sample mass

Table 4.49 shows the measured sample mass at the end of each experiment in the D-series, starting from 5.00 g. The mass intake after long duration experiments showed again that carbon deposition was decisive in this series.

Table 4.49: Sample mass change for the D-series

Experiment	Final sample mass [g]	Mass change [%]
DT1.030	4.90	-2.02
DT2.030	4.82	-3.64
DT3.030	4.77	-4.56
DT1.120	5.77	+15.41
DT2.141	6.53	+30.60
DT3.120	6.39	+27.86

All the samples reacted more than 120 min exhibited mass increases despite the loss of oxygen. The higher mass gain in sample DT2.141 compared to DT3.120 can be explained by a longer exposure to the process gas, despite a lower temperature. The mass loss during the 30 min experiments was increased with increasing temperatures.

4.6.4 Oxygen content

The oxygen content of the product was first determined analyzing the samples after reaction using the O-LECO. In parallel, the CO content in the gas was integrated over the course of the reaction. The two set of data are finally combined to calculate “reconciled” values.

From the O-LECO analyzer

Table 4.36 shows the oxygen content results from the O-LECO equipment. In the D-series, given that the material is a $(Fe,Mg)(Cr,Al)_2O_4$ spinel solid solution, the reduction-carburization is only considered for iron and chromium oxides, but not for the magnesium and aluminium ones. This also means that the material in the D-series is, relatively to the others, the one containing the least amount of oxygen available. The extent of reduction was obtained from the final mass, the oxygen content measured, and the oxygen available.

Table 4.50: Oxygen weight content after reduction-carburization for the D-series

Experiment	Sample mass [g]	Oxygen available [g]	Product mass [g]	Oxygen in the product [wt%]	Extent of reduction [%]
DT1.030	5.00	1.11	4.90	18.0	54.07
DT2.030	5.00	1.11	4.82	13.5	74.87
DT3.030	5.00	1.11	4.77	12.6	79.28
DT1.120	5.00	1.11	5.77	15.9	50.86
DT2.141	5.00	1.11	6.53	8.4	84.03
DT3.120	5.00	1.11	6.39	8.4	85.06

At first glance, the data from O-LECO within the short and long duration experiments are coherent with each other. A higher temperature resulted in a higher extent of reduction, as one could imagine from thermodynamic considerations. One can note that the shift from 950 °C to 1000 °C led to a significant improvement of the extent of reduction in both short and long sets of experiment. However, the improvement was only marginal when the temperature was elevated to 1050 °C. Comparing the experiments carried out at similar temperatures leads to unexpected results. In particular, the DT1.030 experiment exhibited a higher extent of reduction than its 120 min counterpart, DT1.120.

From the CO curves

The unexpected results from the O-LECO analyzer supported further the doubt on its precision and the need of another analysis method. The results shown in **Table 4.51** from the integration of the CO content were generally higher, but most importantly showed very different trends for the D-series.

Table 4.51: Oxygen content from integration of the CO curve after reduction-carburization for the D-series

Experiment	Sample mass [g]	Oxygen available [g]	Oxygen removed [g]	Extent of reduction [%]
DT1.030	5.00	1.11	0.53	54.64
DT2.030	5.00	1.11	0.74	71.38
DT3.030	5.00	1.11	0.82	79.29
DT1.120	5.00	1.11	0.81	76.19
DT2.141	5.00	1.11	1.22	109.22
DT3.120	5.00	1.11	1.21	109.80

The DT1.120 experiment exhibited a much higher extent of reaction than its short duration counterpart with the second method. The question of the accuracy here remains, given the unlikeliness of extent of reduction higher than 100%.

Reconciling O-LECO and integrated CO

The extent of reduction in the D-series exhibited substantial differences depending on the method used. As a result, the “reconciliation” of the methods is uncertain, but still is considered as the best possible estimation. The X-ray diffraction patterns, presented in the following section, also support this third method to obtain the extent of reduction. In particular, the peaks from experiment DT1.030 and DT1.120 indicated an important decrease of the spinel phase relatively to the carbide one. This contradicts the extent of reduction trends based on the O-LECO analysis. The DT3.120 experiment was used as the reference and the new calculated extents of reduction are given in **Table 4.52**.

Table 4.52: Extent of reduction calculated from integrated CO and O-LECO for the D-series

Experiment	Extent of reduction [%] with LECO	Extent of reduction [%] with CO content	Extent of reduction [%] calculated
DT1.030	54.07	54.64	42.33
DT2.030	74.87	71.38	55.30
DT3.030	79.28	79.29	61.42
DT1.120	50.86	76.19	59.02
DT2.141	84.03	109.22	84.61
DT3.120	85.06	109.80	85.06

Large variations are observed between the different methods, especially for the short experiments.

4.6.5 X-ray diffraction

Figure 4.45 presents the X-ray diffraction patterns for the D-series together with the pattern for the raw material, a $(Fe,Mg)(Cr,Al)_2O_4$ solid solution. Overall, both time and temperature seemed to have improved the reduction-carburization, as shown by the progressive decrease of the spinel peaks, and the increase of the carbide ones. For this series, the carburization product was evidenced as Cr_7C_3, again interpreted as a $(Cr,Fe)_7C_3$ solid solution. Graphite was also found in all samples, but especially in the long duration experiments in agreement with the mass gains observed. Contrasting with the C-series, no $(Cr,Al)_2O_3$ phase was found by XRD.

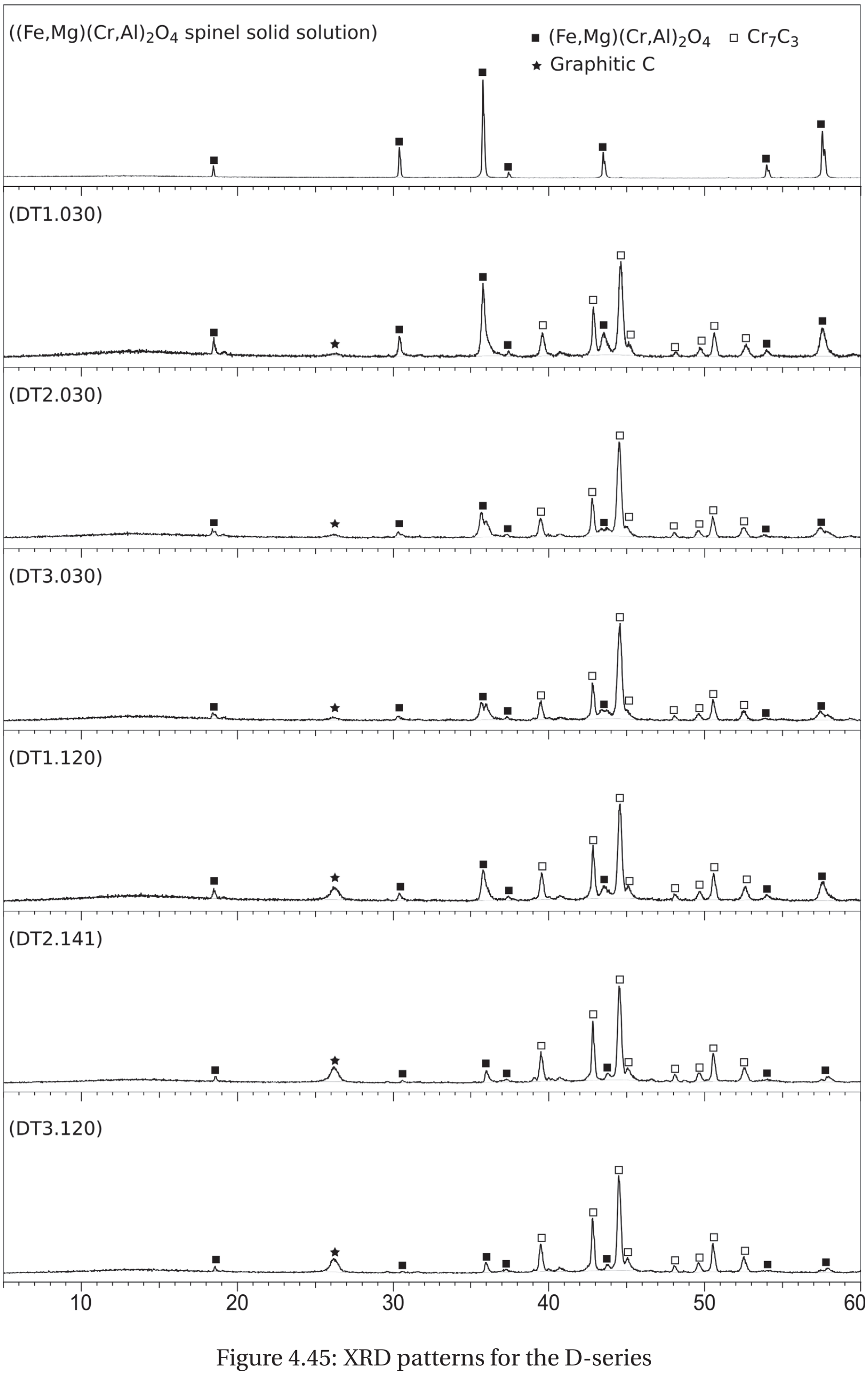

Figure 4.45: XRD patterns for the D-series

4.6.6 Extent of reduction curves

Figure 4.46 provides the extent of reduction curves as a function of time for the D-series. These curves were obtained by integration CO flow out of the furnace, based on the CO content curves given in **Figure 4.44** and the volume change obtained by the formula given in **Section 3.3.4**. The curves are next rescaled based on the calculated extent of reduction at the end of the experiment given in **Section 4.6.4**.

For this final D-series, the experiments carried out at similar temperature led to comparable extent of reduction curves, although the fit is less good than for the other series, especially for DT3.030 and DT3.120.

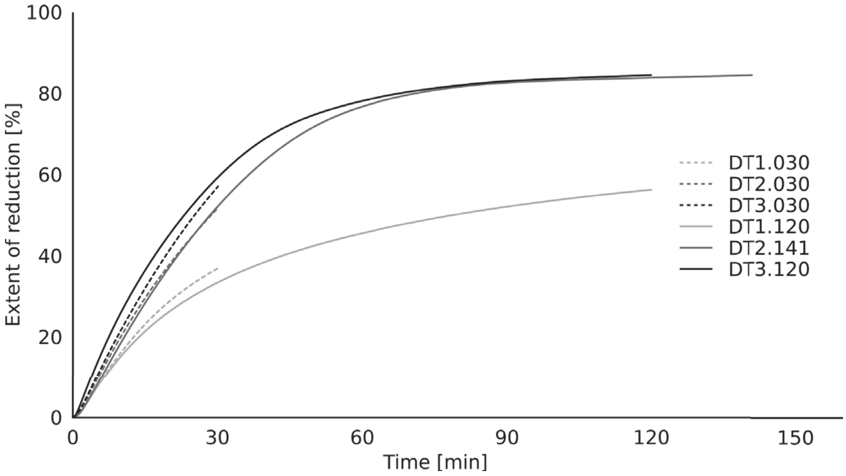

Figure 4.46: Extent of reduction curves for the D-series

As for the the C-series, the temperature increase from 950 to 1000 °C had a clear impact on the reaction rate and extent. In addition, the temperature increase from 1000 to 1050 °C had a mild but perceptible effect on the initial reaction rate, but not on the extent. For the experiments DT2.141 and DT3.120, the extent of reduction curves reach a plateau, while DT1.120 clearly shows that the reaction is unfinished.

4.6.7 Electron microscopy

The samples for the D-series were analyzed using SEM, EDS and EPMA. Alike for the C-series, extensive amounts of deposited carbon were observed, making the analysis challenging.

DT1.030

The reacted grains presented on **Figure 4.47** consisted of two fields: an oxide core and a reacted edge. This is analogous to what was found in the reacted samples of the C-series. Both small and large grains are affected by the reduction-carburization on the pictures presented.

The analyses of the phases in the oxide core, provided in **Table 4.53** indicate that the two oxides exhibited large differences in their iron and magnesium content. The main phase can be regarded as a $(Fe,Mg)(Cr,Al)_2O_4$ spinel solid solution with relatively low aluminium and high magnesium contents. The dark gray lamellae, however, are somewhat depleted of iron and magnesium. As for the C-series, this phase may be a $(Cr,Al)_2O_3$ oxide exsolved from the main phase. To some extent, the lamellae also seem to have formed following specific directions.

At the edge, the material is a complex construction involving three fields and is especially well delineated in the first micrograph. A light gray phase, likely a $(Cr,Fe)_7C_3$ solid solution is placed outwards. On the inner side, this carbide phase is indented and in contact with another phase, possibly a partly reacted material. At the tip of the tines, tiny black fields are observed, and are interpreted as pores. In the bottom right corner of the grain presented in the second picture, a mixture of carbide and oxide formed in a larger field and could indicate the possibility of further growth.

Table 4.53: EDS point measurements for DT1.030

Point	Element [at%]					
	Fe	Mg	Cr	Al	O	C
1	8.79	3.89	24.59	4.10	47.15	11.47
2	3.52	1.81	22.48	11.62	49.54	11.03
3	2.38	1.31	20.53	12.88	48.12	14.79
4	2.55	1.19	19.67	15.91	49.90	10.79
5	30.64	0.63	21.63	3.49	14.56	29.06

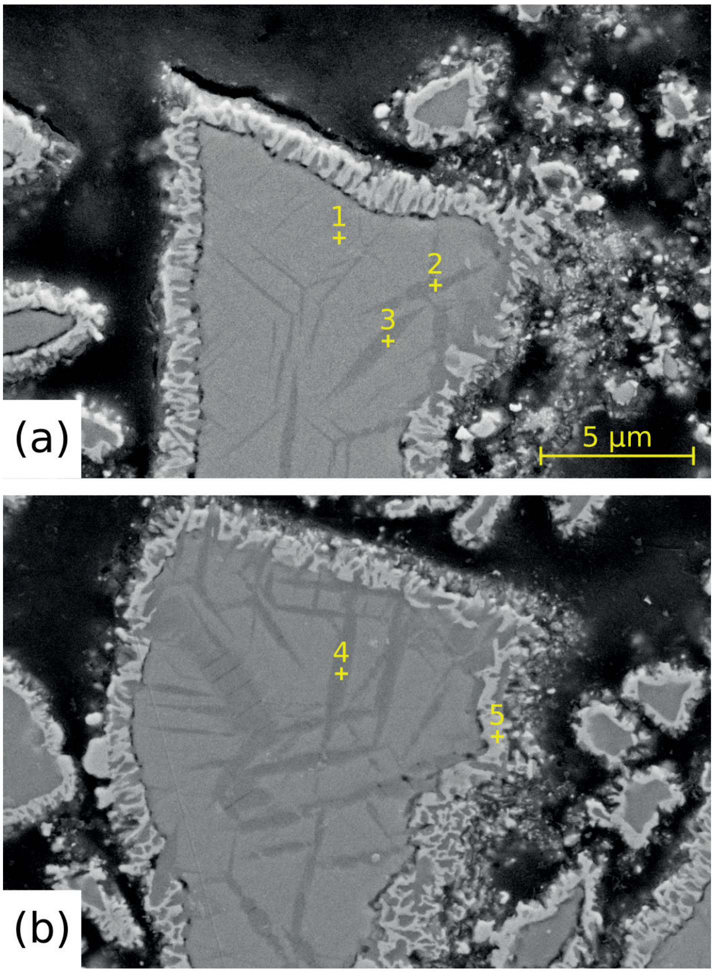

Figure 4.47: Secondary electron micrographs from the DT1.030 experiment

DT2.030

The micrographs presented on **Figure 4.48** show two distinct pellets reacted at 1000 °C for 30 min. The domains found in sample DT1.030 are also evidenced on the first picture. The lamellae were well organized and of a large variety in size. It appeared that the small grains visible on the top of the first picture did not exhibit such lamellae. The EDS point analyses reported in **Table 4.54** evidenced a high concentration in iron around a pore going through the grain. The phase in point 1 most likely is metallic iron, while a mixture of metallic iron and $(Cr,Al)_2O_3$ oxide explains the analyses in point 2 and 3. The grains shown on the first micrographs are overall only marginally reacted, and a substantial share of the material remained as oxide.

The second micrograph stemming from another pellet presents a different story. The grains were further reacted from the edges and a smaller oxide core remained in the center. The analyses of the reacted fields, from point 4 to 7, evidenced a $(Cr,Fe)_7C_3$ together with limited amounts of unreduced oxide. This oxide phase could be imagined as a $(Cr,Al)_2O_3$ solid solution, which would also explain the low magnesium content. The analyses of the central core, on points 8 to 10, indicated a very high concentration of magnesium, and a depletion of iron. The oxide in point 8 seem to be almost fully depleted of iron, and its composition could correspond to a $Mg(Cr,Al)_2O_4$ spinel solid solution. No lamellae were observed in this phase. The interface between the central core and the product carbide looked porous, and the two phases detached.

Table 4.54: EDS point measurements for DT2.030

Point	Element [at%]					
	Fe	Mg	Cr	Al	O	C
1	66.01	···	3.16	···	2.43	28.40
2	42.58	0.60	5.02	9.55	16.91	25.34
3	44.06	0.35	3.91	8.64	14.59	28.44
4	11.25	0.97	28.97	6.14	10.84	41.84
5	10.19	0.84	29.60	6.67	11.03	41.67
6	9.98	0.72	24.19	4.33	8.83	51.96
7	10.85	0.91	31.33	5.67	11.65	39.59
8	0.66	11.46	21.06	5.30	43.22	21.06
9	2.19	7.01	22.51	5.89	43.64	18.76
10	4.08	8.40	19.05	6.20	42.56	19.72
11	1.06	1.28	18.24	13.57	30.64	35.21

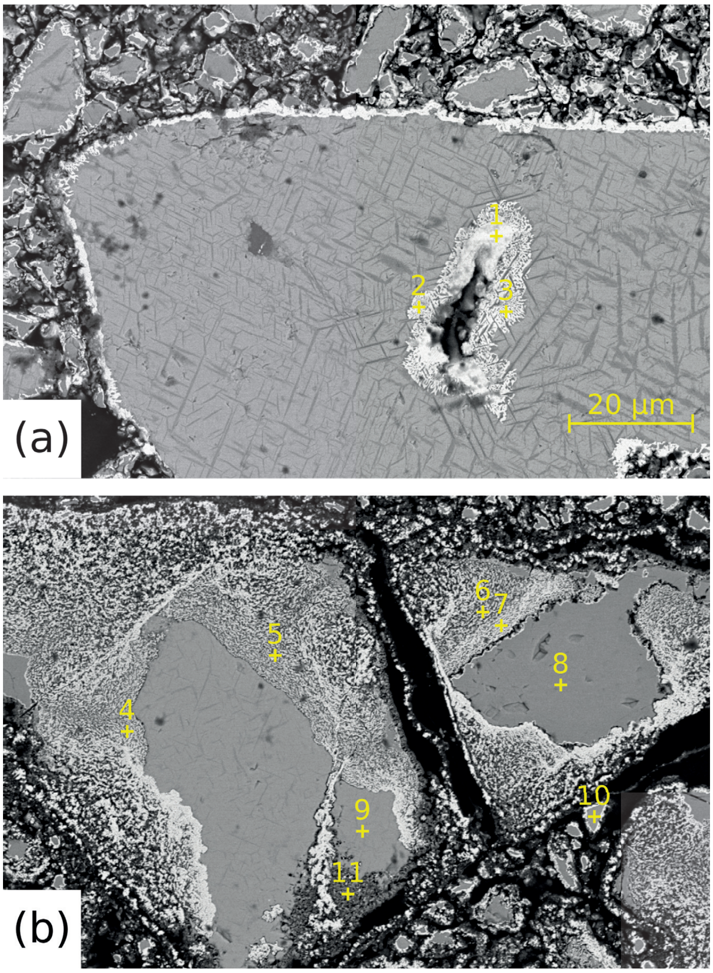

Figure 4.48: Back-scattered electron micrographs from the DT2.030 experiment on two pellets

DT3.030

The electron micrographs from the DT3.030 experiment were, in many ways, similar to those of DT2.030. Different pellets exhibited contrasting extents of reduction, with both marginally and fully reacted grains. Visually, the reaction observed in DT3.030 seemed to follow a shrinking core mechanism on the grain level and the core was often well centered.

A micrograph of a reacted grain is provided in **Figure 4.49** while the corresponding EDS points analyses are given in **Table 4.55**. As seem on the picture, the grain was surrounded by an dense envelope without any visible gap. The composition analyses identified this layer as metallic iron in some spots, or $(\mathrm{Cr,Fe})_7\mathrm{C}_3$ in others. Inwards, $(\mathrm{Cr,Fe})_7\mathrm{C}_3$ was formed in a distinct second layer. Finally, the analyses of the core evidenced a high content of magnesium, and a rather low content of aluminium which was likely exsolved.

Table 4.55: EDS point measurements for DT3.030

Point	Element [at%]					
	Fe	Mg	Cr	Al	O	C
1	27.59	···	27.16	0.97	···	44.28
2	18.87	···	34.01	6.05	13.27	27.80
3	3.15	8.72	26.41	5.41	49.99	6.32
4	67.70	···	5.83	4.41	7.75	14.31
5	21.09	···	37.03	4.28	10.04	27.56
6	···	9.55	27.69	···	54.13	8.64

An interesting feature shown on **Figure 4.50** was the presence of exsolved lamellae on only one of the grains. In addition, compared its surroundings, this grain looked less reacted, judging by the ratio of carbide to oxide phase. This could indicate either that the segregation happens at high temperature and is detrimental to the reduction-carburization, or that this step is transitory and the exsolved phase dissolve back to the spinel after reduction of trivalent cations in excess. Alternatively, if the lamellae formed during the cooling, their formation could be tied to the extent of reduction reached in the grain.

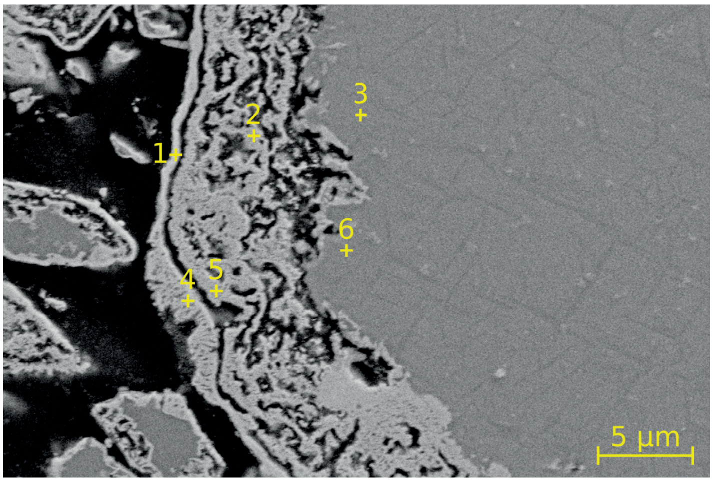

Figure 4.49: Secondary electron micrographs from the DT3.030 experiment

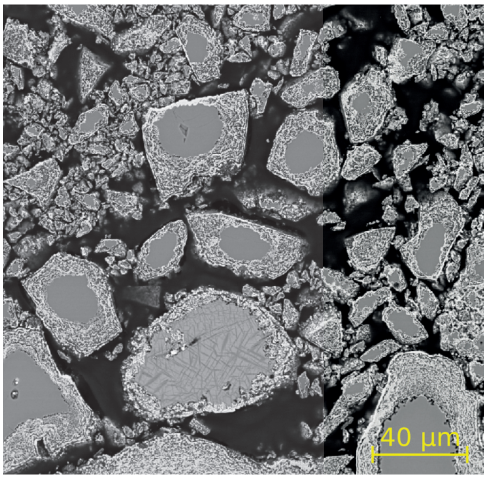

Figure 4.50: Back-scattered electron micrographs from the DT3.030 experiment

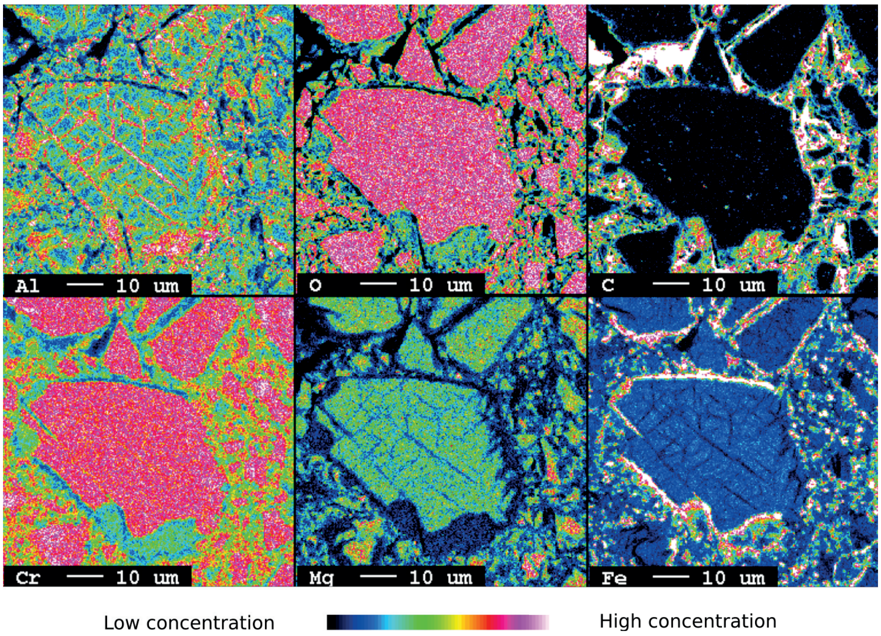

Figure 4.51: Elemental mapping of DT3.030 on a slightly reduced grain

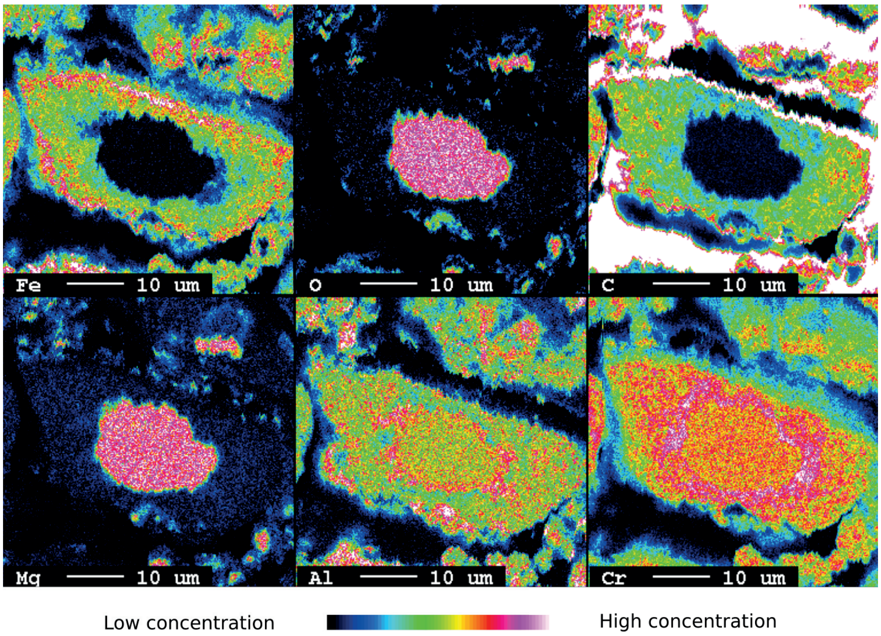

Figure 4.52: Elemental mapping of DT3.030 on a highly reduced grain

The samples from experiment DT3.030 were thoroughly analyzed by EPMA. In **Figure 4.51**, the elemental analysis indicates the forming of an iron rich layer. In addition the lamellae are easily evidenced by their composition, especially their high aluminium and low magnesium and iron contents. These results also confirm the EDS point analyses provided before. However, it remains unclear whether this pellet was just subjected to mild reaction conditions, or can be considered as being at an early stage of the reduction-carburization process.

Figure 4.52 presents a reacted grain from a different pellet. In this case, the reaction seem to be complete. The magnesium had diffused inwards and was concentrated in the leftover oxide, completely depleted of iron. The aluminium had not segregated in a clear manner and was present both in the reacted phase and the oxide leftovers. Contrary to **Figure 4.51** there was no metallic iron layer at the edge of the grain, but rather an iron rich carbide layer containing also chromium. The carbide composition appeared to vary radially from the oxide core's center: the Fe:Cr ratio in the carbide phase decreased when approaching the core. This could be explained by a preferential reduction of the divalent iron early in the reduction-carburization process.

DT1.120

The pellets of the DT1.120 experiment were unequally reacted. While it was expected to find grains exhibiting limited reduction-carburization because of the measured and calculated extents of reduction, it was not necessarily expected to observe fully reacted grains. On **Figure 4.53**, one of these grains is shown. The EDS point analyses given in **Table 4.56** revealed that the surrounding remaining layer was of carbidic nature.

Table 4.56: EDS point measurements for DT1.120

Point	Element [at%]					
	Fe	Mg	Cr	Al	O	C
1	29.96	···	353.2	···	···	34.72
2	···	13.41	25.38	5.80	49.52	5.80
3	28.14	···	37.90	···	···	33.96
4	33.00	···	36.94	0.85	···	29.20
5	···	0.87	5.95	5.35	10.55	77.32
6	29.43	···	43.35	1.17	···	26.05

The oxide phase found in point 2 was completely depleted of iron, indicating that the reaction conditions on that grain were favorable enough to extract all the iron from the spinel, even at 950 °C. The inside of the grain had a “dusty” appearance, reminding the CT2.182 micrographs. The analysis on point 5 revealed a carbon rich nature, likely together with a $(Cr, Al)_2O_3$ oxide.

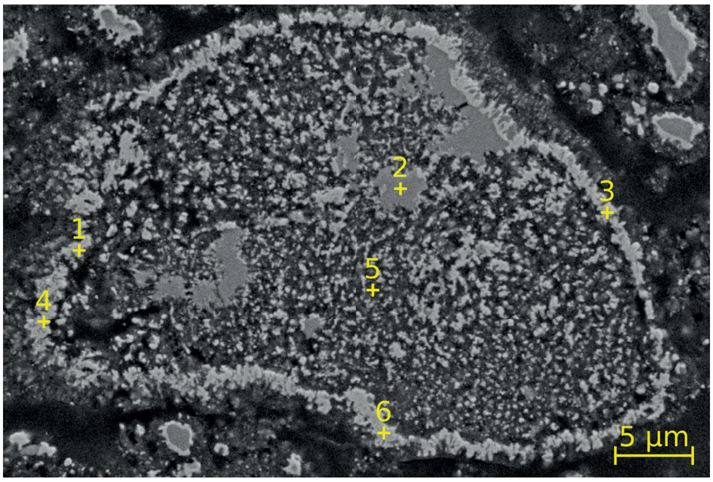

Figure 4.53: Secondary electron micrographs from the DT1.120 experiment

DT3.120

The micrographs from DT3.120 did not differ much from those of DT1.120. A dense layer was also observed around the reacted grains, while the interior was a mixture of carbides and carbon mixed with some oxides. A leftover spinel was also observed in each grain.

Figure 4.54 shows an EPMA mapping of a reduced grain. In addition to the features previously mentioned, it appeared that the surroundings of the $Mg(Cr, Al)_2O_4$ spinel are also depleted of iron. This could indicate that the depletion of iron happened before that the reduction-carburization reaction was complete.

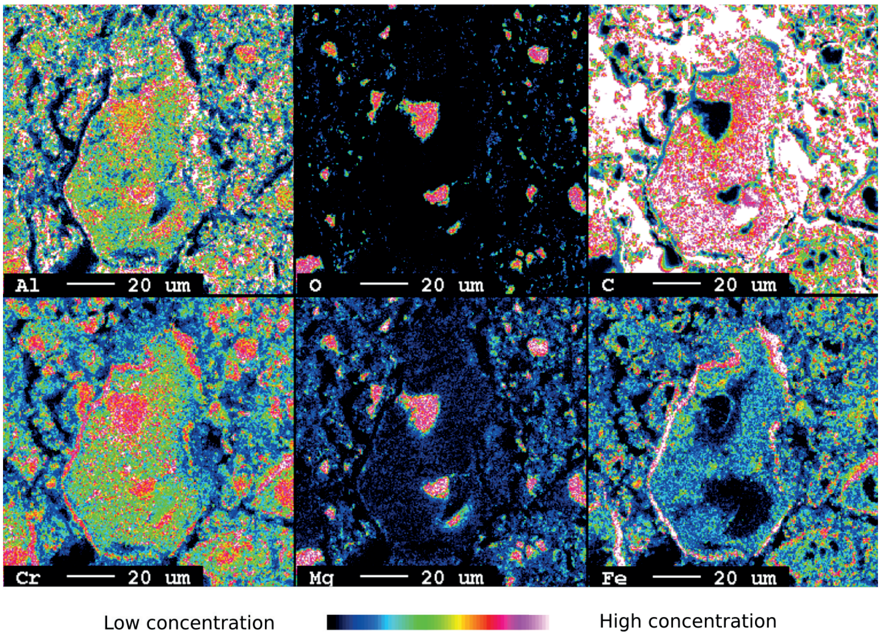

Figure 4.54: Elemental mapping of DT3.120

4.6.8 Summary of the D-series

At the temperatures of the study, $(Fe,Mg)(Cr,Al)_2O_4$ was reduced and carburized to $(Cr,Fe)_7C_3$ and $Mg(Cr,Al)_2O_4$ by a 50%Ar-10%CH_4-40%H_2 gas mixture. The reduction was about 85% complete after 120 min for temperatures above 1000 °C. The reaction was accompanied by an extensive cracking of CH_4 and carbon deposited heavily, increasing the pellets size significantly.

The increase of temperature increased the reaction rate significantly, especially from 950 to 1000 °C, but also slightly from 1000 to 1050 °C. The extent of reduction at 120 min was very impacted by temperature increase from 950 to 1000 °C, temperature at which a plateau was reached. No change in the extent of reduction was observed when increasing the temperature further. According to the CO content in the exhaust gas at the end of DT2.141 and DT3.120, it is unlikely that a longer duration would lead to a higher extent of reduction.

The reaction seemed to follow a shrinking core mechanism at the grain scale. An iron and chromium rich layer formed first as an envelope around the grain. On some micrographs this carbide phase formed tines growing in the oxide core, separated by a second phase likely depleted of iron. Finally, unreduced spinel core were found in fully reacted grains. These spinel cores of $Mg(Cr,Al)_2O_4$ did not contain exsolved lamellae, and were depleted of iron. The elemental mapping suggests that nearly all the magnesium concentrated in these fields, while aluminium was found all over the grains. The Cr:Al ratio in the $Mg(Cr,Al)_2O_4$ core was not found to differ significantly from those of the original unreacted oxide.

4.7 Comparison of the series

The current section aims at comparing the results from the A, B, C and D-series. It was established previously for each of the series that an acceptable fit was observed for the extent of reduction curves taken at a similar reaction temperature. Therefore, the comparison plots do not include the 30 min experiments for clarity purposes. **Figure 4.55**, **4.56** and **4.57** present the extent of reduction curves of the four spinel solid solutions up to 120 min reaction at 950, 1000 and 1050 °C respectively. Since the amount of oxygen available in 5.00 g of sample is a function of the composition, the rates are not directly comparable.

At 950 °C, as shown on **Figure 4.55**, the extent of reduction was heavily influenced by the composition. The reference material $FeCr_2O_4$ was readily reduced (AT1.120 curve), while the reaction of the magnesium-containing sample was strongly inhibited (BT1.120 curve). When aluminium was added to replace chromium in the solid solution, the reduction was also slowed down compared to the pure $FeCr_2O_4$ sample. One can note that the delay before the reaction is shorter for the aluminium containing sample. The curves CT1.120 and DT1.120, corresponding to samples containing aluminium with a composition of $Fe(Cr,Al)_2O_4$ and $(Fe,Mg)(Cr,Al)_2O_4$ respectively, were very close to each other. It appeared also that the addition of magnesium had no significant effect when aluminium was already present in the solid solution.

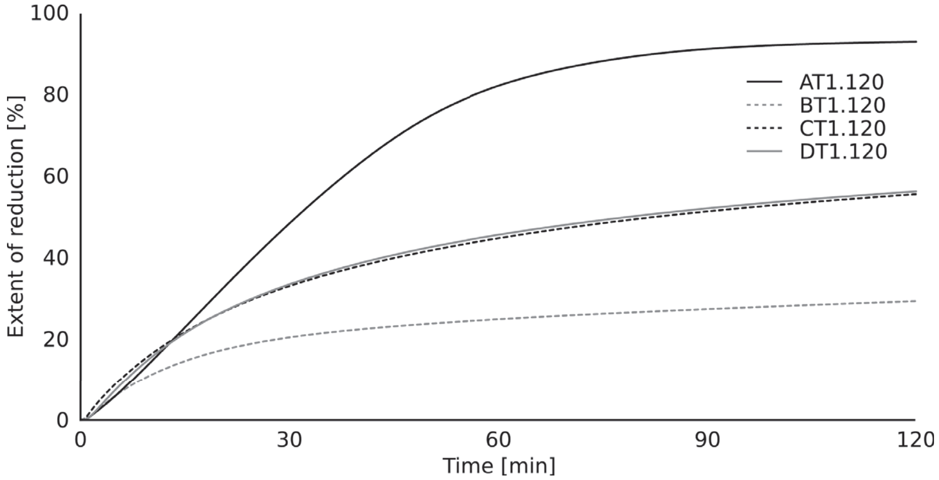

Figure 4.55: Extent of reduction curves at 950 °C

Increasing the temperature to 1000 °C changed the picture dramatically as depicted on **Figure 4.56**. The $FeCr_2O_4$ sample of reference was again reduced quickly. The addition of magnesium as shown on BT2.206 remained detrimental to the reduction but to a lower degree. The extent of reduction curves for $Fe(Cr,Al)_2O_4$ and $(Fe,Mg)(Cr,Al)_2O_4$ remained close to each other except on the first minutes of reaction when $Fe(Cr,Al)_2O_4$ reacted immediately, while $(Fe,Mg)(Cr,Al)_2O_4$ was delayed. Throughout the reaction, the reduction of $Fe(Cr,Al)_2O_4$ always gave marginally better results in terms of extent of reduction than that of $(Fe,Mg)(Cr,Al)_2O_4$.

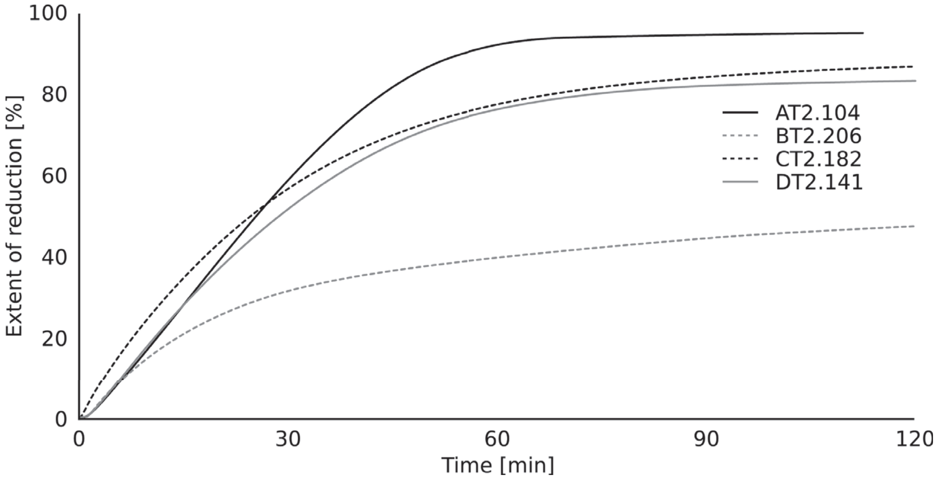

Figure 4.56: Extent of reduction curves at 1000 °C

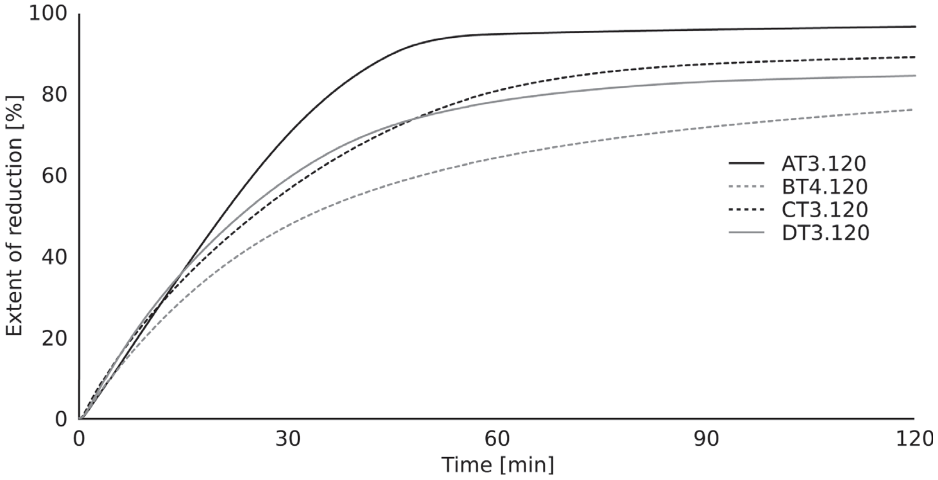

Figure 4.57: Extent of reduction curves at 1050 °C

Few changes were observed at 1050 °C in **Figure 4.57**. As for CT2.182 in **Figure 4.56**, all the samples reacted without delay when meeting the process gas. In addition, the extent of reduction curves show that the samples AT3.120, CT3.120 and DT3.120 behaved similarly to their 1000 °C counterpart. The $(Fe, Mg)Cr_2O_4$ sample, however, benefited again a lot from the temperature increase.

Chapter 5

Kinetic modeling of the reaction

Previous studies mentioned in **Section 2.3.2**, as well as the experimental results in **Chapter 4** seem to indicate that in most samples the reaction follows a shrinking core mechanism at the grain scale. By using the theory elements from **Section 2.4** together with the observed phase and structure changes, the present section aims at modeling the kinetics of the reaction. However substantial uncertainties remain on the mechanism. Therefore, the modeling proposed here is to be seen as tentative, using the available knowledge from each series. Ultimately, the kinetic modeling is used to compare the different series and evidence general trends in the rate limiting steps.

In the following sections, the modeling of each series is attempted using the extended grain model given in **Section 2.4** and its variants. The general formula employed is reminded in **Equation 5.1**:

$$t^* = \underbrace{g_{F_g}(\alpha)}_{\substack{\text{Chemical}\\ \text{reaction}}} + \underbrace{\hat{\sigma}_g^2 \cdot p_{F_g}(\alpha)}_{\substack{\text{Diffusion}\\ \text{in the grain}\\ \text{product layer}}} + \hat{\sigma}^2 \left(\underbrace{p_{F_p}(\alpha)}_{\substack{\text{Diffusion}\\ \text{in the}\\ \text{pellet}}} + \frac{2\alpha}{\underbrace{N_{Sh^*}}_{\substack{\text{External}\\ \text{mass}\\ \text{transfer}}}} \right) \tag{5.1}$$

This was done for a conversion varying from 0 to 1, followed by a subsequent rescaling of the curves obtain to fit the extent of reduction observed. This generally lead the modeled curves to end abruptly and early.

For the B-series, a nucleation and growth based model, presented in **Section 2.4.2**, was used. Its general formula is reminded in **Equation 5.2**:

$$\alpha(t) = 1 - \left[\frac{(k(T)\,t)^{n_S}}{\eta_i} + 1 \right]^{-\eta_i} \tag{5.2}$$

In addition, another nucleation and growth equation, the Austin-Rickett equation, was employed. Its formula is given in **Equation 5.3**:

$$\alpha(t) = 1 - \left[(k(T)t)^n + 1\right]^{-1} \tag{5.3}$$

As a general rule, the modeling was performed by varying as few parameters as possible.

5.1 A-series

In this section, the kinetic modeling for experiments AT1.120, AT2.180 and AT3.120 from the A-series is given. First, the assumptions considered are discussed and used to select the conversion function. In a second time, equation parameters are determined for the best possible fit while complying with the assumptions. Finally, the activation energy is calculated for the reduction-carburization reaction based on the modeling results.

5.1.1 A-series: assumptions

The assumptions considered for the modeling are provided below, and used to justify the choice of the various terms in the equations.

Reaction start-up In every experiment, a delay was observed prior the peak of the reaction rate. To compensate for this, a delay t_0 arbitrary chosen was set-up in the time equation.

Extent of reduction The three long duration experiments in the A-series exhibited varying extents of reduction as seen in **Section 4.3**. Also, the CO curves are characterized by a non-zero asymptotic value which leads to a constant slow increase of the extent of reduction towards the end of the experiment. Such phenomenon, whose origin is not well known, is very detrimental to the kinetic modeling. As a result, the extent of reduction curves were arbitrarily modified so that the when the CO content in the gas reaches value below 0.1 mol%, it is considered as being zero. In practice, the conversion α at a time t is defined as:

$$\alpha(t) = \frac{\displaystyle\int_0^t \overline{n}_{CO}(t)dt}{\displaystyle\int_0^{t_{\text{end}}} \overline{n}_{CO}(t)dt} \tag{5.4}$$

where t_{end} is chosen for $\overline{x}_{\text{CO}} < 0.1$ mol%. The curves obtained by the modeling are then scaled down according the extent of reduction calculated by the reconciliation method presented in **Section 4.3.4**

Pellet shape (F_p) The pellet shape was visually determined. Due to the pelletizing technique, as presented in **Section 3.2.3**, the formed pellets were spherical, hence having a shape factor $F_p = 3$.

Pellet diffusion ($\hat{\sigma}^2$) On one of the pellets observed by EPMA, there is a clear reaction interface in a partly reacted pellet. A sharp interface generally means that the diffusion in the pellet is limiting [52]. However, the position of the interface indicates the opposite as the unreacted material is not at equal distance from the edge. The reaction interface can be seen on **Figure 5.1**. On **Figure 5.2**, two partly reacted pellets are represented. The red arrows, placed radially, shows the decreasing distance from the edge.

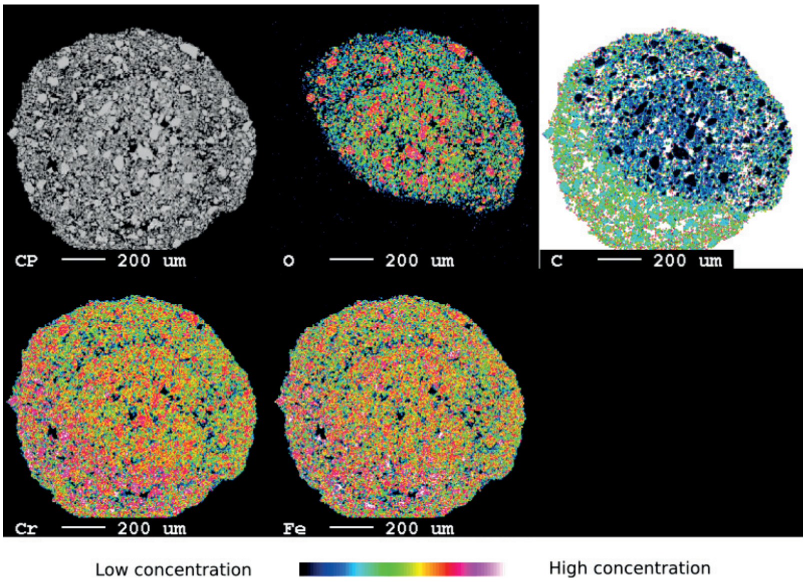

Figure 5.1: Elemental mapping of AT3.030 for a pellet

Picture (a) shows a pellet exhibiting an unreacted core surrounded by a reacted layer and separated by a sharp interface. This case illustrates the diffusion limiting case; the distance the gas must diffuse to reach the reaction interface is globally the same all around the pellet. Picture (b), on the other hand, represents the observed pellet. In this case, the distance varies importantly and some grains close to the surface remain unreacted while others close to the core are fully reduced. Despite the sharp interface, the pellet diffusion was considered weak, and

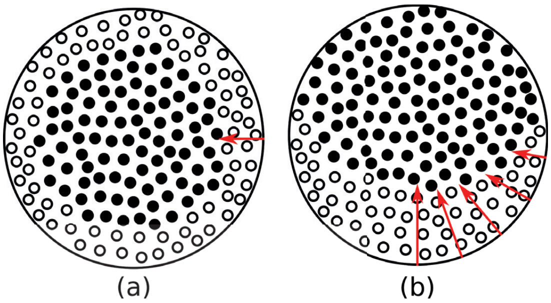

Figure 5.2: Pellet aspects during reduction (a) Controlled by pellet diffusion (b) As observed in the A-series

thus $\hat{\sigma}^2 \ll 1$. A small value of $\hat{\sigma}^2$ is also realistic given the small radius R_p of the pellets considered as $\hat{\sigma}^2 \propto R_p^2$. The value is voluntarily taken non zero, as this would assume that the external mass transfer is not limiting.

External mass transfer (N_{Sh^*}) The A-series is characterized by a fairly constant reaction rate. This can be seen on the CO curves in **Figure 4.9**. In comparison, the curves from the T-series indicate that an increase in the methane content in the gas changes the reaction rate profile. This could indicate that the reaction rate is limited by the supply of raw materials, here of CH_4. This is further supported by the simultaneous presence of unreacted and totally reacted pellets after 30 min of reaction. On a modeling standpoint, this was taken into account through an external mass transfer effect. This choice is arguable as such mechanism relates to the diffusion through the external gas film surrounding the pellet, and not directly to the supply of material. Is it to be seen here as representation of the maximum attainable rate. The chosen value for N_{Sh^*} is likely to be low for the effect to be impactful, since $\hat{\sigma}^2 \ll 1$. Since the gas mixture is kept the same for all the A-series, an additional constrain was to keep the value N_{Sh^*} for the three modeled experiments.

Grain shape (F_g) The choice of the grain shape was done by plotting the conversion function for a chemically controlled mechanism for $F_g = 1$, 2 and 3, the most straight curve determining which value of F_g should be employed. As discussed above, the mechanism is likely not only chemically controlled, but also limited by the supply of reactant in the gas phase. But because this is modeled by a linear function with time, it does not influence the shape of the conversion curves. Also, this was done with the data from AT1.120 as this experiment, exhibiting the lowest rate of reaction, should be less influenced by exhaustion of the process gas.

Figure 5.3 shows the plot of $g_{F_g}(\alpha)$ vs time for $F_g = 1$, 2 and 3.

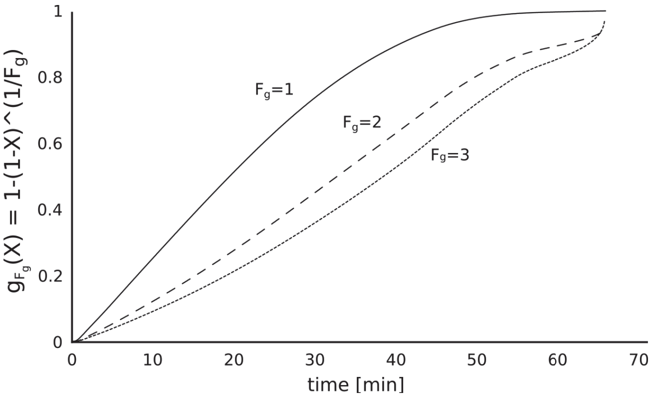

Figure 5.3: Chemical conversion function $g_{F_g}(\alpha)$ for AT1.120 for $F_g = 1$, 2 and 3

For further modeling, a shape factor of $F_g = 2$ is selected as it gives the straightest line.

Grain diffusion ($\hat{\sigma}_g^2$) As shown in the electron micrographs, the product layer around the spinel grains consisted of a highly porous material. It is therefore reasonable to consider the diffusion through the product layer as not limiting, and thus $\hat{\sigma}_g^2 = 0$.

Temperature dependence Both the dimensionless time t^* and the generalized gas-solid reaction modulus $\hat{\sigma}^2$ are proportional to k the reaction rate constant. As the rate can be expected to increase with temperature, both the aforementioned parameters are expected to also increase with temperature in a similar fashion. During modeling, an additional condition was set to keep the external mass transfer alike at each temperature, thus $\frac{t}{t^*} \cdot \hat{\sigma}^2 \approx \text{cst}$.

The final time equation for the kinetic modeling of the A-series can be written as in **Equation 5.5**:

$$\begin{aligned} t &= t_0 + \frac{t}{t^*} \cdot \left(g_{F_g}(\alpha) + \hat{\sigma}^2 \left(p_{F_p}(\alpha) + \frac{2\alpha}{N_{Sh^*}} \right) \right) \\ &= t_0 + \frac{t}{t^*} \cdot \left(1 - (1-\alpha)^{\frac{1}{2}} + \hat{\sigma}^2 \left(1 - 3(1-\alpha)^{\frac{2}{3}} + 2(1-\alpha) + \frac{2\alpha}{N_{Sh^*}} \right) \right) \end{aligned} \tag{5.5}$$

5.1.2 A-series: simulation results

The parameters, namely t_0, $\frac{t}{t^*}$, $\hat{\sigma}^2$ and N_{Sh^*} were optimized following the constrains given earlier. The best fit was achieved using the parameters given in **Figure 5.4** together with the modeling curves and experimental measurements.

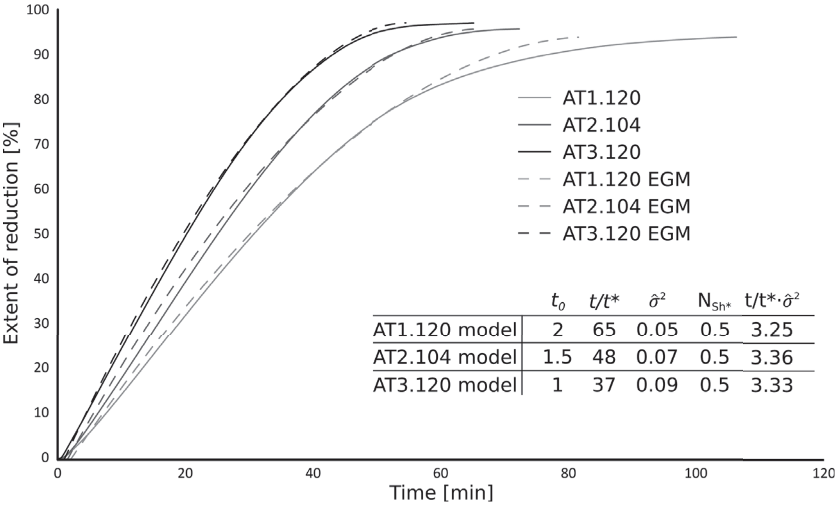

	t_0	t/t^*	$\hat{\sigma}^2$	N_{Sh^*}	$t/t^* \cdot \hat{\sigma}^2$
AT1.120 model	2	65	0.05	0.5	3.25
AT2.104 model	1.5	48	0.07	0.5	3.36
AT3.120 model	1	37	0.09	0.5	3.33

Figure 5.4: Extent of reduction as a function of time from experimental data and modeling for the A-series

Overall, the fit between the model and the experimental data is satisfying. Slight deviations are observed at the start for AT2.180 and AT3.120, as well as misfit towards high degrees of reduction for experiment AT1.120.

5.1.3 A-series: activation energy

Based on the model proposed in the previous section, the activation energy was calculated for the reduction-carburization of $FeCr_2O_4$ to $(Cr, Fe)_7C_3$. First, the chemical reaction part of the model was plotted alone and scaled according of the extent of reduction used previously. The results are provided in **Figure 5.5** where $t = \frac{t}{t^*} \cdot g_{F_g}(\alpha)$ is plotted after rescaling with correct extent of reduction values.

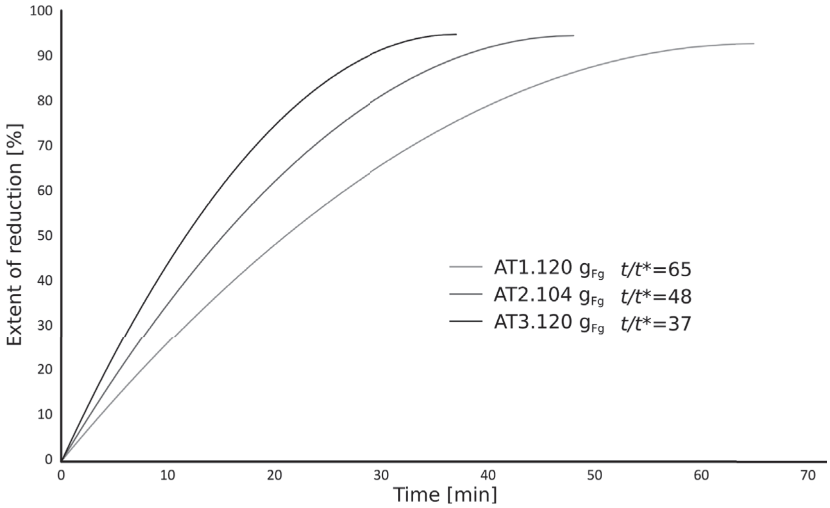

Figure 5.5: Extent of reduction as a function of time for a chemical control only using the EGM

Based on the data from this figure, the activation energy for the chemical reaction is calculated at various extents of reduction from the slope of the plot of -ln(t) vs $\frac{1}{T}$. The temperature used for the calculation corresponds to the average temperature recorded and given in **Table 4.9**. The results are provided in **Table 5.1**.

Table 5.1: Activation energy for the reduction-carburization of $FeCr_2O_4$

Extent of reduction [%]	Slope	Activation energy [kJ/mol]
10	-9432.4	78421
20	-9444.8	78524
30	-9459.9	78649
40	-9479.1	78809
50	-9504.5	79020
60	-9540.5	79319

The activation energies found for the chemical reaction span between 78.4 and 79.3 kJ/mol.

5.2 B-series

The modeling of the B-series was attempted using the extended grain model. However, no conclusive results were obtained. Bearing in mind the characteristic shapes of the carbides in the B-series as shown on **Figure 5.6**, nucleation and growth rate equations should not be excluded for the modeling.

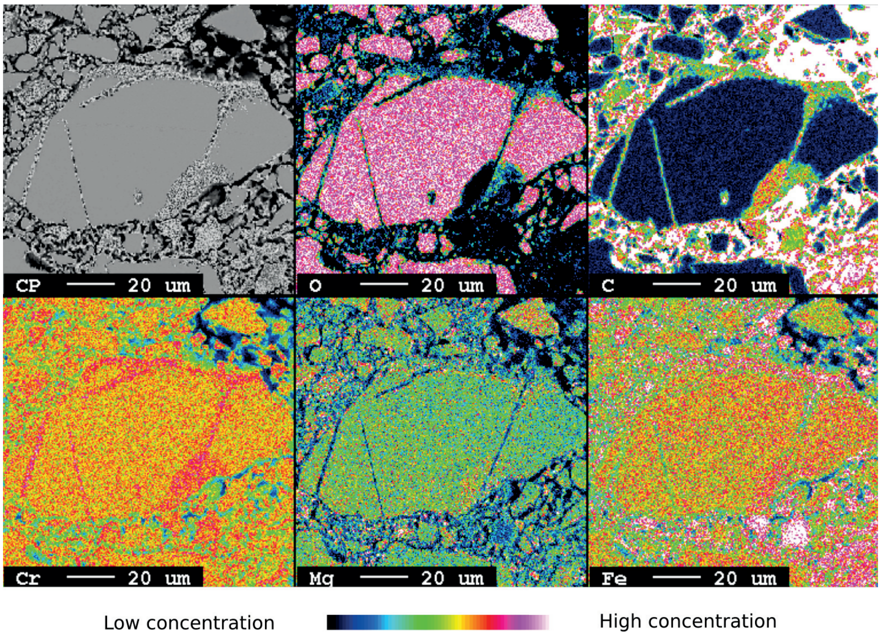

Figure 5.6: Elemental mapping of BT4.030

As a result, two additional models are considered for the B-series: the extended JMAK and the Austin-Rickett equation.

5.2.1 B-series: assumptions

The assumptions and equations employed for each of the models are provided below.

Extended grain model

The assumptions to use the extended grain model are chosen not too constraining. This is done in order to show that despite a high degree of freedom, the model cannot follow the trends observed satisfactorily. Compared to the A-series, most of the assumptions are kept the same. However, external mass transport and pellet diffusion are neglected.

Grain diffusion is however taken into account as the biggest grains appeared more challenging to reduce. Pellet shape and grain shape are considered the same as for the A-series. The conversion α is defined as:

$$\alpha(t) = \frac{\displaystyle\int_0^t \overline{n}_{CO}(t)dt}{\displaystyle\int_0^{t=120\text{ min}} \overline{n}_{CO}(t)dt} \tag{5.6}$$

The time equation for the extended grain model on the B-series is therefore:

$$\begin{aligned} t &= t_0 + \frac{t}{t^*} \cdot \left(g_{F_g}(\alpha) + \hat{\sigma}_g^2 \cdot p_{F_g}(\alpha) \right) \\ &= t_0 + \frac{t}{t^*} \cdot \left(1 - (1-\alpha)^{\frac{1}{2}} + \hat{\sigma}_g^2 \cdot \left(\alpha + (1-\alpha) \cdot \ln(1-\alpha) \right) \right) \end{aligned} \tag{5.7}$$

where t_0, $\frac{t}{t^*}$ and $\hat{\sigma}_g^2$ are parameters determined by curve fitting.

Extended JMAK

The equation proposed by Starink and presented in **Section 2.4.2** was also used to model the reaction. A notable difference with the extended grain model is the curve fitting was carried out on the extent of reduction curves, and not rescaled ones. This indirectly assumes an extent of reduction of 100 % can be reached. In addition, no start up delay t_0 was used in this case.

The conversion function is provided in **Equation 5.8**:

$$\alpha(t) = 1 - \left[\frac{(k(T)t)^{n_S}}{\eta_i} + 1 \right]^{-\eta_i} \tag{5.8}$$

where n_S, $k(T)$ and η_i are parameters of the function.

Austin-Rickett equation

The Austin-Rickett equation was also considered. It can be seen as a special case of the previous **Equation 5.8** where $\eta_i = 1$, giving:

$$\alpha(t) = 1 - \left[(k(T)t)^n + 1 \right]^{-1} \tag{5.9}$$

In this case however, it was considered that the extent of reduction will not reach 100 %. An additional parameter $\alpha_{\max}$ was set leading to the following equation:

$$\alpha(t) = \alpha_{\max} \cdot \left(1 - \left[(k(T)t)^n + 1 \right]^{-1} \right) \tag{5.10}$$

5.2.2 B-series: simulation results

The modeling results are presented in this section for each of the models considered presented above.

Extended grain model

As shown on **Figure 5.7**, the extended grain model failed to follow the trends of the BT4.120 extent of reduction curve. In particular it is found that there is a significant slowdown towards the end of the reaction.

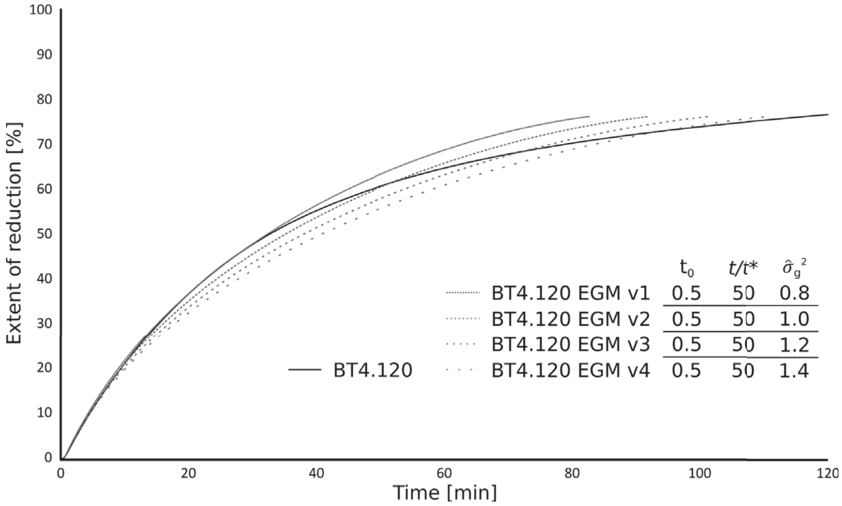

Figure 5.7: Extent of reduction as a function of time from experimental data and modeling for the B-series (extended grain model equation)

Note that the experiment BT4.120 was chosen because it gave the best results for the EGM among all the experiments considered. However, varying the diffusion in the grain product only lead to a displacement of the misfit.

Extended JMAK

Figure 5.8 confronts the curves obtained from the model to the empirical data. For these curves, the parameters n_S and k were kept constant at 1.9 and 0.07 respectively. Varying the value of k did not improve the fitting.

Overall the fit is close for all the curves although a misfit is found for BT4.120.

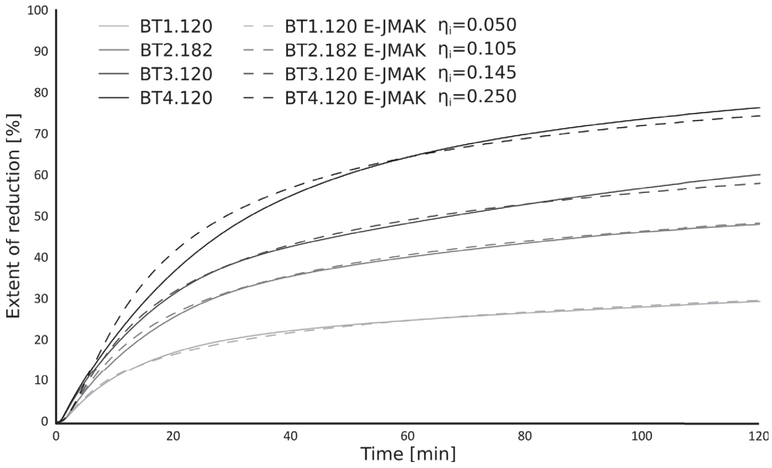

Figure 5.8: Extent of reduction as a function of time from experimental data and modeling for the B-series (extended JMAK equation)

Austin-Rickett equation

The curves obtained using the Austin-Rickett equation are given in **Figure 5.9** together with the parameters employed.

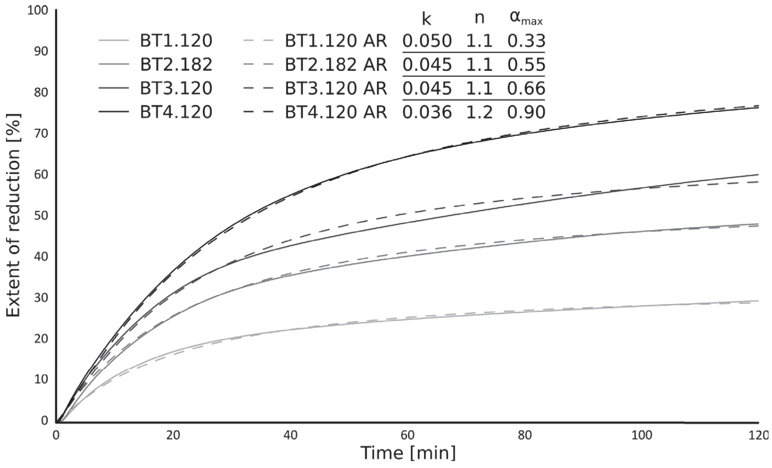

Figure 5.9: Extent of reduction as a function of time from experimental data and modeling for the B-series (Austin-Rickett equation)

A very good fit is obtained in this case, especially for BT1.120, BT2.182 and BT4.120.

5.3 C-series

The kinetics for the aluminium containing samples of the C-series are modeled in this section. In a first time, the parameters kept the same as in the A-series are recalled while the adjustments to the model are detailed. In a second part, the best fitting curves are provided.

5.3.1 C-series: assumptions

A number of assumptions are kept from the modeling the A-series.

Reaction start-up Similarly to what was done for the A-series, a delay t_0 was introduced for the time equation. The values were chosen arbitrarily in order to fit the reaction start observed.

Pellet shape (F_p) The pellets were formed as spheres, $F_p = 3$.

Pellet diffusion ($\hat{\sigma}^2$) For the C-series, the pellet diffusion is also considered low. This is first based on the impossibility to observe a sharp interface in the reacted pellets. Also the pellets sizes and pelletization technique were like those of the A-series, which motivates the use of a similar value for $\hat{\sigma}^2$. In practice $\hat{\sigma}^2 = 0$ was used, as the external mass transfer did not need to be taken into account.

Grain shape (F_g) The reaction studied for the C-series is likely not chemically controlled. It is therefore impossible to use the same determination technique for the grain shape factor F_g . However, since the experimental procedure for the synthesis and the crushing was similar to the A-series, the shape factor is chosen the same and hence $F_g = 2$.

In addition, several of the parameters are also changed to correspond to the observations with the microscope.

Extent of reduction The criteria retained for the A-series to determine the extent of reduction could not be kept as such with the C-series. Indeed, during the experiment CT1.120, the CO content in the process gas did not reach values as low as 0.1 mol%. For this experiment, the conversion $\alpha(t)$ was then defined as:

$$\alpha(t) = \frac{\displaystyle\int_0^t \overline{n}_{CO}(t)dt}{\displaystyle\int_0^{t=120min} \overline{n}_{CO}(t)dt} \tag{5.11}$$

which means in other words that the reaction was considered completed at 120 min. For the other two experiments, the previous criteria was kept and $\alpha(t)$ was then defined as:

$$\alpha(t) = \frac{\displaystyle\int_0^t \overline{n}_{CO}(t)dt}{\displaystyle\int_0^{t_{\text{end}}} \overline{n}_{CO}(t)dt} \tag{5.12}$$

where t_{end} is chosen for $\overline{x}_{\text{CO}} < 0.1$ mol%. The curves obtained by the modeling are then scaled down according the extent of reduction calculated by the reconciliation method presented in **Section 4.5.4**

External mass transfer (N_{Sh^*}) For the C-series, the external mass transfer was not taken into account. This is motivated by the aspect of the CO curves which exhibit a steep decrease at the start as shown on **Figure 4.34**. At the temperatures of the study, the reaction rate did not seem to be capped as for the A-series. The external mass transfer was therefore neglected.

Grain diffusion ($\hat{\sigma}_g^2$) The product material observed in the C-series differed a lot from the porous phase obtained after reduction-carburization of FeCr_2O_4. For the C-series, a dense product phase was observed at the edge of the grains. A zoning phenomenon was also present: a $(\text{Cr},\text{Al})_2\text{O}_3$ phase formed an envelope around the spinel core. All these constructions are likely to modify the diffusion of the of the gas up to the reaction interface in the core of the grains. This is modeled here using a grain diffusion mechanism. Thus, $\hat{\sigma}_g^2$ is one of the parameters for the C-series modeling.

The final time equation for the kinetic modeling of the C-series can be written as in **Equation 5.13**:

$$\begin{aligned} t &= t_0 + \frac{t}{t^*} \cdot \left(g_{F_g}(\alpha) + \hat{\sigma}_g^2 \cdot p_{F_g}(\alpha) \right) \\ &= t_0 + \frac{t}{t^*} \cdot \left(1 - (1-\alpha)^{\frac{1}{2}} + \hat{\sigma}_g^2 \cdot \left(\alpha + (1-\alpha) \cdot \ln(1-\alpha) \right) \right) \end{aligned} \tag{5.13}$$

5.3.2 C-series: simulation results

The parameters, namely t_0, $\frac{t}{t^*}$ and $\hat{\sigma}_g^2$ were optimized following the constrains given earlier. The best fit was achieved using the parameters given in **Figure 5.10** together with the modeling curves and the experimental measurements.

Overall, the fit is good at the first stages of the reaction. Deviations are observed towards the end, as the model predicts faster rates than observed.

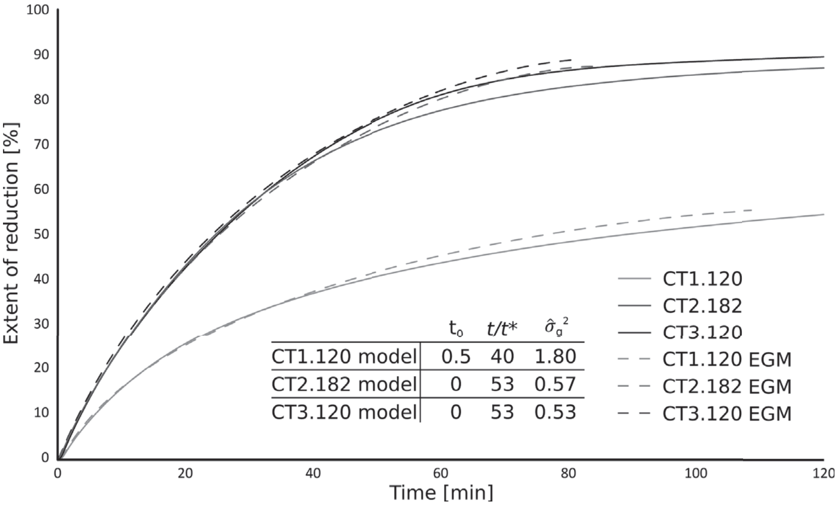

	t_0	t/t^*	$\hat{\sigma}_g^2$
CT1.120 model	0.5	40	1.80
CT2.182 model	0	53	0.57
CT3.120 model	0	53	0.53

Figure 5.10: Extent of reduction as a function of time from experimental data and modeling for the C-series

5.4 D-series

The modeling of the D-series is given in this section. The few differences with the C-series in terms of assumptions are reminded in a first time. The modeling results are provided next using the extended grain model.

5.4.1 D-series: assumptions

All the assumptions employed for the C-series mentioned above are kept invoking the same reasoning. No zoning was observed in the samples of the D-series, however, the grain diffusion was still taken into account as a dense product layer was observed around the reacted grains. Thus, ($\hat{\sigma}_g^2$) is maintained as one of the parameters. The time equation used for the modeling was identical to that of the C-series and written as in **Equation 5.14**:

$$\begin{aligned} t &= t_0 + \frac{t}{t^*} \cdot \left(g_{F_g}(\alpha) + \hat{\sigma}_g^2 \cdot p_{F_g}(\alpha) \right) \\ &= t_0 + \frac{t}{t^*} \cdot \left(1 - (1-\alpha)^{\frac{1}{2}} + \hat{\sigma}_g^2 \cdot \left(\alpha + (1-\alpha) \cdot \ln(1-\alpha) \right) \right) \end{aligned} \tag{5.14}$$

5.4.2 D-series: simulation results

The extent of reduction curves for the D-series are modeled in this section.

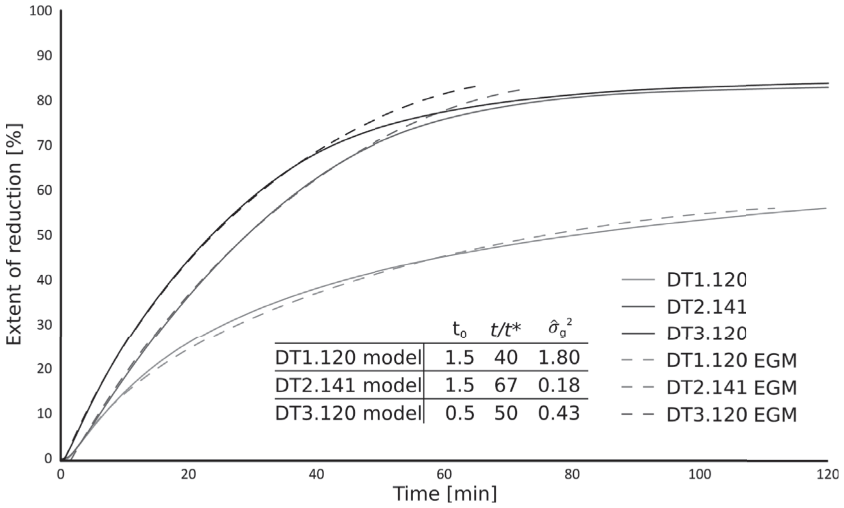

Figure 5.11: Extent of reduction as a function of time from experimental data and modeling for the D-series

The curves obtained experimentally being close to those of the C-series, moderate variations are expected. The parameters t_0, $\frac{t}{t^*}$ and $\hat{\sigma}_g^2$ were optimized following the constrains given earlier. The best fit was achieved using the parameters given in **Figure 5.10** together with the modeling curves and the experimental measurements.

Chapter 6

Discussion

The previous two chapters reported the experimental results as well as the modeling work. The current chapter will confront these results to the literature and will attempt to capture the essence of the reduction-carburization of synthetic chromite by methane. In the first section, the synthesis work is reviewed concerning the technique used as well as the products obtained. The second section will discuss the general trends observed during the reduction-carburization work, especially concerning the phases and mechanisms involved. The sources of errors will be discussed in a third part. At last, the effect of impurities on the reduction-carburization mechanism of each sample is discussed in the light of the previous sections.

6.1 Synthesis of chromite solid solutions

The induction skull melting technique was found to be a successful molten route for the production of synthetic spinels, allowing the production of about 200 g of product per batch in a short time. The short melting duration of about 5 min is a clear advantage compared to other synthesis techniques used in the literature [43; 63; 64; 65].

Technicalities

The synthesis procedure was similar for all the samples although slight variations were necessary. The addition of small amounts of iron in excess was found beneficial to the melting while not being excessively detrimental to the product's purity as most of this excess iron could be recovered before further processing of the spinel. The optimal placement of the raw materials in the furnace is shown in **Figure 6.1**. The iron pieces are spread on the oxide surface, while keeping the biggest pieces close to the center. This way, the formation of a crust at the top of the charge was avoided. The choice of the power input was also key in the synthesis, and a higher power input was necessary for the synthesis of $(Fe, Mg)(Cr, Al)_2O_4$ compared to the other compositions without it being linked to the temperature stability of the spinel only.

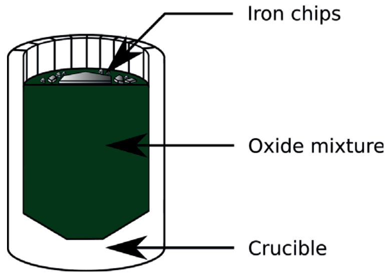

Figure 6.1: Schematic illustration of material positioning in the crucible

The XRD analysis confirmed the spinel nature of the product. The absence of other significant peaks as well as the microscopy studies indicated the high purity of the material produced for each composition. However, metallic iron leftovers from the synthesis could be found in minor quantities.

Limitations

The main drawback in the use of the induction skull melting technique for the production of chromite solid solutions is the dependency on metallic iron. Because iron is used as the susceptor, an increase in the magnesium content of the targeted synthetic chromite composition will result in a more difficult melting. In addition, since the oxide powders tend to sinter, a too slow melting can result in deviations from the targeted composition.

However, it is of interest to synthesize such compositions, as they better approach the natural ores' composition. A possible solution, although unpractical with the setup used, would be to produce the bath in two steps. Firstly a iron rich melt is prepared similarly to what was done in the present study. Secondly, oxides such as MgO, Al_2O_3 or Cr_2O_3 are dissolved directly into the bath according to the desired stoichiometry.

6.2 $FeCr_2O_4$ reduction-carburization

The reduction-carburization of $FeCr_2O_4$, studied with the A-series, was considered as a reference. The reaction route is presented first, and the phases present are discussed. The reaction kinetics and rate determining step for the reaction were derived from the modeling and discussed next. At last, a mechanism is proposed to explain the reduction-carburization of $FeCr_2O_4$.

6.2.1 Reaction and phases

$FeCr_2O_4$ was readily reduced and carburized by methane to form $(Cr, Fe)_7C_3$ as the reaction product. A Cr_2O_3 phase was also evidenced by XRD as an intermediary phase but was ultimately reduced and carburized after long durations. No other intermediary phases were evidenced. The metallic iron found was interpreted as stemming from the synthesis, and not from the reaction. This is based on the impossibility of finding metallic iron at the reaction interface and instead iron was observed as particles within the oxide phase. The overall chemical reaction for the reduction-carburization of $FeCr_2O_4$ can be written as in **Equation 6.1**:

$$FeCr_2O_4 + \frac{37}{7}CH_4 \rightarrow \frac{3}{7}(Cr, Fe)_7C_3 + 4CO + \frac{74}{7}H_2 \qquad (6.1)$$

where the Fe:Cr ratio in $(Cr, Fe)_7C_3$ varies but approaches 0.5 in average.

This reaction contrasts greatly with that presented by Qayyum and coworkers who found Cr_3C_2 and Fe_3C as reaction products [43], while none of these phases were found in the present work. This may originate from differences in the experimental procedures as the set-up used in the present work is also significantly different to Qayyum's: a 50%Ar-10%CH_4-40%H_2 gas mixture was used here while Qayyum and coworkers obtained methane from hydrogenation of the carbon added in their chromite pellets. In other words these two works contrast in the state of methane: stable in the work of Qayyum, and metastable in the present study. This also results in contrasting carbon activities in the gas phase between the two studies: below unity for Qayyum's work, and above 80 in the present study. The high activity of methane could explain the simultaneous reduction-carburization of iron and chromium oxides, and therefore the formation of a single carbide combining iron and chromium.

Investigations of the carbothermic reduction between 1150 and 1300 °C of synthetic iron chromite also differed substantially [64]: carbides were not found, and the reduction concerned only the iron oxides. Methane appear therefore as a better reductant for pure $FeCr_2O_4$ as it also successfully reduces the chromium oxides at low temperatures.

Although the conversion of iron and chromium oxides to carbides happened simultaneously, their respective conversion rate differed as iron oxides were reduced faster. This is evidenced by the higher content of iron in the $(Cr,Fe)_7C_3$ carbide at early stages of the reaction, and by the presence of Cr_2O_3. While this inclination of iron to reduce faster is known in natural spinels even with methane [46], one should note once more that at the temperatures of the present study, iron metal was not formed at early stages nor separated in a distinct carbide phase. In detail, the phases appearing follows the sequence given next:

$$\begin{gathered} FeCr_2O_4 \\ \downarrow \\ FeCr_2O_4 + Cr_2O_3 + (Cr,Fe)_7C_3 \\ \downarrow \\ (Cr,Fe)_7C_3 \end{gathered}$$

where the Fe:Cr ratio in the carbide decreases with the progress of the reaction.

Based on the CO content measurements, the reduction-carburization reaction was found to start at temperatures as low as 760 °C, a slightly lower value than what was observed by Qayyum [43]. At all the temperatures studied, the reaction was essentially completed in full and led to the same products. A temperature increase was found to have a minor effect on the extent of reduction after 120 min.

6.2.2 Reaction kinetics

The reduction-carburization of $FeCr_2O_4$ was characterized by a one-stage reaction with a steady and high rate as can be seen on **Figure 4.11** on page 76. The increase of temperature from 950 to 1050 °C led to a clear rate increase.

The extent of reduction curves were satisfactorily modeled using the extended grain model. The external mass transfer was used to account for the depletion of the process gas and kept constant at all temperatures. The parameters used indicate that the reaction is controlled partially chemically but also by the access to the process gas, this second term being increasingly determining at higher temperatures.

Based on the modeling, the chemical reaction was isolated and the activation energy calculated to range between 78.4 and 79.3 kJ/mol. Because chromium and iron were reacted simultaneously, the activation energy corresponds to the reaction given in **Equation 6.1**. The activation energy mentioned is significantly lower than the values obtained by Qayyum and coworkers [43]. The two-stage reaction they observed led to values of 198 and 280 kJ/mol for the first and second step respectively. The differences in terms of the experimental set-up, inducing different reactions, can be invoked again as the cause of these discrepancies. The large contrast in activation energies, as well as the absence of a break in the curve as observed by Qayyum *et al.* are additional elements to distinguish the reactions studied in the two works.

6.2.3 Mechanism

At the start of the reaction, nuclei of the carbide product formed on the $FeCr_2O_4$ spinel grains. However, the nucleation did not have a significant impact on the reaction due to the high driving force at the temperatures of the study. Overall the material reacted in a shrinking core fashion at the grain scale. The product $(Cr, Fe)_7C_3$ was found to be porous, and was likely not a diffusion barrier for the progress of the reaction. In addition, the general shape of the grains seem to have been conserved during the carburization.

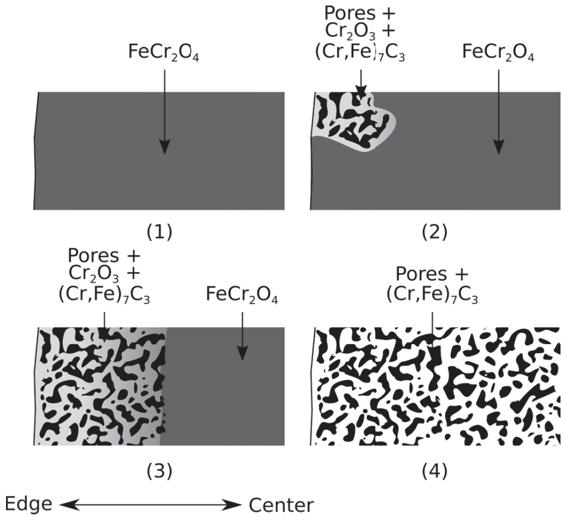

Figure 6.2: Schematic illustrations of the reduction-carburization process for a $FeCr_2O_4$ grain

In **Figure 6.2**, a description of the reaction mechanism is proposed. In the first sketch (1), the material is in its original form and remains stable until the reaction starts. The reaction starts on favorable sites where the spinel is reacted to a mixture of Cr_2O_3 and $(Cr, Fe)_7C_3$, accompanied with a large amount of pores. However, the large driving force causes the reaction to easily spread on the grain surface. The reaction further progresses from the grain edge as in (3) forming a clear reaction front; the spinel core is left unchanged. The reaction continues until all the material is transformed to porous $(Cr, Fe)_7C_3$ as in (4).

6.3 $(Fe, Mg)Cr_2O_4$ reduction-carburization

The reduction-carburization of $(Fe, Mg)Cr_2O_4$ was characterized by a nucleation and growth phenomenon. The chemical reaction is addressed first, together with the formation of the new carbide phase. The modeling results are used next to discuss the reaction kinetics. Finally a mechanism is proposed to explain the reduction-carburization of $(Fe, Mg)Cr_2O_4$.

6.3.1 Reaction and phases

The reduction-carburization of $(Fe, Mg)Cr_2O_4$ resulted in the formation of $(Cr, Fe)_7C_3$. As for $FeCr_2O_4$ reduction-carburization, an intermediary oxide phase of Cr_2O_3 was also evidenced, and metallic iron was absent during the reaction. The final products of the reaction consisted of a mixture of $(Cr, Fe)_7C_3$ and an Mg-rich spinel phase $(Mg, Fe)Cr_2O_4$. This second phase was found spread in the initial grain and did not gather in a single body showing the little mobility of magnesium during this reaction. In detail, the phases appearing during the reduction-carburization of $(Fe, Mg)Cr_2O_4$ follows the sequence given next:

$$(Fe, Mg)Cr_2O_4$$
$$\downarrow$$
$$(Fe, Mg)Cr_2O_4 + Cr_2O_3 + (Cr, Fe)_7C_3$$
$$\downarrow$$
$$(Mg, Fe)Cr_2O_4 + (Cr, Fe)_7C_3$$

The presence of a Mg-rich unreduced spinel, even after 120 min at 1050 °C, confirms the stabilizing effect of magnesium on the spinel. This is in agreement with the general knowledge in the ferrochrome field [66], and also with the work of Qayyum and coworkers [43]. No exception was found for the reduction-carburization involving methane.

Carbon deposition was small indicating that the phases present, $(Mg, Fe)Cr_2O_4$ and $(Cr, Fe)_7C_3$, act as poor catalysts for methane cracking.

Nucleation and growth of carbides

A shrinking core type of mechanism, as observed for $FeCr_2O_4$ reduction-carburization, was only evidenced in a minority of the grains. Instead, the carbide phases, formed when reacting $(Fe,Mg)Cr_2O_4$, showed unique features. The $(Cr,Fe)_7C_3$ carbides primarily developed in peculiar shapes, such as planes, wedges or following grain boundaries. This could comply with the definition of a topochemical reaction by Boldyrev [67]: the carbide product was formed on favorable nucleation sites, sites that are regenerated during the reaction.

In addition, while the planar carbides appeared to grow in one direction only, the other two morphologies seemed able to grow in large portions of the original spinel, suggesting a different nature. The description of topochemical reactions by Boldyrev could be invoked again to help distinguish these mechanisms [67]. It is therefore suggested that the planar carbides are caused by lattice defects, while the wedges and grain boundary growths are caused by crystallographic features such as a favorable crystal plane.

The lowering of the thermodynamic driving force by adding magnesium to the spinel solid solution could be the origin of the nucleation and growth mechanism observed. By lowering the driving force for the reaction, the favorable sites on the oxide crystal are promoted as they locally increase the driving force. This is analogous to what was suggested by Hayes for the role of surface roughness in the gaseous reduction of oxides at low thermodynamic driving forces [55].

Finally, the simultaneous presence of nucleation and growth mechanisms as defined above, together with shrinking core mechanisms, could be caused by variations of the reducing potential of the gas mixture during the course of the reaction. Because the gas passes through a bed of pellets, the bottom pellets are exposed to a fresh mixture while the top pellets are exposed to an exhausted, CO containing gas. When the bottom pellets are extensively reduced-carburized, the quality of the gas passing through the upper layer increases, enabling less favorable sites to react. It is therefore thought that carbide phases formed by nucleation and growth appear earlier, while the shrinking core features observed witness a later reaction.

6.3.2 Reaction kinetics

The behavior of the reduction-carburization of $(Fe,Mg)Cr_2O_4$ with temperature is to be mentioned. An important increase of the reaction rate, coupled with an increase of the extent of reduction, accompanied the increase in the temperature from 950°C to

1050°C. The presence of magnesium additions, lowering the activity of the $FeCr_2O_4$ in the spinel solid solution is named as the cause for such a slowdown. A temperature increase partially compensates the lowering of $a_{FeCr2O4}$, increasing back the driving force. It is believed than even higher temperatures, provided the carbon deposition remains limited, could lead to a reaction similar to that of $FeCr_2O_4$ with CH_4.

The modeling of the reaction using the extended grain model failed to lead to a satisfactory fit with the measured curves. The nucleation and growth models, however, could grasp the shape of the curves much better. This is verified both for the extended JMAK and the Austin-Rickett models and is attributed to the peculiar mechanism observed.

6.3.3 Mechanism

Figure 6.3 shows the reaction mechanism as found in the present work.

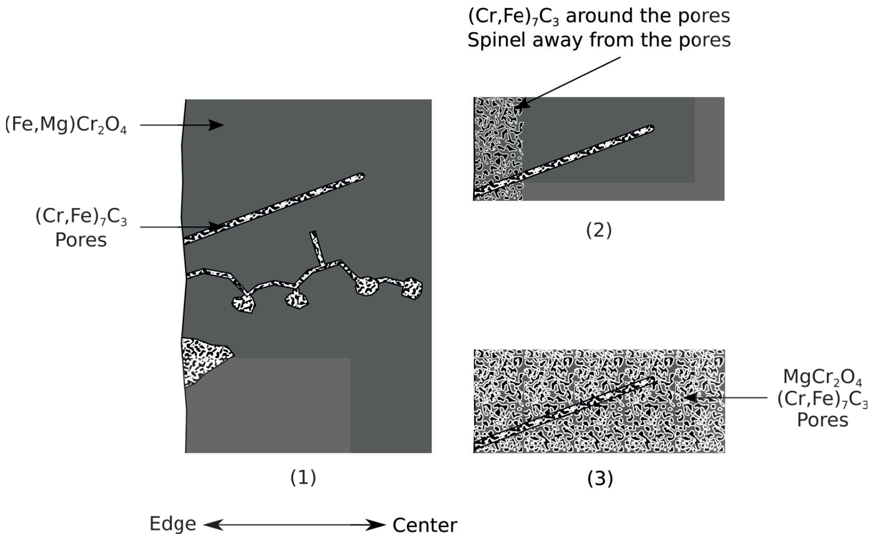

Figure 6.3: Schematic illustrations of the reduction-carburization process for a $(Fe,Mg)Cr_2O_4$ grain

First, the material reacts at favorable sites on the grain's surface (1). These sites led to the formation (from top to bottom) of planar carbides, intergrain growths or wedges. These carbides are further grown thanks to local advantageous thermodynamic conditions. When a richer gas is placed in contact with the spinel, a new mechanism emerges as in (2). Pores are formed together with a $(Cr,Fe)_7C_3$ phase in a shrinking core fashion. A spinel can still be found in two areas: close to the pores where it is enriched in magnesium, or in the grain's core where its composition is mostly unchanged. When the reaction approaches completion, the $(Cr,Fe)_7C_3$ carbide can be found across the whole grain. Planar shaped carbides are still distinguishable from the subsequently formed carbides. A $(Mg,Fe)Cr_2O_4$ spinel phase is also evidenced, spread across the original grain as small fields surrounded by $(Cr,Fe)_7C_3$ carbides.

6.4 $Fe(Cr,Al)_2O_4$ reduction-carburization

The reduction-carburization of $Fe(Cr,Al)_2O_4$ was characterized by exsolution and zoning phenomena, accompanied by extensive carbon deposition. The reaction, including exsolution and zoning, is treated first. The kinetics are discussed in a second part. Finally, a mechanism is proposed.

6.4.1 Reaction and phases

The reduction-carburization of $Fe(Cr,Al)_2O_4$ led to the formation of multiple intermediary phases. The reaction can be separated into two stages. During the first stage the reduction of iron is favored and leads to the formation of a dense layer around the grains. During the second stage, the reduction-carburization progresses in a shrinking core fashion, with the grains exhibiting concentric layers of various phases.

Early reduction and exsolved lamellae

At early stages of the reaction, a dense layer of reduced and/or carburized material was evidenced at the edges of the grains. This layer, rich in iron, was found to consist of a mixture of $(Cr,Fe)_7C_3$ carbides and Fe-Cr alloy. Simultaneously, thin lamellae of a new phase appeared within the $Fe(Cr,Al)_2O_4$ core: these could consist of $(Cr,Al)_2O_3$ or of another spinel composition.

These lamellae could be first interpreted as exsolved $(Cr,Al)_2O_3$ as they resemble the exsolved phases observed in oxidized natural chrome spinels [16], or the Widmanstätten intergrowths found in preoxidized chromite pellets [68]. To explain the exsolution phenomenon, Putnis and Price noted that the spinel structure cannot tolerate non-stoichiometry. An analogous explanation in the present case is that the early reduction of iron has caused such a non-stoichiometry. While the spinel structure was made unstable by oxidation in the case of Putnis and Price, it is here due to the reduction of the divalent iron cations. The lack of iron induced non-stoichiometry and instability in the spinel, later compensated by exsolution of $(Cr,Al)_2O_3$ lamellae restoring the stoichiometry in the spinel.

If the lamellae are indeed of a $(Cr,Al)_2O_3$ nature and not formed upon cooling, it is of interest to determine if the spinel and the sesquioxide solid solutions are at equilibrium using the model proposed by Jacob and Behera [25]. One must first note that the measurements were not ideally positioned and can be somewhat unreliable given the small size of the lamellae. From the position of the spinel composition on the $(Fe_{1-X},Mg_X)(Cr_{1-Y},Al_Y)_2O_4$ plane, the values of Y can be determined by EDS. Using the data from **Table 4.39** on page 113 of a sample reacted at 1223 K, the values of Y in the spinel present in point 4 and 7 are found to be 0.12 and 0.13 respectively. If the former spinel is in equilibrium with a $(Al_Z,Cr_{1-Z})_2O_3$ phase then Z=0.27, while Z=0.34 for the latter. The $\frac{\text{Al}}{\text{Cr+Al}}$ values from the EDS point analysis of the lamellae, which are our best estimation of their Z value, are found to be 0.27 and 0.38 in points 1 and 2 respectively. These values, which are in fairly good agreement with the calculated ones, could indicate that the two phases are close to equilibrium.

Alternatively, these lamellae could be a spinel phase, witnessing a miscibility gap in the solid solution upon cooling. The features found recall the Al-rich lamellae observed in Fe-rich hosts in the study of Loferski and Lipin on Red Lodge chromites [69]. The resemblance is mostly visual, as these natural chromite are significantly different in terms of composition. In the present work, the lamellae are not observed on the spinel samples after synthesis therefore the reduction must have played a role. In addition, given their low iron content, their formation likely relies on the reduction of Cr^{3+} to Cr^{2+} to fulfill the stoichiometry of the spinel.

Further reduction and zoning

Further reduction-carburization of the sample gave rise to new features. A zoning phenomenon was observed: around the inner spinel core, still striped by lamellae, an outer core was formed. The outer core is interpreted as a $(Cr,Al)_2O_3$ oxide as this phase was detected by XRD in partially reduced samples. The contrasting oxygen concentration shown in the elemental mappings of **Figure 6.4** also supports this view: the inner and outer core likely have a different metal to oxygen ratio. This phase was accompanied by the formation of cracks in which metallic iron accumulated in some occurrences.

Such a zoning phenomenon was discussed by Soykan and coworkers during the carbothermic reduction of natural ores from the Bushveld complex [70], although the outer layer they evidenced was also of a spinel nature. The depletion of iron from the outer layer observed in their work is alike what was found in the $(Cr,Al)_2O_3$ phase here.

Using the same thermodynamic model as before and the values from **Table 4.40** on page 115, the measured and calculated Z values are compared at the spinel/corundum

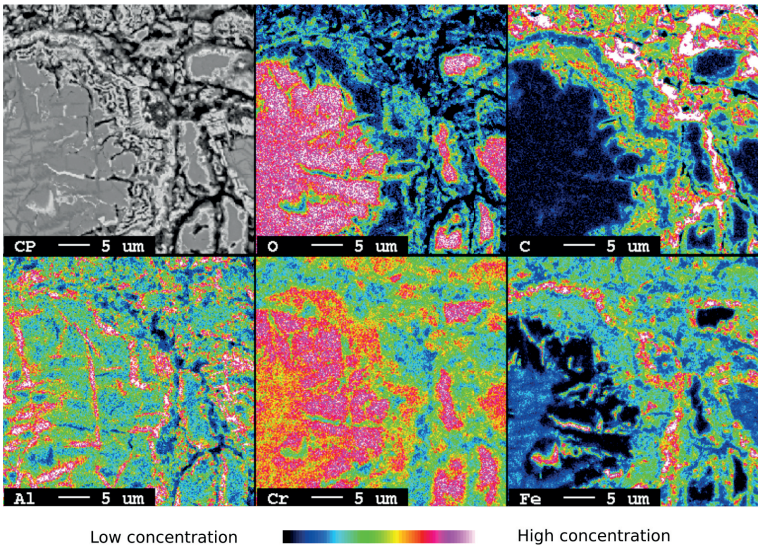

Figure 6.4: Elemental mapping of CT3.030

interface in sample CT2.030 at 1273 K. The two interfaces spinel/corundum considered correspond to the phase change between points 4/3 and 5/6 on **Figure 4.37** on page 113. For the the 4/3 interface, the Z values in the corundum calculated with the model is $Z_{calc.}$=0.14, while $Z_{meas.}$=0.22. For the 5/6 interface, $Z_{calc.}$=0.20 while $Z_{meas.}$=0.17. Although these values are of the same order of magnitude, the trends are opposite and not easy to interpret. The distance between the two EDS measurements can also be the cause of such gap between expected and measured Z values.

After extensive reduction on the sample, the information available was only partial as carbon deposited extensively. The phases present during reduction carburization of $Fe(Cr,Al)_2O_4$ can be written as follows:

$$\begin{gathered}
\mathrm{Fe(Cr,Al)_2O_4} \\
\downarrow \\
\mathrm{Fe(Cr,Al)_2O_4} + \text{Exsolved lamellae} + \mathrm{(Cr,Fe)_7C_3} + \text{Fe-Cr Alloy} \\
\downarrow \\
\mathrm{Fe(Cr,Al)_2O_4} + \text{Exsolved lamellae} + \mathrm{(Cr,Al)_2O_3}_{\text{ shell}} \\
+ \mathrm{(Cr,Fe)_7C_3} + \text{Fe-Cr Alloy} + \mathrm{C_{deposited}} \\
\downarrow \\
\mathrm{(Cr,Fe)_7C_3} + \mathrm{(Cr,Al)_2O_3} + \text{Fe-Cr Alloy} + \mathrm{C_{deposited}}
\end{gathered}$$

where the exsolved lamellae are $(Cr,Al)_2O_3$ or $(Fe,Cr)(Cr,Al)_2O_4$ oxides. This description implicitly considers that the lamellae formed at high temperature. The carbon deposition is explicitly noted as $C_{deposited}$ as the amounts of carbon observed were extensive.

6.4.2 Reaction kinetics

The rate of the $Fe(Cr,Al)_2O_4$ reduction-carburization was found to increase dramatically by increasing the temperature from 950 to 1000 °C, and was also accompanied by an increase of the extent of reduction. However the rates of the reaction at 1000 and 1050 °C were very close.

The extended grain model was successfully used to model the reaction and evidenced a mixed chemical and diffusion control of the reaction. The diffusion term of the model is predominant at 950 °C, but is diminished with increasing temperature.

6.4.3 Mechanism

Overall, the reaction follows a shrinking core mechanism at the grain scale. Multiple shells are observed which are likely to induce a substantial diffusion limitation. **Figure 6.5** depicts the chemical reactions and structural changes as observed in the material.

Firstly as in (1), a dense Fe-rich layer, metallic or carbidic is formed. Exsolution of sesquioxide or spinel was also observed on the cooled samples, likely due to the preferential reduction of iron at the start. Further reaction leads to the thickening of the shell of reduced materials. A zoning phenomenon is observed and a outer shell of $(Cr,Al)_2O_3$ is found around the Al-depleted spinel core. Iron accumulated in newly formed cracks. After reduction, as in (3), the whole grain is drowned into carbon. $(Cr,Al)_2O_3$ rimmed by $(Cr,Fe)_7C_3$ are found in the core, and the original iron rich edge is still noticeable.

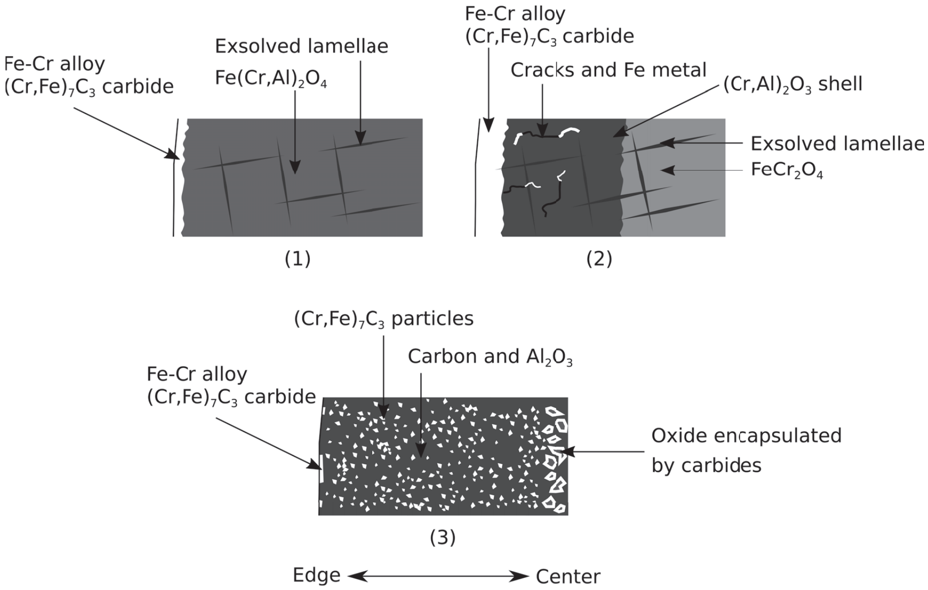

Figure 6.5: Schematic illustrations of the reduction-carburization process for a Fe(Cr, Al)$_2$O$_4$ grain

6.5 (Fe, Mg)(Cr, Al)$_2$O$_4$ reduction-carburization

The reduction-carburization of (Fe, Mg)(Cr, Al)$_2$O$_4$ was characterized by an exsolution phenomenon and the formation of a Mg-rich core, accompanied by extensive carbon deposition. The early reaction is addressed first, followed by a study of the reaction interface aspect. Finally the reaction kinetics and modeling are reviewed and a mechanism is proposed.

6.5.1 Reaction and phases

The reduction-carburization of (Fe, Mg)(Cr, Al)$_2$O$_4$, in many aspects, resembles that of Fe(Cr, Al)$_2$O$_4$ with two stages: the formation of a dense layer at the start, and the further progress of the reaction within the material. During this second step, however, magnesium migrated inwards and iron outwards, forming a single Mg(Cr, Al)$_2$O$_4$ core.

Early reduction and exsolved lamellae

At early stages of the reaction, a dense layer of(Cr, Fe)$_7$C$_3$ carbides and Fe-Cr alloy was evidenced at the edges of the grains. The low amounts of aluminium and oxygen found by EDS could indicate the presence of (Cr, Al)$_2$O$_3$ although this phase could not be detected by XRD techniques.

In the spinel, exsolved lamellae were also evidenced. The EDS point analyses indicated that such lamellae exhibit a low content of iron and magnesium, and a high content of chromium and aluminium. Similarly to what was discussed before for the $Fe(Cr, Al)_2O_4$ samples, these can be interpreted either as $(Cr, Al)_2O_3$ or as spinel exsolution.

In the former situation, calculation can be attempted using the model from Jacob and Behera [25] for spinel with a composition on the $(Fe_{1-X}, Mg_X)(Cr_{1-Y}, Al_Y)_2O_4$ plane. Of course the same limitations, especially the lack of reliability of the EDS measurements, are to keep in mind. Using the data of **Table 4.53** on page 131 for the DT1.030 sample, X=0.31 and Y=0.14 on point 1. If such spinel is at equilibrium with an $(Al_Z, Cr_{1-Z})_2O_3$ phase, the Z value is calculated to be Z=0.23. This calculated value contrasts with the measured values on points 2 and 3, of Z=0.34 and Z=0.39 respectively. According to the model, if the phase formed is a $(Cr, Al)_2O_3$ oxide obtained at 1223 K, the equilibrium was not reached.

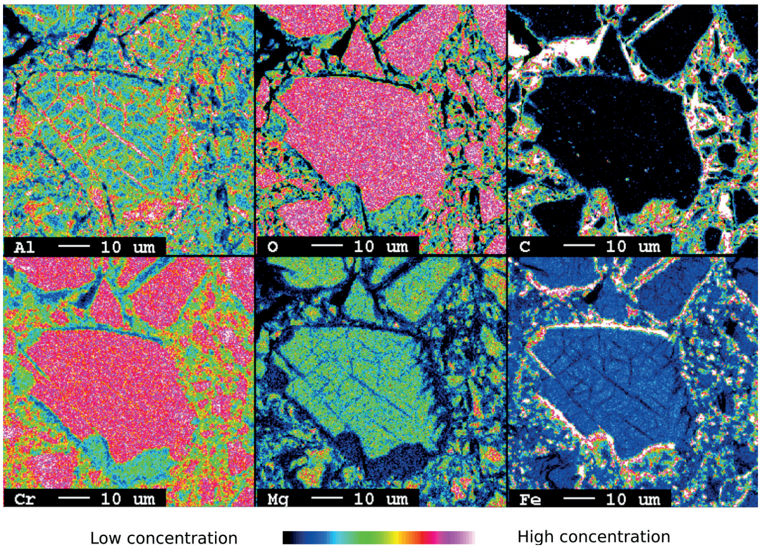

Figure 6.6: Elemental mapping of DT3.030 on a slightly reduced grain

The lamellae could also be witnessing a miscibility gap in the solid solution upon cooling as for the $Fe(Cr, Al)_2O_4$ samples. The possibility that the lamellae are in fact spinels could be backed up by the impossibility to observe variations in the oxygen content in the core using elemental mapping, as on **Figure 6.6**.

The reaction interface

The reaction interface in the reduction-carburization of $(Fe, Mg)(Cr, Al)_2O_4$ is worth an examination. On **Figure 6.7**, a close up of the reaction interface from **Figure 4.47** on page 132 is given (a), together with a schematic representation (b). A simplified scheme is also added (c). It appears that the contact between the spinel and the product phase is ensured by a third party phase in which iron and chromium possibly transit. Also, the presence of pores at the contact with the three phases could indicate that the reaction gas is acting directly on the spinel.

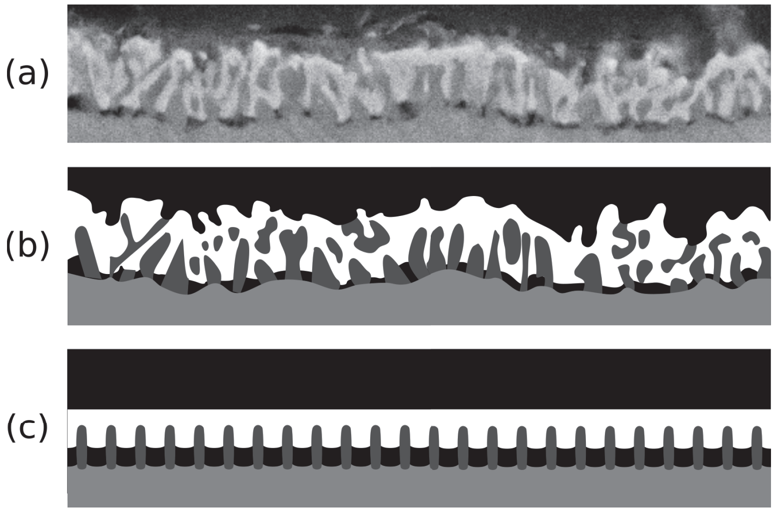

Figure 6.7: Reaction interface and two schematic representations. Black = pores or void, white = carbide, light gray = parent spinel, dark gray = intermediary oxide.

Such construction resembles the coupled growth of pore and metal, as thought by Hayes [55], with the addition of an intermediary oxide. The coupled growth is considered by Hayes as an advantageous mechanism and leads to a high reaction rate. Maintaining such a mechanism could be critical in ensuring a fast conversion to carbides.

Further reduction and Mg-rich core

Further reaction of the $(Fe, Mg)(Cr, Al)_2O_4$ spinel is marked by an increasing concentration of magnesium in the unreduced spinel core. Starting from a theoretical content of about 25% of the divalent cation, the content of magnesium in the core progressively increased up to full replacement of the divalent iron atoms. This could indicate an outward diffusion of Fe^{2+} iron accompanied by an inward diffusion of Mg^{2+} via Frenkel defects in a similar fashion to what was suggested by Perry and coworkers [71]. The spinel core formed did not exhibit an increased concentration of aluminium. Instead, the Al:Cr ratio was found alike that of the original spinel. Finally, longer reduction-carburization led to extensive methane cracking and carbon deposition as for the $\mathrm{Fe(Cr,Al)_2O_4}$ samples.

The phases present during reduction carburization of $\mathrm{(Fe,Mg)(Cr,Al)_2O_4}$ can be written as follows:

$$\begin{gathered}\mathrm{(Fe,Mg)(Cr,Al)_2O_4}\\ \downarrow\\ \mathrm{(Fe,Mg)(Cr,Al)_2O_4} + \text{Exsolved lamellae} + \mathrm{(Cr,Fe)_7C_3} + \text{Fe-Cr Alloy}\\ \downarrow\\ \mathrm{Mg(Cr,Al)_2O_4} + \mathrm{(Cr,Fe)_7C_3} + \text{Fe-Cr Alloy} + \mathrm{C_{deposited}}\end{gathered}$$

where the exsolved lamellae are $\mathrm{(Cr,Al)_2O_3}$ or $\mathrm{(Fe,Mg,Cr)(Cr,Al)_2O_4}$ oxides. Again, this description implicitly considers that the lamellae formed at high temperature. Some $\mathrm{(Cr,Al)_2O_3}$ is also assumed to exist within the product fields.

6.5.2 Reaction kinetics

The rate of reduction for the $\mathrm{(Fe,Mg)(Cr,Al)_2O_4}$ sample increased significantly with increasing the temperatures from 950 to 1050 °C, while the extent of reduction only increased from 950 to 1000 °C.

The extended grain model was successfully used to model the reaction and evidenced a mixed chemical and diffusion control of the reaction. The diffusion term of the model is predominant at 950 °C, but is weakened when increasing the temperature. However, the best fit at 1050 °C involved a relative increase of the diffusion parameter, compared to the modeling of the reaction at 1000 °C.

6.5.3 Mechanism

Schematically, the reaction mechanism observed is represented in **Figure 6.8**.

First, in (1), early reduction leads to the formation of a Fe-rich layer. Exsolved lamellae are observed on the cooled down samples. Further reduction represented in (2) leads to the formation of $\mathrm{(Cr,Fe)_7C_3}$. Some aluminium can be detected in this product layer, likely as a $\mathrm{(Cr,Al)_2O_3}$ oxide, but magnesium migrates to the spinel core and progressively replaces iron in the tetrahedral sites. After full reduction, as in (3), artifacts of the previous phases are observed together with carbon stemming from the decompo-

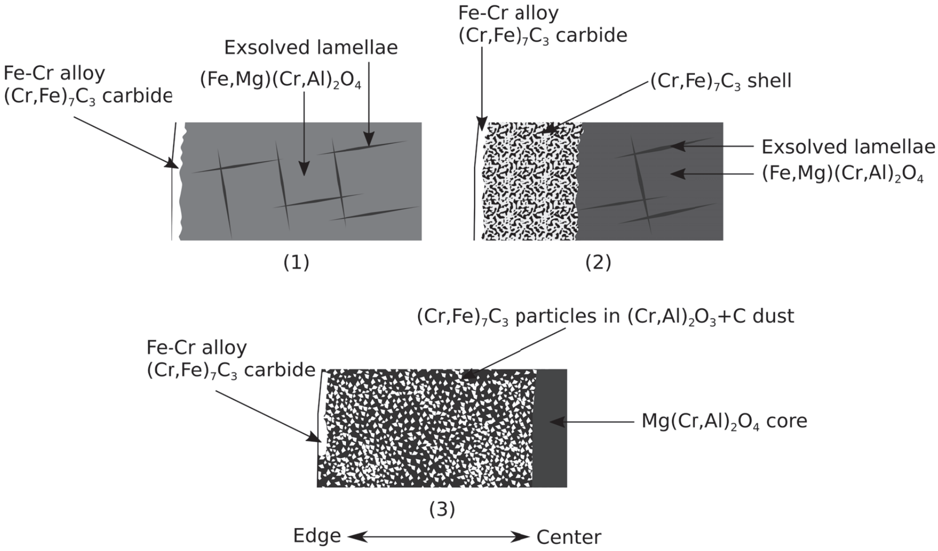

Figure 6.8: Schematic illustrations of the reduction-carburization process for a $(Fe,Mg)(Cr,Al)_2O_4$ grain

sition of methane. Iron has completely disappeared from the spinel core together with the lamellae, while the Cr:Al ratio seems unchanged.

6.6 Direct measurements, calculations and possible error sources

The extent of reduction calculation could be considered as the vulnerable element of the analysis as the values used are a compromise between two methods. With a better knowledge of the reaction, these values can be reassessed.

Concerning the reduction-carburization of $FeCr_2O_4$, one can assume that carbon deposition was absent, and that the reaction followed **Equation 6.1** on page 163. The predicted values for the different extents of reduction, from O-LECO oxygen analysis, integrated CO and the reconciled method are provided in **Table 6.1**:

Although the results are fairly close to the measurements using the third method (O-LECO+CO), it appears that the integrated CO based extents of reduction give better estimations for the 30 min experiments. However, for long durations, the estimations remain erroneous as they would imply the removal of more oxygen than present in the oxide. The difference between the mass measured and predicted by O-LECO or

Table 6.1: Sample mass measured and predicted based on the extent of reduction from various methods for the A-series

Experiment	Mass measured [g]	Mass predicted (O-LECO) [g]	Mass predicted (CO) [g]	Mass predicted (O-LECO+CO) [g]
AT1.030	4.40	4.46	4.37	4.47
AT2.030	4.28	4.39	4.25	4.37
AT3.030	4.08	4.20	4.05	4.20
AT1.120	4.01	3.99	3.81	3.99
AT2.104	3.97	3.98	3.79	3.98
AT3.120	3.93	3.95	3.77	3.96

O-LECO+CO could be caused either by the underestimation of the extent of reduction or the overestimation of the carburization degree. The use of two references, one for the long experiments and one for the 30 min ones could potentially improve the prediction of the mass at the end of the experiment. But independently of the method employed, carbon deposition must have been insignificant.

6.7 Influence of the impurities

The addition of iron in the oxide, giving a pure iron chromite spinel $FeCr_2O_4$, was not detrimental to the reduction-carburization. The effectiveness of CH_4 for the reduction-carburization of Cr_2O_3, observed by many authors, was advantageously transposed to the conversion of $FeCr_2O_4$ to carbides. The formation of a combined carbide $(Cr, Fe)_7C_3$ permitted high rates throughout the reaction. Presenting no diffusion resistance due to its porous nature, $(Cr, Fe)_7C_3$ also preserved the reducing power of the gas mixture by not catalyzing cracking.

When magnesium was introduced in the spinel solid solution, giving $(Fe, Mg)Cr_2O_4$, the driving force for the reaction was reduced due to a decrease of the activity of iron chromite $a_{FeCr2O4}$ in the solid solution. This led to an increased role of the nucleation sites during the reaction and the emergence of unique carbide growths. A temperature increase was found very impactful, compensating for the aforementioned low driving force but ultimately could not allow the reduction of chromium oxides in magnesiochromites $MgCr_2O_4$. The presence of magnesium did not lead to extensive carbon deposition.

The addition of aluminium in the solid solution, giving $Fe(Cr, Al)_2O_4$, dramatically changed the reaction mechanism. The reduction of iron was promoted at early stages, leading to the formation of a dense layer. Further conversion was inhibited by the compact product phase, zoning and/or extensive carbon deposition. Methane cracking was promoted with the additions of aluminium because of a catalytic effect either from aluminium itself in a $(Cr,Al)_2O_3$ phase or from the Fe-Cr alloy.

The simultaneous presence of both magnesium and aluminium within the spinel solution in $(Fe,Mg)(Cr,Al)_2O_4$ is overall comparable to the sole presence of aluminium in $Fe(Cr,Al)_2O_4$. The reduction of iron was promoted in the same way during the first stage, leading to a dense product layer likely to inhibit the gas diffusion. Methane cracking was also favored similarly to the $Fe(Cr,Al)_2O_4$ sample; in other words magnesium did not have a noticeable effect in either direction. In terms of reaction rate, it appears that in the presence of aluminium, magnesium did not have the retarding effect observed in the reduction-carburization of $(Fe,Mg)Cr_2O_4$.

Chapter 7

Conclusion

Pure iron chromite and chromite solid solutions containing Mg and Al impurities were successfully synthesized by the induction skull melting technique. These spinels were subsequently reduced and carburized to various extents by an Ar-CH_4-H_2 gas mixture between 950 and 1050 °C. The reaction led to the formation of $(Cr, Fe)_7C_3$ as the main product phase. Each of the four compositions studied, $FeCr_2O_4$, $(Fe, Mg)Cr_2O_4$, $Fe(Cr, Al)_2O_4$ and $(Fe, Mg)(Cr, Al)_2O_4$ had its own reaction mechanism although the two former and the two latter constitute different groups. This distinction is imputed to the presence and role of aluminium.

The synthesis technique used was pertinent for the targeted compositions. The raw material positioning was decisive to ensure a good synthesis. Metallic iron, placed on the top of the charge, was necessary for a successful melting of the raw materials. In addition, excess of iron was beneficial to avoid the sintering of a crust while having a limited impact on the composition. Once appropriate synthesis parameters were determined, the induction skull melting technique was satisfactory, associating speed, reliability and high production capacity. After synthesis and pelletizing, the hardening in argon gave an acceptable strength to the pellets without altering their composition.

The pure iron chromite ($FeCr_2O_4$) was readily converted to porous $(Cr, Fe)_7C_3$ carbides by Ar-CH_4-H_2 gas mixtures following the reaction given in **Equation 7.1**:

$$FeCr_2O_4 + \frac{37}{7}CH_4 \rightarrow \frac{3}{7}(Cr, Fe)_7C_3 + 4CO + \frac{74}{7}H_2 \tag{7.1}$$

With this sample composition, high rates and extents of reduction were achieved. A temperature increase led to a rise in the reaction rate, but did not improve the extent of reduction significantly. No carbon deposition accompanied the reaction as the phases present were poor catalysts for methane cracking.

In the spinel grains, the reaction followed a shrinking core mechanism where iron oxides reduced simultaneously but faster than chromium oxides. This led to a gradient in the Fe:Cr ratio in the carbide phase. Although some Cr_2O_3 can be evidenced early, it is ultimately converted into carbides.

The modeling by the extended grain model revealed that the reaction was controlled chemically and by the supply of reductants. The activation energy for the reaction in **Equation 7.1** was found to range between 78.4 and 79.3 kJ/mol.

The magnesium containing spinel ($(Fe, Mg)Cr_2O_4$) was the most challenging sample to react with Ar-CH_4-H_2 gas mixtures due to an important decrease of the driving force. Although the product phase still consisted of porous $(Cr, Fe)_7C_3$, unreduced $(Mg, Fe)Cr_2O_4$ phases remained. The decrease of the driving force resulted in lower extents of reduction, lower reaction rates and a high temperature dependence for the experiments; a temperature increase partially compensated for the presence of magnesium. Carbon deposition, nearly absent with this second material, was not affected by the presence of magnesium in the spinel.

The reaction mechanism was visibly impacted as nucleation and growth phenomena gained in importance. The carbides formed first in favorable sites and grew in an autocatalytic fashion. As a result, carbides of various shapes, such as planes or wedges, were observed. Because the driving force increased locally during the experiment, a shrinking core mechanism could also be observed.

The modeling by the extended grain model was not convincing. However, nucleation and growth-based models achieved better results, especially when using the Austin-Rickett equation.

The aluminium additions to the spinel ($Fe(Cr, Al)_2O_4$) had a much lower impeding effect than magnesium in terms of rate and extent. However, the reaction gained in complexity as additional intermediary phases and products appeared.

The reaction mechanism followed a shrinking core at the grain scale. At the beginning of the reaction, a dense iron rich layer formed at the grains' edge. Iron discrepancy caused an exsolution of an aluminium rich phase in the spinel, either during or after the experiment. Upon further reduction, $(Cr, Fe)_7C_3$ was formed as a product, while zoning appeared in the oxide core due to depletion in iron. A temperature increase from 950 to 1000 °C dramatically enhanced the reaction rate and extent, while no significant change was observed between 1000 and 1050 °C. Extensive methane cracking was observed, causing an important deposition of carbon at all temperatures.

The extended grain model successfully fitted the extent of reduction curves. It revealed the importance of the diffusion at low temperatures.

When aluminium and magnesium were present together in $(Fe, Mg)(Cr, Al)_2O_4$, the rate and extents of reduction where close to those for the reaction of $Fe(Cr, Al)_2O_4$. However, magnesium stabilized the unreduced phases in a $Mg(Cr, Al)_2O_4$ spinel.

The reaction followed a shrinking core, forming a dense iron-rich layer first. Because of the early extraction of iron, exsolution of an aluminium rich phase was observed on the cooled samples. Further reduction led to the formation of a $(Cr, Fe)_7C_3$ layer, but zoning was not observed. Instead, magnesium diffused in the unreduced core replacing iron in the spinel solid solution, resulting in a $Mg(Cr, Al)_2O_4$ core. A temperature increase from 950 to 1000 °C enhanced the rate and extent of reduction. With further increase from 1000 to 1050 °C, only the rate was increased. Extensive methane cracking and carbon deposition were observed at all temperatures for this material.

The extended grain model fitted satisfactorily the measured curves, the mechanism being mixed controlled by chemical reaction and diffusion. The diffusion was most impactful at 950 °C.

Overall, this work is promising for the use of hydrocarbon gases for chromite reduction. Not only was the reduction-carburization possible, but higher extents were obtained at lower temperatures when compared to carbothermic reactions. In addition, the impeding effect induced by the presence of magnesium in the solid solution was diminished by the simultaneous presence of aluminium. Since both are found in natural spinels, the selection of an ore with a suitable composition will be essential.

Chapter 8

Future Work

The study of chromite reduction-carburization by hydrocarbon gases could be continued in many directions. In that regard, the work carried out for this thesis is an unfolding of the possibilities of the reduction-carburization of chromite by gas mixtures.

New synthetic chromite compositions could be investigated. Further approaching natural ores' chemistry, especially with additional amounts of magnesium or trivalent iron in the spinel, could be a worthy challenge. Comparison between natural ones and synthetic ones of a close composition could validate further the method. The present work has focused on four compositions only, but numerous possibilities remain to understand better the effects of impurities.

New gas mixtures could also be experimented. Although natural gas is available in Norway, where the present work was conducted, it remains a non-renewable resource. Gas mixtures based on carbon neutral processes could be an attractive route for further research. On a scientific and process point of view, H_2S additions to the gas mixtures could lead to interesting results. Indeed, it was shown by studies in the corrosion field that H_2S can favor the formation of carbides while stopping carbon deposition, however at the expense of the reaction rate.

A wide range of experimental conditions could be further investigated. The effect of temperature on the reaction could be studied in a broader range, with a higher resolution. The pellet size and properties, such as porosity and grain size distribution, could also be varied and investigated. Other apparatuses, such as fluidized beds, could also be considered.

Developments outside of the metallurgy field could be considered. Further study of the reduction-carburization reactions on synthetic chromites could be carried out with the viewpoint of the corrosion field. Alternatively, the $(Cr, Fe)_7C_3$ carbides produced from the carburization of $FeCr_2O_4$ by CH_4 could be studied separately for their properties and applications.

Finally, this work is a step forward for the use of hydrocarbon gases as reductants for the ferrochrome field. Additional work is still necessary, and further research will hopefully arouse the interest of the industry. **The industrial development, maybe more reliant on audacity than science, will then remain as the ultimate and most decisive challenge.**

Bibliography

[1] J.F. Papp and B.R. Lupin. Chromium. Technical report, USGS, 2001.

[2] P.D. Malhotra and G.H.S.V. Prasado. On the Composition of Some Indian Chromites. *American Mineralogist*, 41:460–473, 1956.

[3] U.S. Geological Survey. Mineral commodity summaries 2017. Technical report, 2017.

[4] J. Basson and J. Daavittila. Chapter 9 - High Carbon Ferrochrome Technology. In M. Gasik, editor, *Handbook of Ferroalloys*, pages 317–363. Butterworth-Heinemann, 2013.

[5] R.T. Jones, Q.G. Reynolds, T.R. Curr, and D. Sagger. Some myths about DC arc furnaces. In *Southern African Pyrometallurgy 2011*, pages 15–32, 2011.

[6] D.D. Slatter. Technological Trends in Chromium Unit Production and Supply. In *Infacon VII*, pages 249–262, 1995.

[7] R.H. Eric. Production of Ferroalloys. In *Treatise on Process Metallurgy*, pages 477–532. Elsevier, 2014.

[8] T. Hamada, Y. Takada, H. Katayama, T. Inatani, K. Igawa, S. Takeuchi, and T. Fukutake. Development of a new smelting reduction process for the production of ferroalloys. In *Fifth International Iron and Steel Congress*, pages 19–25, 1986.

[9] O. Naiker. The Development and Advantages of Xstrata's Premus Process. In *Infacon XI: Innovation in Ferroalloy Industry*, pages 112–119, 2007.

[10] S. McCullough, S. Hockaday, C. Johnson, and N.A. Barcza. Pre-reduction and Smelting Characteristics of Kazakhstan Ore Samples. In *Infacon XII: Sustainable Future*, pages 249–262, 2010.

[11] L.R. Nelson. *Evolution of the Mega-Scale in Ferro-Alloy Electric Furnace Smelting*, pages 39–68. Springer International Publishing, Cham, 2014.

[12] Eskom. Historical average price and increase, 2017.

[13] W.A. Deer, J. Howie, and J. Zussman. *An Introduction to Rock Forming Minerals*. Longman, 2nd edition, 1966.

[14] R.E. Stevens. Composition of some Chromites of the Western Hemisphere. *The American Mineralogist*, 29:1–34, 1944.

[15] A. Muan. Phase relations in chromium oxide-containing systems at elevated temperatures. *Geochimica et Cosmochimica Acta*, 39(6-7):781–802, 1975.

[16] A. Putnis and G.D. Price. The nature and significance of exsolved phases in some chrome spinels from the Rhum layered intrusion. *Mineralogical Magazine*, 43:519–526, 1979.

[17] V.D. Tathavakar, M.P. Antony, and A. Jha. The physical chemistry of thermal decomposition of South African chromite minerals. *Metallurgical and Materials Transactions B*, 36(1):75–84, 2005.

[18] M. Allibert, H. Gaye, J. Geisler, D. Janke, B.J. Keene, D. Kirner, M. Kowalski, J. Lehmann, K.C. Mills, D Neuschutz, R Parra, C Saint Jours, P J Spencer, M Susa, M Tmar, and E Woermann. *Slag atlas*. Verlag Stahleisen GmbH, 1995.

[19] A.M. Alper, R.N. McNally, R.C. Doman, and F.G. Keihn. Phase Equilibria in the System MgO-$MgCr_2O_4$. *Journal of the American Ceramic Society*, 47(1):30–33, 1964.

[20] F.Y. Galakhov. Alumina regions of ternary aluminosilicate systems communication 1. The systems FeO-Al_2O_3-SiO_2 and MnO-Al_2O_3-SiO_2. *Bulletin of the Academy of Sciences of the USSR Division of Chemical Science*, 6(5):539–545, 1957.

[21] G.A. Rankin and H.E. Merwin. The Ternary System CaO-Al_2O_3-MgO. *Journal of the American Chemical Society*, 38(3):568–588, 1916.

[22] A.M. Alper, R.N. McNally, P.H. Ribbe, and R.C. Doman. The System MgO-$MgAl_2O_4$. *Journal of the American Ceramic Society*, 45(6):263–268, 1962.

[23] A. Muan and S. Somiya. Phase Relations in the System Iron Oxide-Cr_2O_3 in Air. *Journal of the American Ceramic Society*, 43(4):204–209, 1960.

[24] A. Muan and C.L. Gee. Phase Equilibrium Studies in the System Iron Oxide Al_2O_3 in Air and at 1 Atm. O_2 Pressure. *Journal of the American Ceramic Society*, 39(6):207–214, 1956.

[25] K.T. Jacob and C.K. Behera. Equilibria involving the reciprocal spinel solid solution $(Mg_xFe_{1-x})(Al_yCr_{1-y})_2O_4$: modeling and experiment. *Metallurgical and Materials Transactions B*, 31(6):1247–1259, 2000.

[26] K.T. Jacob and C.K. Behera. Spinel-corundum equilibria and activities in the system MgO-Al_2O_3-Cr_2O_3 at 1473 K. *Metallurgical and Materials Transactions B*, 31(6):1323–1332, 2000.

[27] T. Mathews and K.T. Jacob. Seebeck coefficient of magnetite: A reinterpretation invoking Jahn-Teller entropy. *Solid State Communications*, 84(10):975–978, 1992.

[28] T. Rosenqvist. Chapter 4 - Melts and Solutions. In McGraw-Hill, editor, *Principles Of Extractive Metallurgy*, pages 66–100. 1983.

[29] K.T. Jacob. Electrochemical Determination of Activities in Cr_2O_3-Al_2O_3 Solid Solution. *Journal of The Electrochemical Society*, 125(2):175–179, 1978.

[30] J.-O. Andersson. A thermodynamic evaluation of the Fe-Cr-C system. *Metallurgical Transactions A*, 19(3):627–636, 1988.

[31] A.V. Khvan, B. Hallstedt, and C. Broeckmann. A thermodynamic evaluation of the Fe–Cr–C system. *CALPHAD: Computer Coupling of Phase Diagrams and Thermochemistry*, 46:24–33, 2014.

[32] P.J. Read, D.A. Reeve, J.H. Walsh, and J.E. Rehder. Reduction of chromites in methane-hydrogen mixtures-chromium sesquioxide. *Canadian Metallurgical Quarterly*, 13(4):587–595, 1974.

[33] C.E. Bamberger and K.B. Alexander. The pseudomorphic conversion of platelets of and Cr_2O_3 into CrN and Cr_3C_2. *Journal of Crystal Growth*, 126:525–529, 1993.

[34] N. Anacleto and O. Ostrovski. Solid-state reduction of chromium oxide by methane-containing gas. *Metallurgical and Materials Transactions B*, 35(4):609–615, 2004.

[35] B. Khoshandam, R.V. Kumar, and E. Jamshidi. Producing chromium carbide using reduction of chromium oxide with methane. *AIChE Journal*, 52(3):1094–1102, 2006.

[36] R. Ebrahimi-Kahrizsangi, H.M. Zadeh, and V. Nemati. Synthesis of chromium carbide by reduction of chromium oxide with methane. *International Journal of Refractory Metals and Hard Materials*, 28(3):412–415, 2010.

[37] H.J. Grabke. Evidence on the surface concentration of carbon on gamma iron from the kinetics of the carburization in CH_4-H_2. *Metallurgical Transactions*, 1(10):2972–2975, 1970.

[38] K. Ohla and H.J. Grabke. On the "coke" growth in carburizing and sulfidizing atmospheres upon High temperature corrosion of iron and nickel base alloys. *Materials and Corrosion/Werkstoffe und Korrosion*, 33(6):341–346, 1982.

[39] T. Xing, X. Cui, W. Chen, and R. Yang. Synthesis of porous chromium carbides by carburization. *Materials Chemistry and Physics*, 128(1):181–186, 2011.

[40] S.-C. Wang, H.-T. Lin, P.K. Nayak, S.-Y. Chang, and J.-L. Huang. Carbothermal reduction process for synthesis of nanosized chromium carbide via metal-organic vapor deposition. *Thin Solid Films*, 518(24):7360–7365, 2010.

[41] H. Li, Y. Zheng, L.W. Benum, M. Oballa, and W. Chen. Carburization behaviour of Mn-Cr-O spinel in high temperature hydrocarbon cracking environment. *Corrosion Science*, 51(10):2336–2341, 2009.

[42] F.S. Boericke. Selective reduction of iron in chromite by methane-hydrogen and similar gas mixtures. Technical report, 1946.

[43] M.A. Qayyum and D.A. Reeve. Reduction of chromites to sponge ferrochromium in methane-hydrogen mixtures. *Canadian Metallurgical Quarterly*, 15(3):193–200, 1976.

[44] J. Zhang and O. Ostrovski. Effect of Sulphur on Iron Carbide Formation and Stability. *ISIJ International*, 41(4):340–344, 2001.

[45] M. De Campos and R.H. Eric. Reduction behaviour of chromite in the presence of a hydrocarbon gas. In *Sohn International Symposium; Advanced Processing of Metals and Materials Volume 1: Thermo and Physicochemical Principles: Non-Ferrous High-Temperature Processing*, pages 613–621, 2006.

[46] M. Leikola. *Solid State Reduction of Chromite with Methane and Hydrogen*. Master's thesis, Aalto University, 2015.

[47] H. Dalaker and P. Tetlie. *Decomposition of Methane During Oxide Reduction with Natural Gas*, pages 537–546. Springer International Publishing, Cham, 2016.

[48] H.J. Grabke. Carburization, carbide formation, metal dusting, coking. *Materiali in tehnologije*, 36(6):297–306, 2002.

[49] S. Hayashi and Y. Iguchi. lron Carbide Synthesis by Reaction of lron Ore with H_2-CH_4 Gas Mixtures Containing Traces of Sulfur. *ISIJ International*, 37(1):345–349, 1997.

[50] A. Schneider and H.J. Grabke. Effect of H_2S on metal dusting of iron. 339(10):793–798, 2003.

[51] A. Khawam and D.R. Flanagan. Basics and Applications of Solid-State Kinetics: A Pharmaceutical Perspective. *Journal of Pharmaceutical Sciences*, 95(3):472–498, 2006.

[52] J. Szekely, J.W. Evans, and H.Y. Sohn. *Gas-solid reactions*. Academic Press, 1976.

[53] M.J. Starink. On the meaning of the impingement parameter in kinetic equations for nucleation and growth reactions. *Journal of Materials Science*, 36(18):4433–4441, 2001.

[54] M.J. Starink. Kinetic equations for diffusion-controlled precipitation reactions. *Journal of Materials Science*, 32(15):4061–4070, 1997.

[55] P.C. Hayes. Stability Criteria for Product Microstructures Formed on Gaseous Reduction of Solid Metal Oxides. *Metallurgical and Materials Transactions B*, 41(1):19–34, 2010.

[56] V.V. Osiko, M.A. Borik, and E.E. Lomonova. *Chapter 14 - Synthesis of Refractory Materials by Skull Melting Technique*, pages 433–477. Springer Berlin Heidelberg, Berlin, Heidelberg, 2010.

[57] R. Aragón, H.R. Harrison, R.H. McCallister, and C.J. Sandberg. Skull melter single crystal growth of magnetite (Fe_3O_4) - ulvospinel (Fe_2TiO_4) solid solution members. *Journal of Crystal Growth*, 61(2):221–228, 1983.

[58] V. Canaguier. *Synthesis of Ilmenite*. Master's thesis, NTNU, Norwegian University of Science and Technology, 2014.

[59] P.H. Kim. *Impurities in Ilmenite: Magnesium*. Master's thesis, NTNU, Norwegian University of Science and Technology, 2015.

[60] S. Norhaug. *Impurities in Ilmenite*. Master's thesis, NTNU, Norwegian University of Science and Technology, 2015.

[61] A. Verdin. *Gas Analysis Instrumentation*. Macmillan, 1973.

[62] J. Epp. X-Ray Diffraction (XRD) Techniques for Materials Characterization. In *Materials Characterization Using Nondestructive Evaluation (NDE) Methods*. 2016.

[63] S. Klemme, H.St.C. O'Neill, W. Schnelle, and E. Gmelin. The heat capacities of $MgCr_2O_4$, $FeCr_2O_4$ and Cr_2O_3 at low temperatures, and derived thermodynamic properties. *American Mineralogist*, 84:1686–1693, 2000.

[64] N.S. Sundar Murti and V. Seshadri. Kinetics of reduction of synthetic chromite with carbon. *Transactions of the Iron and Steel Institute of Japan*, 22(12):925–933, 1982.

[65] X.R. Wu, C. Chen, H.H. Lü, and L.S. Li. Synthesis, structure characterization and magnetic property of $(Mg_{1-y}Fe_y)(Al_{0.4}Cr_xFe_{1.6-x})O_4$ spinel solid solution. In *Material Science and Environmental Engineering: Proceedings of the 3rd Annual 2015 International Conference on Material Science and Environmental Engineering*, pages 109–113, 2015.

[66] I.J. Geldenhuys. Aspects of DC chromite smelting at Mintek - An overview. In *Infacon XIII: Efficient technologies in ferroalloy industry*, pages 31–47, 2013.

[67] V.V. Boldyrev. Topochemistry and topochemical reactions. *Reactivity of Solids*, 8(3-4):231–246, 1990.

[68] J. Pan, C. Yang, and D. Zhu. Solid State Reduction of Preoxidized Chromite-iron Ore Pellets by Coal. *ISIJ International*, 55(4):727–735, 2015.

[69] P.J. Loferski and B.R. Lipin. Exsolution in metamorphosed chromite from the Red Lodge district, Montana. *American Mineralogist*, 68:777–789, 1983.

[70] O. Soykan, R.H. Eric, and R.P. King. Kinetics of the reduction of bushveld complex chromite ore at 1416 °C. *Metallurgical Transactions B*, 22(6):801–810, 1991.

[71] K.P.D. Perry, C.W.P. Finn, and R.P. King. An ionic diffusion mechanism of chromite reduction. *Metallurgical Transactions B*, 19(4):677–684, 1988.

Glossary

Chromite The various definition of chromite are given in the Theory chapter. Throughout the work, the terms chromite and spinel are often used interchangeably to refer to the various compositions of the $(Fe, Mg)(Cr, Al)_2O_4$ solid solution, which has a spinel structure.

Cracking The cracking is the process of decomposition of hydrocarbons. In the present work, the cracking refers to the decomposition of CH_4 to C and H_2, independently of the state of carbon.

Exsolution The exsolution process refers to the separation of a solid solution into two phases upon cooling. In the present work, the exsolve phases refer to the lamellae observed in the reacted samples of $Fe(Cr, Al)_2O_4$ and $(Fe, Mg)(Cr, Al)_2O_4$, although the origin of of the lamellae remains uncertain.

Laterite Laterite is a type of rock rich in iron and aluminium. It is formed by the weathering of various rocks, and can contain chromites when formed from peridotite.

Metastable A metastable state is a locally stable state. In other words, it is stable for small perturbations, but unstable for large ones. In the present work, methane is often said metastable, as it should readily crack given the gas compositions and the temperatures considered, but did not necessarily.

Podiform Podiform deposits refer to irregular pod-shaped cluster of material.

Spinel Although the term spinel refers to the $MgAl_2O_4$ compound, it can also refer to the spinel group $A^{2+}B_2^{3+}O_4^{2-}$. In the present work, it generally refers to the chromite solid solution $(Fe, Mg)(Cr, Al)_2O_4$ which belongs to the spinel group.

Stratiform Stratiform deposits refer to layered deposits. Most of the natural chromite ores mentioned in this work are found in such deposits, as Bushveld, Kemi or Bird River chromites.

Appendix A

Appendix A

A.1 $(Fe_{1-X},Mg_X)(Cr_{1-Y},Al_Y)_2O_4$ solid solution: calculated thermodynamic data

From **Table A.1** to **A.4**, the calculation results from the thermodynamic modeling are given. The three first tables report the calculated activities at 1223, 1273 and 1323 K, while the last one gives the composition of the corundum phase at each of the three temperatures.

Table A.1: Calculated activities in $(Fe_{1-X}, Mg_X)(Cr_{1-Y}, Al_Y)_2O_4$ at 1223 K

	$a_{FeCr_2O_4}$					X					
Y	0	0.1	0.2	0.3	0.4	0.5	0.6	0.7	0.8	0.9	1
0	1	0.8980	0.7929	0.6861	0.5790	0.4729	0.3692	0.2690	0.1734	0.0835	0
0.1	0.7817	0.7108	0.6355	0.5567	0.4757	0.3934	0.3111	0.2296	0.1500	0.0732	0
0.2	0.6410	0.5886	0.5315	0.4704	0.4062	0.3396	0.2715	0.2026	0.1339	0.0661	0
0.3	0.5400	0.5003	0.4560	0.4075	0.3554	0.3002	0.2425	0.1830	0.1223	0.0611	0
0.4	0.4646	0.4341	0.3992	0.3600	0.3169	0.2703	0.2207	0.1683	0.1137	0.0574	0
0.5	0.4042	0.3808	0.3531	0.3213	0.2855	0.2459	0.2027	0.1562	0.1067	0.0545	0
0.6	0.3488	0.3312	0.3098	0.2843	0.2549	0.2216	0.1845	0.1436	0.0991	0.0512	0
0.7	0.2866	0.2743	0.2586	0.2394	0.2166	0.1900	0.1597	0.1256	0.0876	0.0457	0
0.8	0.2028	0.1956	0.1860	0.1736	0.1585	0.1403	0.1191	0.0946	0.0666	0.0351	0
0.9	0.0886	0.0861	0.0825	0.0777	0.0716	0.0640	0.0548	0.0440	0.0313	0.0167	0
1	0	0	0	0	0	0	0	0	0	0	0

	$a_{MgCr_2O_4}$					X					
Y	0	0.1	0.2	0.3	0.4	0.5	0.6	0.7	0.8	0.9	1
0	0	0.0835	0.1734	0.2690	0.3692	0.4729	0.5790	0.6861	0.7929	0.8980	1
0.1	0	0.0564	0.1189	0.1871	0.2602	0.3378	0.4191	0.5031	0.5891	0.6761	0.76294
0.2	0	0.0415	0.0882	0.1400	0.1966	0.2577	0.3230	0.3918	0.4636	0.5378	0.61372
0.3	0	0.0316	0.0677	0.1083	0.1535	0.2031	0.2568	0.3145	0.3758	0.4404	0.50789
0.4	0	0.0247	0.0533	0.0860	0.1228	0.1638	0.2090	0.2582	0.3115	0.3686	0.42935
0.5	0	0.0196	0.0426	0.0692	0.0996	0.1339	0.1722	0.2147	0.2614	0.3122	0.3672
0.6	0	0.0154	0.0338	0.0553	0.0802	0.1088	0.1411	0.1773	0.2178	0.2626	0.31176
0.7	0	0.0116	0.0256	0.0422	0.0617	0.0843	0.1102	0.1397	0.1730	0.2105	0.25227
0.8	0	0.0076	0.0168	0.0278	0.0409	0.0563	0.0742	0.0949	0.1186	0.1456	0.17612
0.9	0	0.0030	0.0068	0.0113	0.0168	0.0233	0.0309	0.0399	0.0503	0.0623	0.07606
1	0	0	0	0	0	0	0	0	0	0	0

	$a_{FeAl_2O_4}$					X					
Y	0	0.1	0.2	0.3	0.4	0.5	0.6	0.7	0.8	0.9	1
0	0	0	0	0	0	0	0	0	0	0	0
0.1	0.0594	0.0476	0.0374	0.0288	0.0216	0.0157	0.0109	0.0071	0.0040	0.0017	0
0.2	0.1952	0.1600	0.1288	0.1016	0.0781	0.0580	0.0412	0.0273	0.0160	0.0070	0
0.3	0.3305	0.2753	0.2253	0.1805	0.1410	0.1065	0.0768	0.0517	0.0308	0.0137	0
0.4	0.4389	0.3705	0.3072	0.2495	0.1976	0.1513	0.1107	0.0756	0.0457	0.0206	0
0.5	0.5211	0.4450	0.3735	0.3071	0.2462	0.1910	0.1416	0.0980	0.0600	0.0274	0
0.6	0.5880	0.5076	0.4308	0.3583	0.2906	0.2282	0.1713	0.1200	0.0744	0.0345	0
0.7	0.6529	0.5695	0.4885	0.4108	0.3370	0.2677	0.2033	0.1442	0.0906	0.0425	0
0.8	0.7306	0.6437	0.5579	0.4741	0.3932	0.3159	0.2428	0.1743	0.1108	0.0527	0
0.9	0.8383	0.7458	0.6530	0.5608	0.4702	0.3820	0.2970	0.2157	0.1389	0.0668	0
1	1	0.8985	0.7947	0.6897	0.5846	0.4803	0.3777	0.2776	0.1809	0.0882	0

	$a_{MgAl_2O_4}$					X					
Y	0	0.1	0.2	0.3	0.4	0.5	0.6	0.7	0.8	0.9	1
0	0	0	0	0	0	0	0	0	0	0	0
0.1	0	0.0114	0.0212	0.0293	0.0358	0.0409	0.0445	0.0469	0.0481	0.0483	0.0477
0.2	0	0.0341	0.0647	0.0915	0.1144	0.1333	0.1483	0.1595	0.1672	0.1716	0.1729
0.3	0	0.0526	0.1012	0.1453	0.1843	0.2181	0.2463	0.2690	0.2862	0.2983	0.3054
0.4	0	0.0637	0.1241	0.1804	0.2317	0.2775	0.3174	0.3511	0.3786	0.3998	0.4150
0.5	0	0.0692	0.1362	0.2001	0.2598	0.3147	0.3641	0.4076	0.4448	0.4756	0.4998
0.6	0	0.0716	0.1423	0.2111	0.2769	0.3389	0.3963	0.4485	0.4950	0.5355	0.5695
0.7	0	0.0731	0.1465	0.2193	0.2905	0.3591	0.4243	0.4854	0.5415	0.5924	0.6374
0.8	0	0.0753	0.1523	0.2300	0.3075	0.3838	0.4580	0.5293	0.5969	0.6601	0.7183
0.9	0	0.0797	0.1625	0.2477	0.3342	0.4211	0.5074	0.5924	0.6751	0.7547	0.8305
1	0	0.0879	0.1807	0.2778	0.3782	0.4811	0.5855	0.6905	0.7952	0.8987	1

Table A.2: Calculated activities in $(Fe_{1-X}, Mg_X)(Cr_{1-Y}, Al_Y)_2O_4$ at 1273 K

	$a_{FeCr_2O_4}$					X					
Y	0	0.1	0.2	0.3	0.4	0.5	0.6	0.7	0.8	0.9	1
0	1	0.8981	0.7932	0.6866	0.5798	0.4739	0.3703	0.2701	0.1744	0.0841	0
0.1	0.7797	0.7091	0.6341	0.5557	0.4751	0.3932	0.3111	0.2298	0.1503	0.0734	0
0.2	0.6368	0.5847	0.5280	0.4675	0.4038	0.3378	0.2702	0.2018	0.1335	0.0660	0
0.3	0.5334	0.4941	0.4503	0.4025	0.3511	0.2966	0.2397	0.1810	0.1211	0.0605	0
0.4	0.4552	0.4253	0.3910	0.3526	0.3105	0.2649	0.2162	0.1650	0.1115	0.0564	0
0.5	0.3920	0.3692	0.3422	0.3114	0.2766	0.2382	0.1964	0.1513	0.1034	0.0528	0
0.6	0.3339	0.3169	0.2962	0.2718	0.2436	0.2118	0.1763	0.1372	0.0947	0.0489	0
0.7	0.2699	0.2582	0.2433	0.2251	0.2036	0.1786	0.1500	0.1179	0.0822	0.0429	0
0.8	0.1873	0.1806	0.1715	0.1601	0.1460	0.1292	0.1096	0.0870	0.0613	0.0323	0
0.9	0.0800	0.0777	0.0744	0.0700	0.0644	0.0575	0.0493	0.0395	0.0281	0.0150	0
1	0	0	0	0	0	0	0	0	0	0	0

	$a_{MgCr_2O_4}$					X					
Y	0	0.1	0.2	0.3	0.4	0.5	0.6	0.7	0.8	0.9	1
0	0	0.0841	0.1744	0.2701	0.3704	0.4740	0.5798	0.6867	0.7932	0.8981	1
0.1	0	0.0566	0.1192	0.1872	0.2602	0.3375	0.4184	0.5020	0.5876	0.6741	0.76063
0.2	0	0.0414	0.0880	0.1395	0.1958	0.2564	0.3210	0.3892	0.4603	0.5338	0.6089
0.3	0	0.0314	0.0672	0.1074	0.1520	0.2009	0.2538	0.3106	0.3709	0.4344	0.50073
0.4	0	0.0243	0.0525	0.0846	0.1207	0.1608	0.2049	0.2530	0.3050	0.3606	0.4198
0.5	0	0.0191	0.0415	0.0674	0.0969	0.1301	0.1672	0.2083	0.2533	0.3023	0.35524
0.6	0	0.0149	0.0326	0.0532	0.0771	0.1044	0.1352	0.1698	0.2083	0.2509	0.29762
0.7	0	0.0110	0.0243	0.0400	0.0584	0.0796	0.1040	0.1316	0.1629	0.1979	0.23693
0.8	0	0.0070	0.0156	0.0259	0.0380	0.0522	0.0687	0.0878	0.1095	0.1342	0.1622
0.9	0	0.0028	0.0062	0.0103	0.0153	0.0211	0.0280	0.0361	0.0454	0.0561	0.06843
1	0	0	0	0	0	0	0	0	0	0	0

	$a_{FeAl_2O_4}$					X					
Y	0	0.1	0.2	0.3	0.4	0.5	0.6	0.7	0.8	0.9	1
0	0	0	0	0	0	0	0	0	0	0	0
0.1	0.0538	0.0430	0.0338	0.0261	0.0196	0.0142	0.0099	0.0064	0.0037	0.0016	0
0.2	0.1809	0.1483	0.1195	0.0943	0.0725	0.0540	0.0384	0.0254	0.0149	0.0065	0
0.3	0.3117	0.2598	0.2127	0.1706	0.1334	0.1009	0.0729	0.0491	0.0293	0.0130	0
0.4	0.4201	0.3547	0.2944	0.2393	0.1897	0.1454	0.1066	0.0729	0.0441	0.0199	0
0.5	0.5051	0.4315	0.3624	0.2982	0.2393	0.1859	0.1380	0.0956	0.0586	0.0268	0
0.6	0.5760	0.4975	0.4225	0.3516	0.2854	0.2243	0.1686	0.1183	0.0735	0.0341	0
0.7	0.6452	0.5630	0.4832	0.4065	0.3337	0.2653	0.2017	0.1432	0.0901	0.0423	0
0.8	0.7266	0.6404	0.5552	0.4721	0.3918	0.3150	0.2422	0.1740	0.1108	0.0527	0
0.9	0.8371	0.7449	0.6524	0.5605	0.4701	0.3821	0.2972	0.2161	0.1392	0.0670	0
1	1	0.8985	0.7948	0.6899	0.5849	0.4807	0.3781	0.2781	0.1813	0.0733	0

	$a_{MgAl_2O_4}$					X					
Y	0	0.1	0.2	0.3	0.4	0.5	0.6	0.7	0.8	0.9	1
0	0	0	0	0	0	0	0	0	0	0	0
0.1	0	0.0103	0.0191	0.0263	0.0322	0.0367	0.0399	0.0420	0.0431	0.0433	0.0428
0.2	0	0.0315	0.0597	0.0844	0.1054	0.1228	0.1366	0.1470	0.1541	0.1583	0.1597
0.3	0	0.0494	0.0951	0.1365	0.1731	0.2047	0.2313	0.2527	0.2690	0.2806	0.2875
0.4	0	0.0608	0.1185	0.1721	0.2210	0.2647	0.3028	0.3351	0.3616	0.3821	0.3969
0.5	0	0.0670	0.1318	0.1935	0.2513	0.3043	0.3522	0.3944	0.4306	0.4606	0.4845
0.6	0	0.0701	0.1393	0.2065	0.2708	0.3315	0.3877	0.4389	0.4846	0.5244	0.5581
0.7	0	0.0722	0.1448	0.2166	0.2869	0.3546	0.4190	0.4793	0.5350	0.5854	0.6301
0.8	0	0.0749	0.1515	0.2288	0.3058	0.3817	0.4554	0.5263	0.5936	0.6566	0.7148
0.9	0	0.0797	0.1626	0.2476	0.3339	0.4207	0.5069	0.5917	0.6742	0.7538	0.8296
1	0	0.0881	0.1811	0.2783	0.3787	0.4815	0.5858	0.6907	0.7953	0.9397	1

Table A.3: Calculated activities in $(Fe_{1-X}, Mg_X)(Cr_{1-Y}, Al_Y)_2O_4$ at 1323 K

	$a_{FeCr_2O_4}$					X					
Y	0	0.1	0.2	0.3	0.4	0.5	0.6	0.7	0.8	0.9	1
0	1	0.8981	0.7934	0.6871	0.5805	0.4749	0.3714	0.2712	0.1753	0.0846	0
0.1	0.7780	0.9252	0.6357	0.5586	0.4788	0.3974	0.3154	0.2337	0.1533	0.0751	0
0.2	0.6329	0.5838	0.5296	0.4710	0.4088	0.3436	0.2762	0.2074	0.1379	0.0685	0
0.3	0.5273	0.4917	0.4511	0.4059	0.3564	0.3032	0.2468	0.1877	0.1264	0.0637	0
0.4	0.4468	0.4210	0.3904	0.3552	0.3155	0.2715	0.2237	0.1722	0.1175	0.0599	0
0.5	0.3810	0.3627	0.3399	0.3125	0.2807	0.2444	0.2037	0.1587	0.1096	0.0566	0
0.6	0.3206	0.3082	0.2918	0.2712	0.2463	0.2169	0.1828	0.1442	0.1008	0.0527	0
0.7	0.2553	0.2479	0.2371	0.2227	0.2044	0.1820	0.1552	0.1239	0.0877	0.0464	0
0.8	0.1741	0.1706	0.1649	0.1565	0.1452	0.1307	0.1128	0.0910	0.0652	0.0350	0
0.9	0.0727	0.0720	0.0703	0.0674	0.0632	0.0575	0.0502	0.0410	0.0297	0.0162	0
1	0	0	0	0	0	0	0	0	0	0	0

	$a_{MgCr_2O_4}$					X					
Y	0	0.1	0.2	0.3	0.4	0.5	0.6	0.7	0.8	0.9	1
0	0	0.1054	0.2183	0.3378	0.4626	0.5915	0.7231	0.8558	0.9882	1.1186	1
0.1	0	0.0970	0.1461	0.2298	0.3199	0.4155	0.5159	0.6201	0.7271	0.8358	0.94495
0.2	0	0.0495	0.1056	0.1680	0.2365	0.3109	0.3908	0.4755	0.5646	0.6574	0.75299
0.3	0	0.0366	0.0788	0.1267	0.1803	0.2396	0.3046	0.3749	0.4504	0.5308	0.61556
0.4	0	0.0276	0.0601	0.0976	0.1403	0.1884	0.2420	0.3012	0.3660	0.4363	0.5121
0.5	0	0.0211	0.0463	0.0759	0.1101	0.1494	0.1939	0.2440	0.2997	0.3614	0.42908
0.6	0	0.0159	0.0353	0.0583	0.0855	0.1172	0.1536	0.1953	0.2425	0.2956	0.35506
0.7	0	0.0114	0.0255	0.0426	0.0630	0.0871	0.1154	0.1482	0.1860	0.2292	0.27841
0.8	0	0.0070	0.0158	0.0266	0.0398	0.0556	0.0743	0.0964	0.1223	0.1524	0.18715
0.9	0	0.0027	0.0060	0.0102	0.0154	0.0218	0.0294	0.0385	0.0494	0.0622	0.07728
1	0	0	0	0	0	0	0	0	0	0	0

	$a_{FeAl_2O_4}$					X					
Y	0	0.1	0.2	0.3	0.4	0.5	0.6	0.7	0.8	0.9	1
0	0	0	0	0	0	0	0	0	0	0	0
0.1	0.0490	0.0407	0.0296	0.0224	0.0165	0.0118	0.0080	0.0051	0.0029	0.0012	0
0.2	0.1685	0.1358	0.1076	0.0835	0.0631	0.0462	0.0323	0.0211	0.0122	0.0052	0
0.3	0.2952	0.2424	0.1955	0.1545	0.1191	0.0888	0.0633	0.0421	0.0247	0.0109	0
0.4	0.4033	0.3363	0.2756	0.2213	0.1732	0.1312	0.0950	0.0642	0.0384	0.0172	0
0.5	0.4906	0.4148	0.3448	0.2808	0.2231	0.1715	0.1261	0.0865	0.0526	0.0238	0
0.6	0.5651	0.4840	0.4077	0.3365	0.2710	0.2113	0.1576	0.1097	0.0676	0.0312	0
0.7	0.6381	0.5534	0.4720	0.3947	0.3221	0.2546	0.1925	0.1359	0.0850	0.0397	0
0.8	0.7230	0.6345	0.5479	0.4641	0.3836	0.3072	0.2354	0.1686	0.1069	0.0507	0
0.9	0.8360	0.7424	0.6489	0.5565	0.4659	0.3781	0.2936	0.2131	0.1371	0.0659	0
1	1	0.8985	0.7949	0.6901	0.5852	0.4811	0.3786	0.2786	0.1817	0.0887	0

	$a_{MgAl_2O_4}$					X					
Y	0	0.1	0.2	0.3	0.4	0.5	0.6	0.7	0.8	0.9	1
0	0	0	0	0	0	0	0	0	0	0	0
0.1	0	0.0127	0.0202	0.0274	0.0327	0.0365	0.0390	0.0402	0.0405	0.0399	0.0386
0.2	0	0.0342	0.0637	0.0884	0.1085	0.1242	0.1358	0.1436	0.1480	0.1494	0.1482
0.3	0	0.0536	0.1015	0.1433	0.1790	0.2085	0.2320	0.2497	0.2619	0.2692	0.2719
0.4	0	0.0656	0.1260	0.1806	0.2289	0.2706	0.3056	0.3339	0.3557	0.3712	0.3809
0.5	0	0.0717	0.1395	0.2026	0.2601	0.3116	0.3568	0.3952	0.4270	0.4521	0.4706
0.6	0	0.0744	0.1464	0.2151	0.2797	0.3393	0.3935	0.4416	0.4835	0.5189	0.5478
0.7	0	0.0758	0.1509	0.2243	0.2950	0.3622	0.4252	0.4832	0.5359	0.5828	0.6235
0.8	0	0.0776	0.1563	0.2348	0.3124	0.3881	0.4611	0.5305	0.5958	0.6563	0.7115
0.9	0	0.0813	0.1654	0.2513	0.3381	0.4249	0.5108	0.5949	0.6764	0.7546	0.8288
1	0	0.0883	0.1815	0.2788	0.3792	0.4819	0.5862	0.6909	0.7954	0.8987	1

Table A.4: Calculated Al_2O_3 content in $(Al_Z, Cr_{1-Z})_2O_3$ in equilibrium with $(Fe_{1-X}, Mg_X)(Cr_{1-Y}, Al_Y)_2O_4$ at 1223, 1273 and 1323 K

	Z Value at 1223 K					X					
Y	0	0.1	0.2	0.3	0.4	0.5	0.6	0.7	0.8	0.9	1
0	0	0	0	0	0	0	0	0	0	0	0
0.1	0.1635	0.1477	0.1339	0.1218	0.1111	0.1015	0.0929	0.0851	0.0780	0.0716	0.0657
0.2	0.8520	0.8316	0.8045	0.7647	0.6887	0.4392	0.3387	0.2851	0.2474	0.2182	0.1943
0.3	0.9203	0.9134	0.9055	0.8964	0.8858	0.8733	0.8581	0.8391	0.8142	0.7788	0.7176
0.4	0.9420	0.9376	0.9328	0.9274	0.9214	0.9145	0.9067	0.8976	0.8871	0.8745	0.8592
0.5	0.9531	0.9499	0.9463	0.9424	0.9381	0.9333	0.9279	0.9218	0.9148	0.9069	0.8977
0.6	0.9607	0.9581	0.9554	0.9523	0.9490	0.9453	0.9412	0.9367	0.9316	0.9259	0.9194
0.7	0.9675	0.9656	0.9634	0.9611	0.9585	0.9557	0.9527	0.9493	0.9455	0.9413	0.9367
0.8	0.9756	0.9742	0.9727	0.9710	0.9692	0.9673	0.9652	0.9628	0.9603	0.9575	0.9544
0.9	0.9863	0.9855	0.9847	0.9839	0.9830	0.9820	0.9809	0.9797	0.9785	0.9771	0.9756
1	1	1	1	1	1	1	1	1	1	1	1

	Z Value at 1273 K					X					
Y	0	0.1	0.2	0.3	0.4	0.5	0.6	0.7	0.8	0.9	1
0	0	0	0	0	0	0	0	0	0	0	0
0.1	0.1510	0.1371	0.1249	0.1140	0.1043	0.0955	0.0876	0.0804	0.0739	0.0679	0.0625
0.2	0.8002	0.7639	0.7058	0.5768	0.4187	0.3415	0.2922	0.2557	0.2267	0.2028	0.1825
0.3	0.9025	0.8935	0.8832	0.8711	0.8566	0.8390	0.8168	0.7871	0.7437	0.6652	0.4912
0.4	0.9312	0.9259	0.9200	0.9134	0.9059	0.8973	0.8875	0.8759	0.8622	0.8456	0.8247
0.5	0.9455	0.9417	0.9376	0.9330	0.9279	0.9221	0.9157	0.9084	0.9000	0.8904	0.8792
0.6	0.9552	0.9523	0.9491	0.9457	0.9418	0.9376	0.9329	0.9277	0.9218	0.9152	0.9077
0.7	0.9637	0.9615	0.9591	0.9565	0.9536	0.9505	0.9471	0.9433	0.9391	0.9344	0.9292
0.8	0.9731	0.9716	0.9700	0.9682	0.9662	0.9641	0.9618	0.9593	0.9565	0.9535	0.9501
0.9	0.9852	0.9844	0.9835	0.9826	0.9816	0.9806	0.9794	0.9782	0.9768	0.9754	0.9738
1	1	1	1	1	1	1	1	1	1	1	1

	Z Value at 1323 K					X					
Y	0	0.1	0.2	0.3	0.4	0.5	0.6	0.7	0.8	0.9	1
0	0	0	0	0	0	0	0	0	0	0	0
0.1	0.1410	0.1095	0.1139	0.1028	0.0929	0.0842	0.0764	0.0694	0.0630	0.0573	0.0522
0.2	0.7212	0.6240	0.4711	0.3714	0.3101	0.2664	0.2326	0.2052	0.1824	0.1630	0.1463
0.3	0.8817	0.8675	0.8502	0.8287	0.8006	0.7616	0.7001	0.5829	0.4377	0.3521	0.2967
0.4	0.9192	0.9114	0.9024	0.8919	0.8797	0.8651	0.8472	0.8248	0.7952	0.7532	0.6848
0.5	0.9374	0.9319	0.9258	0.9189	0.9110	0.9019	0.8914	0.8789	0.8640	0.8458	0.8227
0.6	0.9494	0.9453	0.9408	0.9357	0.9300	0.9236	0.9163	0.9080	0.8983	0.8870	0.8736
0.7	0.9597	0.9566	0.9533	0.9496	0.9454	0.9408	0.9357	0.9299	0.9233	0.9159	0.9073
0.8	0.9707	0.9686	0.9663	0.9638	0.9611	0.9581	0.9547	0.9510	0.9469	0.9423	0.9371
0.9	0.9841	0.9830	0.9819	0.9806	0.9793	0.9778	0.9762	0.9744	0.9725	0.9703	0.9680
1	1	1	1	1	1	1	1	1	1	1	1